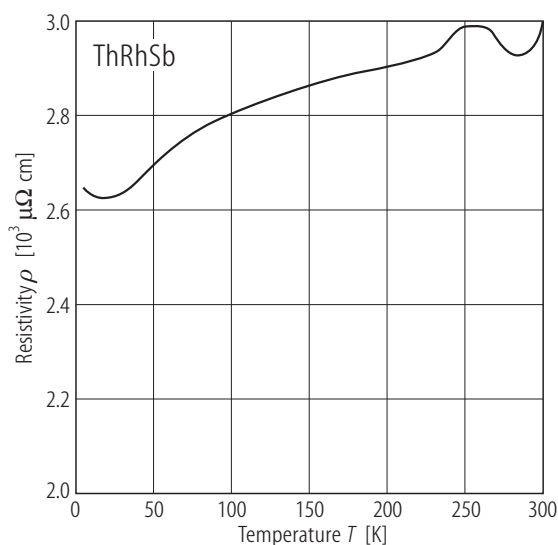
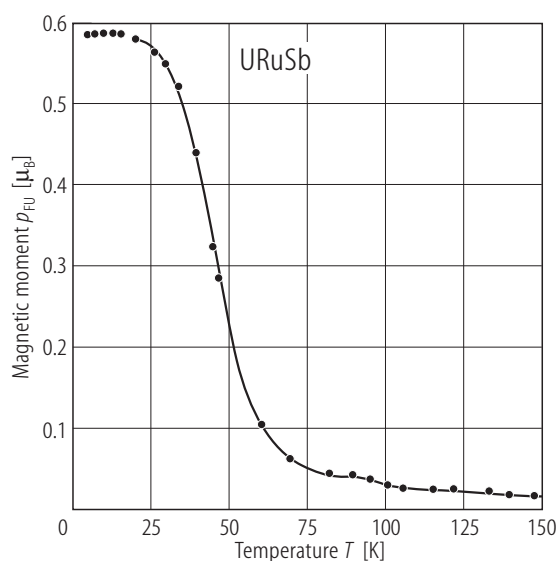


## 1.3.3.4.2. Figures and tables



**Fig. 1.** ThRhSb. Electrical resistivity,  $\rho$ , vs. temperature,  $T$  [87PNVV]. Note very large absolute values of the resistivity.



**Fig. 2.** URuSb. Magnetic moment,  $p_{\text{FU}}$ , vs. temperature,  $T$ , measured in a field of 1 T [87PNVV]. The compound orders ferromagnetically at  $T_C = 45$  K.

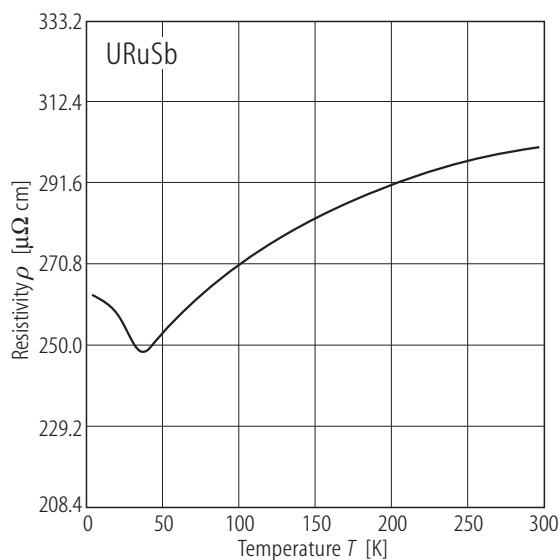


**Fig. 3.** URuSb. Electrical resistivity,  $\rho$ , vs. temperature,  $T$  [87PNVV]. The ferromagnetic phase transition at  $T_C = 45$  K manifests itself as a minimum in  $\rho(T)$ .

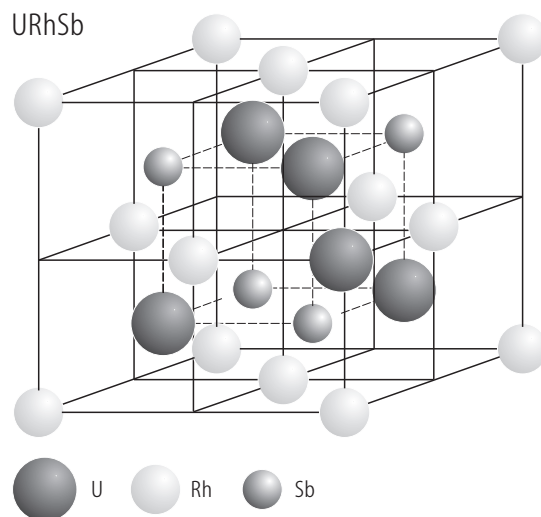


**Fig. 4.** URhSb. Crystal structure of the MgAgAs type [85BDPN].

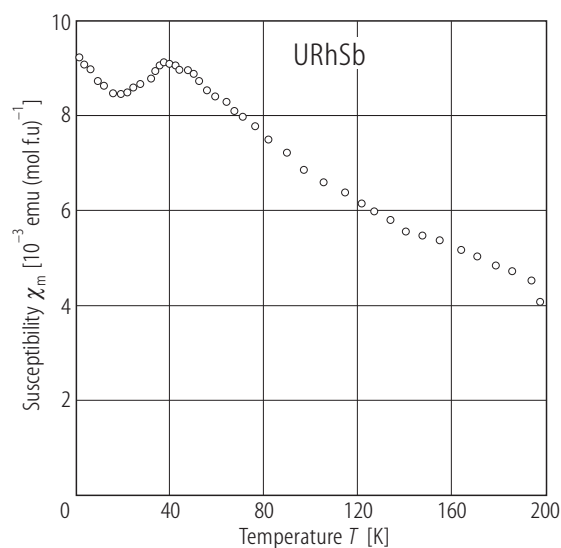


**Fig. 5.** URhSb. Molar magnetic susceptibility,  $\chi_m$ , vs. temperature,  $T$  [87PNVV]. The compound orders antiferromagnetically at  $T_N = 40$  K. At high temperatures the susceptibility follows a Curie-Weiss law with the parameters given in Table B.

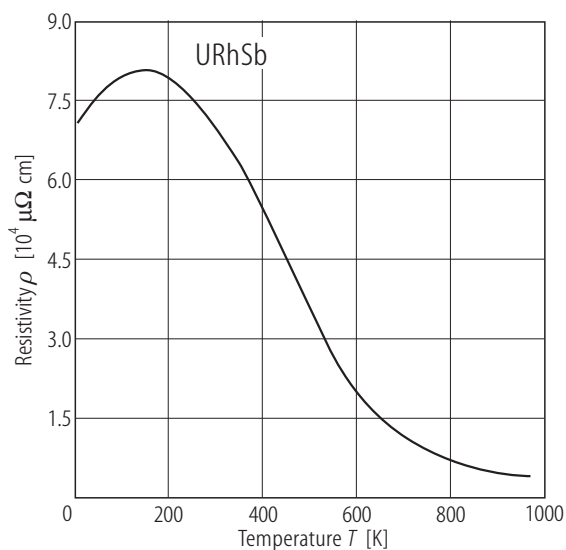


**Fig. 6.** URhSb. Electrical resistivity,  $\rho$ , vs. temperature,  $T$  up to 1000 K [87PNVV]. Note that there occurs no notable anomaly in  $\rho(T)$  at the onset of magnetic ordering at  $T_N = 40$  K (see Fig. 5). Above a pronounced maximum ( $8 \cdot 10^4 \mu\Omega$ cm) at 150 K, the resistivity exhibits a semiconducting-like behaviour. Fitting the high temperature data with an activation law yields the gap energy  $E_g$  of 0.44 eV. Deviation from the exponential behaviour at low temperatures the authors ascribed to a change of  $E_g$  due to the magnetic ordering.

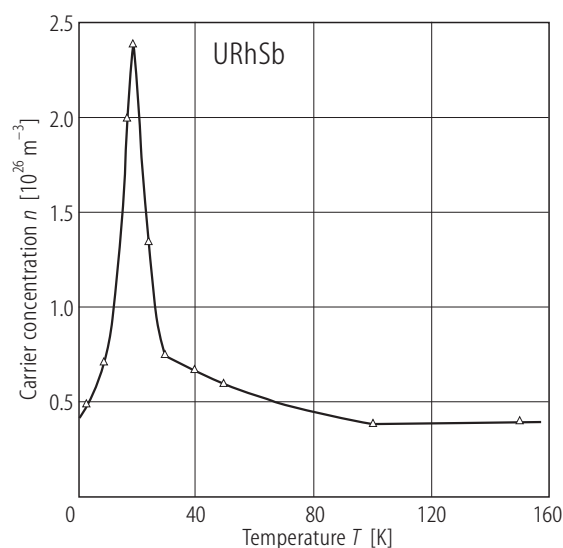


**Fig. 7.** URhSb. Carrier concentration,  $n$ , vs. temperature,  $T$ , as calculated from the Hall resistance measurements [87PNVV]. The dominant carriers are probably holes. Note that  $n$  is a factor 100 less than expected for metallic conductors and does not change much with decreasing temperature except for a peak around 20 K. The latter feature may be associated with a decrease of the semiconducting gap at the onset of magnetic ordering (see Fig. 6).

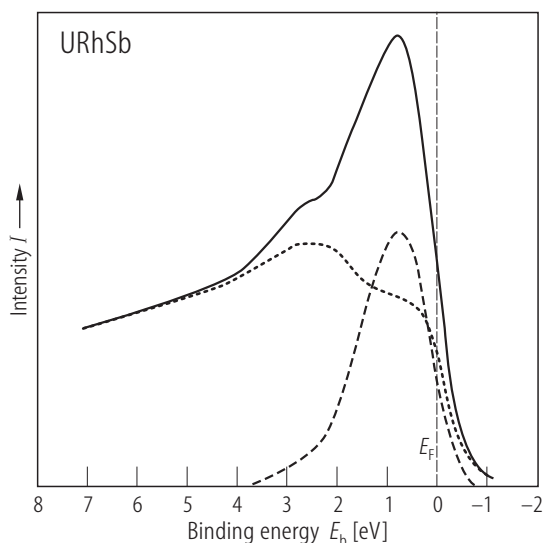


**Fig. 8.** URhSb. Valence band photoelectron energy distribution curves measured at 96 eV (dotted curve) and 98 eV (solid curve) photon energy [86HTB]. The spectra have been normalized against the photon intensity. Note a strong enhancement of the emission near  $E_F$  for a small increase of photon energy by 2 eV. The dashed curve is the U-5f contribution, obtained by subtracting the two experimental spectra. The width (FWHM) of this resonance is about 1.5 eV. Broadening of the 5f states as well as a shift of the d-like band from  $E_F$  towards higher binding energies is caused by f-d hybridization.

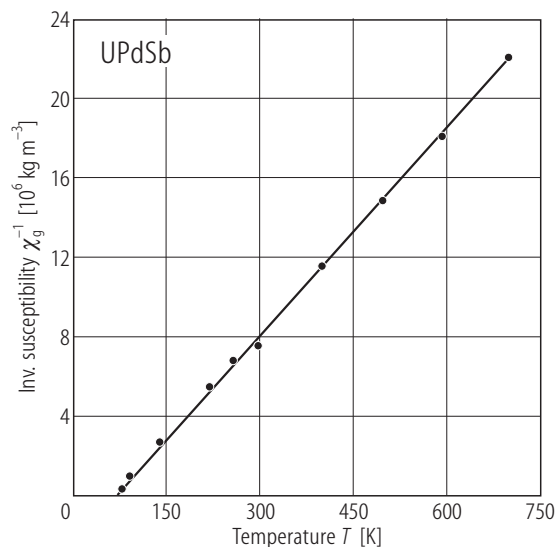


**Fig. 10.** UPdSb. Reciprocal mass magnetic susceptibility,  $\chi_g^{-1}$ , vs. temperature,  $T$ , up to 700 K [85BDPN]. The solid line is a Curie-Weiss fit with the parameters listed in Table B.

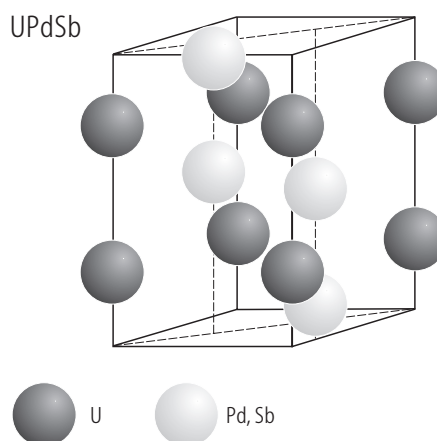


**Fig. 9.** UPdSb. Crystal structure of the  $\text{CaIn}_2$  type [85BDPN].

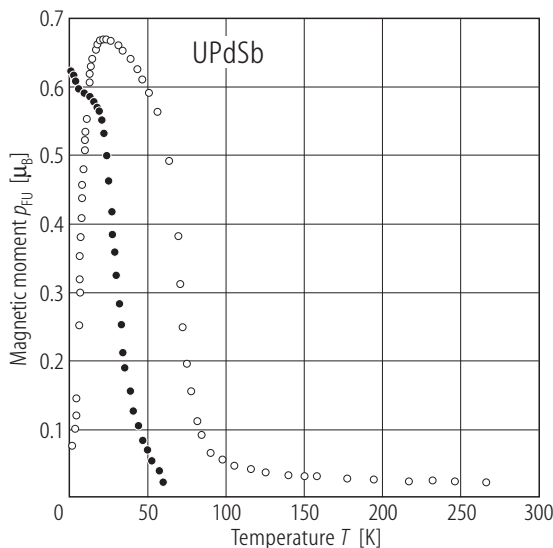


**Fig. 11.** UPdSb. Magnetic moment,  $p_{FU}$ , vs. temperature,  $T$ , measured in a field of 1 T (open circles) and remanence,  $p_{FU}^R$ , vs.  $T$  (full circles) [87PNVV]. The compound orders ferromagnetically at  $T_C = 65$  K. The remanent magnetization is  $0.65 \mu_B/\text{f.u.}$

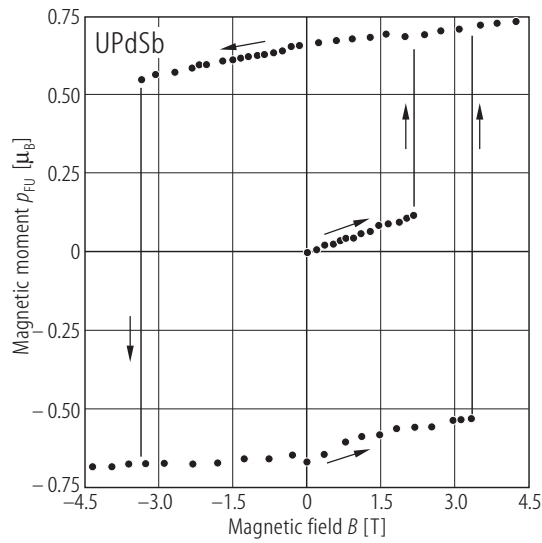


**Fig. 12.** UPdSb. Hysteresis loop,  $p_{\text{FU}}(B)$ , taken at  $T = 1.57$  K [87PNVV]. Note a very sharp transitions at the coercive field  $B_c = \pm 3.6$  T. Shape of the initial magnetization curve is characteristic of narrow domain-walls ferromagnets.

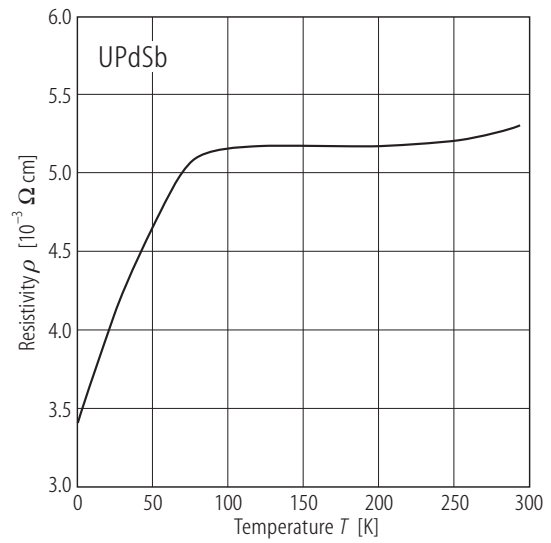


**Fig. 13.** UPdSb. Electrical resistivity,  $\rho$ , vs. temperature,  $T$  [87PNVV]. The pronounced kink in  $\rho(T)$  occurs at the temperature close to the ferromagnetic phase transition (see Fig. 11). Note very large absolute values of  $\rho$ , partly caused by the existence of many microcracks in the sample measured.

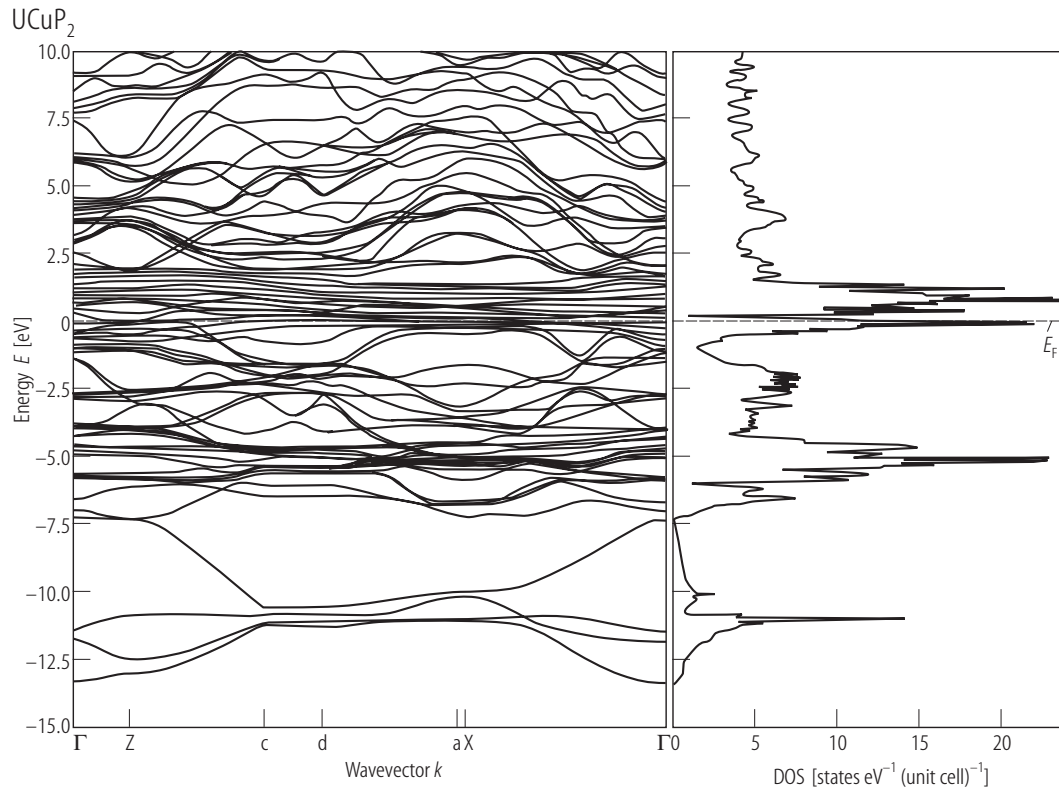


**Fig. 14.** UCuP<sub>2</sub>. Energy band structure and total density of states DOS [in states/(unit cell·eV)], calculated by the fully relativistic, spin-polarised LMTO method and density functional theory in the local spin-density approximation [02HNAH]. The von Barth – Hedin parametrization of the exchange potential was applied. The  $\mathbf{k}$  integrated functions were calculated on a grid of 349  $\mathbf{k}$  points in the irreducible part of the Brillouin zone.



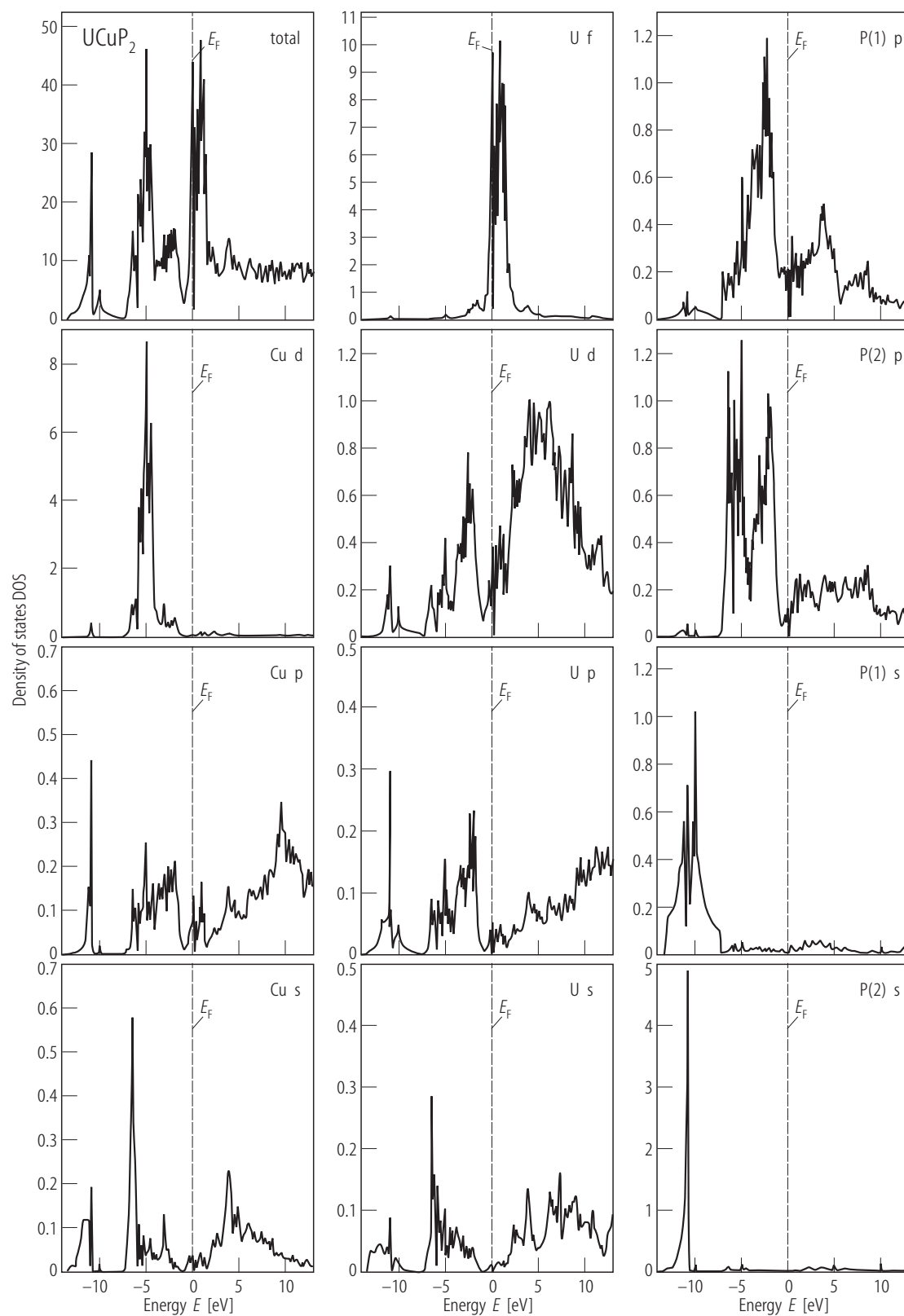


**Fig. 15.** For caption see next page

**Fig. 15.** UCuP<sub>2</sub>. Fully relativistic, spin-polarised total density of states [in states/(unit cell · eV); top panel] and partial densities of states [in states/(atom · eV)], calculated as in Fig. 14 [02HNAH]. The bands in the lowest energy region (from –13.4 up to –7.2 eV) have predominantly a P s character with some amount of U and Cu spd character mixed in. The bands between –7.2 and –0.4 eV consist of the P 3p states strongly hybridised with the Cu 3d and U 6d states. The Cu 3d states are fully occupied and located around 5.0 eV below the Fermi energy. The uranium 5f bands are located near  $E_F$  in the region –0.4 to 3.0 eV. At still higher energies there are antibonding U 6d states. Note a quasigap between phosphorus s and p states and a striking difference between the 3p partial DOS of the two crystallographically distinct P atoms (see Fig. 16). The P(1) site involves hybridization of P 3p states with U 6d states which results in a one-peak DOS structure below  $E_F$ , whereas the P(2) site yields hybridization of P 3d states with both U 6d and Cu 3d states and thus a two-peak DOS is observed at these energies.

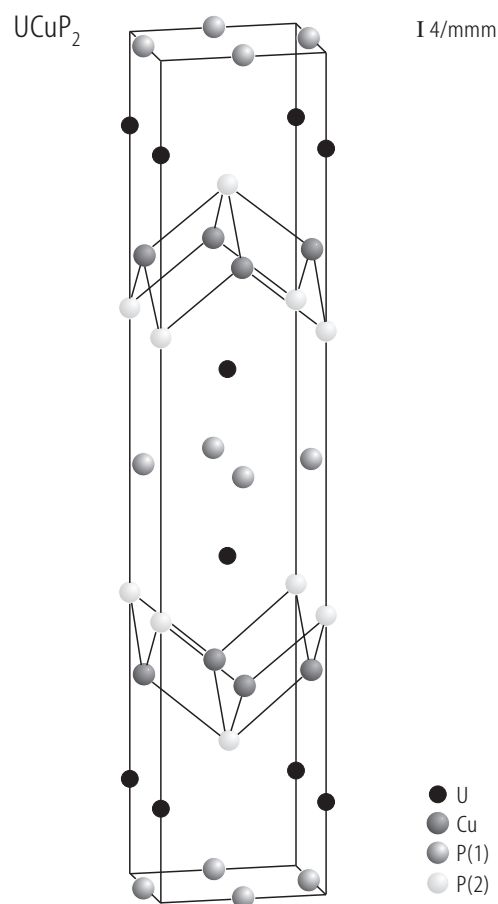


**Fig. 16.** UCuP<sub>2</sub>. Crystal structure [87NZKT1]. Thin full lines show a pyramidal arrangement of Cu and P(2) atoms.

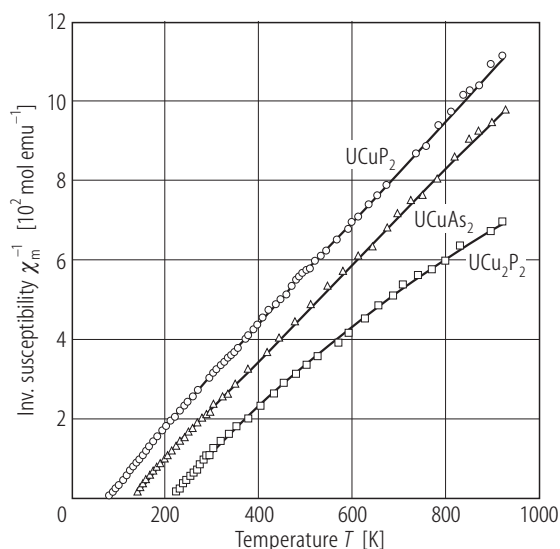


**Fig. 17.** UCuP<sub>2</sub>, UCuAs<sub>2</sub>, UCu<sub>2</sub>P<sub>2</sub>. Reciprocal molar magnetic susceptibility,  $\chi_m^{-1}$ , vs. temperature,  $T$ , up to 950 K [86ZKTN]. The compounds order ferromagnetically at 76, 131 and 216 K for UCuP<sub>2</sub> (circles), UCuAs<sub>2</sub> (triangles) and UCu<sub>2</sub>P<sub>2</sub> (squares), respectively. The solid lines are fits of  $\chi_m^{-1}(T)$  to the formula  $\chi_m^{-1} = \left( \frac{A}{T} + B \right)^{-1} + \lambda$  from which the effective magnetic moment  $p_p = (8A)^{1/2}$  of 2.53, 2.48 and 2.28  $\mu_B$  is calculated for UCuP<sub>2</sub>, UCuAs<sub>2</sub> and UCu<sub>2</sub>P<sub>2</sub>, respectively.

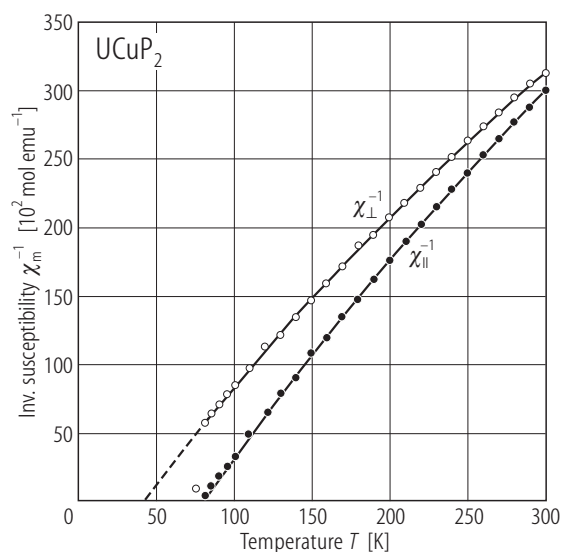


**Fig. 18.**  $\text{UCuP}_2$ . Longitudinal,  $\chi_{||}^{-1}$ , (full circles) and transversal,  $\chi_{\perp}^{-1}$ , (open circles) reciprocal molar magnetic susceptibility vs. temperature,  $T$  [91KTN]. The solid lines are modified Curie-Weiss fits with the parameters given in Table B.

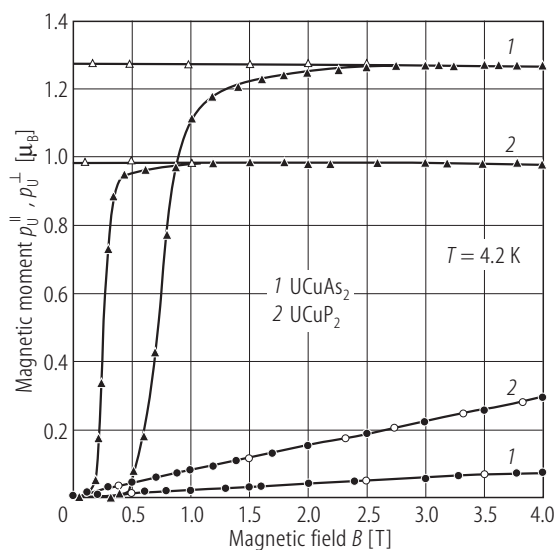


**Fig. 21.**  $\text{UCuP}_2$ ,  $\text{UCuAs}_2$ . Magnetic moment,  $p_U$ , measured at 4.2 K along (triangles) and perpendicular (circles) to the tetragonal  $c$ -axis, respectively, with increasing (full symbols) and decreasing (open symbols) magnetic field vs. magnetic field,  $B$  [91KTN]. Note a strong uniaxial anisotropy with the easy-magnetization direction being the  $c$ -axis. The anisotropy constant  $K_1$  is estimated as  $9 \cdot 10^5$  and  $5 \cdot 10^6 \text{ J/m}^3$  for the phosphide and the arsenide, respectively. The corresponding anisotropy field is about 13 and 70 T, respectively. The saturation uranium magnetic moment amounts to 0.98 and  $1.27 \mu_B$  in  $\text{UCuP}_2$  and  $\text{UCuAs}_2$ , respectively.

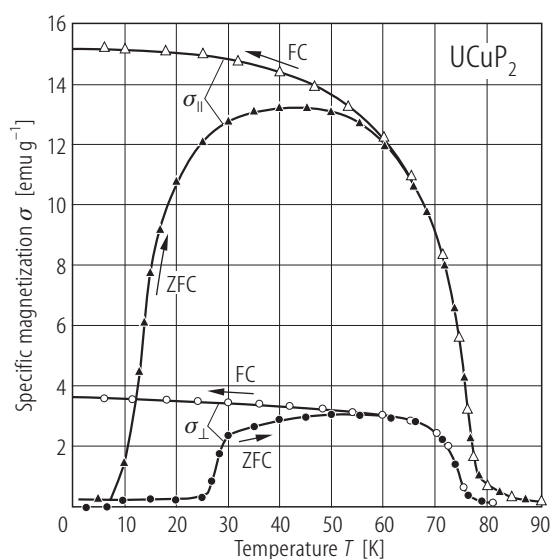


**Fig. 19.**  $\text{UCuP}_2$ . Specific magnetization,  $\sigma_{||}$  and  $\sigma_{\perp}$ , measured in a field of 0.1 T along (triangles) and perpendicular (circles) to the tetragonal  $c$ -axis, respectively, with cooling the sample with (FC, open symbols) and without (ZFC, full symbols) an applied magnetic field, vs. temperature,  $T$  [91KTN]. The compound orders ferromagnetically at  $T_C = 75 \text{ K}$ . Note a pronounced domain effect and strong magnetic anisotropy.

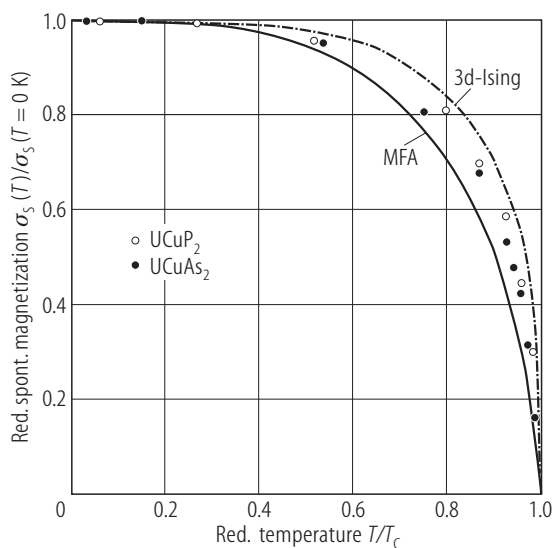


**Fig. 20.**  $\text{UCuP}_2$ ,  $\text{UCuAs}_2$ . Reduced spontaneous magnetization,  $\sigma_s(T)/\sigma_s(T = 0 \text{ K})$  vs. reduced temperature,  $T/T_C$ , as derived from the data of Figs. 22 and 38 by means of the Arrott plots of the type shown in Fig. 22(b) [91KTN]. Open circles:  $\text{UCuP}_2$ ; full circles:  $\text{UCuAs}_2$ . The full and dashed lines are the theoretical functions obtained within the molecular field approximation and the 3d-Ising model, respectively.

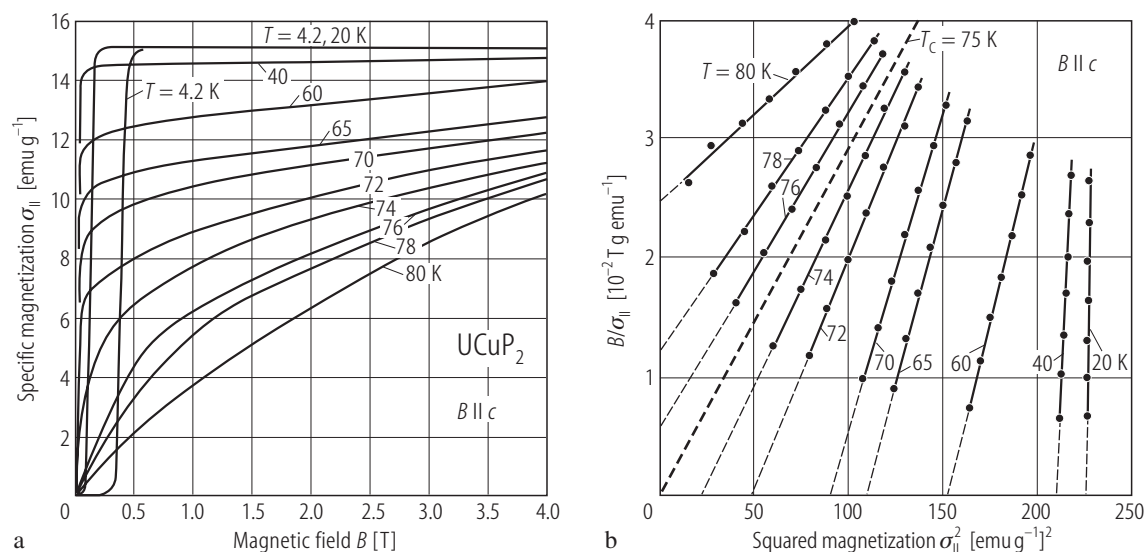


**Fig. 22.**  $\text{UCuP}_2$ . (a) Specific magnetization,  $\sigma_{||}$ , along to the easy-magnetization  $c$ -axis vs. magnetic field,  $B$ , measured at several temperatures specified in the figure [91KTN]. Note a rather large value of the nucleation field of magnetization taken at 4.2 K,  $B_{\text{nf}} = 0.3$  T, that indicates the presence at

low temperatures of a compensated narrow-wall domain structure, which is rapidly reconstructed at  $B_{\text{nf}}$ . (b) Arrott plot,  $B/\sigma_{||}$  vs.  $\sigma_{||}^2$ , of the data from panel (a) [91KTN]. The Curie temperature is 75 K.

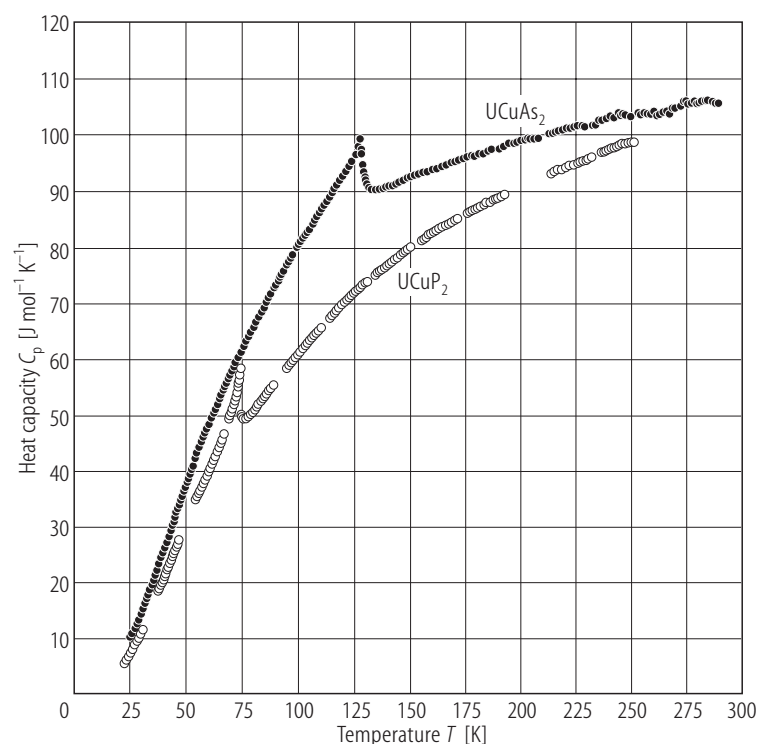


**Fig. 23.**  $\text{UCuP}_2$ ,  $\text{UCuAs}_2$ . Heat capacity,  $C_p$ , vs. temperature,  $T$ , in the range 20...300 K measured on small single crystals with a dynamic adiabatic technique [93BKWS]. The ferromagnetic phase transitions at  $T_C$  of 74.3 and 128.8 K for the phosphide and the arsenide, respectively, are clearly seen. The magnetic entropy of ordering, estimated using an approximation of the lattice contribution to the heat capacity by a Debye function with a temperature dependent Debye temperature, amounts to about 1.2 J/mol K for  $\text{UCuP}_2$  and 3.1 J/mol K for  $\text{UCuAs}_2$ . These strongly reduced values of the entropy ( $< R \ln 2$ ) may suggest slightly delocalised character of the 5f electrons, as supported also by the reduced values of the ordered magnetic moments (see Fig. 21) and the presence of Kondo effect (see Figs. 25 and 40). Alternatively, the low entropy may be explained by a crystal field effect that results in a singlet ground state.

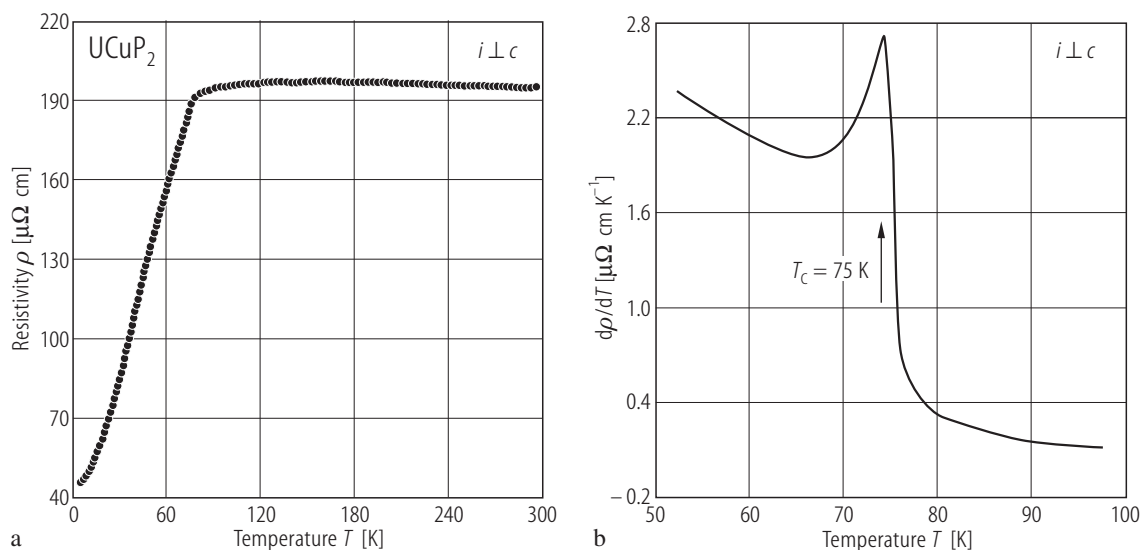


**Fig. 24.**  $\text{UCuP}_2$ . (a) Electrical resistivity,  $\rho$ , vs. temperature,  $T$ , measured on a single crystal with  $i \perp c$ -axis [91KTN]. Below 17 K the resistivity can be approximated by the function:  $\rho(T) = \rho_0 + c_m T^2$  with the parameters:  $\rho_0 = 48 \mu\Omega\text{cm}$  and  $c_m = 0.1 \mu\Omega\text{cm/K}^2$ , which describes scattering of

the conduction electrons on impurities and magnons. For  $\rho(T)$  measured up to 1000 K see Fig. 25. (b) Temperature derivative of the resistivity,  $d\rho/dT$ , vs.  $T$  in the vicinity of  $T_C$  [91KTN]. Note a sharp maximum at  $T_C = 75 \text{ K}$ .

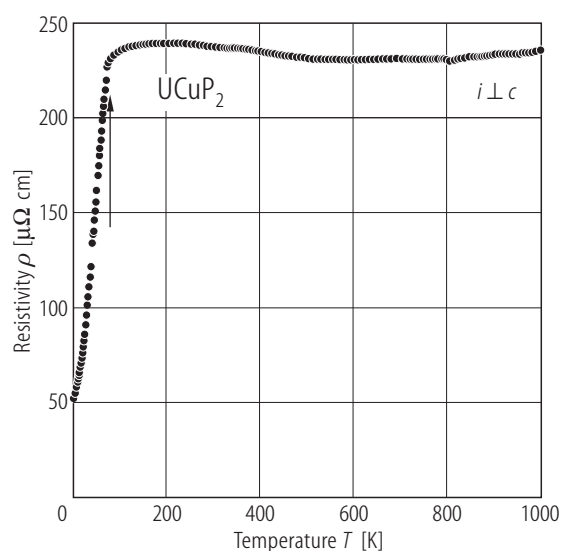


**Fig. 25.**  $\text{UCuP}_2$ . Electrical resistivity,  $\rho$ , vs. temperature,  $T$ , up to 1000 K, measured on a single crystal with  $i \perp c$ -axis [89KSK]. The arrow marks a ferromagnetic phase transition at  $T_C = 73(1) \text{ K}$ . For  $T < 10 \text{ K}$  the resistivity follows a  $T^2$  law (compare Fig. 24). Above 400 K the resistivity can be described by the formula  $\rho(T) = a + c_{ph} T - c_K \ln T$ , with the parameters  $a = 392.75 \mu\Omega\text{cm}$ ,  $c_{ph} = 0.049 \mu\Omega\text{cm/K}$  and  $c_K = 30 \mu\Omega\text{cm}$ , suggesting the presence of a weak Kondo effect. The electron concentration calculated from  $c_K$  is 0.15  $e^-/\text{formula unit}$  (see the caption of Fig. 26 for the value derived from the Hall data).

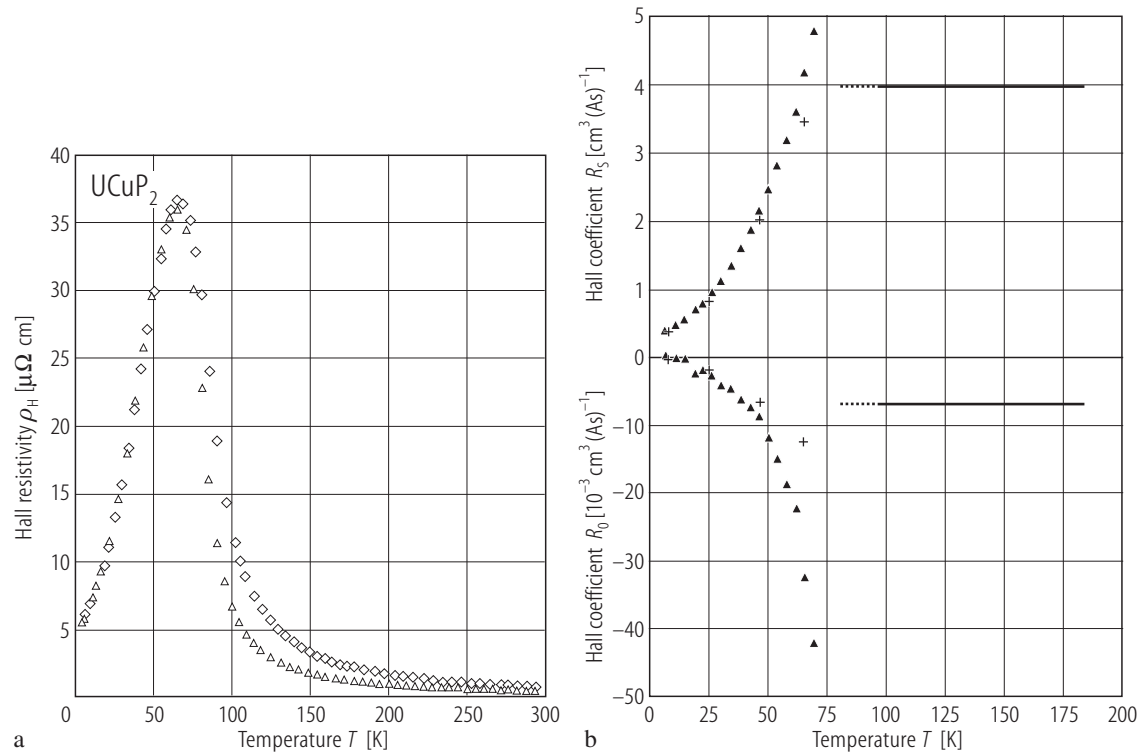


**Fig. 26.** UCuP<sub>2</sub>. **(a)** Hall resistivity,  $\rho_H$ , vs. temperature,  $T$ , measured on a single crystal with  $i \perp c$ -axis in a magnetic field of 2 T (triangles) and 4 T (diamonds) applied parallel to the easy magnetization  $c$ -axis [89KSK]. **(b)** Ordinary,  $R_0$ , and extraordinary,  $R_s$ , Hall coefficients vs.  $T$  [89KSK]. Crosses: the data obtained from Hall measurements at a few constant temperatures as a function of magnetic field strength up to 10 T; triangles: the data calculated from the

curves shown in panel (a). The horizontal lines denote  $R_0$  and  $R_s$  in the paramagnetic region where they are assumed to be constant. For  $T > T_C$ :  $R_0 = -6.7 \cdot 10^{-3} \text{ cm}^3/\text{As}$ ,  $R_s = 3.97 \text{ cm}^3/\text{As}$ . The concentration of free carriers estimated from  $R_0$  within a single parabolic band model amounts to only 0.063 electrons per formula unit (see the caption of Fig. 25 for the value derived from the electrical resistivity data).

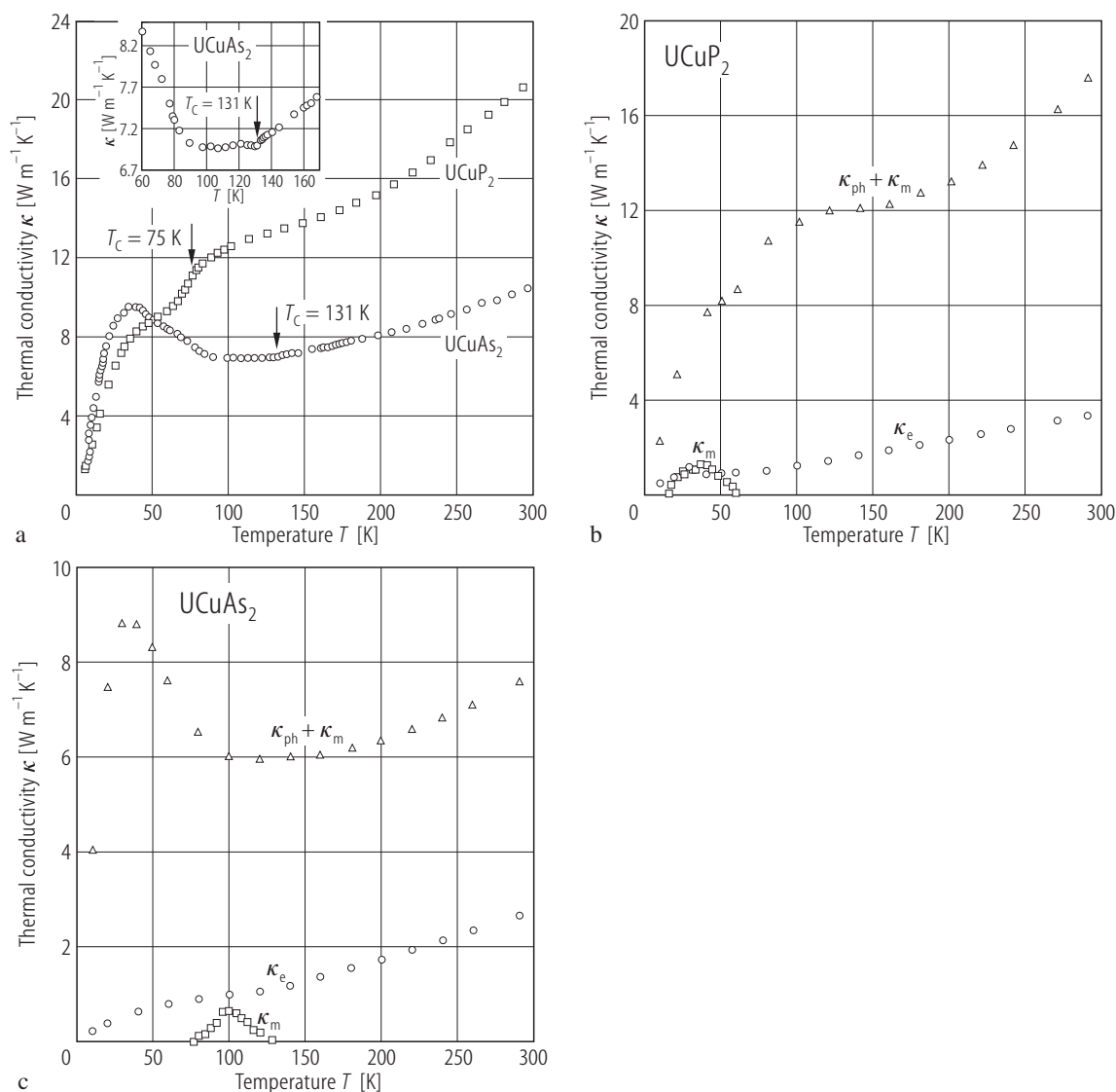


**Fig. 27.**  $\text{UCuP}_2$ ,  $\text{UCuAs}_2$ . **(a)** Thermal conductivity,  $\kappa$  vs. temperature,  $T$ , measured on single crystals within the tetragonal  $ab$ -plane [92MMKJ]. Squares:  $\text{UCuP}_2$ ; circles:  $\text{UCuAs}_2$ . The arrows mark the ferromagnetic phase transitions. Inset:  $\kappa(T)$  for  $\text{UCuAs}_2$  in the vicinity of  $T_c$ . **(b)** Electronic,  $\kappa_e$ , (circles) lattice + magnon,  $\kappa_{ph} + \kappa_m$ , (triangles) and magnon,  $\kappa_m$ , (squares) contributions to the

total thermal conductivity vs.  $T$  for  $\text{UCuP}_2$  [92MMKJ]. **(c)** Electronic,  $\kappa_e$ , (circles) lattice + magnon,  $\kappa_{ph} + \kappa_m$ , (triangles) and magnon,  $\kappa_m$ , (squares) contributions to the total thermal conductivity vs.  $T$  for  $\text{UCuAs}_2$  [92MMKJ]. For the method of decomposition of  $\kappa(T)$  shown in panel (a) into the contributions presented in panels (b) and (c) refer to the original paper.

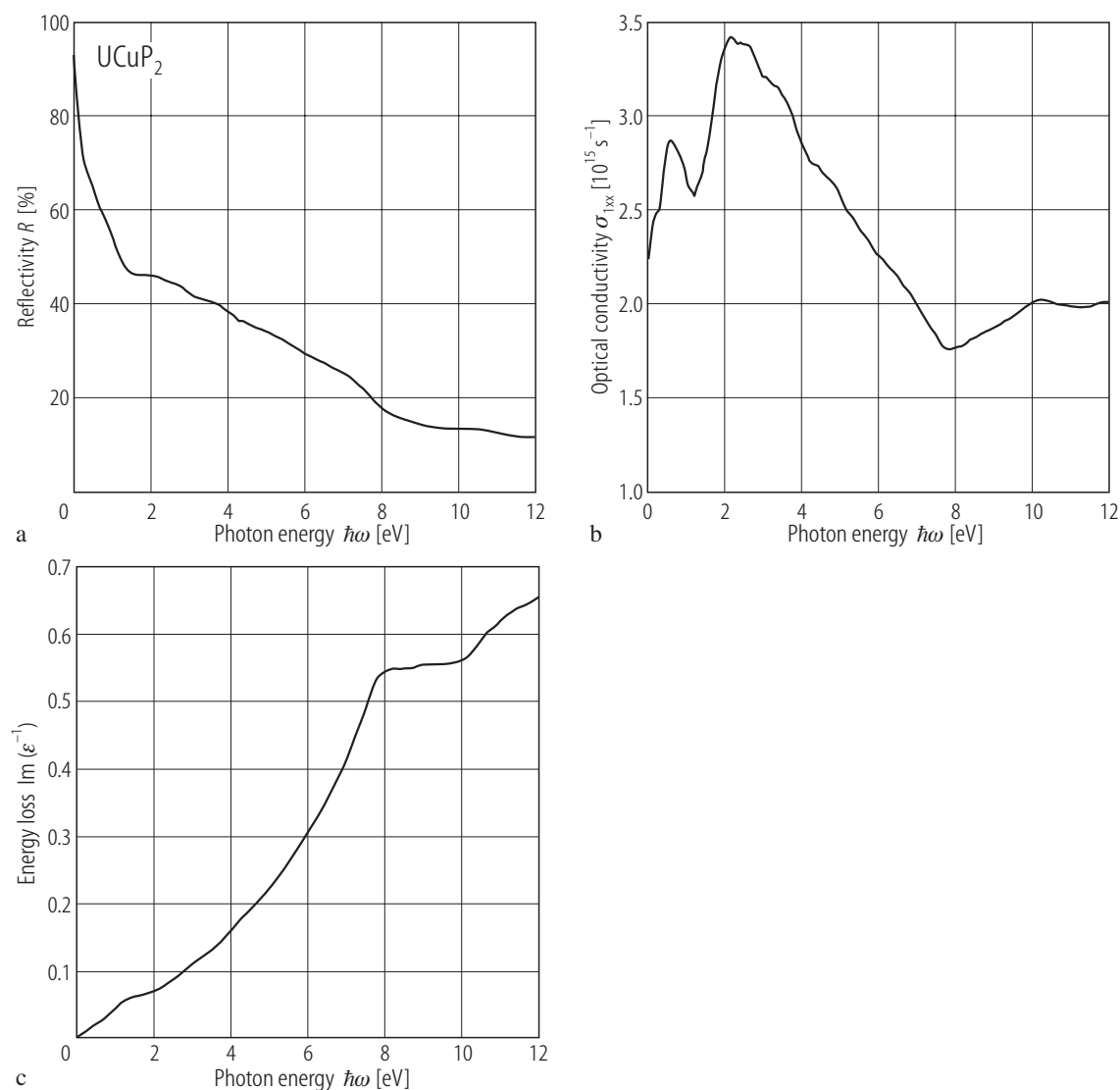


**Fig. 28.** UCuP<sub>2</sub>. **(a)** Near normal optical reflectivity,  $R$ , vs. photon energy,  $\hbar\omega$ , in the range of 0.03 to 12 eV, measured at 300 K on a natural grown surface perpendicular to the  $c$ -axis [88FSK]. Note a metallic behaviour with a very steep decrease of  $R$  at the lowest energies and a weakly pronounced plasma minimum. Both findings indicate that free carriers in the compound are strongly damped and that they overlap with interband transitions (visible at higher energies). **(b)** Real part of the optical conductivity,  $\sigma_{1xx}$ , vs.  $\hbar\omega$ , calculated from the data shown in panel **(a)** [88FSK]. The peak at 0.55 eV is an  $f \rightarrow d$  interband transition (see

Fig. 29), the peaks at 2.6, 3.4 and 4.6 eV have predominantly  $p \rightarrow d$  or  $p \rightarrow s$  character with some contribution of a transition of bonding phosphorus  $p$  and uranium  $d$  states into empty uranium  $f$  states. **(c)** Energy loss,  $\text{Im}(\epsilon^{-1})$ , vs.  $\hbar\omega$ , calculated from the reflectivity data shown in panel **(a)** [88FSK]. The maxima at 1.5 and 7.8 eV are associated with plasmons. The number of free carriers is estimated as being several tenths of an electron per formula unit and these are assigned to uranium derived  $d$  conduction electrons.



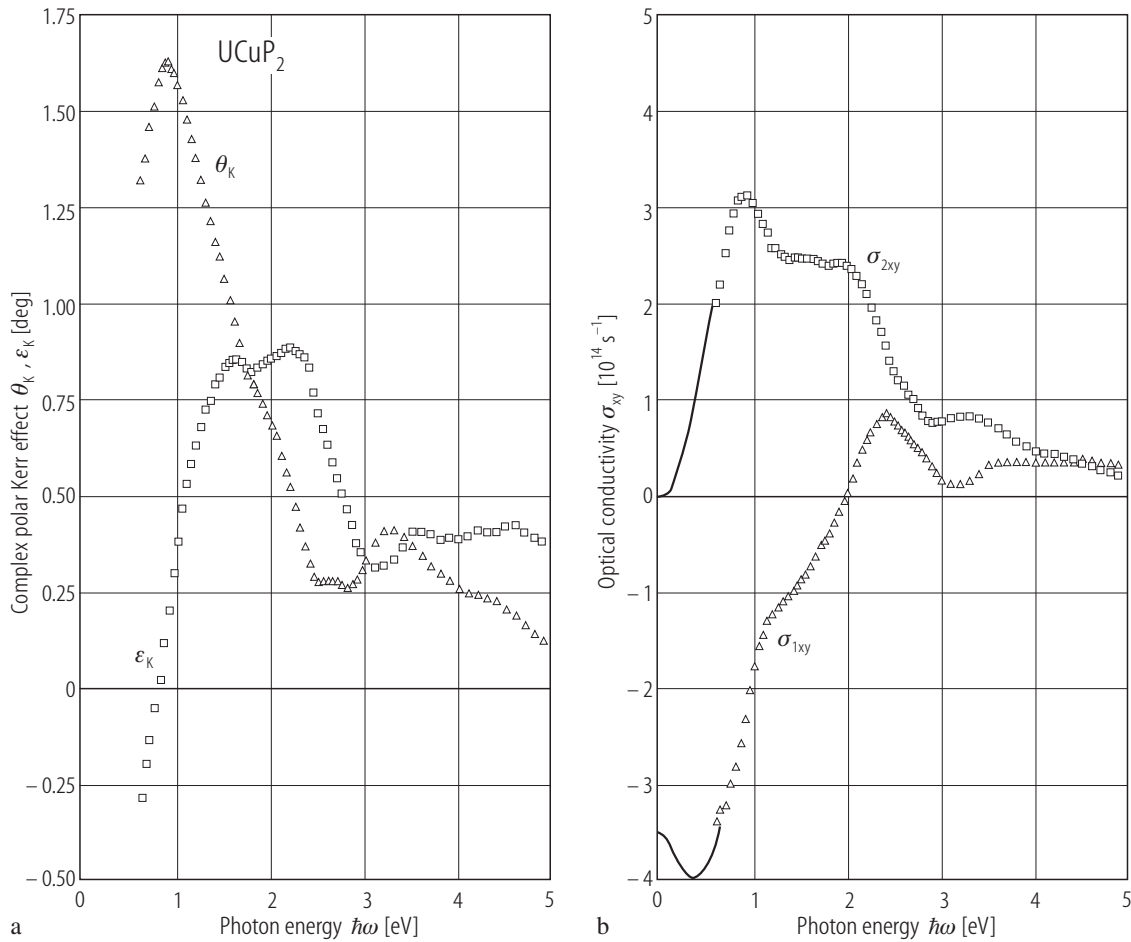


**Fig. 29.** UCuP<sub>2</sub>. **(a)** Polar Kerr rotation,  $\theta_K$ , and polar Kerr ellipticity,  $\epsilon_K$ , vs. photon energy,  $\hbar\omega$ , in the range of 0.6 to 5 eV, measured at 10 K and at a magnetic field  $B$  of 4 T ( $B \parallel c$ -axis) on a natural grown surface perpendicular to the easy magnetization  $c$ -axis [88FSK]. The maximum value of  $\theta_K$  is 1.6 deg at 0.8 eV. **(b)** Real,  $\sigma_{1xy}$ , and imaginary,  $\sigma_{2xy}$ , part of the off-diagonal conductivity vs.  $\hbar\omega$ , calculated from the Kerr effect shown in panel (a) using the reflectivity data from Fig. 28 [88FSK]. The solid lines are extrapolations to zero energy, obtained using the mutual Kramers-Kronig

transformation between  $\sigma_{1xy}$  and  $\sigma_{2xy}$ . The structure in  $\sigma_{1xy}$  at 0.35 eV corresponds to the peak at 0.55 eV in the real part of the optical conductivity (see Fig. 28) and is attributed to an  $f \rightarrow d$  transition. The energy difference of 0.2 eV between these two structures can be accounted for by free electron contribution. The peak at 2.0 eV (seen also in  $\sigma_{1xx}$ ; compare Fig. 28) is assigned to a transition from bonding phosphorus p and uranium d states into empty uranium f states

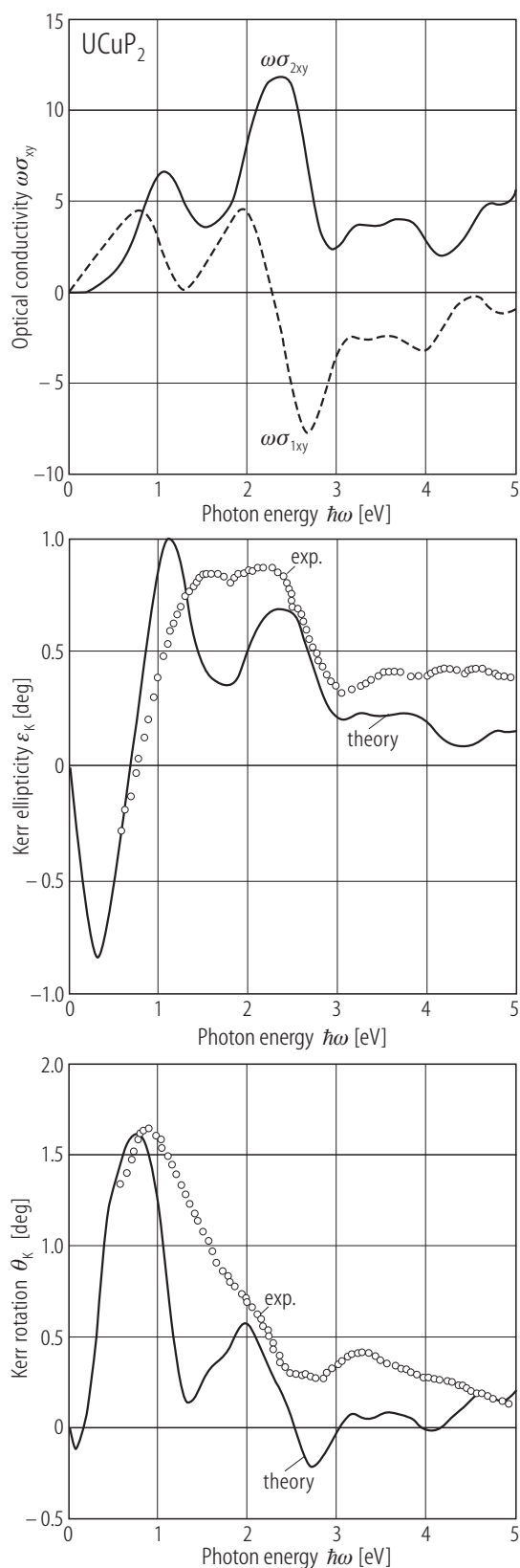


**Fig. 30.**  $\text{UCuP}_2$ . Kerr rotation,  $\theta_K$  (bottom panel), Kerr ellipticity,  $\varepsilon_K$  (middle panel), and off-diagonal optical conductivity,  $\omega\sigma_{xy}$  (upper panel), vs. photon energy,  $\hbar\omega$ , calculated ab initio by the LSDA method (solid and dashed lines), as compared to the experimental data (circles) taken from [88FSK] (see Fig. 29) [02HNAH]. Note a good agreement between the theoretical and experimental magneto-optical data except for a small energy shift by about 0.1 eV in the position of the prominent peak both in  $\theta_K(\omega)$  and  $\varepsilon_K(\omega)$ , and the fact that the calculated spectra exhibit much sharper features than the experimental ones. The peaks in  $\theta_K(\omega)$  observed at 0.7 and 2.0 eV originate mainly from U 6d  $\rightarrow$  5f interband transitions, while the interband transitions from Cu 3d to U 5f bands occur above 4 eV (compare Fig. 29).

For Fig. 31 see next page

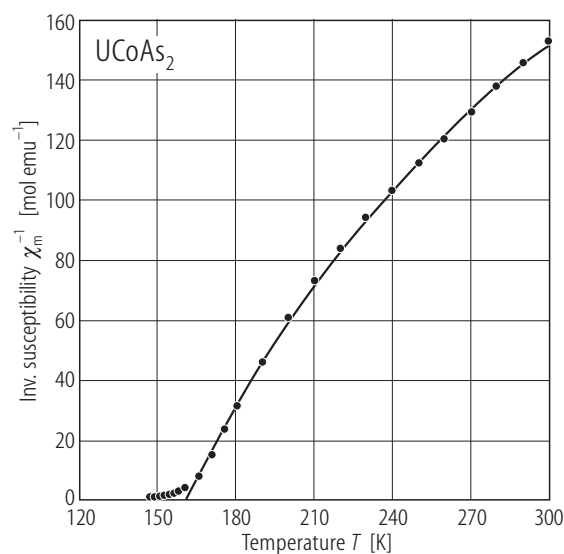


**Fig. 32.**  $\text{UCoAs}_2$ . Reciprocal molar magnetic susceptibility,  $\chi_m^{-1}$ , vs. temperature,  $T$ , above 150 K [00KNP]. The solid line is a modified Curie-Weiss fit with the parameters given in Table B. The compound orders ferromagnetically at  $T_C = 150(3)$  K (see Fig. 33).

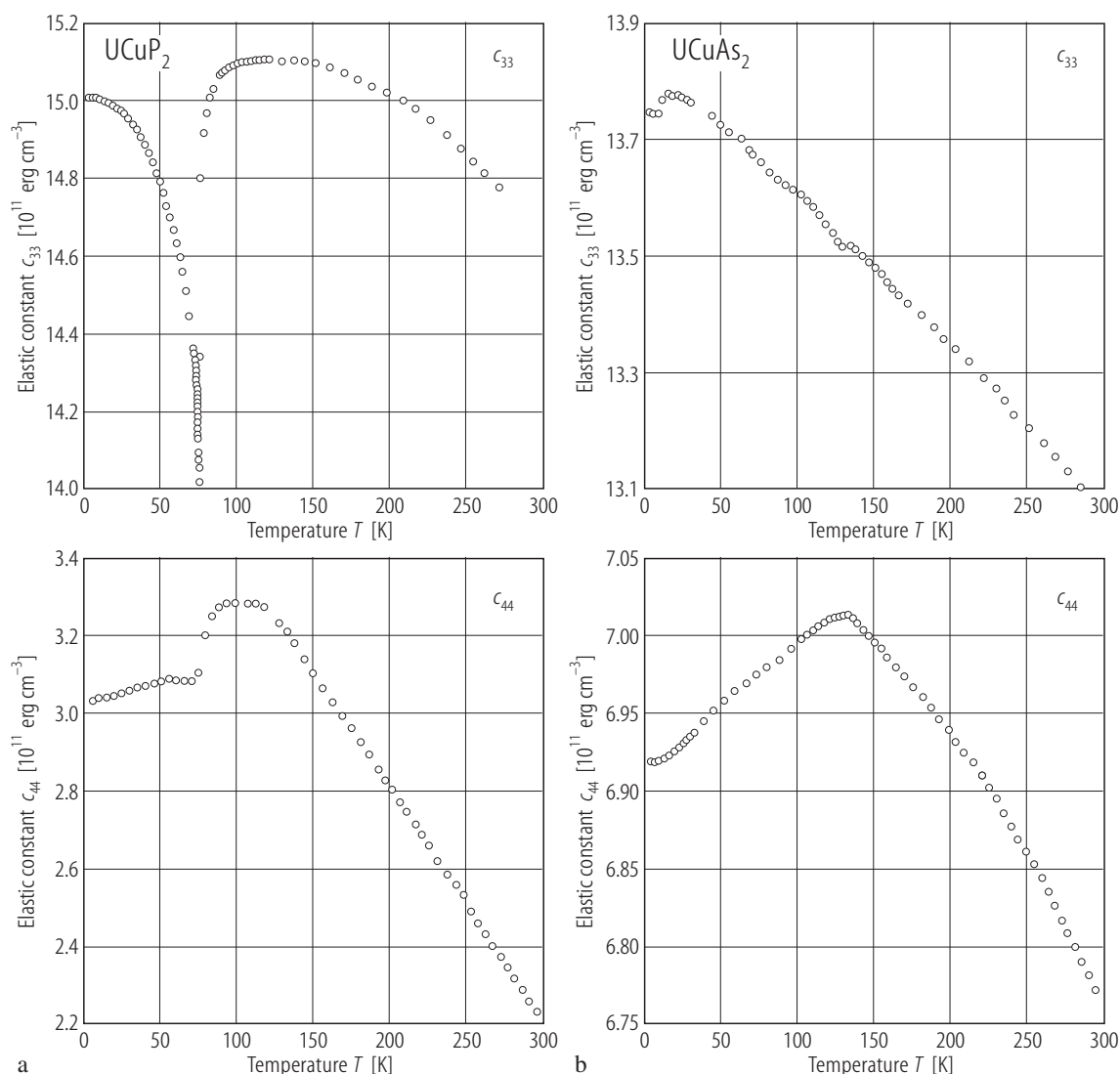


**Fig. 31.**  $\text{UCuP}_2$ ,  $\text{UCuAs}_2$ . Longitudinal,  $c_{33}$ , and shear,  $c_{44}$ , elastic constants vs. temperature,  $T$ , measured with ultrasound propagating along the  $c$ -axis [93KFL]. **(a)**  $\text{UCuP}_2$ ; **(b)**  $\text{UCuAs}_2$ . For  $\text{UCuP}_2$  note a strong softening (ca. 7%) of both constants near the ferromagnetic phase transition at 75 K and  $c_{33}(T)$  resembling the temperature variation of the squared magnetization. For  $\text{UCuAs}_2$  the absence of any minimum in  $c_{44}(T)$  at  $T_C = 131$  K indicates that the small dip seen in  $c_{33}(T)$  may be caused by volume magnetostrictive spin-phonon interaction. For both

compounds the elastic properties in the ordered region are dominated by phonon-magnon interactions, while in the paramagnetic region they reflect a sound-wave coupling either to spin fluctuations or spin energy density both influenced by crystal field effect. Velocity of sound propagating at  $T = 4.2$  K in  $\text{UCuP}_2$  along  $[001]$ :  $4.1 \cdot 10^3$  and  $2.0 \cdot 10^3$  m/s for ion displacement along and perpendicular to  $[001]$ , respectively. The same velocities for  $\text{UCuAs}_2$ :  $3.7 \cdot 10^3$  and  $2.6 \cdot 10^3$  m/s, respectively.

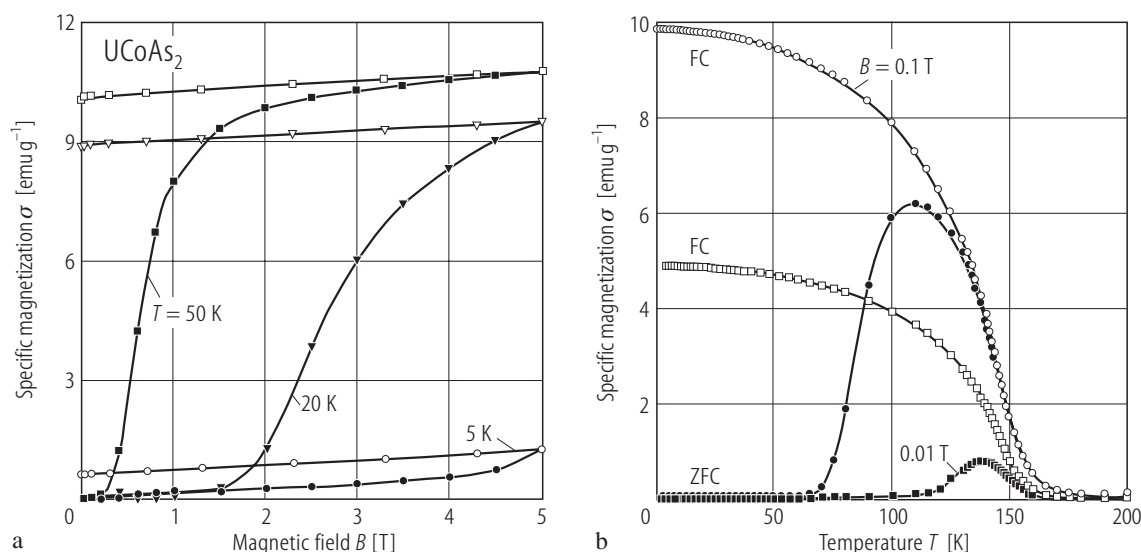


**Fig. 33.**  $\text{UCoAs}_2$ . **(a)** Specific magnetization,  $\sigma$ , vs. magnetic field,  $B$ , measured at 5 K (circles), 20 K (triangles) and 50 K (squares) with increasing (filled symbols) and decreasing (open symbols) magnetic field [00KNP]. **(b)** Specific magnetization,  $\sigma$ , vs. temperature,  $T$ , measured in a magnetic field of 0.01 T (squares) and 0.1 T

(circles) upon cooling in zero (filled symbols) and non-zero (open symbols) field [00KNP]. The solid lines serve as guides for the eye. The compound is ferromagnetic below  $T_C = 150(3)$  K with the spontaneous magnetic moment of about  $1.8 \mu_B$ . Note pronounced domain effects in both  $\sigma(B)$  and  $\sigma(T)$ .

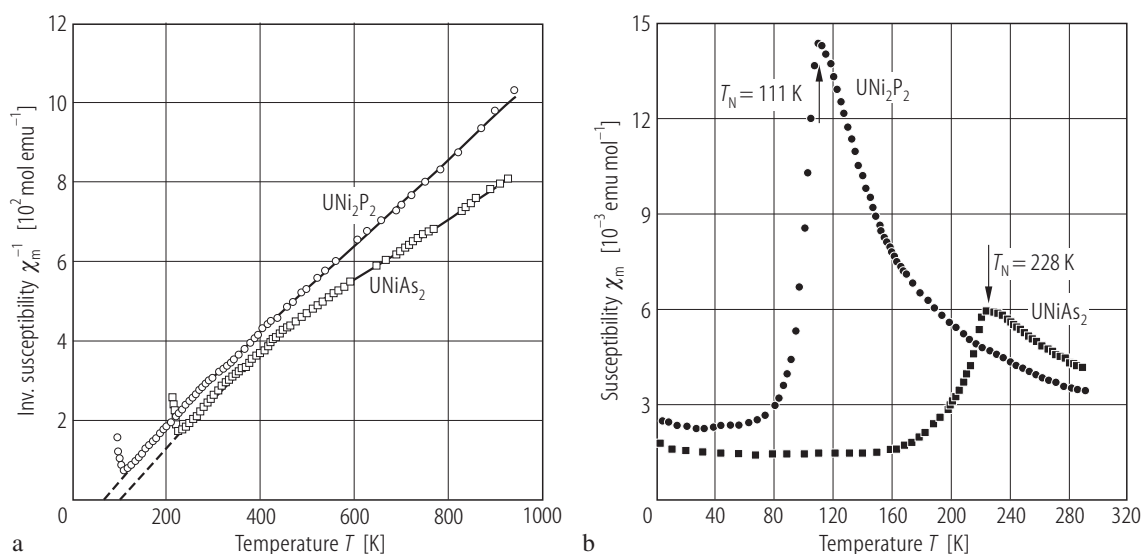
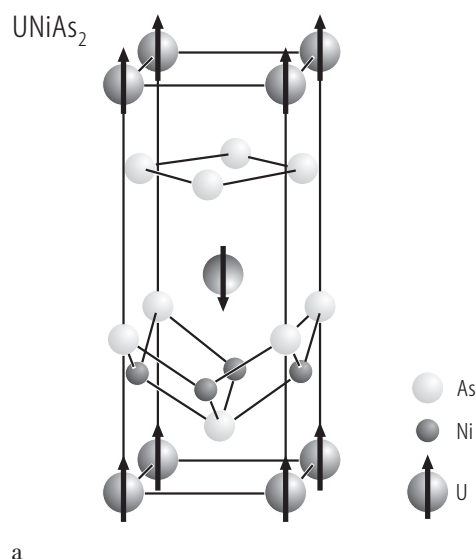
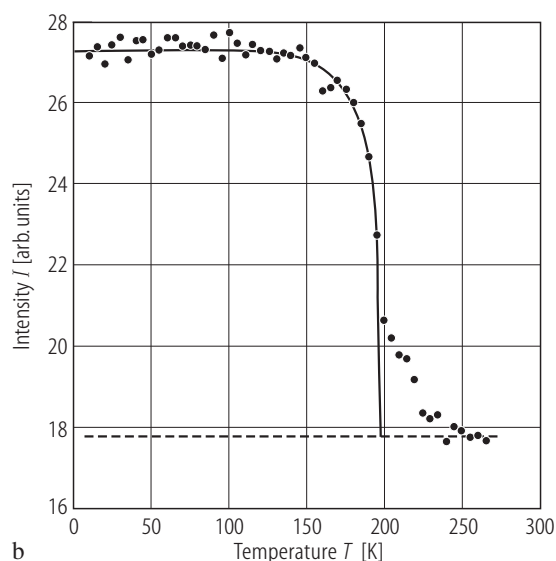


**Fig. 34.**  $\text{UNi}_2\text{P}_2$ ,  $\text{UNiAs}_2$ . **(a)** Reciprocal molar magnetic susceptibility,  $\chi_m^{-1}$ , vs. temperature,  $T$ , up to 950 K [86ZKTN]. The compounds are antiferromagnets with  $T_N$  of 111 K for  $\text{UNi}_2\text{P}_2$  (circles) and 228 K for  $\text{UNiAs}_2$  (squares). The lines are fits of  $\chi_m^{-1}(T)$  to the formula

$\chi_m^{-1} = \left( \frac{A}{T} + B \right)^{-1} + \lambda$  from which the effective magnetic moment  $p_p = (8A)^{1/2}$  of  $2.45$  and  $2.26 \mu_B$  is calculated for  $\text{UNi}_2\text{P}_2$  and  $\text{UNiAs}_2$ , respectively. **(b)** Molar magnetic susceptibility,  $\chi_m$ , vs.  $T$  [86ZKTN]. The arrows mark the magnetic phase transitions.



a



b

**Fig. 35.**  $\text{UNiAs}_2$ . **(a)** Magnetic structure [90MFK]. The structure is of the AF-I – type with the magnetic moments aligned along the four-fold axis, which form ferromagnetic (001) sheets coupled antiferromagnetically along the  $c$ -axis with a sequence  $+-+-$ . **(b)** Peak intensity of the magnetic reflection (100),  $I$ , vs. temperature,  $T$  [89FMKT]. The solid line is a guide for the eye, the dashed line marks the

background intensity. The uranium ordered magnetic moment at 7.5 K amounts to  $1.85(6) \mu_B$ . The Néel temperature is 195 K, i.e. considerably lower than that found from magnetic susceptibility measurements (compare Fig. 34). However, a pronounced tail above 195 K may suggest the occurrence of another magnetic phase before reaching the paramagnetic region.

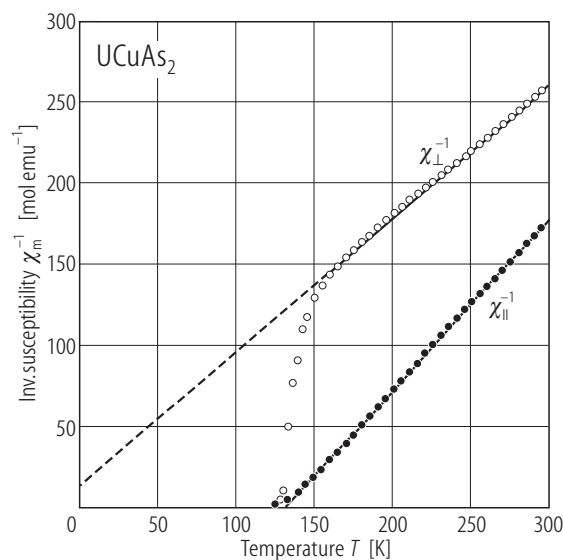


**Fig. 36.**  $\text{UCuAs}_2$ . Longitudinal,  $\chi_{||}^{-1}$ , (full circles) and transversal,  $\chi_{\perp}^{-1}$ , (open circles) reciprocal molar magnetic susceptibility vs. temperature,  $T$  [91KTN]. The solid lines are modified Curie-Weiss fits with the parameters given in Table B. Note a large anisotropy due to crystal field effect.

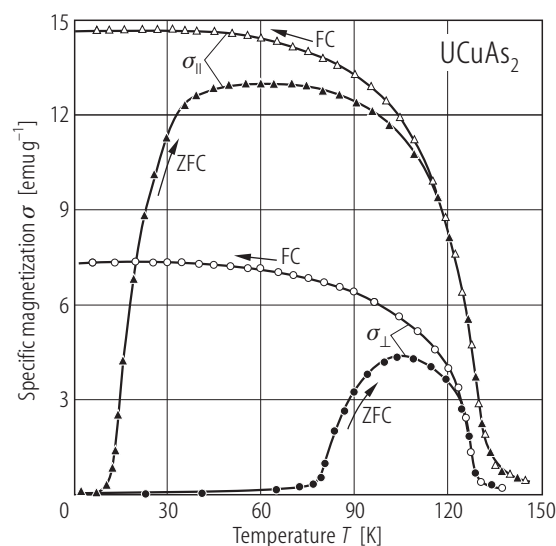


**Fig. 37.**  $\text{UCuAs}_2$ . Specific magnetization,  $\sigma_{||}$  and  $\sigma_{\perp}$ , measured in a field of 0.2 T along (triangles) and perpendicular (circles) to the tetragonal  $c$ -axis, respectively, with cooling the sample with (FC, open symbols) and without (ZFC, full symbols) an applied magnetic field, vs. temperature,  $T$  [91KTN]. The compound orders ferromagnetically at  $T_C = 133$  K. Note a pronounced domain effect and strong magnetic anisotropy.

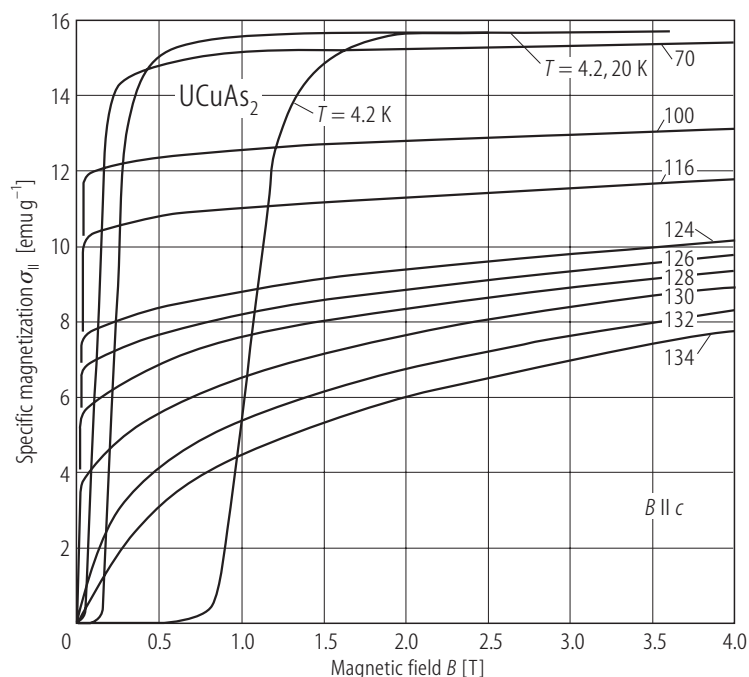
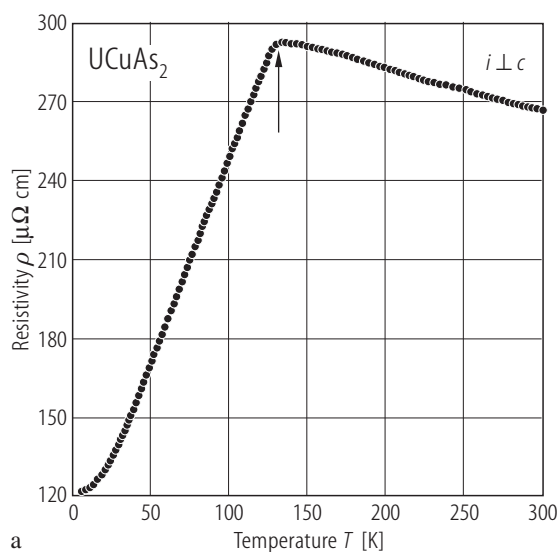
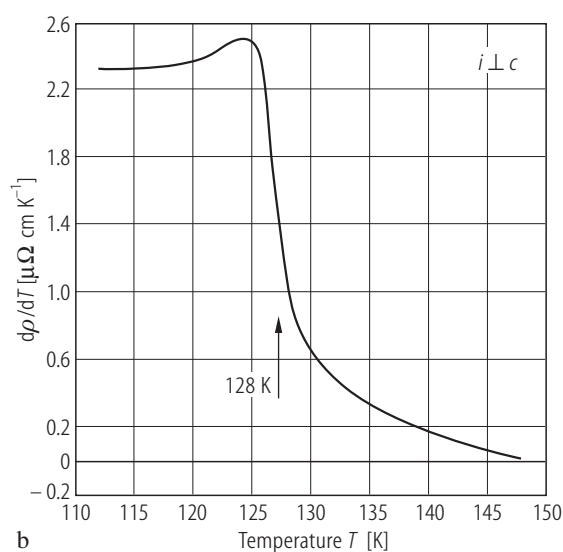


**Fig. 38.**  $\text{UCuAs}_2$ . Specific magnetization,  $\sigma_{||}$ , along the easy-magnetization  $c$ -axis vs. magnetic field,  $B$ , measured at several temperatures specified in the figure [91KTN]. Note a rather large value of the nucleation field of magnetization taken at 4.2 K,  $B_{\text{nf}} = 0.5$  T, that indicates at low temperatures the presence of a compensated narrow-wall domain structure, which is rapidly reconstructed at  $B_{\text{nf}}$ .



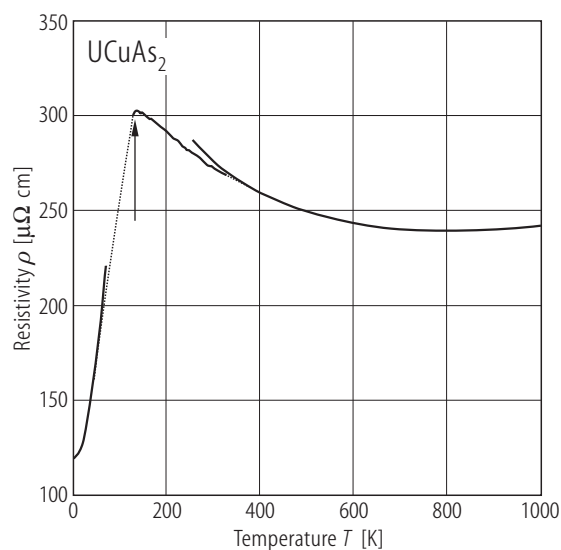
a



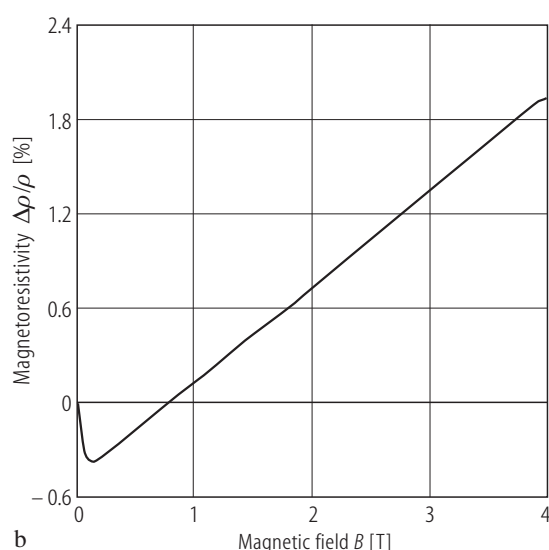
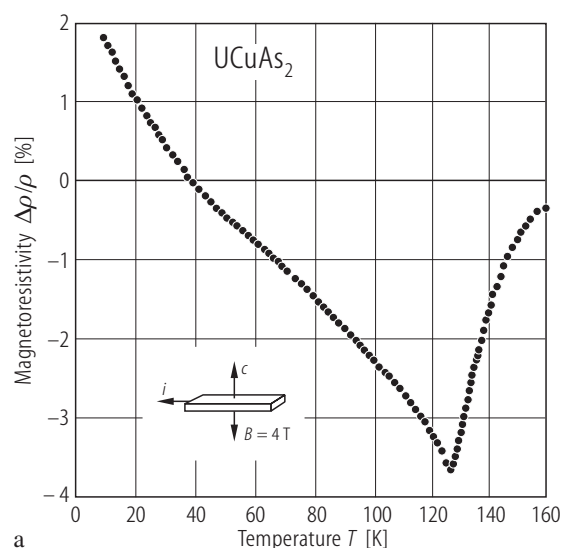
b

**Fig. 39.**  $\text{UCuAs}_2$ . (a) Electrical resistivity,  $\rho$ , vs. temperature,  $T$ , measured on a single crystal with  $i \perp c$ -axis [91KTN]. The arrow marks a ferromagnetic phase transition at  $T_C = 131$  K. Below 45 K the resistivity can be approximated by the function:  $\rho(T) = \rho_0 + c_m T^2$  with the parameters:  $\rho_0 = 120 \mu\Omega\text{cm}$  and  $c_m = 0.2 \mu\Omega\text{cm/K}^2$ , which

describes scattering of the conduction electrons on impurities and magnons. A negative slope in  $\rho(T)$  in the paramagnetic region suggests the presence of Kondo interactions (see also Fig. 40). (b) Temperature derivative of the resistivity,  $d\rho/dT$ , vs.  $T$  in the vicinity of the Curie temperature [91KTN].

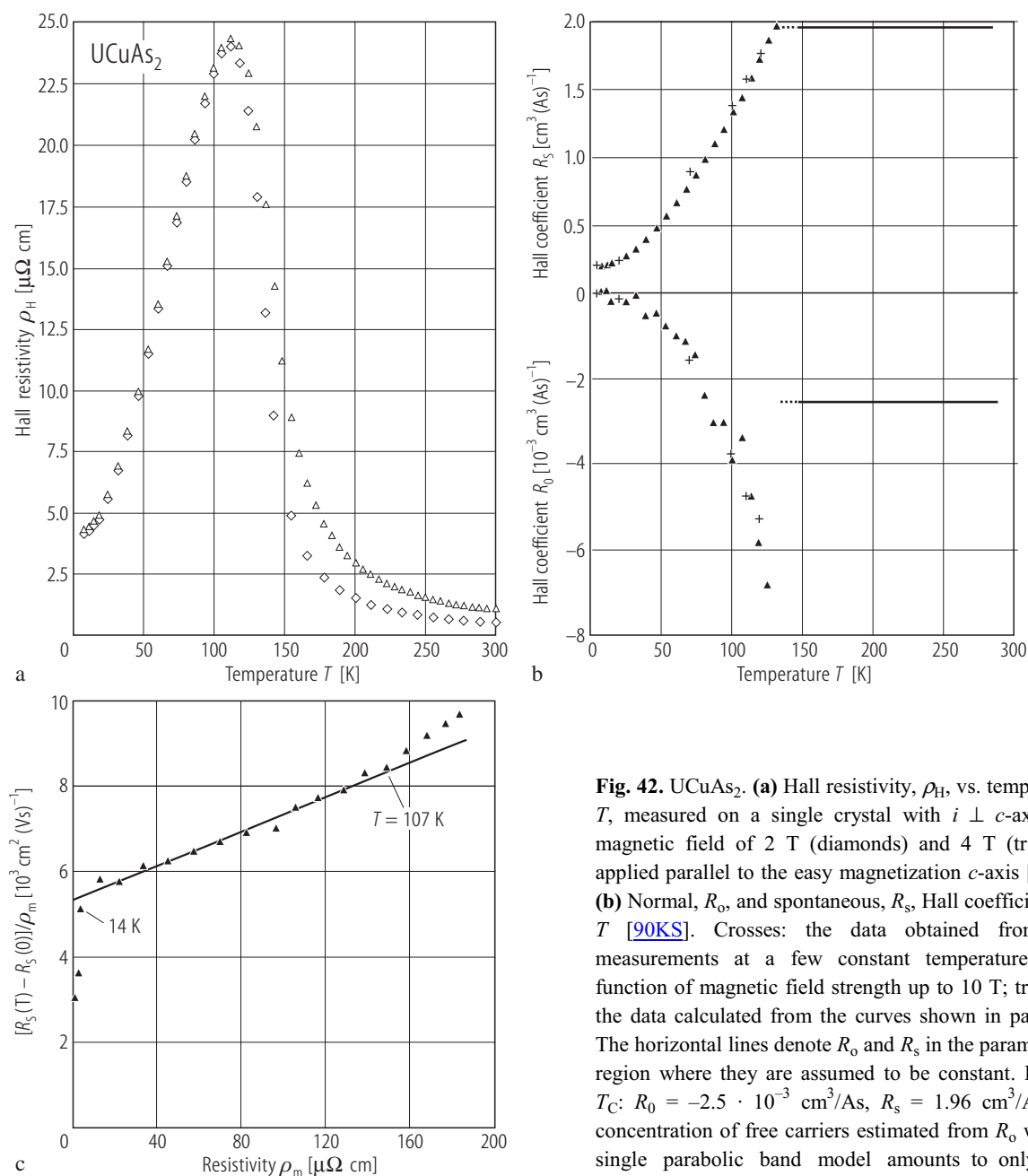


**Fig. 40.** UCuAs<sub>2</sub>. Electrical resistivity,  $\rho$ , vs. temperature,  $T$ , from 2 K up to 1000 K measured on a single crystal with  $i \perp c$ -axis [90KS]. The arrow marks a ferromagnetic phase transition at  $T_C = 131$  K. Note a negative slope in  $\rho(T)$  in the paramagnetic region with a shallow minimum around 840 K, which is interpreted as a Kondo effect. The solid curves are least-squares fits of the resistivity to the functions:  $\rho(T) = \rho_0 + c_m T^2$  (for  $T < 50$  K) and  $\rho(T) = \rho_0 + \rho_0^\infty + c_{ph} T - c_K \ln T$  (for  $T > 369$  K) with the following parameters:  $\rho_0 = 119 \mu\Omega\text{cm}$ ,  $c_m = 0.21 \mu\Omega\text{cm/K}^2$ ,  $\rho_0^\infty = 704 \mu\Omega\text{cm}$ ,  $c_{ph} = 0.13 \mu\Omega\text{cm/K}$  and  $c_K = 103 \mu\Omega\text{cm}$  (for the meaning of all the terms see the original paper).



**Fig. 41.** UCuAs<sub>2</sub>. **(a)** Transverse magnetoresistivity,  $\Delta\rho/\rho$ , vs. temperature,  $T$ , measured on a single crystal with  $i \perp c$ -axis in a magnetic field of 4 T oriented along the easy-magnetization  $c$ -axis [91KTN]. Note a sharp minimum at the Curie temperature  $T_C = 131$  K. The magnetoresistivity is

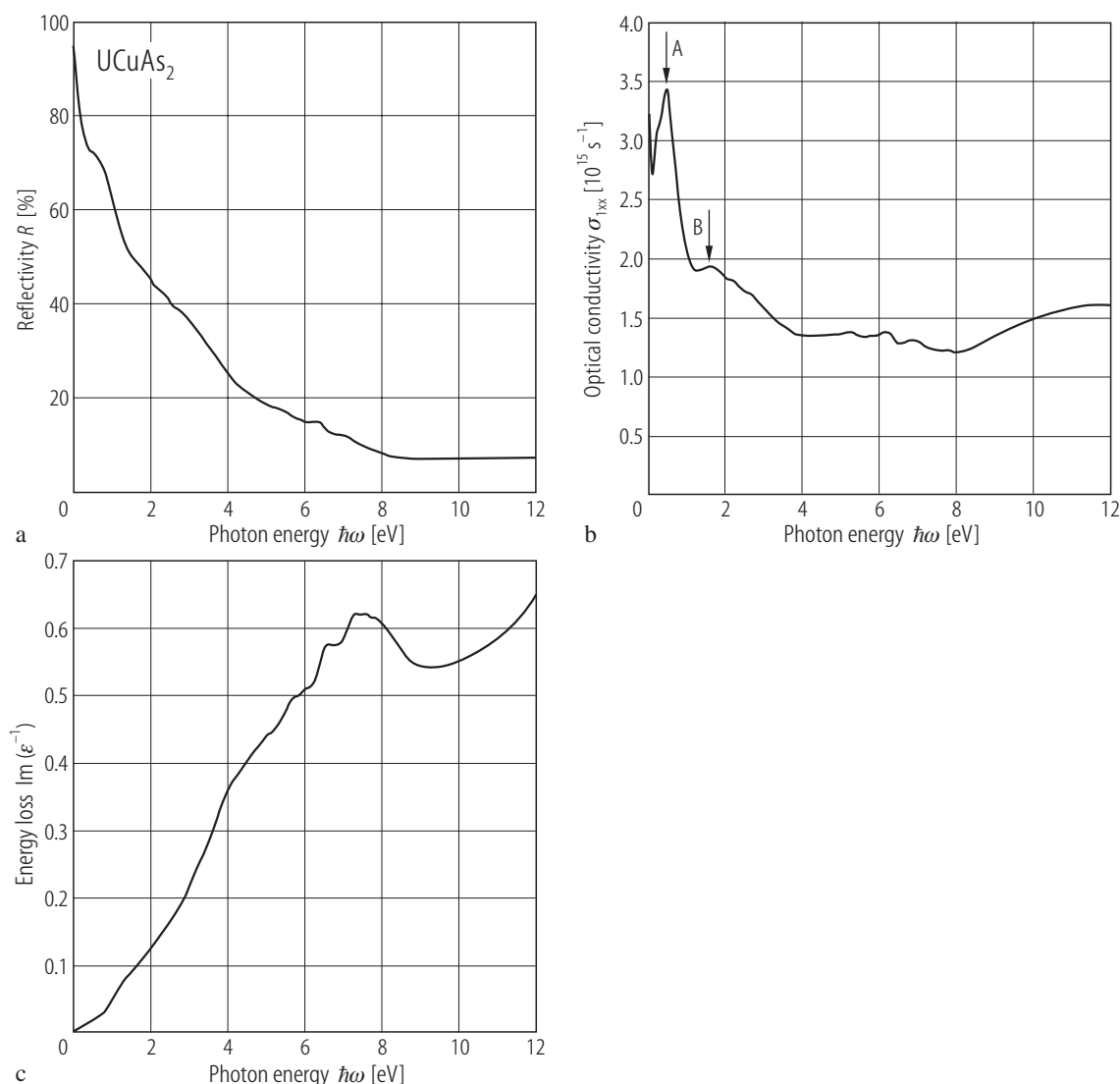
negative except at the lowest temperatures where pronounced domain effect occurs (see Fig. 37). **(b)** Transverse magnetoresistivity,  $\Delta\rho/\rho$ , vs. magnetic field,  $B$ , taken at 4.2 K in the configuration as in panel (a) [91KTN].



**Fig. 42.** UCuAs<sub>2</sub>. **(a)** Hall resistivity,  $\rho_H$ , vs. temperature,  $T$ , measured on a single crystal with  $i \perp c$ -axis in a magnetic field of 2 T (diamonds) and 4 T (triangles) applied parallel to the easy magnetization  $c$ -axis [90KS]. **(b)** Normal,  $R_0$ , and spontaneous,  $R_s$ , Hall coefficients vs.  $T$  [90KS]. Crosses: the data obtained from Hall measurements at a few constant temperatures as a function of magnetic field strength up to 10 T; triangles: the data calculated from the curves shown in panel (a). The horizontal lines denote  $R_0$  and  $R_s$  in the paramagnetic region where they are assumed to be constant. For  $T > T_C$ :  $R_0 = -2.5 \cdot 10^{-3}$  cm<sup>3</sup>/As,  $R_s = 1.96$  cm<sup>3</sup>/As. The concentration of free carriers estimated from  $R_0$  within a single parabolic band model amounts to only 0.18

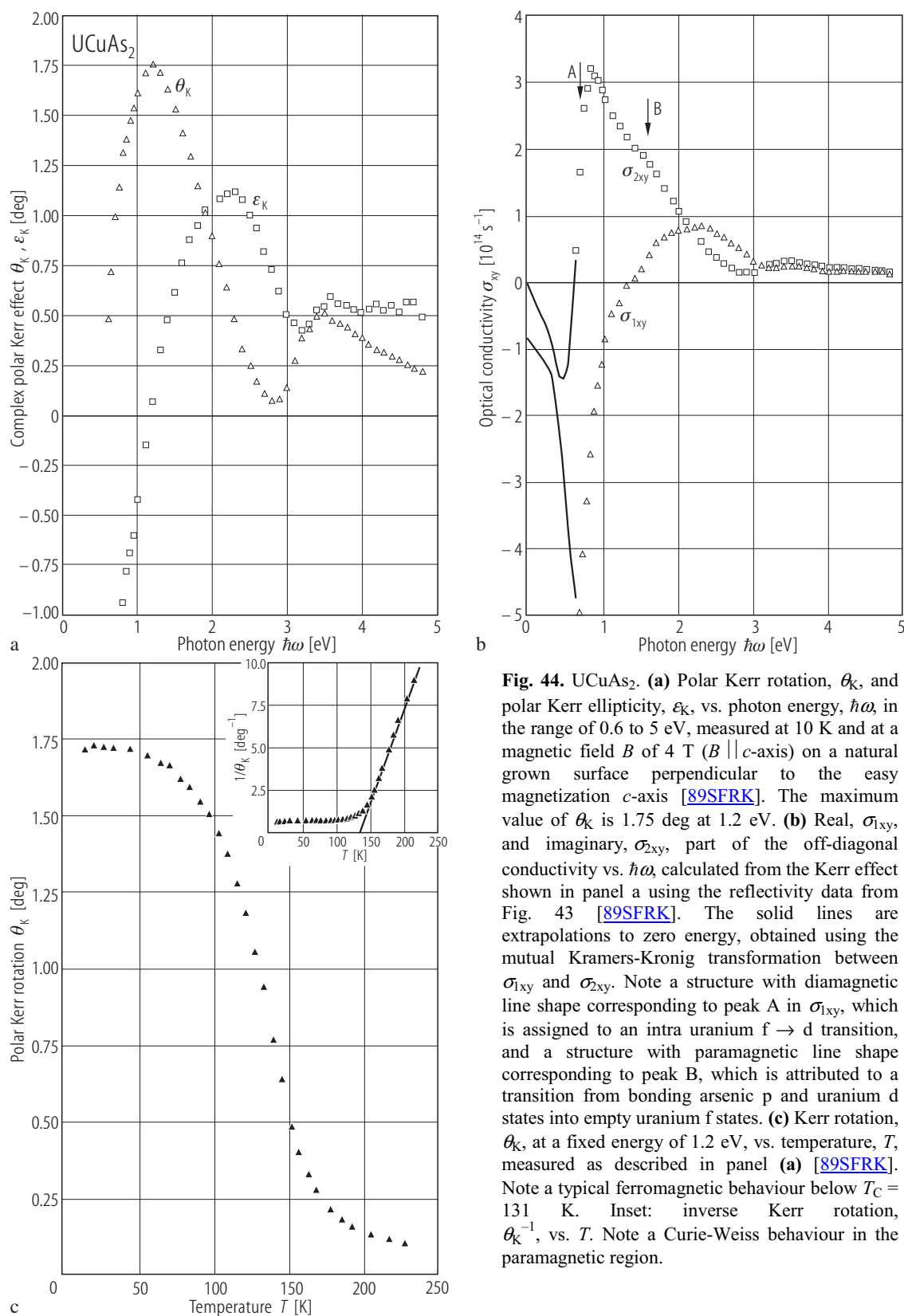
electrons per formula unit, in agreement with the magnetooptical data (see Fig. 43). Note a step-like decrease of  $R_0$  at the Curie point, related to changes with magnetic ordering of the Fermi surface in a material with flat bands near  $E_F$ , disappearance of  $R_0$  for  $T \rightarrow 0$ , suggesting a semimetallic band structure, in which the difference between the mobilities of holes and electrons diminishes with decreasing temperature. **(c)** Spontaneous Hall coefficient, plotted as  $[R_s(T) - R_s(0)]/\rho_m(T)$  vs.  $\rho_m(T)$ , where  $\rho_m$  is the magnetic contribution to the electrical resistivity of UCuAs<sub>2</sub>, determined as shown in Fig. 40 [90KS]. The solid line marks the applicability of the Ansatz  $R_s(T) - R_s(0) = a\rho_m(T) + b\rho_m^2(T)$  (in the temperature range 14...107 K), which describes the spontaneous Hall effect in terms of skew scattering and side-jump scattering theories (the first and the second term, respectively). In UCuAs<sub>2</sub>  $R_s(T)$  arises mainly from the skew-scattering processes.

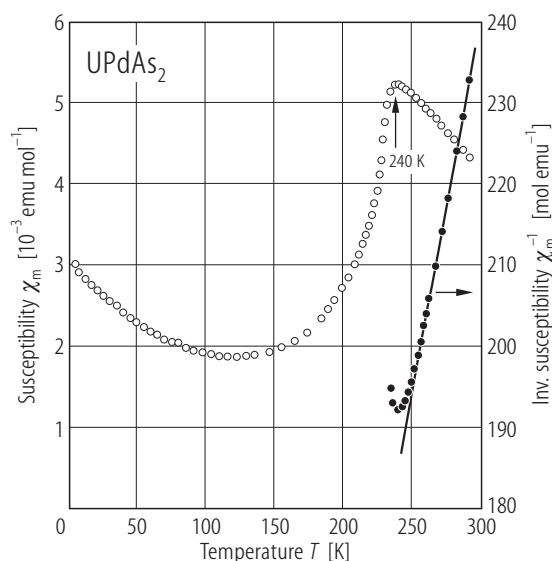




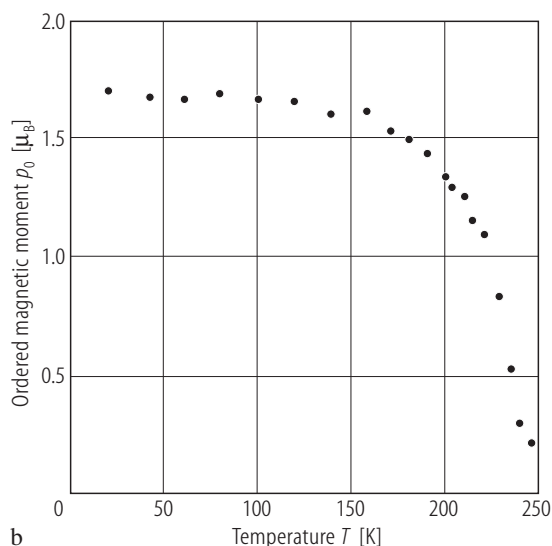
**Fig. 43.** UCuAs<sub>2</sub>. **(a)** Near normal incidence optical reflectivity,  $R$ , vs. photon energy,  $\hbar\omega$ , in the range of 0.03 to 12 eV, measured at 300 K on an as-grown surface perpendicular to the  $c$ -axis [89SFRK]. Note a metallic behaviour. A very steep decrease of  $R$  at the lowest energies indicates a strongly damped free carrier concentration. **(b)** Real part of the optical conductivity,  $\sigma_{1xx}$ , vs.  $\hbar\omega$ , calculated by Kramers-Kronig transformation from the data shown in panel (a) [88FSRK]. The peak at 0.51 eV (labeled A) is an uranium  $f \rightarrow d$  interband transition (see Fig. 44), the peak at 1.6 eV (marked by arrow B) is assigned to a transition from bonding arsenic  $p$  and uranium  $d$  states into

empty uranium  $f$  states. The structures above 3 eV are probably charge transfer transitions from arsenic  $p$  states into uranium derived  $6d$  and  $7s$  states and into copper  $4s$  states. Some intra copper  $3d \rightarrow 4s$  transitions are also likely. Fitting of the free electron part in  $\sigma_{1xx}$  gives a value of 1.73 eV for the unscreened plasma frequency and a damping of 0.11 eV that corresponds to 0.16 electrons per formula unit, setting the effective mass equal to the free electron mass. **(c)** Energy loss function,  $\text{Im}(\epsilon^{-1})$ , vs.  $\hbar\omega$ , calculated from the reflectivity data shown in panel (a) [88FSRK]. The peak at 7.5 eV and the shoulder near 4 eV are both associated with plasmons.

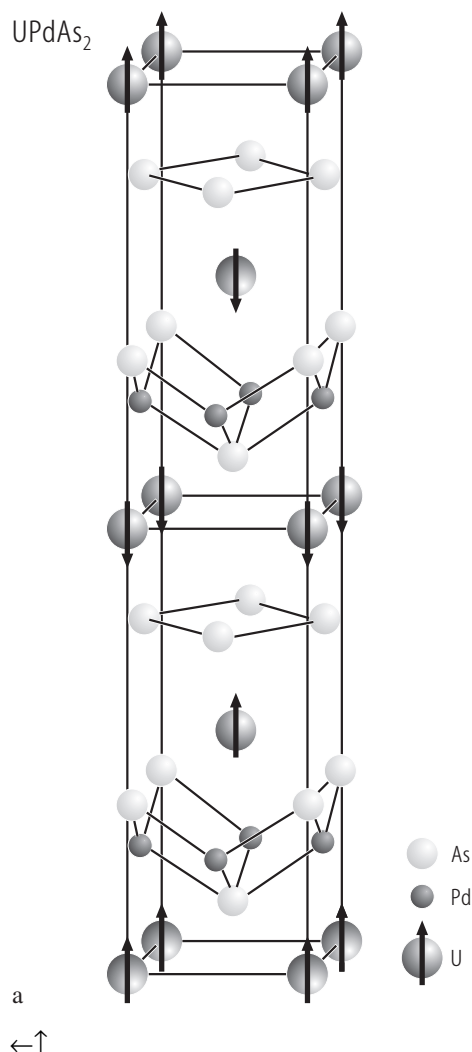




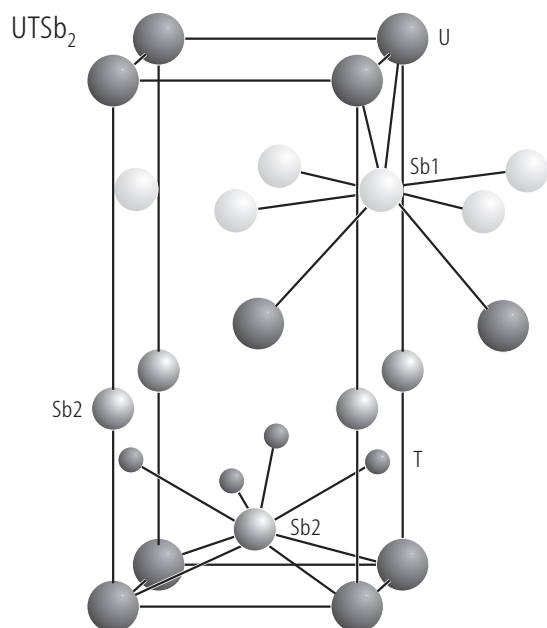
**Fig. 45.**  $\text{UPdAs}_2$ . Molar magnetic susceptibility,  $\chi_m$ , vs. temperature,  $T$ , (left-hand scale) and reciprocal molar magnetic susceptibility,  $\chi_m^{-1}$ , vs.  $T$ , (right-hand scale) [90MFK]. The arrow marks an antiferromagnetic phase transition at 240 K. The solid line is a Curie-Weiss fit with the parameters given in Table B.



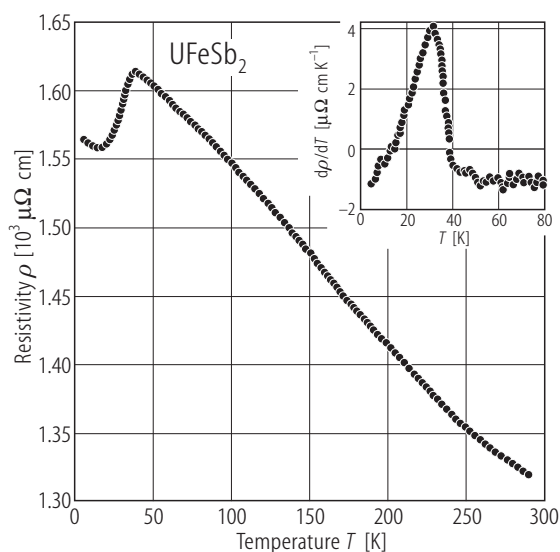
**Fig. 46(b).**



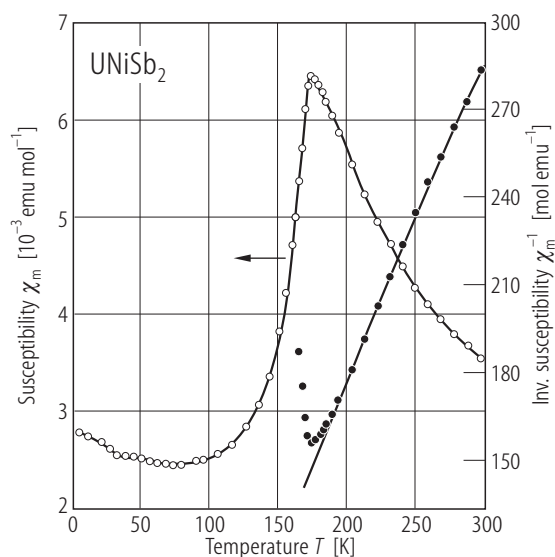
**Fig. 46.**  $\text{UPdAs}_2$ . (a) Magnetic structure [90MFK]. The structure is of the AF-IA – type with the magnetic moments aligned along the four-fold axis, which form ferromagnetic (001) sheets coupled antiferromagnetically along the  $c$ -axis with a sequence  $++--$ . The magnetic unit cell is twice the chemical one. (b) Uranium ordered magnetic moment,  $p_0$ , vs. temperature,  $T$ , as determined from the temperature variation of the magnetic (101) peak intensity [90MFK]. The ordered moment at 8.7 K amounts to  $1.69(5) \mu_B$ . The Néel temperature is 235 K (compare Fig. 45).



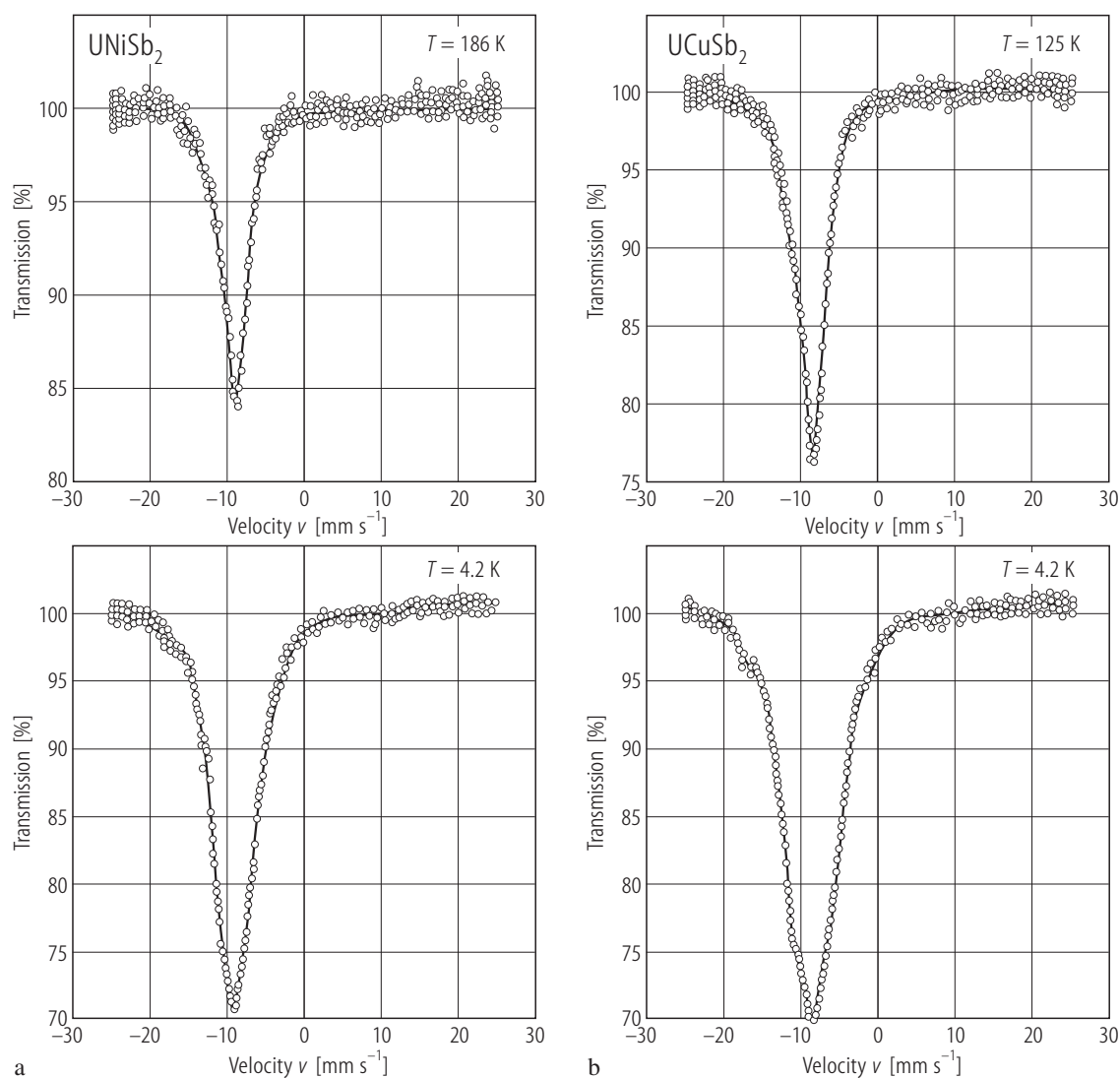
**Fig. 47.**  $UTsSb_2$ ,  $T = Fe, Ru, Co, Ni, Pd, Cu, Ag, Au$ . Crystal structure [98KKSM].



**Fig. 48.**  $UFeSb_2$ . Electrical resistivity,  $\rho$ , vs. temperature,  $T$  [98KKSM]. Inset: temperature derivative of the resistivity at low temperatures. Note a ferromagnetic-type anomaly at about 30 K (compare e.g. Fig. 61), which may suggest that the compound becomes ferromagnetic at low temperatures.



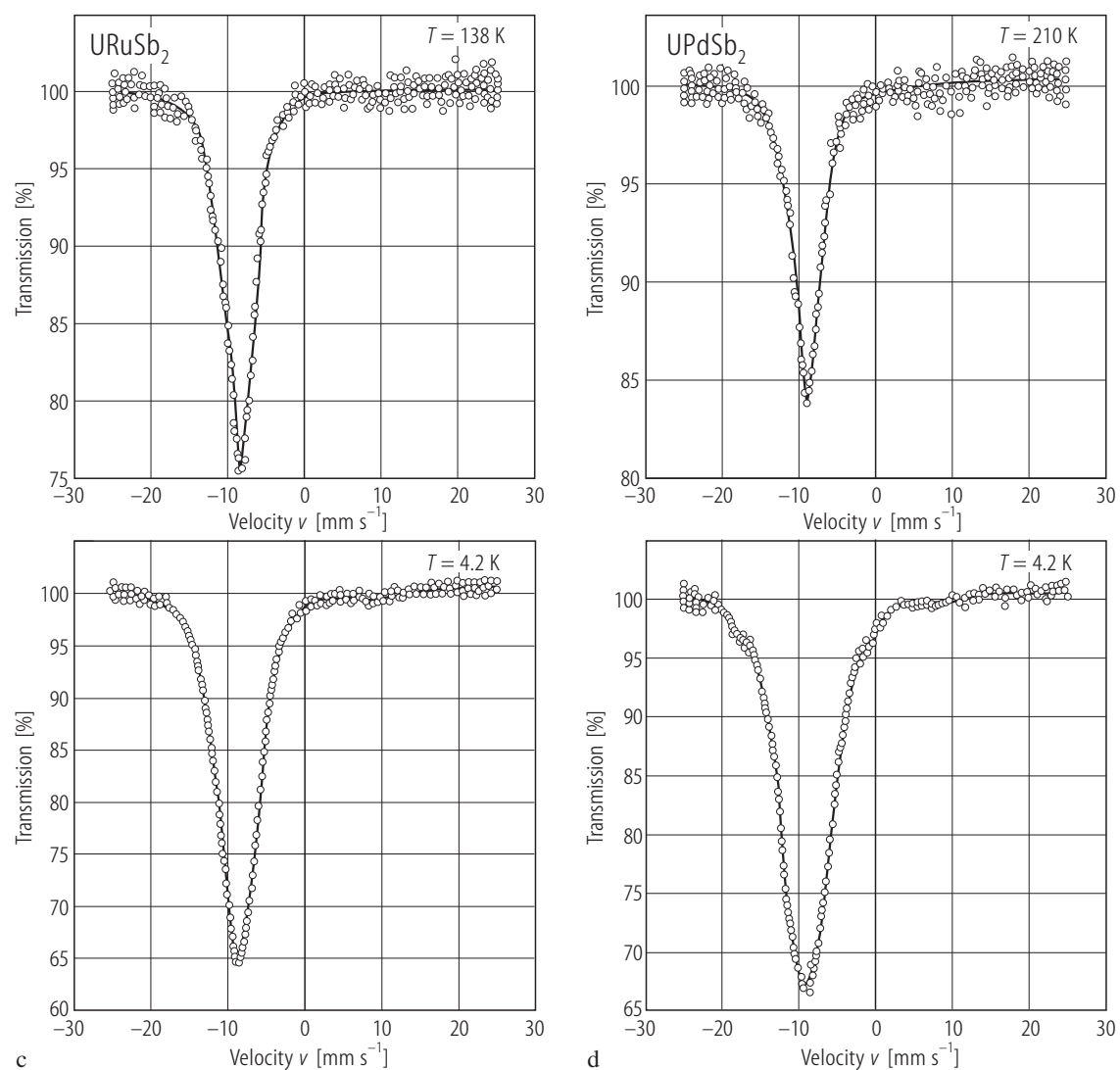
**Fig. 49.**  $UNiSb_2$ . Molar magnetic susceptibility,  $\chi_m$ , (left-hand scale) and reciprocal molar magnetic susceptibility,  $\chi_m^{-1}$ , (right-hand scale) vs. temperature,  $T$  [98KKSM]. The compound orders antiferromagnetically at  $T_N = 175(1)$  K. The solid line is a modified Curie-Weiss fit with the parameters given in Table B.



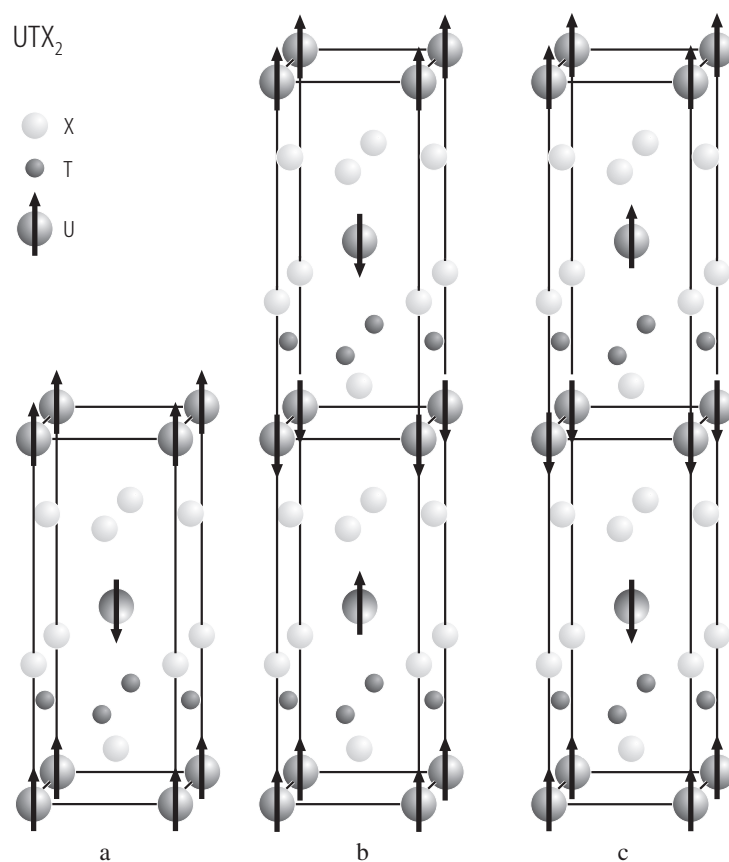
**Fig. 50.**  $\text{UTSb}_2$ ,  $T = \text{Cu, Ni, Pd, Ru}$ .  $^{121}\text{Sb}$  Mössbauer spectra for (a)  $\text{UNiSb}_2$ , (b)  $\text{UCuSb}_2$ , (c)  $\text{URuSb}_2$  and (d)  $\text{UPdSb}_2$  taken in the ordered region at  $T = 4.2 \text{ K}$  (lower spectra) and in the paramagnetic region (upper spectra) at  $T = 125 \text{ K}$  ( $\text{UCuSb}_2$ ),  $186 \text{ K}$  ( $\text{UNiSb}_2$ ),  $210 \text{ K}$  ( $\text{UPdSb}_2$ ) or  $138 \text{ K}$  ( $\text{URuSb}_2$ ) [98KKSM]. The solid lines are fits of the experimental data with two sites by constraining the relative intensities due to Sb1 and Sb2 atoms (see Fig. 47) in the proportion 1:1. In the paramagnetic state the spectra consist of an asymmetric absorption line enlarged by the quadrupolar interactions experienced by the Sb atoms. In

the ordered state there occur magnetic splittings but because of a large natural linewidth of the  $^{121}\text{Sb}$  resonance and rather small hyperfine fields transferred to the Sb atoms, the lines of the spectra are poorly resolved. From the analysis of the transferred hyperfine fields complemented by the neutron data (see the original paper) the authors concluded on the magnetic structures of  $\text{UNiSb}_2$ ,  $\text{UPdSb}_2$  and  $\text{URuSb}_2$ : the arrangement of ferromagnetically coupled (001) uranium atom layers along the  $c$ -axis is  $+-+ -$  in the two first compounds and  $+-$  in the latter compound (see Fig. 51). The hyperfine parameters are collected in Table C.

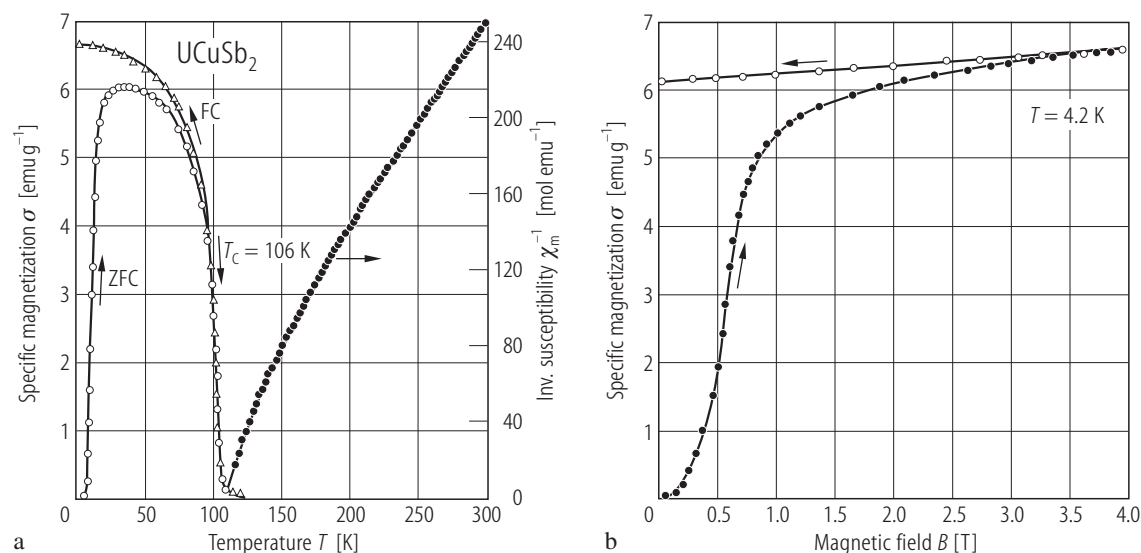
For Fig. 50(c, d) see next page



**Fig. 50(c, d).** For caption see previous page.

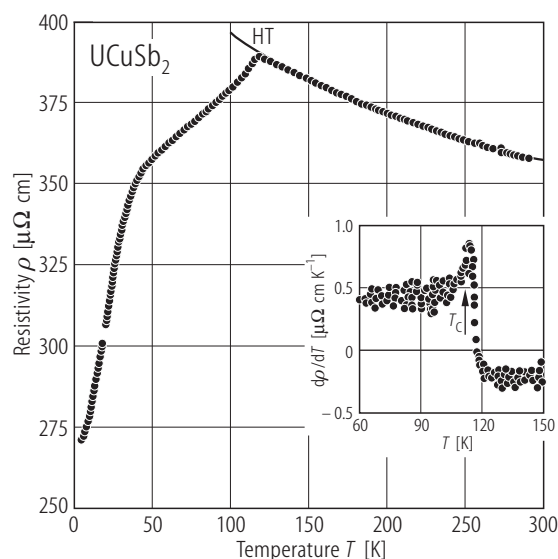


**Fig. 51.** UTX<sub>2</sub>. Magnetic structures of the antiferromagnets crystallising with the tetragonal HfCuSi<sub>2</sub>-type crystal structure [98KKSM]. The arrows indicate the alignment of the uranium magnetic moments in: (a) URuSb<sub>2</sub> and UNiAs<sub>2</sub> (the data from [89FMKT], see Fig. 35); (b) UPdAs<sub>2</sub> (the data from [90MFK], see Fig. 46); (c) UNiSb<sub>2</sub> and UPdSb<sub>2</sub>.

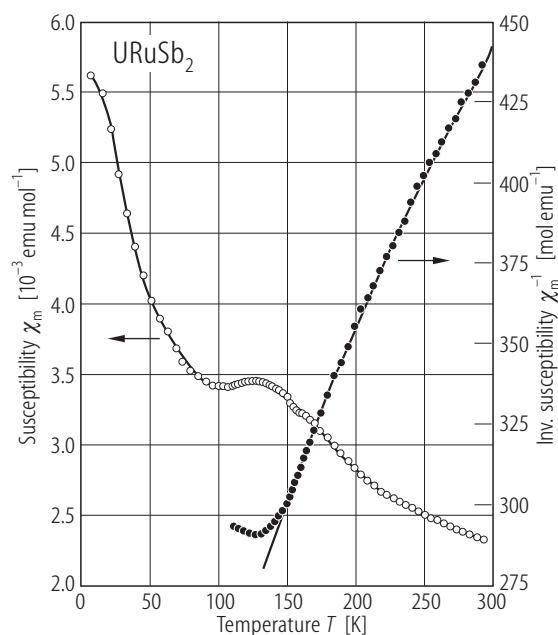


**Fig. 52.** UCuSb<sub>2</sub>. (a) Specific magnetization,  $\sigma$ , measured in a field of 0.2 T with cooling the sample with (FC, triangles) and without (ZFC, open circles) an applied magnetic field (left-hand scale) and reciprocal molar magnetic susceptibility,  $\chi_m^{-1}$ , (right-hand scale) vs. temperature,  $T$  [92K]. The compound orders ferromagnetically at  $T_C = 106$  K. Note a pronounced

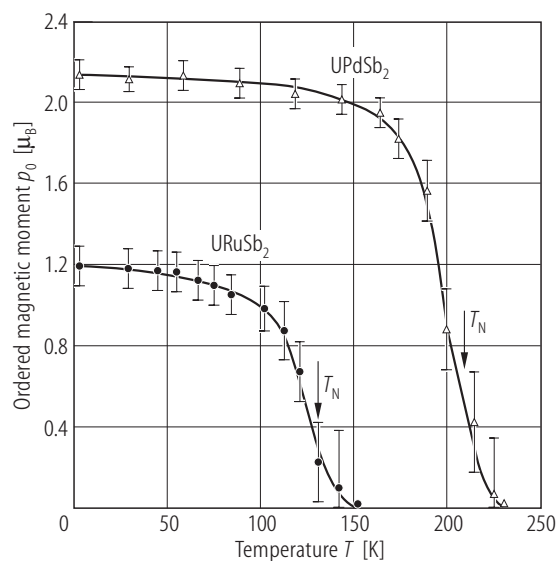
domain effect at low temperatures. The solid line is a modified Curie-Weiss fit with the parameters given in Table B. (b) Specific magnetization,  $\sigma$ , vs. magnetic field,  $B$ , taken at 4.2 K with increasing (full circles) and decreasing (open circles) magnetic field [92K]. The saturation magnetic moment is 1.3(1)  $\mu_B$  (upon correction for an uniaxial magnetic anisotropy).



**Fig. 53.** UCuSb<sub>2</sub>. Electrical resistivity,  $\rho$ , vs. temperature,  $T$  [98KKSM]. Note a negative temperature coefficient in  $\rho(T)$  in the paramagnetic region and a cusp like anomaly at the ferromagnetic phase transition at 114 K. The solid line (HT) is a fit of the resistivity to the formula  $\rho(T) = \rho_0 + \rho_0^\infty - c_K \ln T$ , describing scattering of free carriers on defects, disordered spins and Kondo impurities (the first, second and third term, respectively), with the parameters:  $\rho_0 + \rho_0^\infty = 592 \mu\Omega\text{cm}$  and  $c_K = 35.9 \mu\Omega\text{cm}$ . Note a large value of  $c_K$  implying enhanced density of states at the Fermi level. Inset: temperature derivative of the resistivity in the vicinity of  $T_C$ . The arrow marks the phase transition.

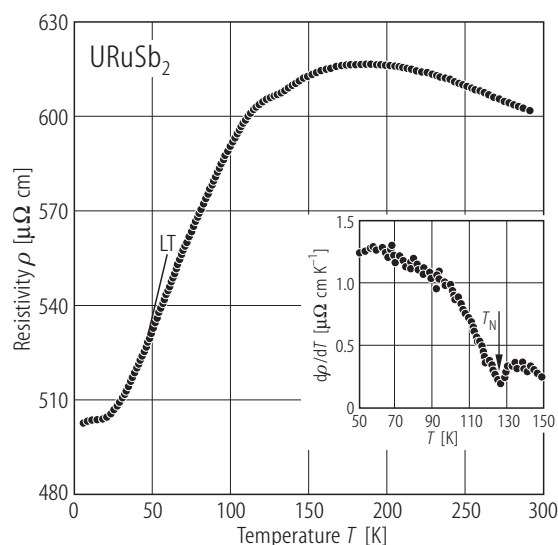


**Fig. 54.** URuSb<sub>2</sub>. Molar magnetic susceptibility,  $\chi_m$ , (left-hand scale) and reciprocal molar magnetic susceptibility,  $\chi_m^{-1}$ , (right-hand scale) vs. temperature,  $T$  [98KKSM]. The compound orders antiferromagnetically at  $T_N = 127(5)$  K, as derived from the neutron diffraction studies (see Fig. 55). A low-temperature upturn in  $\chi_m(T)$  results probably from the presence of some strongly paramagnetic impurities in the sample measured which amount below the detection limit of X-ray diffraction. The solid line is a modified Curie-Weiss fit with the parameters given in Table B.

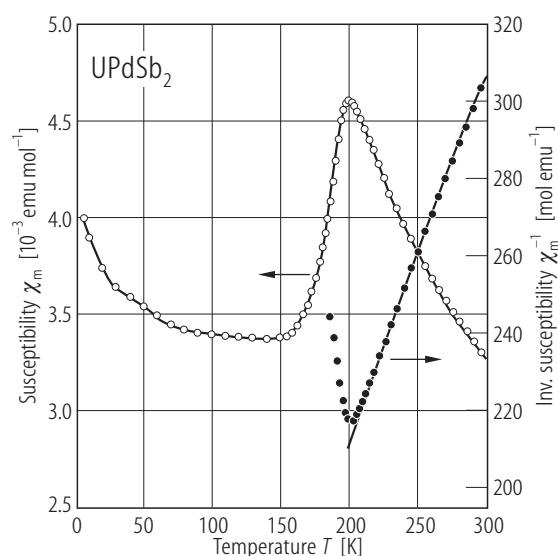


**Fig. 55.** UTSb<sub>2</sub>,  $T = \text{Ru, Pd}$ . Uranium ordered magnetic moment,  $p_0$ , vs. temperature,  $T$ , for URuSb<sub>2</sub> (circles) and UPdSb<sub>2</sub> (triangles) as derived from powder neutron diffraction [98KKSM]. The bars mark the errors. The arrows indicate the antiferromagnetic phase transitions. At 2 K the uranium magnetic moment amounts to 1.2(1) and 2.2(1)  $\mu_B$  in URuSb<sub>2</sub> and UPdSb<sub>2</sub>, respectively.

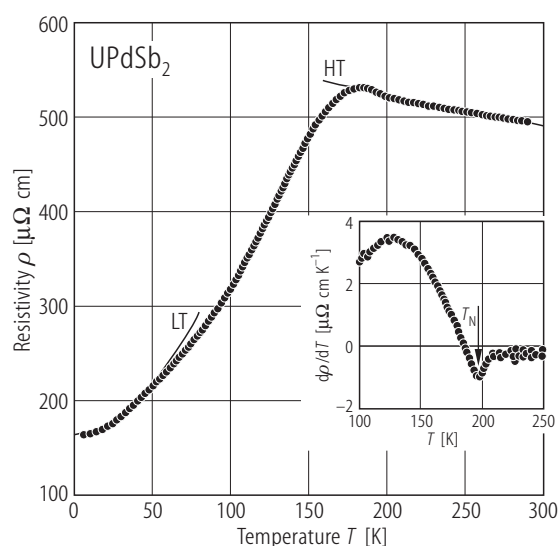




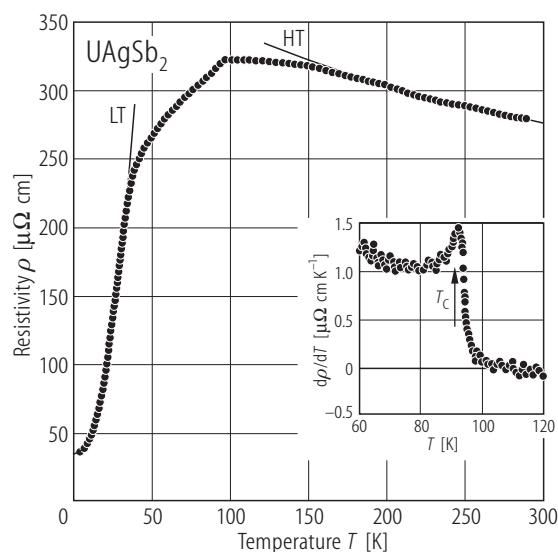
**Fig. 56.** URuSb<sub>2</sub>. Electrical resistivity,  $\rho$ , vs. temperature,  $T$  [98KKSM]. Note a broad maximum and negative temperature coefficient in  $\rho(T)$  in the paramagnetic region and a small maximum just below the antiferromagnetic phase transition at 127 K. The solid line LT is a fit of the resistivity to the formula  $\rho(T) = \rho_0 + c_m T^2 \exp(-\Delta/T)$ , describing scattering of conduction electrons on defects in the lattice and spin wave excitations over an energy gap  $\Delta$  (the first and second term, respectively), with the parameters:  $\rho_0 = 503 \mu\Omega\text{cm}$ ,  $c_m = 0.03 \mu\Omega\text{cm/K}^2$  and  $\Delta = 46 \text{ K}$ . Inset: temperature derivative of the resistivity in the vicinity of  $T_N$ . The arrow marks the phase transition.



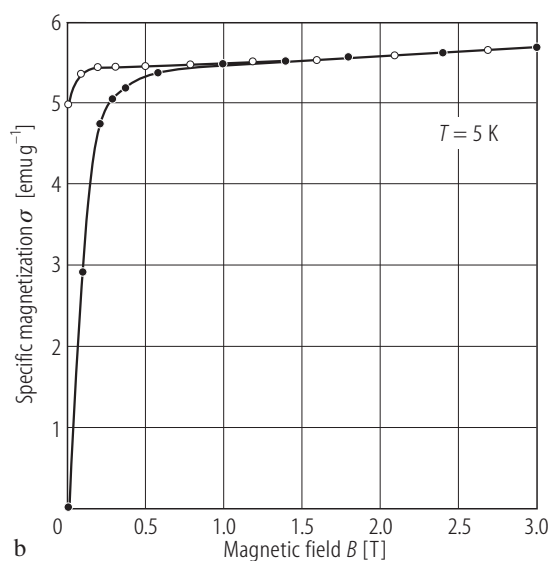
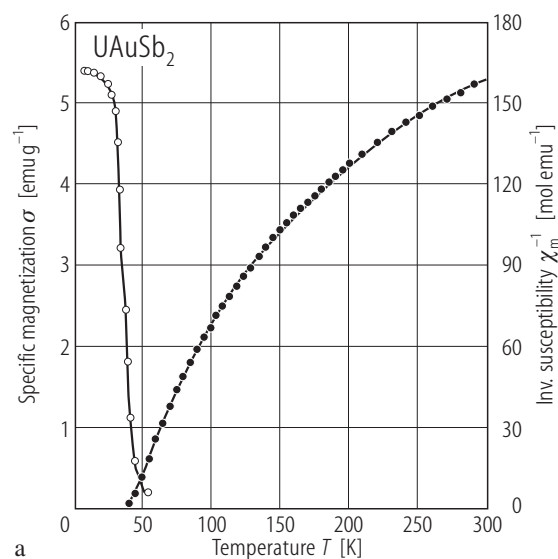
**Fig. 57.** UPdSb<sub>2</sub>. Molar magnetic susceptibility,  $\chi_m$ , (left-hand scale) and reciprocal molar magnetic susceptibility,  $\chi_m^{-1}$ , (right-hand scale) vs. temperature,  $T$  [98KKSM]. The compound orders antiferromagnetically at  $T_N = 196(2) \text{ K}$ . The solid line is a modified Curie-Weiss fit with the parameters given in Table B.



**Fig. 58.** UPdSb<sub>2</sub>. Electrical resistivity,  $\rho$ , vs. temperature,  $T$  [98KKSM]. Note a negative temperature coefficient in  $\rho(T)$  in the paramagnetic region and a maximum below the antiferromagnetic phase transition at 196 K (see Fig. 57). The solid line LT is a fit of the resistivity to the formula  $\rho(T) = \rho_0 + c_m T^2$ , describing scattering of conduction electrons on defects in the lattice and spin wave excitations (the first and second term, respectively), with the parameters:  $\rho_0 = 164 \mu\Omega\text{cm}$  and  $c_m = 0.02 \mu\Omega\text{cm/K}^2$ . The solid line (HT) is a fit of the resistivity to the formula  $\rho(T) = \rho_0 + \rho_0^\infty - c_K \ln T$ , describing scattering of free carriers on defects, disordered spins and Kondo impurities (the first, second and third term, respectively), with the parameters:  $\rho_0 + \rho_0^\infty = 931 \mu\Omega\text{cm}$  and  $c_K = 77.5 \mu\Omega\text{cm}$ . Note a large value of  $c_K$  implying enhanced density of states at the Fermi level. Inset: temperature derivative of the resistivity in the vicinity of  $T_N$ . The arrow marks the phase transition.

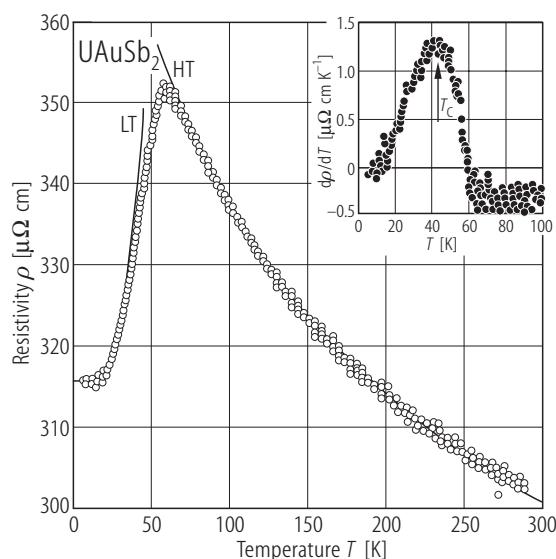


**Fig. 59.** UAgSb<sub>2</sub>. Electrical resistivity,  $\rho$ , vs. temperature,  $T$  [98KKSM]. Note a negative temperature coefficient in  $\rho(T)$  in the paramagnetic region and a cusp like anomaly at the ferromagnetic phase transition at 92 K. The solid line LT is a fit of the resistivity to the formula  $\rho(T) = \rho_0 + c_m T^2$ , describing scattering of conduction electrons on defects in the lattice and spin wave excitations (the first and second term, respectively), with the parameters:  $\rho_0 = 33 \mu\Omega\text{cm}$  and  $c_m = 0.19 \mu\Omega\text{cm/K}^2$ . The solid line HT is a fit of the resistivity to the formula  $\rho(T) = \rho_0 + \rho_0^\infty - c_K \ln T$ , describing scattering of free carriers on defects, disordered spins and Kondo impurities (the first, second and third term respectively), with the parameters:  $\rho_0 + \rho_0^\infty = 650 \mu\Omega\text{cm}$  and  $c_K = 65.6 \mu\Omega\text{cm}$ . Note a large value of  $c_K$  implying enhanced density of states at the Fermi level. Inset: temperature derivative of the resistivity in the vicinity of  $T_C$ . The arrow marks the phase transition.



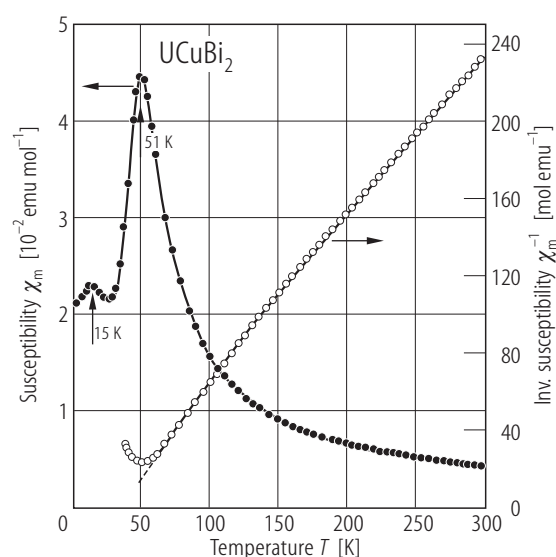
**Fig. 60.** UAuSb<sub>2</sub>. **(a)** Specific magnetization,  $\sigma$ , measured in a field of 0.5 T with cooling the sample with an applied magnetic field (open circles, left-hand scale) and reciprocal molar magnetic susceptibility,  $\chi_m^{-1}$ , (filled circles; right-hand scale) vs. temperature,  $T$  [98KKSM]. The compound orders ferromagnetically at  $T_C = 36(3)$  K. The solid line is a

modified Curie-Weiss fit with the parameters given in Table B. **(b)** Specific magnetization,  $\sigma$ , vs. magnetic field,  $B$ , taken at 5 K with increasing (full circles) and decreasing (open circles) magnetic field [98KKSM]. The saturation magnetic moment is  $1.4(2) \mu_B$  (upon correction for an uniaxial magnetic anisotropy).

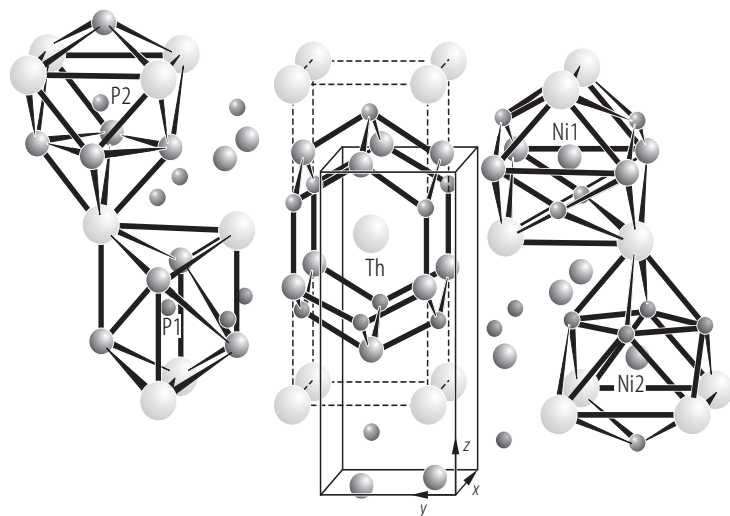
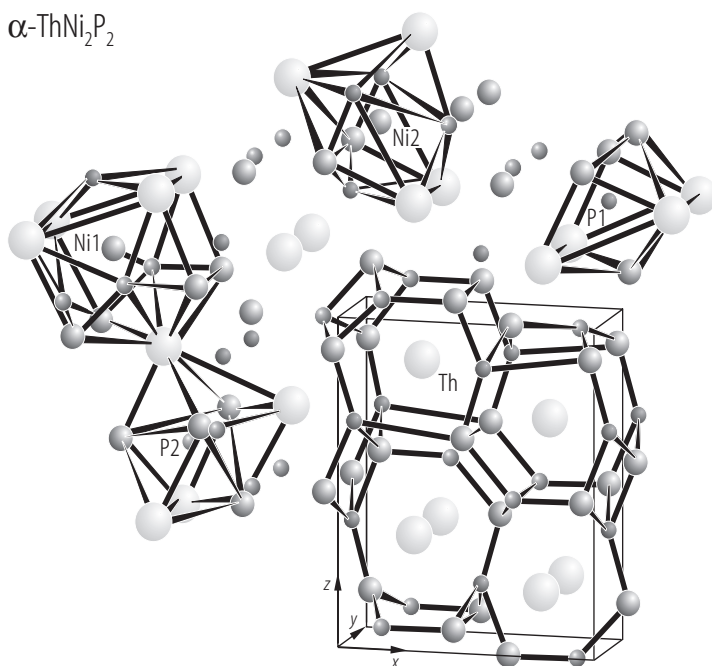


**Fig. 61.** UAuSb<sub>2</sub>. Electrical resistivity,  $\rho$ , vs. temperature,  $T$  [98KKSM]. Note a negative temperature coefficient in  $\rho(T)$  in the paramagnetic region and a rapid drop of the resistivity at the ferromagnetic phase transition at 36 K (see Fig. 60). The solid line LT is a fit of the resistivity to the formula  $\rho(T) = \rho_0 + c_m T^2 \exp(-\Delta/T)$ , describing scattering of conduction electrons on defects in the lattice and spin wave excitations over an energy gap  $\Delta$  (the first and second term, respectively), with the parameters:  $\rho_0 = 315 \mu\Omega\text{cm}$ ,  $c_m = 0.07 \mu\Omega\text{cm/K}^2$  and  $\Delta = 61 \text{ K}$ . The solid

line (HT) is a fit of the resistivity to the formula  $\rho(T) = \rho_0 + \rho_0^\infty - c_K \ln T$ , describing scattering of free carriers on defects, disordered spins and Kondo impurities (the first, second and third term, respectively), with the parameters:  $\rho_0 + \rho_0^\infty = 489 \mu\Omega\text{cm}$  and  $c_K = 33.1 \mu\Omega\text{cm}$ . Note a large value of  $c_K$  implying enhanced density of states at the Fermi level. Inset: temperature derivative of the resistivity in the vicinity of  $T_C$ . The arrow marks the phase transition



**Fig. 62.** UCuBi<sub>2</sub>. Molar magnetic susceptibility,  $\chi_m$ , (left-hand scale) and reciprocal molar magnetic susceptibility,  $\chi_m^{-1}$ , (right-hand scale) vs. temperature,  $T$  [92K]. The arrows mark two subsequent antiferromagnetic phase transitions at 51 and 15 K. The solid line for  $\chi_m^{-1}$  is a modified Curie-Weiss fit with the parameters given in Table B.

$\beta$ -ThNi<sub>2</sub>P<sub>2</sub> $\alpha$ -ThNi<sub>2</sub>P<sub>2</sub>**Fig. 63.**  $\alpha$ -ThNi<sub>2</sub>P<sub>2</sub>,  $\beta$ -ThNi<sub>2</sub>P<sub>2</sub>. Crystal structures and coordination polyhedra [94AJ].

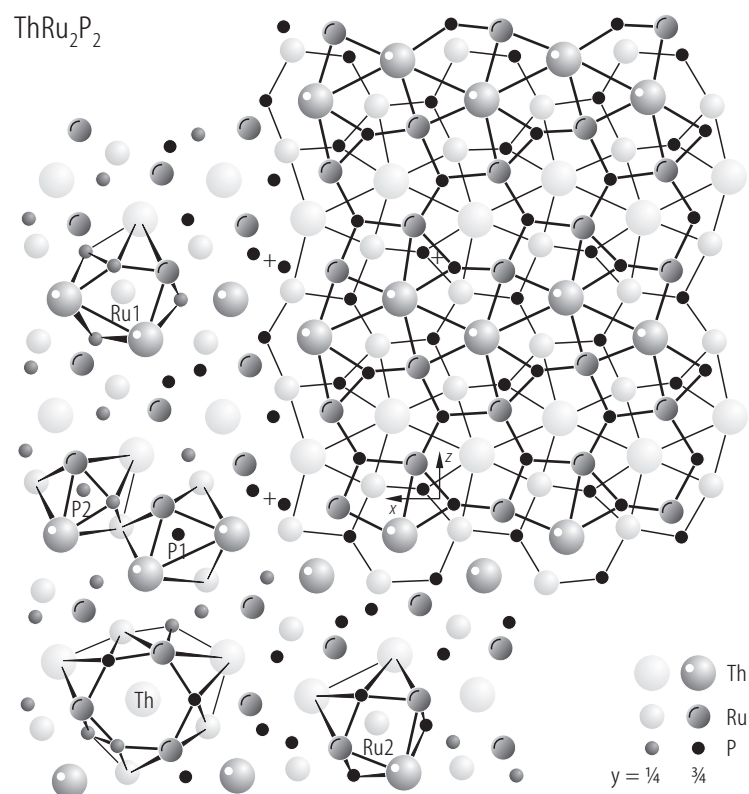


**Fig. 64.** ThRu<sub>2</sub>P<sub>2</sub>. Crystal structure and coordination polyhedra [92GAJB]. The atoms connected by the thick and thin lines are at  $y = \frac{3}{4}$  and  $\frac{1}{4}$  respectively.

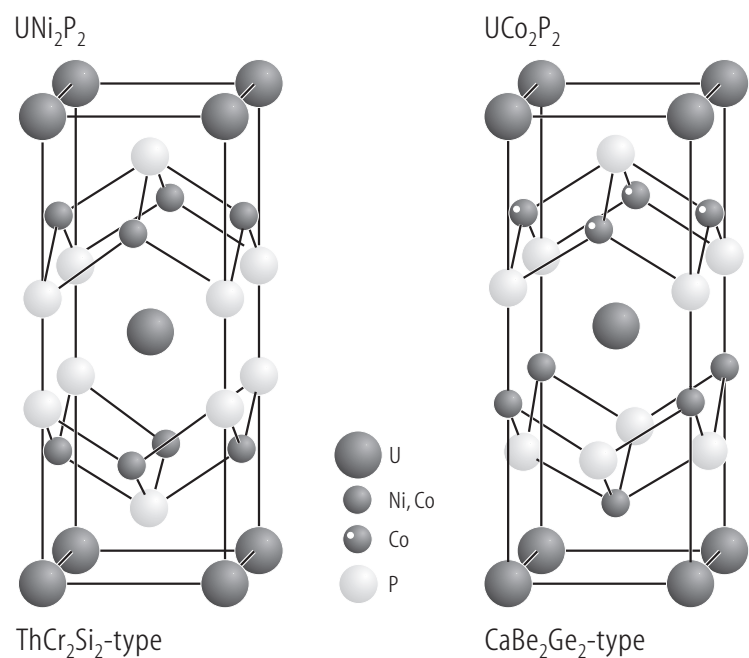


**Fig. 65.** UCo<sub>2</sub>P<sub>2</sub>. Crystal structure of the CaBe<sub>2</sub>Ge<sub>2</sub>-type as compared to that of the ThCr<sub>2</sub>Si<sub>2</sub>-type (characteristic of e.g. UNi<sub>2</sub>P<sub>2</sub>) [91RVJ].

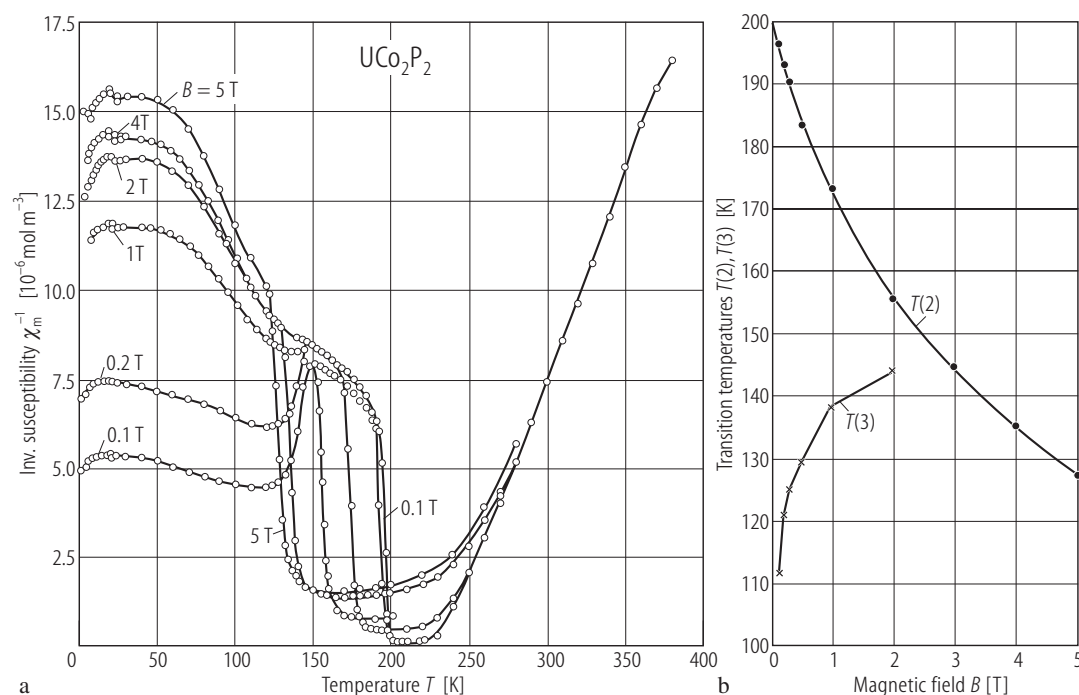


**Fig. 66.**  $\text{UCo}_2\text{P}_2$ . **(a)** Reciprocal molar magnetic susceptibility,  $\chi_m^{-1}$  (SI units), vs. temperature,  $T$ , up to 380 K, measured at different magnetic field specified in the figure [91RVJ]. The compound orders ferromagnetically at  $T_C = 225(3)$  K, and then undergoes additional field-dependent transitions at  $T(2) = 125$  to 200 K and  $T(3) = 115$  to 144 K for magnetic fields of 5 to 0.1 T and 0.1 to 2 T, respectively. At  $T(4) = 23(1)$  K there occurs a fourth transition which is independent of the magnetic field. The anomaly at  $T(3)$  is likely due to some small impurity admixture of ferromagnetic  $\text{U}_3\text{P}_4$  ( $T_C = 138$  K). For comparison see Fig. 67, where the transitions at  $T(3)$  and  $T(4)$  have not been observed. The field dependence of the susceptibility above  $T_C$  up to 260 K the authors attributed to the short range ordering. For the discussion of the magnetic structure refer to Fig. 69. See also the Curie-Weiss fit parameters given in Table B. **(b)** Transition temperatures,  $T(2)$  and  $T(3)$ , vs. magnetic field,  $B$  [91RVJ].

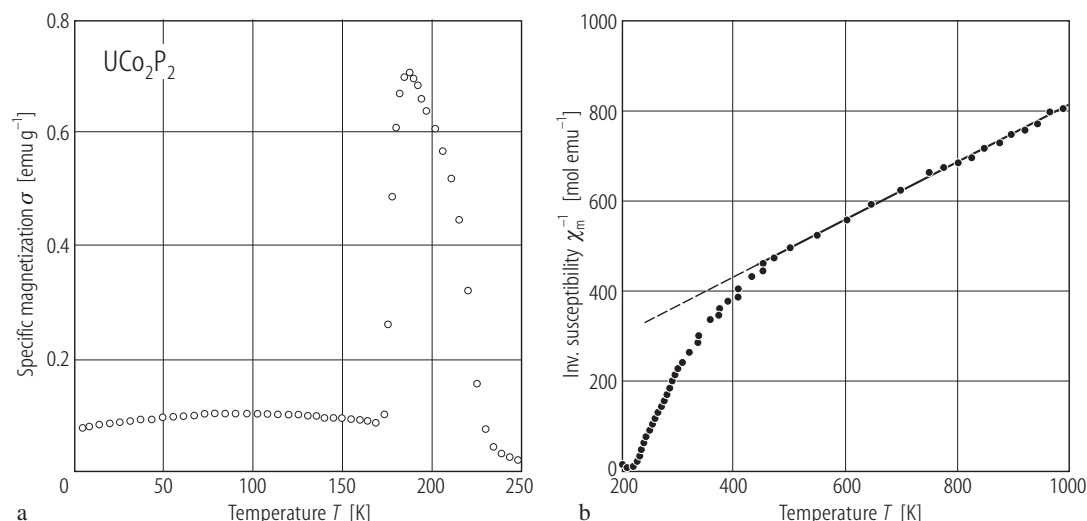


**Fig. 67.**  $\text{UCo}_2\text{P}_2$ . **(a)** Specific magnetization,  $\sigma$ , measured in a field of 0.15 T upon cooling the sample in zero magnetic field vs. temperature,  $T$  [93TKKS]. Below 175 K the compound is in an antiferromagnetic state and its magnetization is a linear function of magnetic field (not shown). In between 175 and 220 K the magnetic structure is ferromagnetic-like. See Fig. 69 for the details on the magnetic structures. **(b)** Reciprocal molar magnetic susceptibility,  $\chi_m^{-1}$ , vs. temperature,  $T$  in the paramagnetic region up to 1000 K [93TKKS].

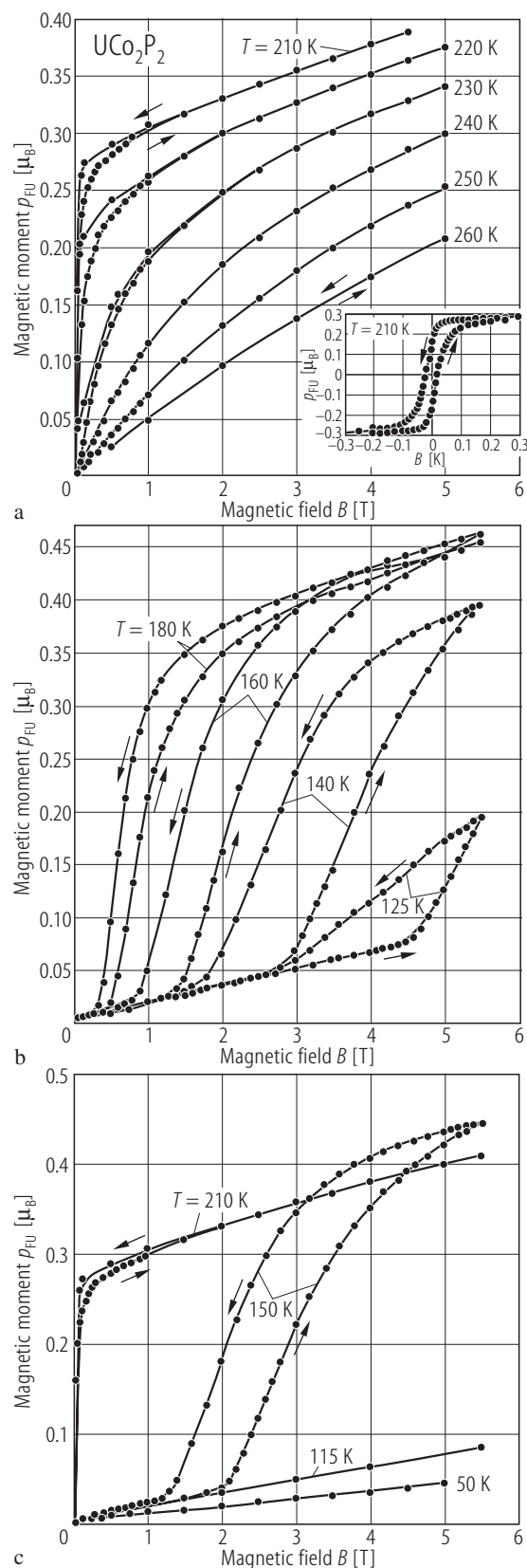


**Fig. 68.**  $UCo_2P_2$ . Magnetic moment,  $p_{FU}$ , vs. magnetic field,  $B$ , measured with increasing and decreasing magnetic field (marked by the arrows) at the temperatures between 50 and 260 K, specified in the figure [94RVJ]. (a) The magnetization behavior of the ferromagnetic phase in the vicinity of the Curie temperature  $T_C = 225(5)$  K. Inset: the hysteresis loop taken at  $T = 210$  K (b) The magnetization behavior of the antiferromagnetic phase. Note clear metamagnetic transitions. (c) Summary on the transition from the ferromagnetic to the antiferromagnetic phase. The latter phase is stable at low temperatures and accordingly weak magnetic fields. Compare the magnetic phase diagram shown in Fig. 69.

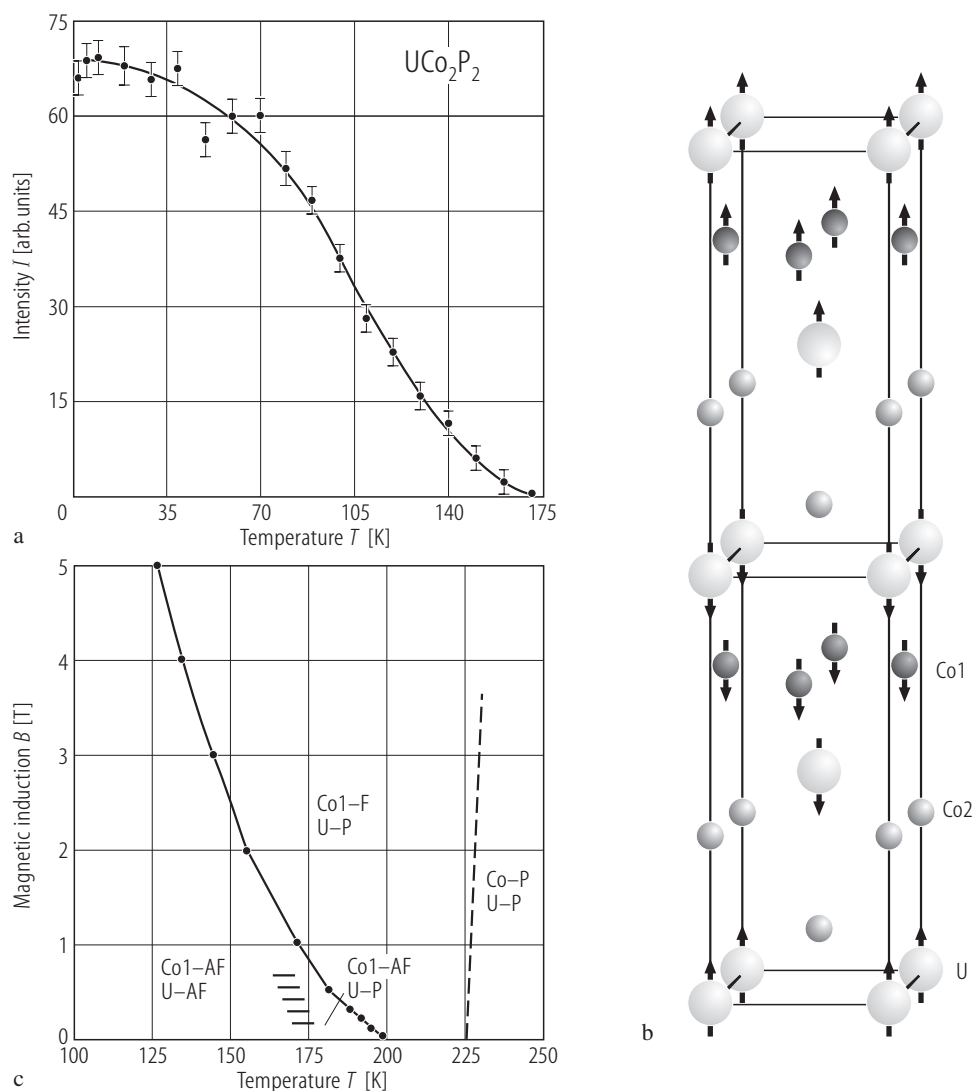


**Fig. 69.**  $\text{UCo}_2\text{P}_2$ . **(a)** Neutron diffraction intensity of the magnetic reflection ( $10\frac{1}{2}$ ),  $I$ , vs. temperature,  $T$  [94RVJ]. The bars indicate standard deviations. The solid line is a guide for the eye. **(b)** Magnetic structure at low temperatures [94RVJ]. The propagation vector  $\mathbf{k} = [00\frac{1}{2}]$ . The stacking sequence of the uranium magnetic moments along the  $c$ -axis is:  $+ - - +$  and that of the cobalt moments is:  $0-0+$ . Note that the magnetic moments of one half of the cobalt atoms, i.e. Co2, are disordered. All the moments are aligned along the  $c$ -axis. At 2 K:  $p(\text{U}) = 1.58(5) \mu_{\text{B}}$  and

$p(\text{Co1}) = 1.14(7) \mu_{\text{B}}$ . At 160 K:  $p(\text{U}) = 0.14 \mu_{\text{B}}$  and  $p(\text{Co1}) = 0.88(9) \mu_{\text{B}}$ . **(c)** Magnetic phase diagram [94RVJ]. Above  $T_{\text{C}} = 225(5)$  K both uranium and cobalt magnetic moments are disordered. In between  $T_{\text{C}}$  and  $T(2)$ , which changes from 199(2) K in 0 T to 127(2) K in 5 T, the uranium subsystem is still paramagnetic but the Co1 atoms order ferromagnetically. Below  $T(2)$  both U and Co(1) atoms are arranged in an antiferromagnetic manner as shown in panel **(b)**. The shading at around 175 K indicates the diffuse character of the order-disorder transition of the U moments.



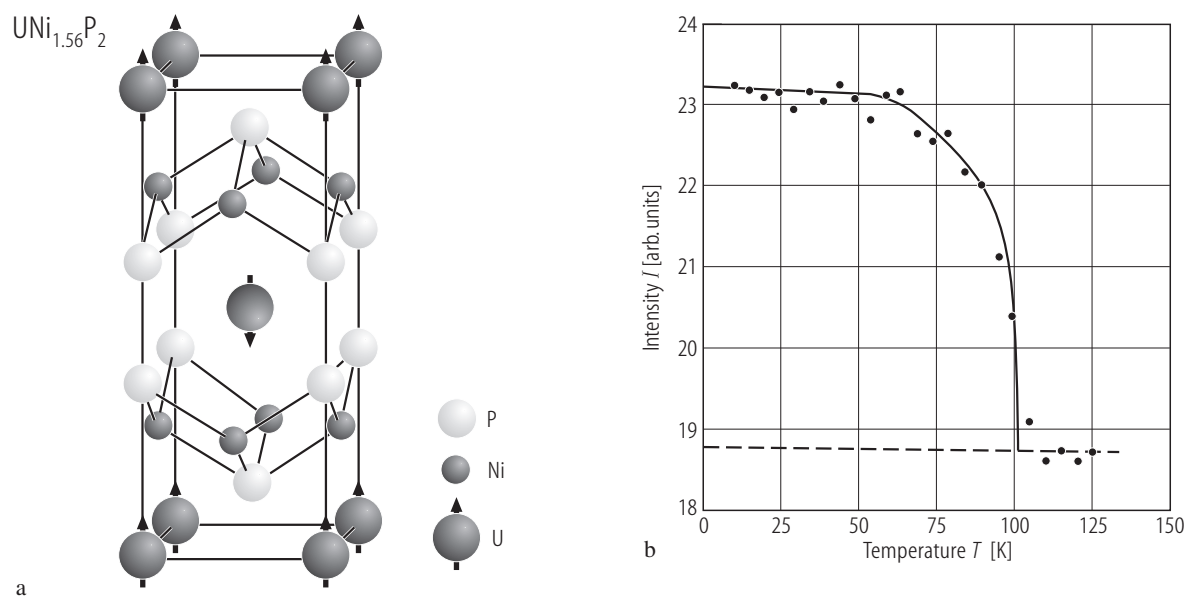


**Fig. 70.**  $\text{UNi}_{1.56}\text{P}_2$ . **(a)** Magnetic structure [90MFK]. The structure is of the AF-I – type with the magnetic moments aligned along the four-fold axis, which form ferromagnetic (001) sheets coupled antiferromagnetically along the  $c$ -axis with a sequence  $+-+-$ . **(b)** Peak intensity of the magnetic reflection (100),  $I$ , vs. temperature,  $T$  [89FMKT]. The solid

line is a guide for the eye, the dashed line marks the background intensity. The uranium ordered magnetic moment at 7.5 K amounts to  $1.59(7) \mu_{\text{B}}$ . The Néel temperature is 101 K, i.e. considerably lower than that found from magnetic susceptibility measurements (compare Fig. 34).

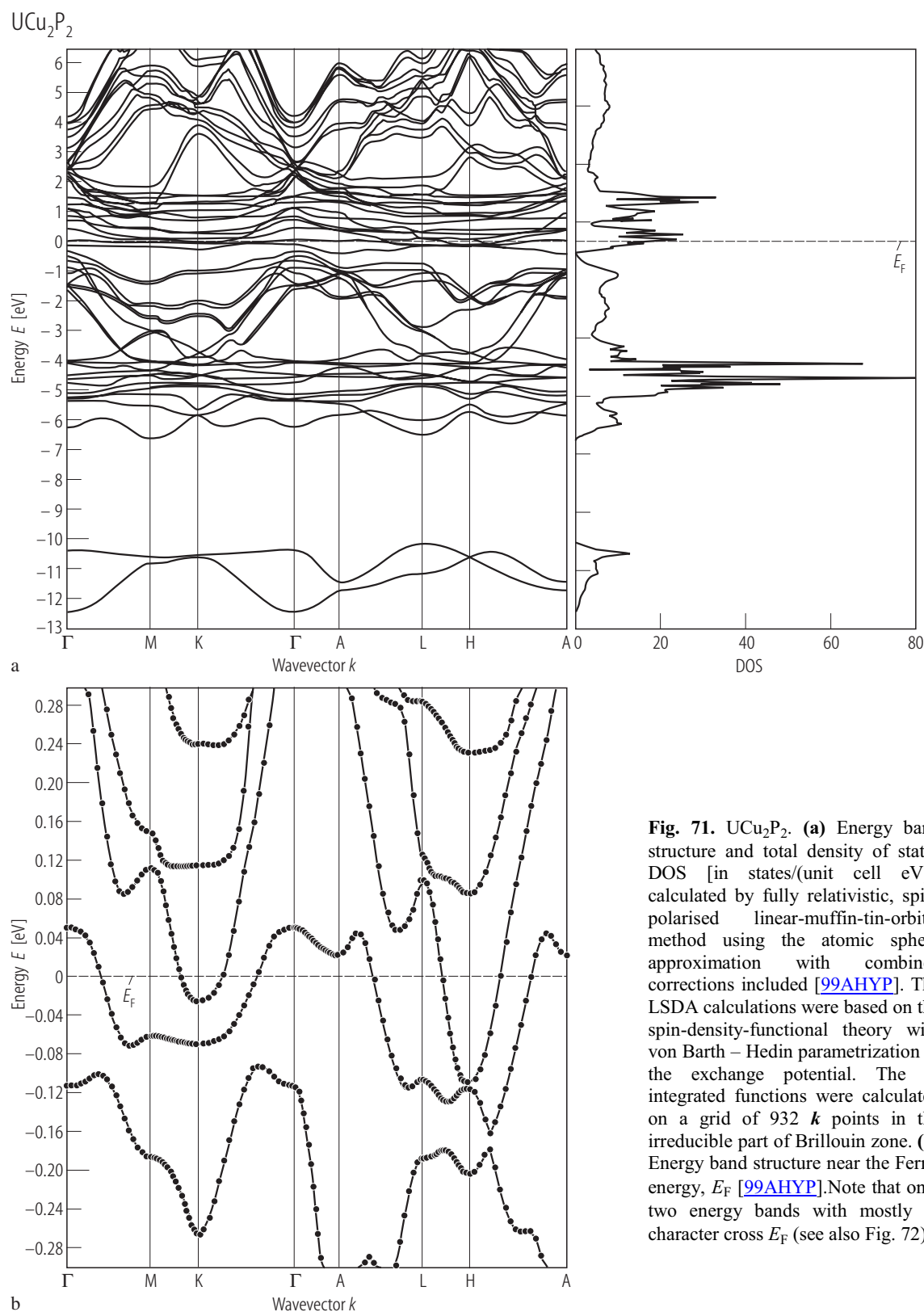


**Fig. 71.** UCu<sub>2</sub>P<sub>2</sub>. **(a)** Energy band structure and total density of states DOS [in states/(unit cell eV)], calculated by fully relativistic, spin-polarised linear-muffin-tin-orbital method using the atomic sphere approximation with combined corrections included [99AHYP]. The LSDA calculations were based on the spin-density-functional theory with von Barth – Hedin parametrization of the exchange potential. The  $k$ -integrated functions were calculated on a grid of 932  $k$  points in the irreducible part of Brillouin zone. **(b)** Energy band structure near the Fermi energy,  $E_F$  [99AHYP]. Note that only two energy bands with mostly 5f character cross  $E_F$  (see also Fig. 72).

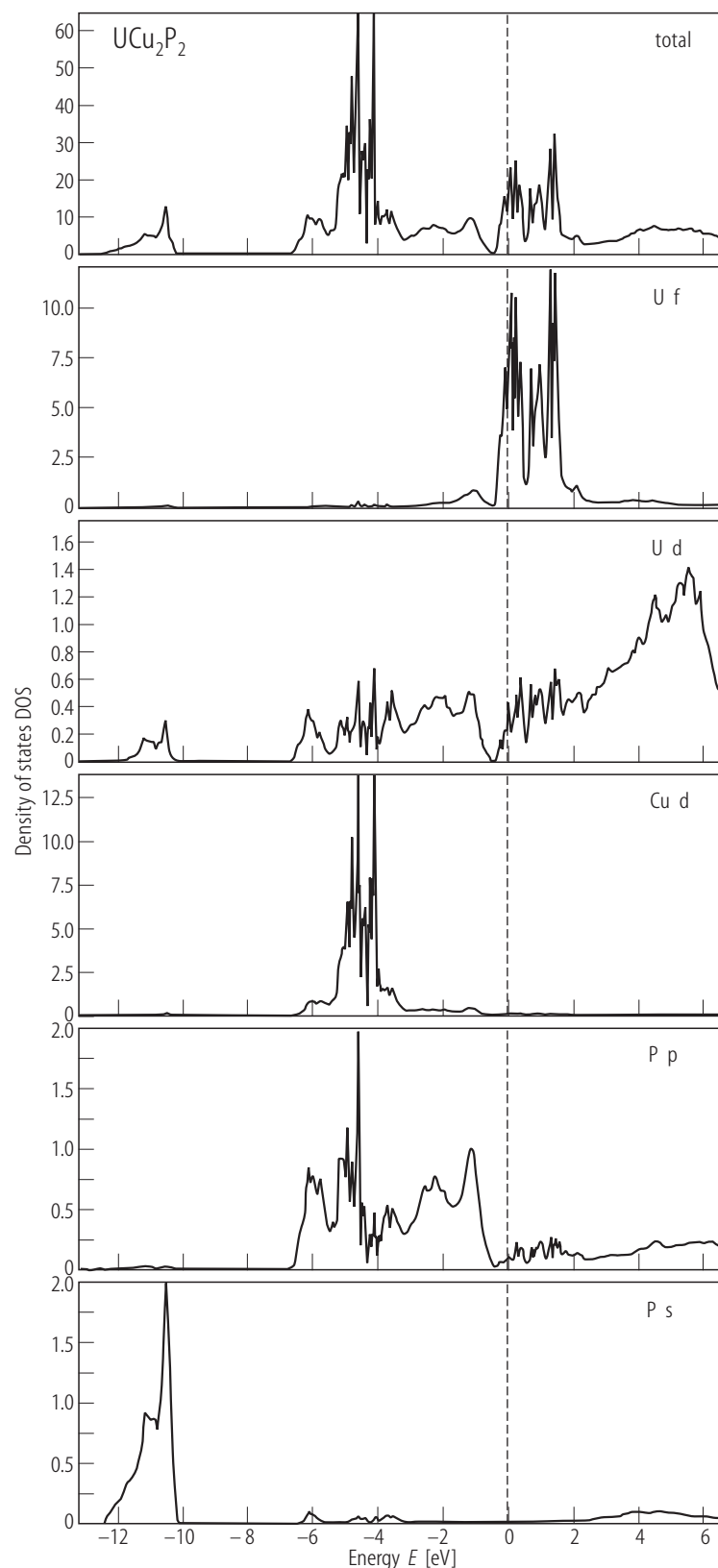


**Fig. 72.**  $\text{UCu}_2\text{P}_2$ . Fully relativistic, spin-polarised total density of states [in states/(unit cell eV); top panel] and partial densities of states [in states/(atom eV)], calculated as in Fig. 71 [99AHYP]. Note that the bands in the lowest energy region (from  $-12.4$  up to  $-10.1$  eV) have predominantly a P s character with some amount of U spd character mixed in. The bands between  $-6.7$  and  $-0.4$  eV consist of the 3p states of phosphorus strongly hybridised with the 3d states of copper which extend from  $-5.5$  to  $-4.0$  eV. The uranium 5f bands are located near the Fermi energy in the region  $-0.4$  to  $2.0$  eV. At still higher energies there are antibonding U 6d states.

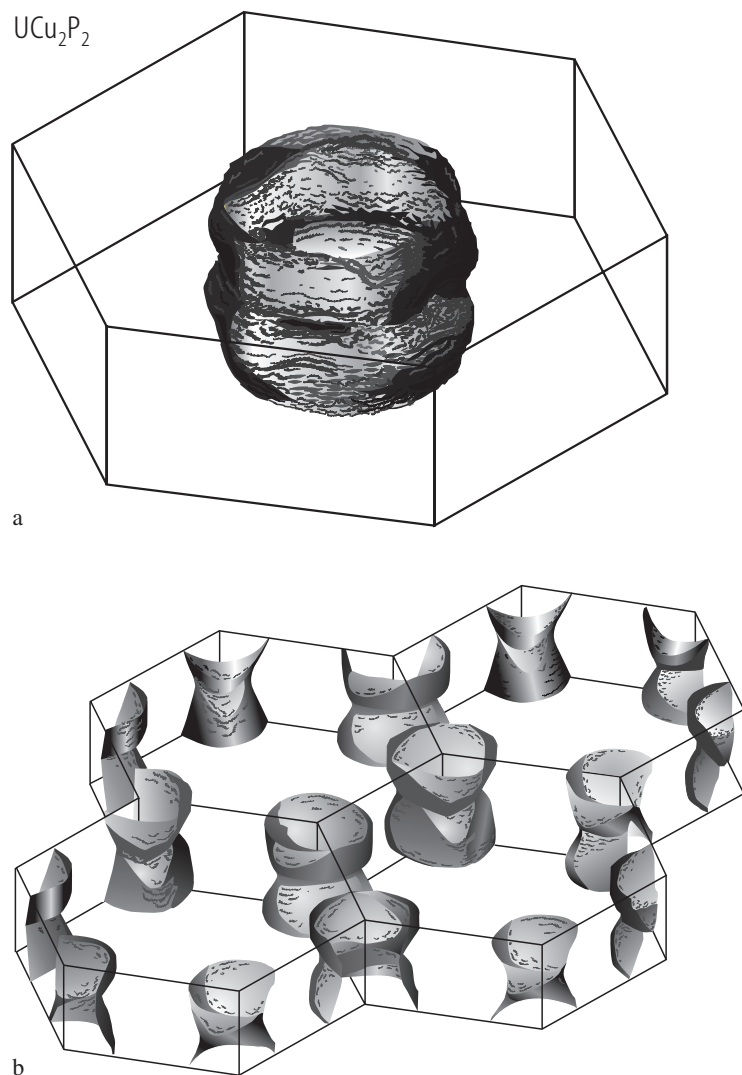


**Fig. 73.**  $\text{UCu}_2\text{P}_2$ . Fermi surface (calculated as in Fig. 71) represented as two open sheets: (a) gofer hole cylinder ( $h_{38}$ ) around the  $\Gamma$ -A direction, and (b) an electron cup ( $e_{39}$ ) along the K-H direction [99AHYP].

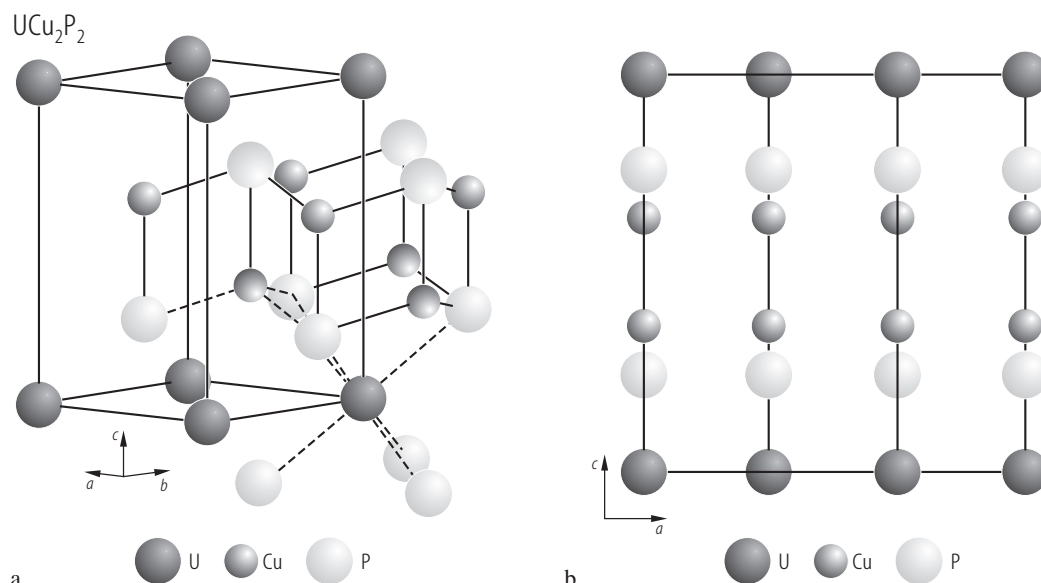


**Fig. 74.**  $\text{UCu}_2\text{P}_2$ . **(a)** Crystal structure and the coordination polyhedra of the uranium and copper atoms [94DZTK]. Note that the uranium atom is coordinated by six phosphorus atoms forming a nearly perfect octahedron. **(b)**

Crystal structure projected on the  $ac$ -plane [87ZNK]. Note a layered character of the unit cell with the uranium atom sheets separated by as many as four sheets of nonmagnetic atoms.

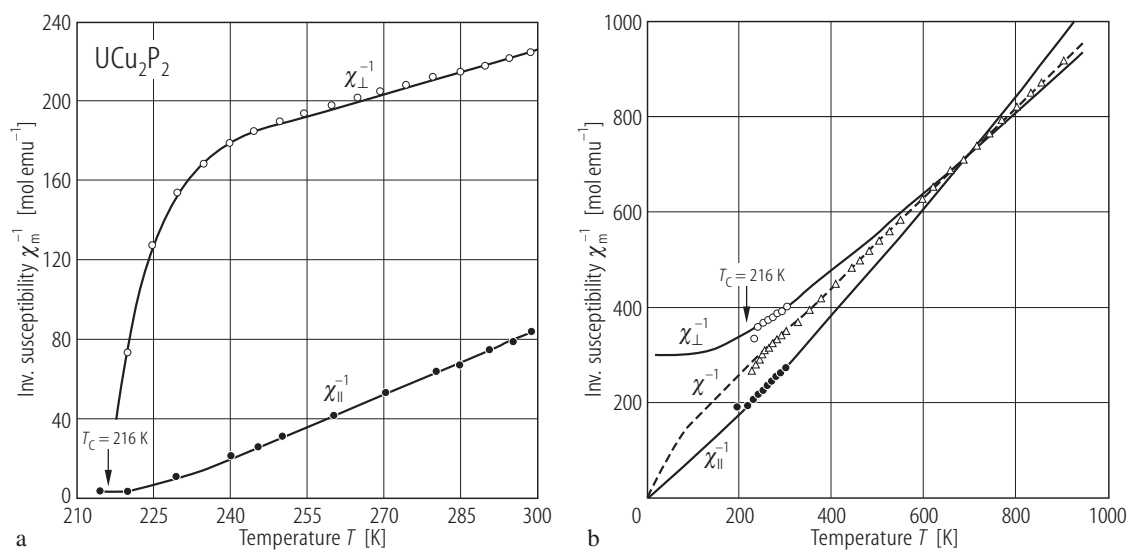


**Fig. 75.**  $\text{UCu}_2\text{P}_2$ . **(a)** Longitudinal,  $\chi_{\parallel}^{-1}$ , (full circles) and transversal,  $\chi_{\perp}^{-1}$ , (open circles) reciprocal molar magnetic susceptibility vs. temperature,  $T$ , in the range 216...300 K [88K]. The compound orders ferromagnetically at 216 K. The solid lines serve as a guide to the eye. **(b)** Experimental data from panel (a), shifted upwards by the molecular field constants  $\lambda_{\parallel} = -195$  mol/cm $^3$  and  $\lambda_{\perp} = -178$  mol/cm $^3$  (for the longitudinal and transversal susceptibility respectively) as compared to the calculated  $\chi_{\parallel}^{-1}(T)$  and  $\chi_{\perp}^{-1}(T)$  dependencies (solid lines) for the doublet  $\Gamma_{3T}$ -singlet  $\Gamma_{1(2)T}$  system of lowest lying crystal field levels originating from the uranium  $^3\text{H}_4$  ground multiplet split in a trigonal  $\text{D}_{3d}$  crystal field potential [88K]. For details on the crystal field approach see the original paper. The dashed line is the average reciprocal susceptibility calculated as  $\chi^{-1}(T) = \frac{1}{3}(\chi_{\parallel}^{-1} + 2\chi_{\perp}^{-1})$ . Triangles: measured powder reciprocal molar magnetic susceptibility vs.  $T$  up to 900 K, corrected by the molecular field constant  $\lambda_{\parallel} = -183$  mol/cm $^3$ . Note a good agreement between the experimental and calculated curves.

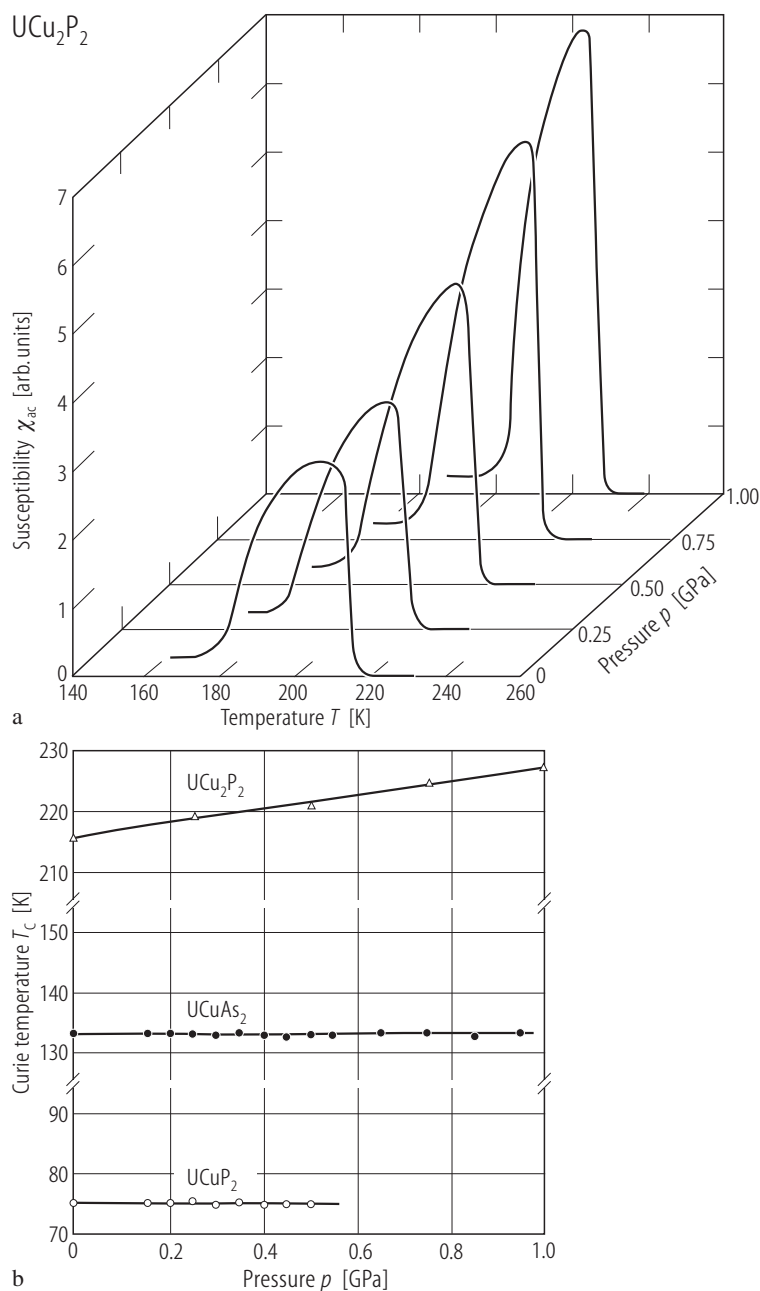


**Fig. 76.**  $\text{UCu}_2\text{P}_2$ ,  $\text{UCuP}_2$ ,  $\text{UCuAs}_2$ . **(a)** ac magnetic susceptibility,  $\chi_{ac}$ , vs. temperature,  $T$ , measured on a single crystal of  $\text{UCu}_2\text{P}_2$ , with an ac magnetic field of  $10^{-3}$  T and frequency of several hundreds Hz applied along the easy magnetization  $c$ -axis, in the vicinity of a ferromagnetic phase transition at hydrostatic pressures of 0, 0.25, 0.5, 0.75 and 1.0 GPa [89KDT]. Note a behaviour characteristic of

strongly anisotropic ferromagnets with pronounced domain effects. **(b)** Curie temperature,  $T_C$ , vs. pressure,  $p$ , as derived from ac susceptibility measurements [89KDT]. Note a strong linear increase of  $T_C$  in  $\text{UCu}_2\text{P}_2$  ( $dT_C/dp = 10(1)$  K/GPa), which may suggest a well localised character of its 5f electrons. For  $\text{UCuP}_2$  and  $\text{UCuAs}_2$   $T_C$  is hardly affected by pressure.

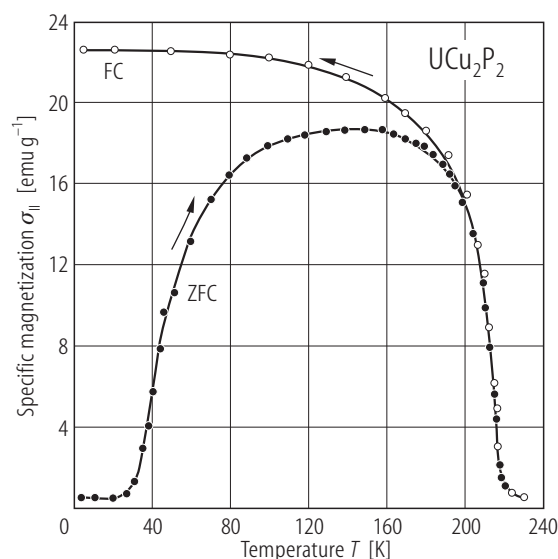


**Fig. 77.**  $\text{UCu}_2\text{P}_2$ . Specific magnetization,  $\sigma_{\parallel}$ , measured in a field of 0.1 T along the hexagonal  $c$ -axis with cooling the sample with (FC, open symbols) and without (ZFC, full symbols) an applied magnetic field, vs. temperature,  $T$  [90KT]. The compound orders ferromagnetically at  $T_C = 216$  K. Note a pronounced domain effect.

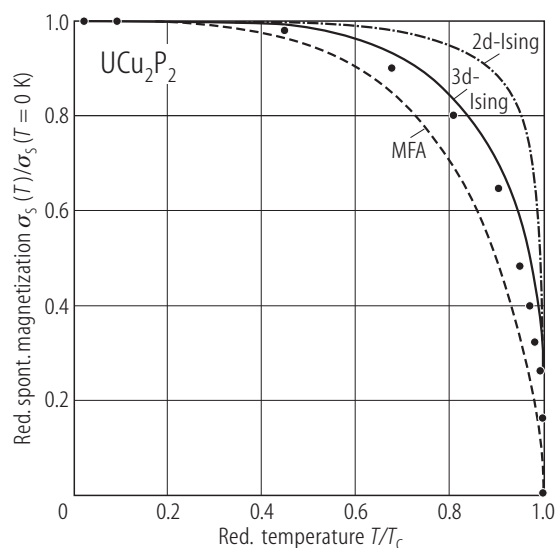


**Fig. 78.**  $\text{UCu}_2\text{P}_2$ . Reduced spontaneous magnetization,  $\sigma_s(T)/\sigma_s(T = 0 \text{ K})$  vs. reduced temperature,  $T/T_C$ , as derived from the data of Fig. 80 by means of the Arrott's plots [90KT]. The dashed, dashed-dotted and solid lines are the theoretical functions obtained within the molecular field approximation, the 2d Ising model and the 3d Ising model, respectively. The calculations were performed for the effective spin  $S = 1/2$  appropriate for a doublet ground state (see Fig. 75). Note that the best description of the experimental results was obtained with the 3d Ising model.

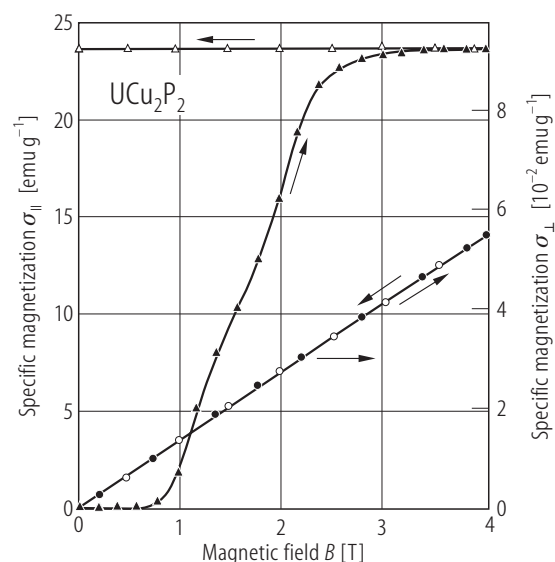


**Fig. 79.**  $\text{UCu}_2\text{P}_2$ . Specific magnetization,  $\sigma_{\parallel}$  and  $\sigma_{\perp}$ , measured at 4.2 K along (left-hand scale, triangles) and perpendicular (right-hand scale, circles) to the hexagonal  $c$ -axis, respectively, with increasing (full symbols) and decreasing (open symbols) magnetic field,  $B$  [90KT]. Note a strong uniaxial anisotropy with the easy-magnetization direction being the  $c$ -axis, a wide hysteresis loop of  $\sigma_{\parallel}(B)$  with nearly 100% remanence and a linear behaviour of  $\sigma_{\perp}(B)$ . The anisotropy constant  $K_1$  was estimated to be as large  $1.5 \cdot 10^3 \text{ J/kg}$ , which corresponds to the anisotropy field of about 100 T. The saturation uranium magnetic moment amounts to  $1.78 \mu_B$ .

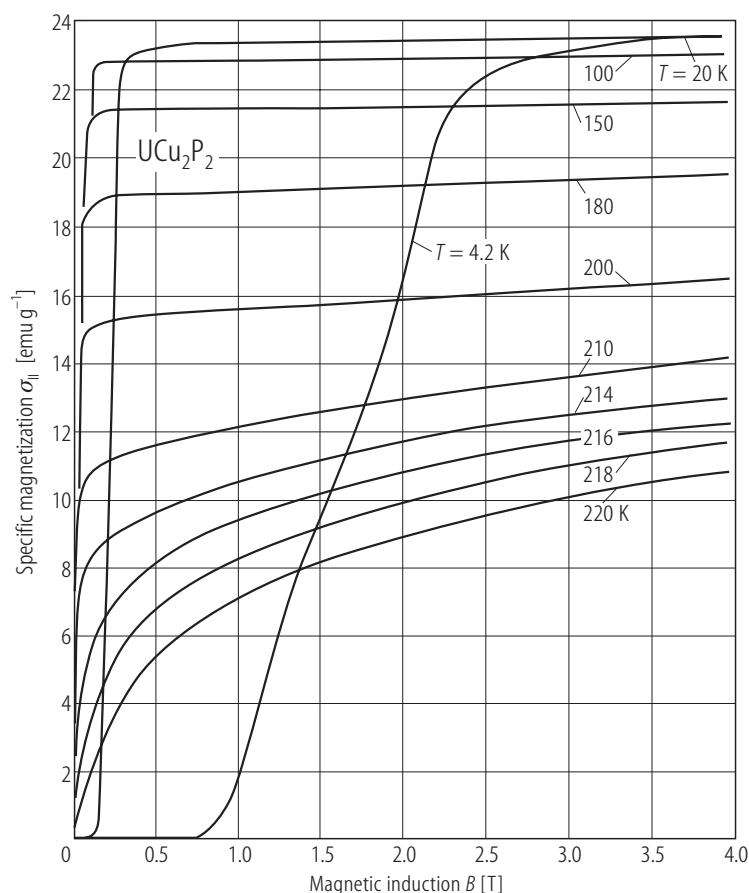


**Fig. 80.**  $\text{UCu}_2\text{P}_2$ . Specific magnetization,  $\sigma_{||}$ , along the easy-magnetization  $c$ -axis vs. magnetic field,  $B$ , measured at several temperatures below and above  $T_C = 216$  K, specified in the figure [90KT]. Note a very large value of the nucleation field of the magnetization taken at 4.2 K,  $B_{\text{nf}} = 0.7$  T, that indicates the presence of a compensated narrow-wall domain structure, at low temperatures which is suddenly reconstructed at  $B_{\text{nf}}$ . With increasing temperature  $B_{\text{nf}}$  quickly decreases. A strong curvature of the  $\sigma_{||}(B)$  isotherms taken above  $T_C$  presumably results from short-range interactions.

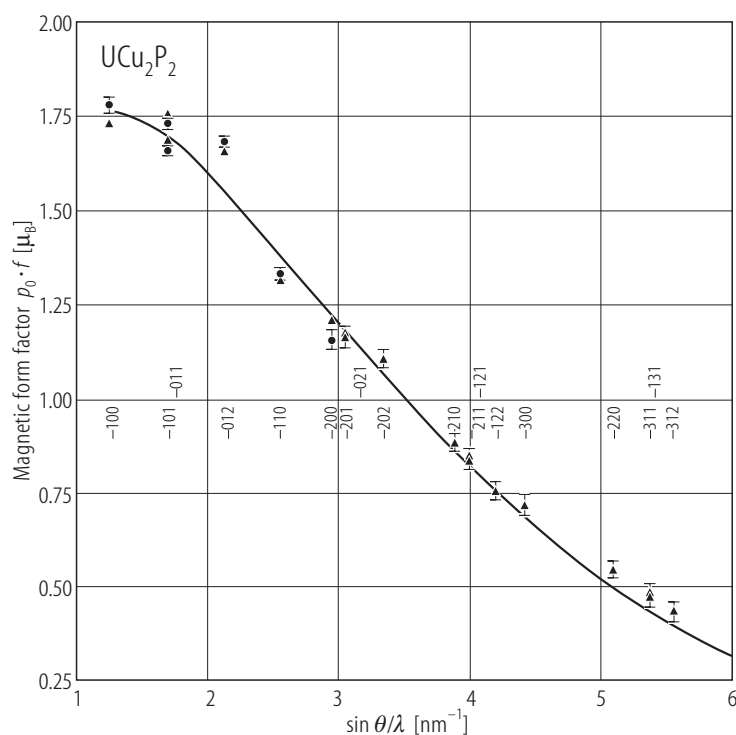


**Fig. 81.**  $\text{UCu}_2\text{P}_2$ . Magnetic amplitude of the uranium ions measured on a single crystal by polarised neutron diffraction at 10 K with a magnetic field of 3.5 T applied along the easy-magnetization  $c$ -axis (small circles with error bars) [94DZTK]. The solid line is the form factor of the  $\text{U}^{3+}$  ion. The triangles represent the values calculated within a model of  $\bar{3}m$  symmetry applied on the U 6d electrons and cubic symmetry applied on the Cu 3d electrons. For explanations see the original paper. Deviations from a theoretical form factor are due to the covalency effect at low values of  $\sin\theta/\lambda$  and due to crystal field and covalency effects at high values of  $\sin\theta/\lambda$ . The anisotropy of the measured form factor at low values of  $\sin\theta/\lambda$  the authors explained by a real occupation of the U 6d states which admix to the U 5f states due to overlapping and covalency effects.



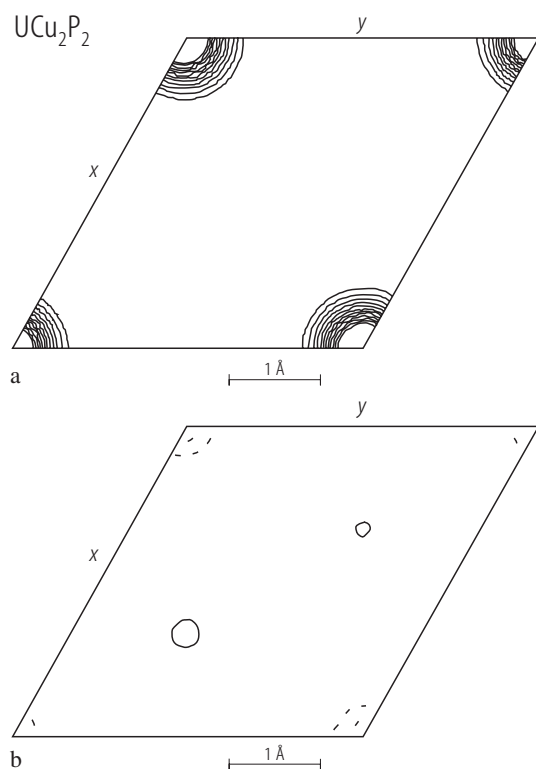


**Fig. 82.**  $\text{UCu}_2\text{P}_2$ . Fourier transform of the experimental amplitudes from Fig. 83 [94DZTK]. Contours represent  $0.02 \mu_{\text{B}}/\text{\AA}^3$ . **(a)** section  $z=0$  showing the U atoms; **(b)** section  $z=0.366$  showing the Cu atoms (see the crystal structure in Fig. 74). Note that no anisotropy is observed on the uranium atom sites. A one-contour signal at the Cu positions indicates that a small magnetic moment is present on the Cu atoms. Note that the signal is different at the positions  $(1/3, 2/3, z)$  and  $(2/3, 1/3, z)$ .

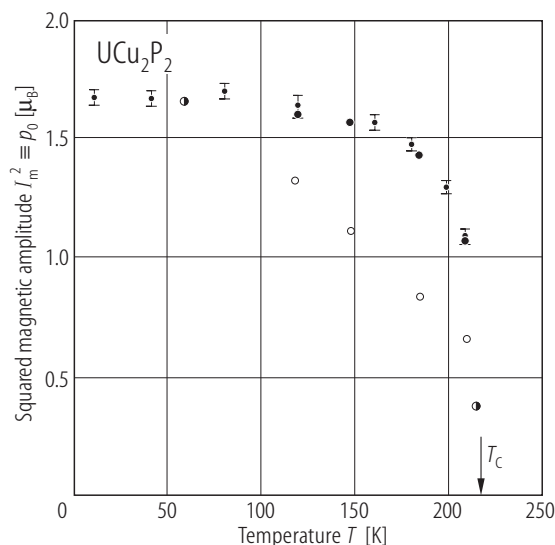


**Fig. 83.**  $\text{UCu}_2\text{P}_2$ . Squared amplitude of the magnetic reflection  $(101)$ ,  $I_M^2 = p_0$ , vs. temperature,  $T$ , as compared to the same dependence reported in [94BTKN] for the two uranium atoms in  $\text{U}_4\text{Cu}_4\text{P}_7$  (see Fig. 162) [94DZTK]. Small circles with error bars: U in  $\text{UCu}_2\text{P}_2$ ; open circles:  $\text{U}(1)^{4+}$  in  $\text{U}_4\text{Cu}_4\text{P}_7$ ; filled circles:  $\text{U}(2)^{3+}$  in  $\text{U}_4\text{Cu}_4\text{P}_7$ . For the sake of clarity the temperatures and the correspondent magnetic moments observed for  $\text{U}_4\text{Cu}_4\text{P}_7$  have been normalised to the results obtained for  $\text{UCu}_2\text{P}_2$ . From the apparent similarity between  $I_M(T)$  measured for  $\text{UCu}_2\text{P}_2$  and that found for the  $\text{U}(2)$  ions in  $\text{U}_4\text{Cu}_4\text{P}_7$  the authors concluded a trivalent state for uranium atoms in  $\text{UCu}_2\text{P}_2$ . See Fig. 175 for contrary arguments indicating the presence of  $\text{U}^{4+}$  ions.

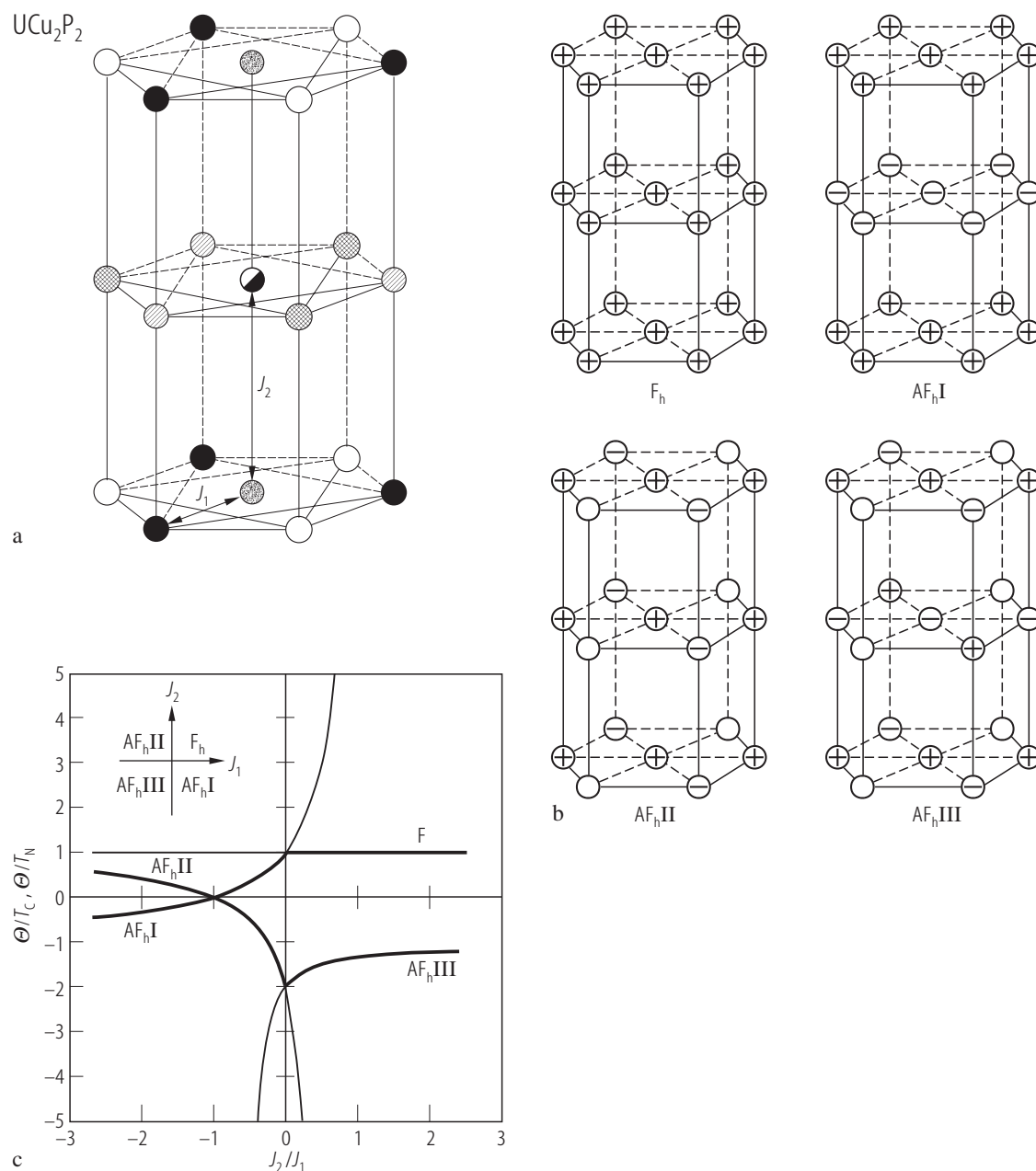


**Fig. 84.**  $\text{UCu}_2\text{P}_2$ . (a) Possible magnetic moment configurations in a hexagonal structure of the  $\text{CeAl}_2\text{Si}_2$ -type, calculated by the Smart's method within the molecular field approximation [90KT]. The two main exchange integrals,  $J_1$  and  $J_2$ , which were used in the calculations are shown in panel (a) on a schematic view of the crystal structure. The magnetic atoms belonging to six different Néel sublattices considered are denoted by different symbols. Panel (b) presents four simple ordering schemes denoted by  $F_h$ ,  $\text{AF}_h\text{I}$ ,  $\text{AF}_h\text{II}$  and  $\text{AF}_h\text{III}$  where the symbols + and - stand for ferro- and antiferromagnetic coupling,

respectively, while the empty circles indicate the sites which cannot be correlated by the isotropic exchange interactions considered in the calculations (for explanation refer to the original paper). The structure established for  $\text{UCu}_2\text{P}_2$  is  $F_h$ . (c) Paramagnetic Curie temperature to ordering temperature ratio,  $\Theta/T_C$  or  $\Theta/T_N$ , vs. relative strength of exchange interactions,  $J_2/J_1$ , for the magnetic structures from panel (b) [90KT]. Inset: stability diagram for these structures in the  $J_1$  -  $J_2$  plane. For the discussion see the original paper.

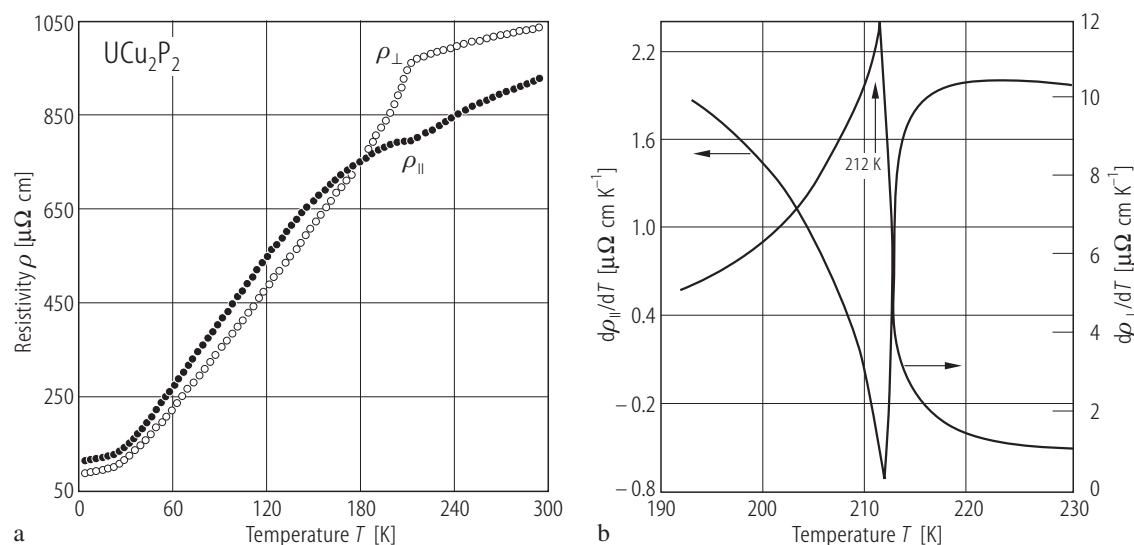


**Fig. 85.**  $\text{UCu}_2\text{P}_2$ . **(a)** Electrical resistivity,  $\rho$ , vs. temperature,  $T$ , measured on single crystals with  $i \parallel c$ -axis (filled circles) and  $i \perp c$ -axis (open circles) [90KT]. Note a different behaviour of  $\rho_{\parallel}(T)$  and  $\rho_{\perp}(T)$  near the ferromagnetic phase transition at 216 K but rather small anisotropy in the resistivity behaviour being in contrast to a huge anisotropy seen in the magnetic properties (see Fig. 79). Below 70 K the resistivity can be fitted by the formula  $\rho(T) = \rho_0 + c_m T^2 \exp(-\Delta/T)$ , describing the scattering of conduction electrons on defects in the lattice and spin wave excitations over an energy gap  $\Delta$  (the first and second term, respectively). The fitting parameters are:  $\rho_0 = 91 \mu\Omega\text{cm}$ ,  $c_m = 0.05 \mu\Omega\text{cm/K}^2$  and  $\Delta = 25 \text{ K}$  for  $\rho_{\perp}(T)$ , and

$\rho_0 = 113 \mu\Omega\text{cm}$ ,  $c_m = 0.06 \mu\Omega\text{cm/K}^2$  and  $\Delta = 26 \text{ K}$  for  $\rho_{\parallel}(T)$ . Above 260 K both tensors follow the formula  $\rho(T) = \rho_0 + \rho_0^{\infty} + c_{\text{ph}} T$ , describing the scattering of free carriers on defects, disordered spins and phonons (the first, second and third term respectively), with the  $\rho_0$  parameters as above and:  $\rho_0^{\infty} = 758 \mu\Omega\text{cm}$  and  $c_{\text{ph}} = 0.64 \mu\Omega\text{cm/K}$  for  $\rho_{\perp}(T)$  and  $\rho_0^{\infty} = 448 \mu\Omega\text{cm}$  and  $c_{\text{ph}} = 1.23 \mu\Omega\text{cm/K}$  for  $\rho_{\parallel}(T)$ . **(b)** Temperature derivative of  $\rho_{\parallel}(T)$  and  $\rho_{\perp}(T)$  in the vicinity of  $T_C$  [90KT]. The arrow marks the phase transition. Note the opposite behaviour of the two derivatives

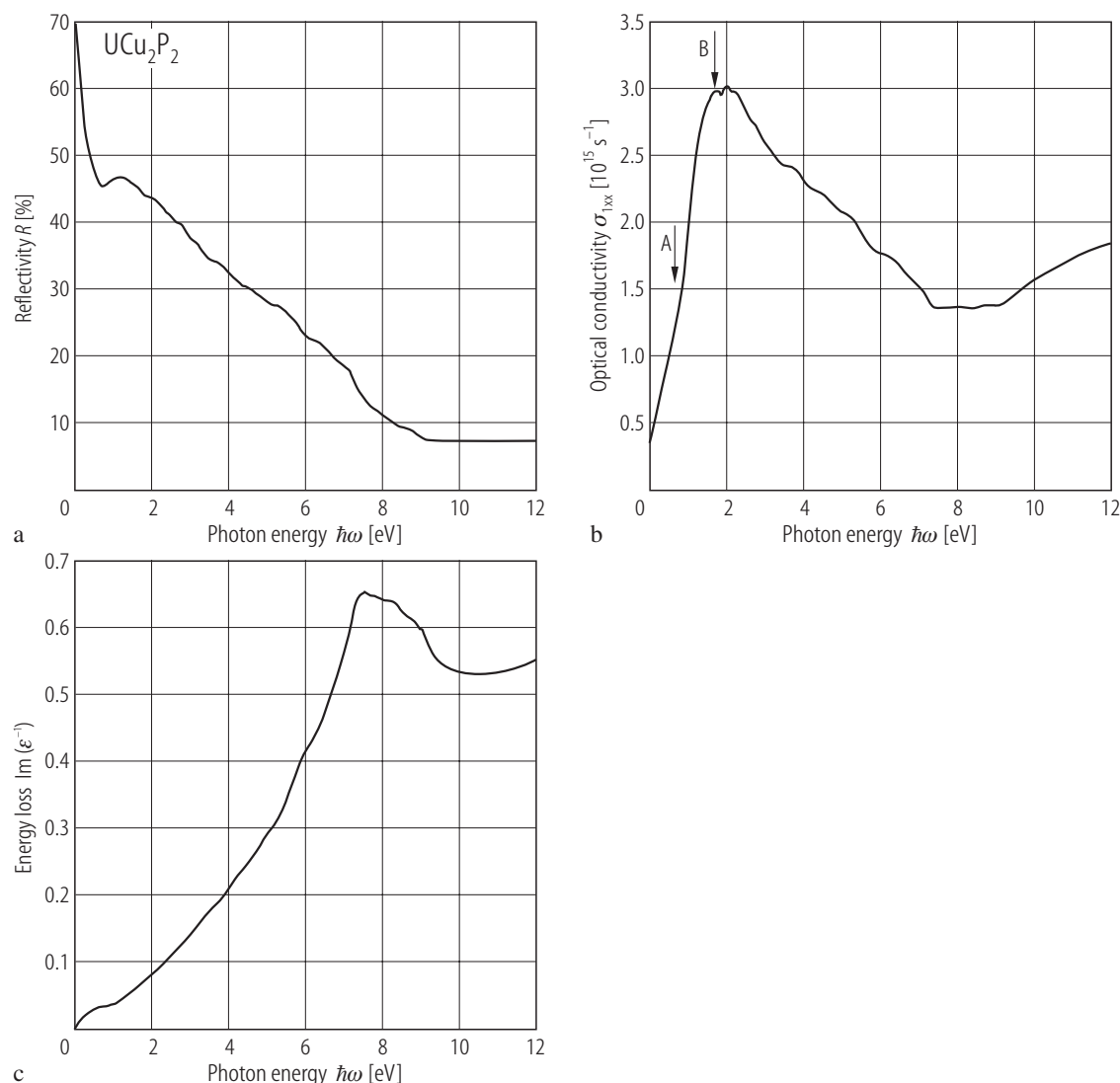


**Fig. 86.**  $\text{UCu}_2\text{P}_2$ . **(a)** Near normal incidence optical reflectivity,  $R$ , vs. photon energy,  $\hbar\omega$ , in the range of 0.03 to 12 eV, measured at 300 K on a mechanically polished surface perpendicular to the  $c$ -axis [89SFRK]. Note a metallic behaviour with  $R$  tending to 100 % as  $\hbar\omega$  goes to zero. A very steep decrease of  $R$  at the lowest energies indicates a strongly damped free carrier concentration. **(b)** Real part of the optical conductivity,  $\sigma_{xx}$ , vs.  $\hbar\omega$ , calculated by Kramers-Kronig transformation from the data shown in panel (a) [88FSRK]. Note a very small intraband contribution. The shoulder near 0.7 eV (marked by arrow

A) is identified with an uranium  $f \rightarrow d$  interband transition (see Fig. 44), the broad peak at 2 eV (labeled B) is presumably due to a transition from bonding phosphorus  $p$  and uranium  $d$  states into empty uranium  $f$  states. The small structures between 4 and 6 eV are probably charge transfer transitions from phosphorus  $p$  states into uranium derived  $6d$  and  $7s$  states and into copper  $4s$  states with some contribution from intra copper  $3d \rightarrow 4s$  transitions. **(c)** Energy loss function,  $\text{Im}(\epsilon^{-1})$ , vs.  $\hbar\omega$ , calculated from the reflectivity data shown in panel (a) [88FSRK]. The maximum at 7.5 eV is associated with a plasmon.

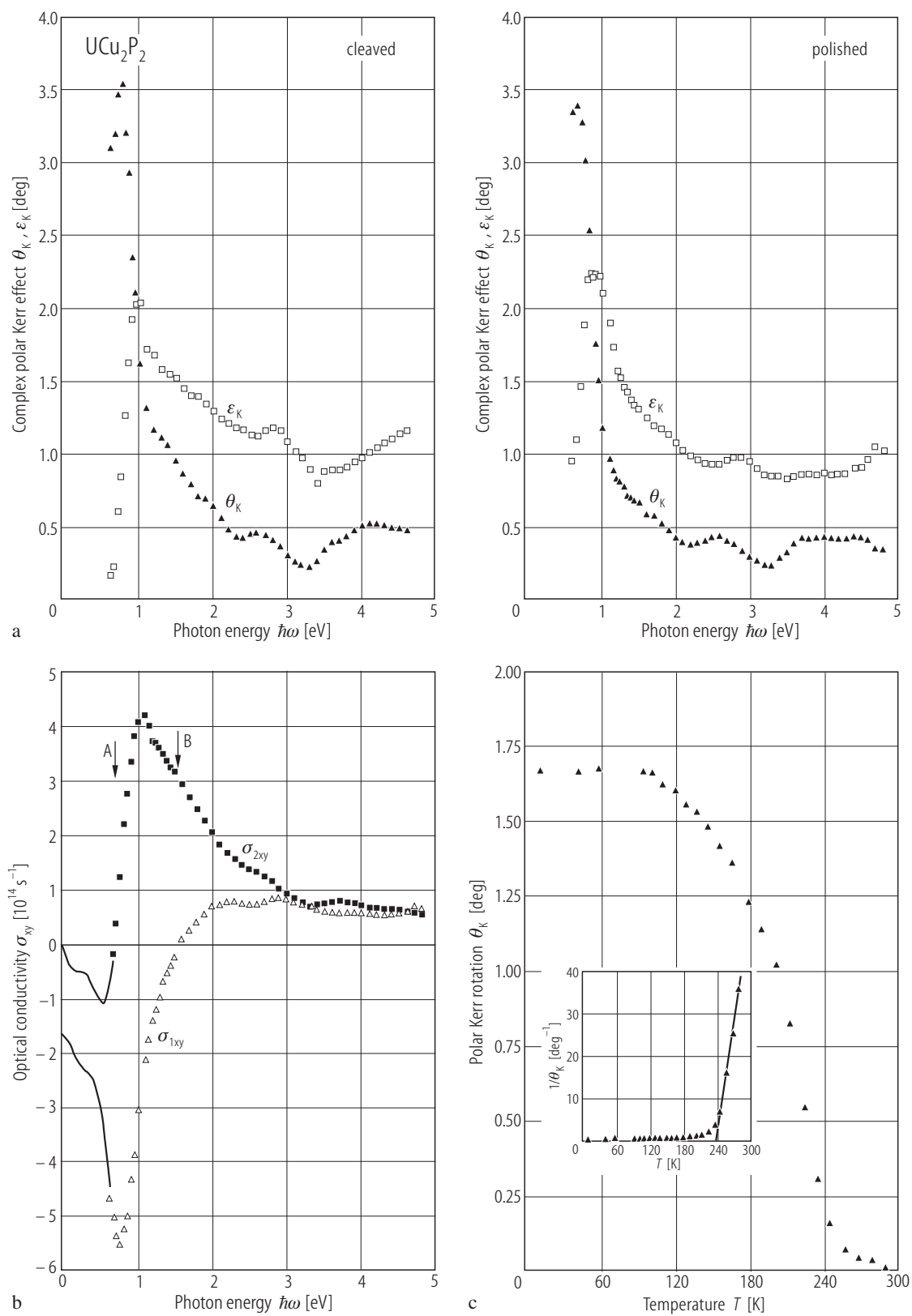
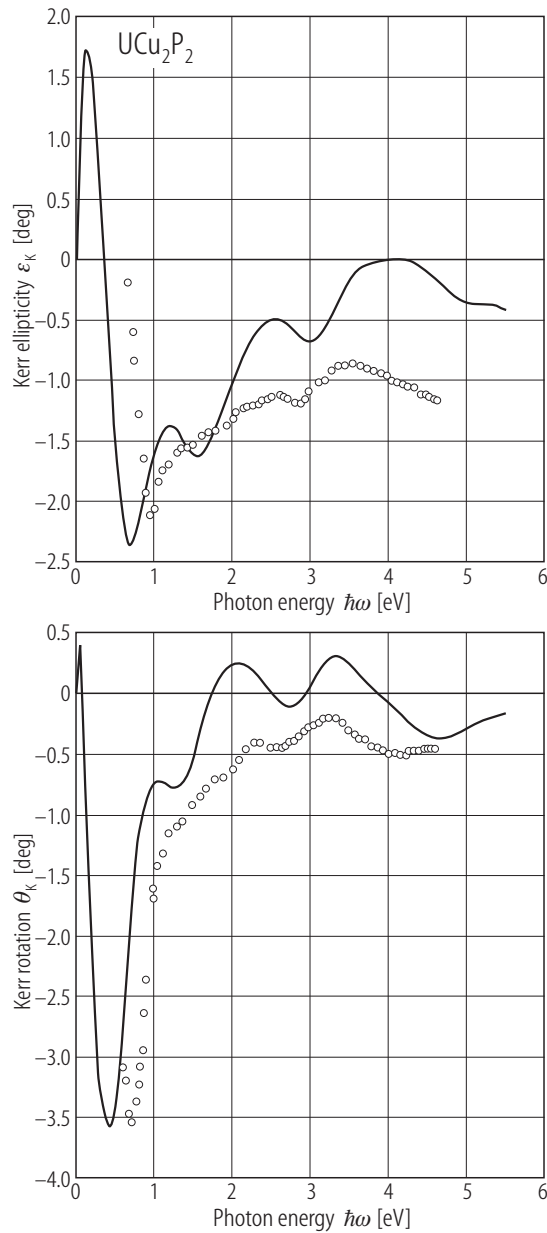
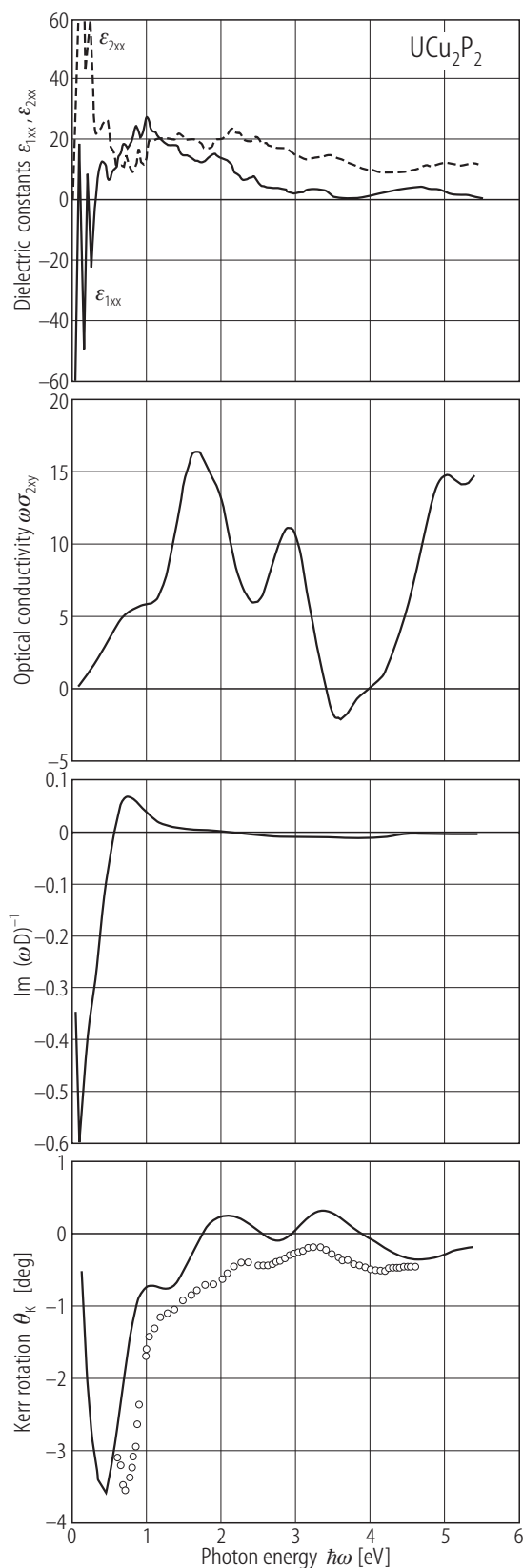


Fig. 87. For caption see next page.

**Fig. 87.**  $\text{UCu}_2\text{P}_2$ . **(a)** Polar Kerr rotation,  $\theta_K$ , and polar Kerr ellipticity,  $\varepsilon_K$ , vs. photon energy,  $\hbar\omega$ , in the range of 0.6 to 5 eV, measured at 10 K and at a magnetic field  $B$  of 4 T ( $B \parallel c$ -axis) on a cleaved and mechanically polished surface perpendicular to the easy magnetization  $c$ -axis [89SFRK]. Note a very large maximum Kerr rotation value of 3.5 deg at 0.75 eV for the cleaved and 3.4 deg at 0.65 eV for the polished crystal. **(b)** Real,  $\sigma_{1xy}$ , and imaginary,  $\sigma_{2xy}$ , part of the off-diagonal conductivity vs.  $\hbar\omega$ , calculated from the Kerr effect shown in panel (a) using the reflectivity data from Fig. 86 [89SFRK]. The solid lines are extrapolations to zero energy, obtained using the mutual Kramers-Kronig transformation between  $\sigma_{1xy}$  and  $\sigma_{2xy}$ . Note a structure with diamagnetic line shape corresponding to peak A in  $\sigma_{1xy}$ , which is assigned to an intra uranium  $f \rightarrow d$  transition, and a structure with paramagnetic line shape corresponding to peak B, which is attributed to a transition from bonding phosphorus  $p$  and uranium  $d$  states into empty uranium  $f$  states. **(c)** Kerr rotation,  $\theta_K$ , at a fixed energy of 1 eV, vs. temperature,  $T$ , measured on a cleaved crystal as described in panel (a) [89SFRK]. Note a typical ferromagnetic behaviour below  $T_C = 216$  K. Inset: inverse Kerr rotation,  $\theta_K^{-1}$ , vs.  $T$ . Note a Curie-Weiss behaviour in the paramagnetic region.



**Fig. 88.**  $\text{UCu}_2\text{P}_2$ . Kerr rotation,  $\theta_K$ , and Kerr ellipticity,  $\varepsilon_K$ , vs. photon energy,  $\hbar\omega$ , calculated ab initio by LSDA method (solid lines), as compared to the experimental data (circles) taken from [89SFRK] (see Fig. 87) [99AHYP]. Note a good agreement between the theoretical and experimental results except for a small shift of about 0.3 eV of the prominent peak both in  $\theta_K(\omega)$  and  $\varepsilon_K(\omega)$ , which results from a combination of a deep resonance structure in the denominator and interband transitions contributing to  $\sigma_{2xx}$  (see Fig. 89). The peaks at 2.0 and 3.3 eV originate mainly from U  $6d \rightarrow 5f$  interband transitions, while the interband transitions from Cu  $3d$  to U  $5f$  bands occur above 4 eV (compare Fig. 72). The obtained good theoretical description of the experimental magneto-optical data led the authors to the conclusion that the uranium  $5f$  electrons in  $\text{UCu}_2\text{P}_2$  are delocalised. The itinerant picture is however quite incompatible with the measured magnetic properties of this compound, which clearly reflect a well-localised character of the  $5f$  electrons (see Figs. 76, 78 and 79).



←

**Fig. 89.**  $\text{UCu}_2\text{P}_2$ . Decomposition of the calculated Kerr rotation spectrum from Fig. 88 into separate contributions [99AHYP]. Top panel: real,  $\epsilon_{1xx}$ , and imaginary,  $\epsilon_{2xx}$ , part of the dielectric function vs. photon energy,  $\hbar\omega$ ; second panel from the top:  $\omega\sigma_{2xy}$  vs.  $\hbar\omega$ ; third panel from the top: the imaginary part of  $(\omega D)^{-1}$  vs.  $\hbar\omega$ , where  $D(\omega) = \sigma_{xx}(1 + (4\pi i/\omega)\sigma_{xx})^{1/2}$ ; bottom panel: the Kerr rotation,  $\theta_K$ , which results as a product of  $\text{Im}(\omega D)^{-1}$  and  $\omega\sigma_{2xy}$  vs.  $\hbar\omega$ , as compared to the experimental data from [89SFRK]. For the explanation see the original paper. Note that the structures in the Kerr rotation occurring above 1.0 eV originate mainly from the shape of  $\sigma_{2xy}$ .

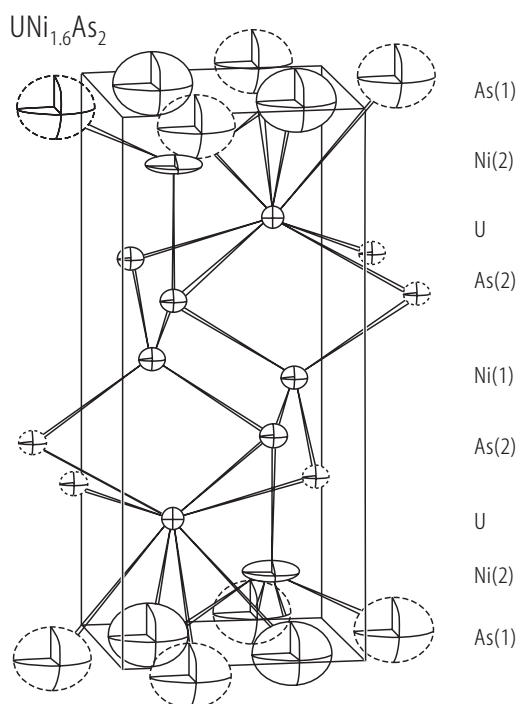


**Fig. 90.**  $\text{UNi}_{1.6}\text{As}_2$ . Crystal structure in a three dimensional "ORTEP" representation [90TKNG2]. The Ni(2) site is partially filled (population factor 0.592). The ellipsoids mark the anisotropy in the thermal displacement of all the atoms.

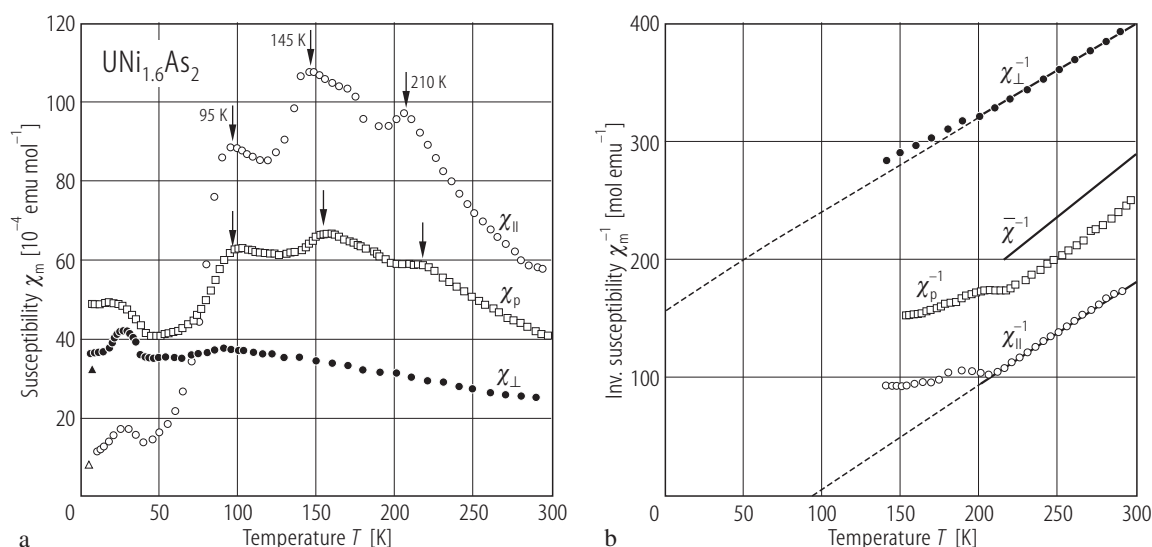


**Fig. 91.**  $\text{UNi}_{1.6}\text{As}_2$ . (a) Molar magnetic susceptibility,  $\chi_m$ , vs. temperature,  $T$ , measured on a single crystal with a magnetic field of 0.2 T oriented along (open circles) and perpendicular (filled circles) to the  $c$ -axis as well as on a powder sample (squares) [94TBNK]. Open and filled triangles denote the values of the longitudinal and transverse susceptibility, respectively, as determined from the data presented in Fig. 92. Note a very complex behaviour of  $\chi_m(T)$  with as many as three pronounced maxima at about 95, 145 and 210 K and an unusual anomaly at about 25 K, all seen in the longitudinal and powder susceptibilities. In the transverse susceptibility there

is only a tiny cusp at 95 K and a maximum at 25 K. Note a very large anisotropy in both the ordered and paramagnetic state. (b) Reciprocal molar magnetic susceptibility,  $\chi_m^{-1}$ , vs. temperature,  $T$ , in the paramagnetic region, obtained from the data presented in panel (a) [94TBNK]. The solid line represents  $\chi_m^{-1}(T)$  calculated as a weighted average of the longitudinal and transverse susceptibilities. The apparent disagreement between this function and the result obtained on a powder sample indicates the presence of some preferential orientation of crystallites ( $B \parallel c$ -axis) in the sample studied. The dashed lines are Curie-Weiss fits with the parameters given in Table B.

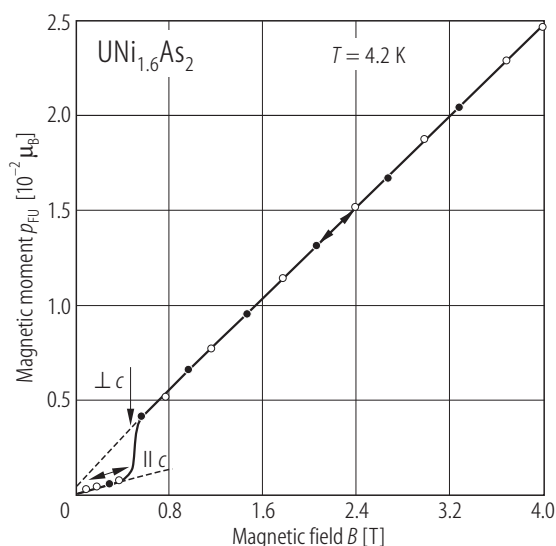


**Fig. 92.**  $\text{UNi}_{1.6}\text{As}_2$ . Magnetic moment,  $p_{\text{FU}}$ , vs. field,  $B$ , taken at 4.2 K with increasing (open circles) and decreasing (filled circles) magnetic field on a set of several single-crystalline platelets freely placed in a sample holder [94TBNK]. The arrow marks the field strength where a reorientation of the sample has occurred: the magnetic field was perpendicular to the tetragonal  $ab$ -plane in weak magnetic fields and was parallel to it in strong fields. Note in Fig. 91 that indeed below 70 K the transverse susceptibility is larger than the longitudinal one and that the susceptibility values at 4.2 K derived from the two slopes of  $p_{\text{FU}}(B)$  (dashed lines) correspond well to those found in the susceptibility measurements (see the triangles in Fig. 91). The linear behaviour of  $p_{\text{FU}}(B)$  indicates the absence of any ferromagnetic impurities in the sample studied.



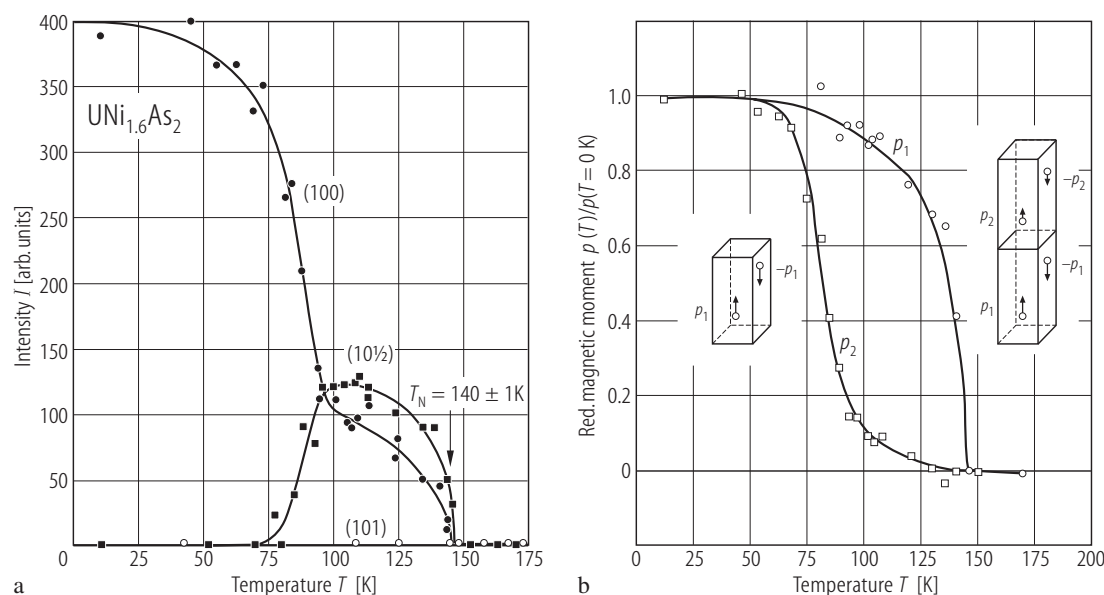


**Fig. 93.**  $\text{UNi}_{1.6}\text{As}_2$ . (a) Neutron diffraction intensity of the magnetic reflections (100) and (10½) as well as the nuclear reflection (101),  $I$ , vs. temperature,  $T$  [94TBNK]. Note that the magnetic intensities become zero already above  $T_N = 140(1)$  K and not above 210 K, as could be expected on the basis of the susceptibility data (see Fig. 91). In the temperature range  $T_1 = 95$  K  $< T < T_N$  two sets of magnetic Bragg peaks were found which correspond to the propagation vectors  $\mathbf{k}_1 = [000]$  and  $\mathbf{k}_2 = [00\frac{1}{2}]$  and to the magnetic Fourier components of about the same amplitude aligned along the  $c$ -axis. Below  $T_1$  only the component with  $\mathbf{k} = [000]$  was found. (b) Normalised magnetic moment,  $\rho(T)/\rho(T = 0\text{ K})$ , vs. temperature,  $T$ , for two different moments (circles and squares) carried by uranium atoms. These dependencies were derived from the intensity variations presented in panel (a), accounting for the presence of two inequivalent uranium sites in a nuclear superstructure (doubling along the  $c$ -axis), which arises due to an ordering of defects at nickel atoms sites. For the details on the superstructure refer to the original paper. Insets show schematically the magnetic structures at low temperatures ( $T < T_1$ ; left-hand side) and higher temperatures ( $T_1 < T < T_N$ ; right-hand side). The magnetic structure at low temperatures corresponds to a simple antiferromagnetic sequence  $+-$  of ferromagnetically coupled (001) planes with the moments aligned along the  $c$ -axis. The ordered moment at 1.5 K amounts to  $1.60(5) \mu_B$ . The high temperature phase can be described by the sequence  $(p_1, -p_1, p_2, -p_2)$  or  $(p_2, -p_2, p_1, -p_1)$  of the two different moments:  $p_1 = p_{k1} + p_{k2}$  and  $p_2 = p_{k1} - p_{k2}$ , which belong to subsequent (001) planes. At 100 K the components of wave vectors  $\mathbf{k}_1$  and  $\mathbf{k}_2$  are  $p_{k1} = 0.85(10) \mu_B$  and  $p_{k2} = 0.78(10) \mu_B$ , i.e. the uranium magnetic moments amount to  $1.58(2)$  and  $0.07(20) \mu_B$  for  $p_1$  and  $p_2$ , respectively. Note that  $p_1$  develops continuously below  $T_N$  whereas  $p_2$  keeps small values down to 100 K and increases when  $p_1$  nearly saturates.

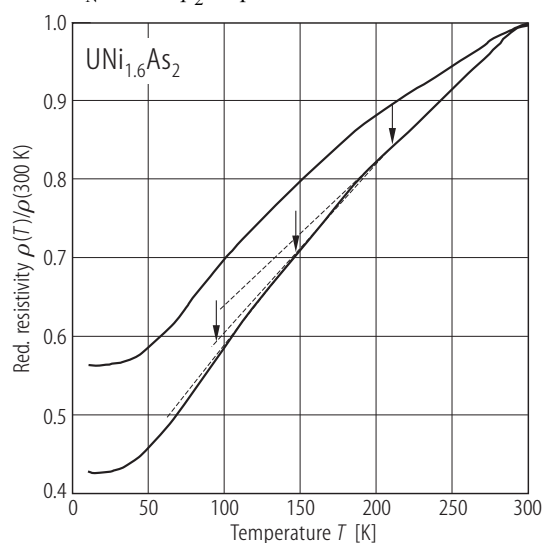


**Fig. 94.**  $\text{UNi}_{1.6}\text{As}_2$ . Normalised electrical resistivity,  $\rho/\rho(300\text{ K})$ , vs. temperature,  $T$ , measured on two small single crystals [94TBNK]. The difference between the curves probably results from different orientation of the current flow direction with respect to the crystallographic axes. Note that the phase transitions at 95, 145 and 210 K, determined in the magnetic studies (see Fig. 91) manifest itself as some changes in the slope of  $\rho(T)$  (marked by the arrows and dashed lines).

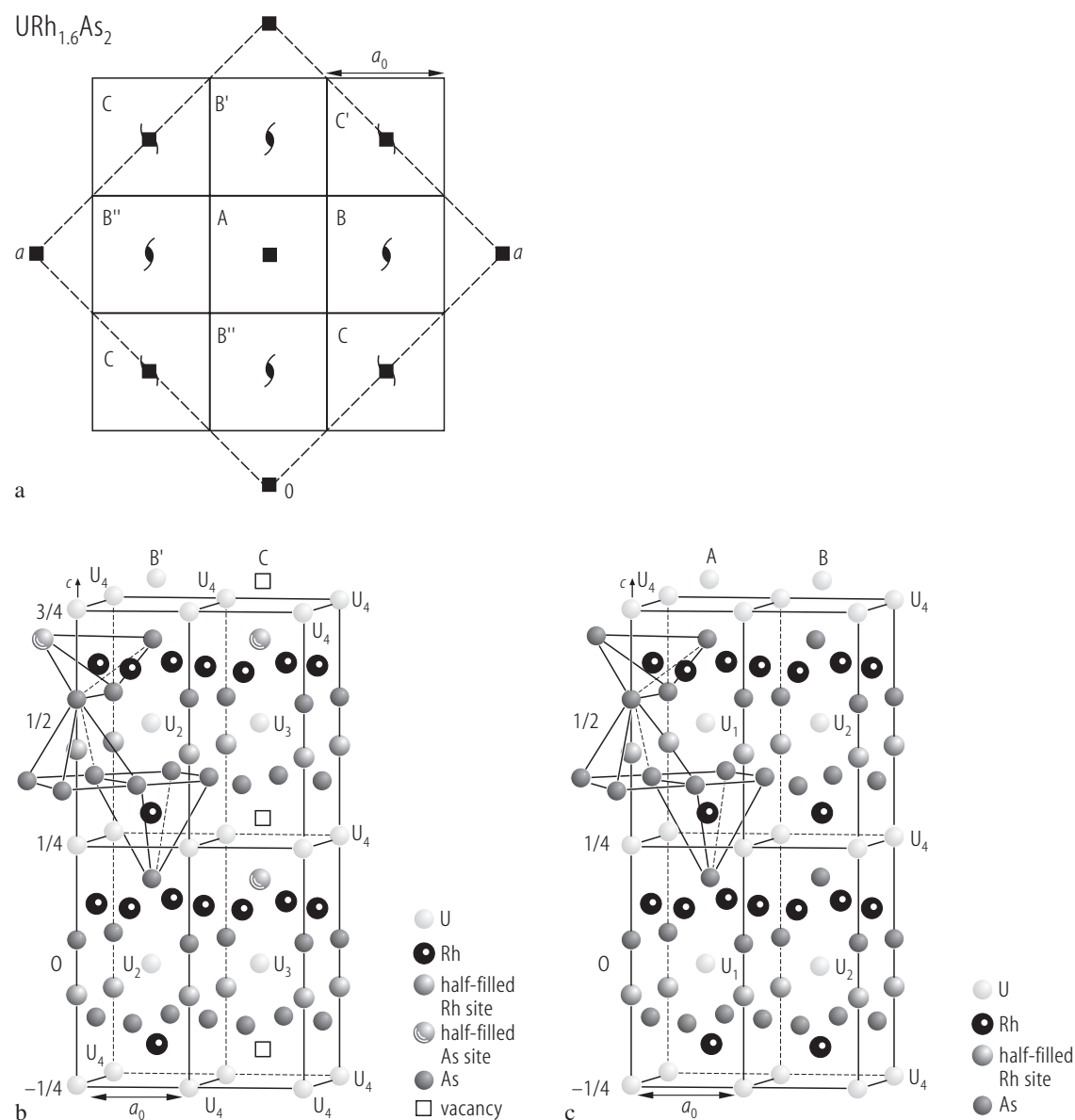


**Fig. 95.** URh<sub>1.6</sub>As<sub>1.9</sub>. **(a)** Superstructure cell schematically showing the arrangement of the building units A, B and C, each derived from two unit cells of the CaBe<sub>2</sub>Ge<sub>2</sub> type, as displayed in panels **(b)** and **(c)** [88ZVLV]. The B' and B''

units are obtained from B by a rotation of  $2\pi/4$ ,  $4\pi/4$ ,  $6\pi/4$  around axis 4 while the C' unit is derived from C by a rotation of  $2\pi/4$  around axis  $4_2$  (for further details see the original paper).

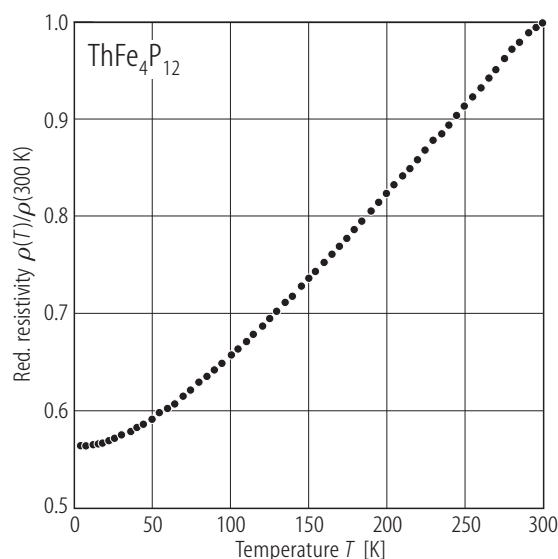


**Fig. 96.**  $\text{ThFe}_4\text{P}_{12}$ . Electrical resistivity normalized to its room temperature value,  $\rho/\rho(300\text{ K})$ , vs. temperature,  $T$ , measured on a single crystal [87TCDG]. Note a monotonic metallic behaviour.

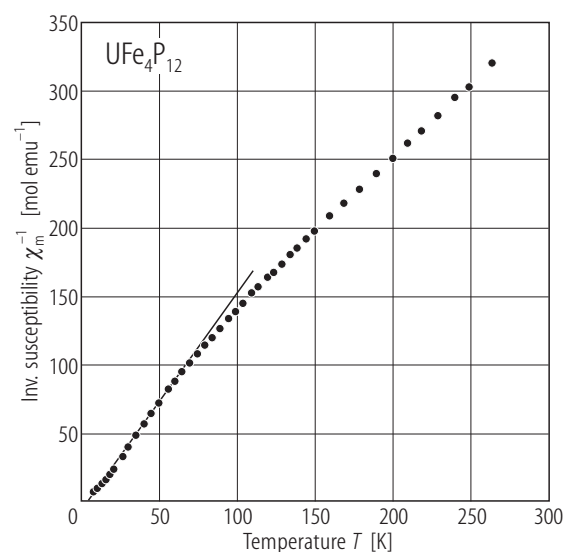


**Fig. 98.**  $\text{UFe}_4\text{P}_{12}$ . Reciprocal molar magnetic susceptibility,  $\chi_m^{-1}$ , vs. temperature,  $T$  [85MTYM]. The thin solid line represents a Curie-Weiss fit at low temperatures with the parameters given in Table B. The authors mention a ferromagnetic-like phase transition detected at  $T_C = 3.15\text{ K}$  in the ac magnetic susceptibility measurements, strong field dependence of the magnetization taken at  $1.9\text{ K}$  (the magnetic moment attains  $1.2\ \mu_B$  in a field of  $3\text{ T}$ ) and some magnetic hysteresis observed for  $T < T_C$  (not shown). For comparison see Fig. 100.

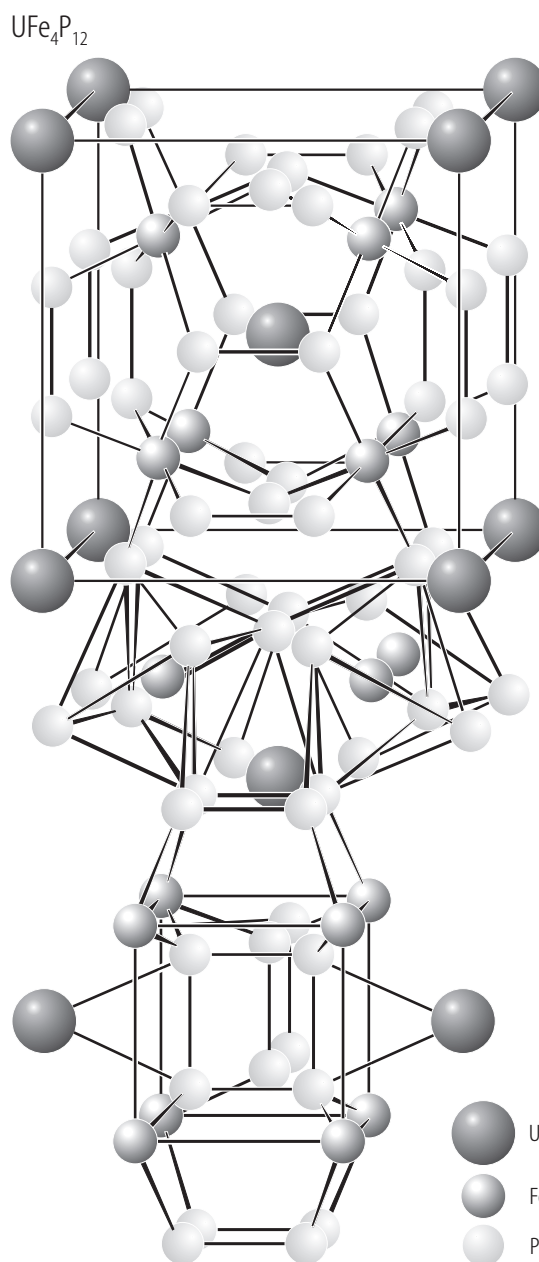


**Fig. 97.**  $\text{UFe}_4\text{P}_{12}$ . Crystal structure [95EJBB]. Emphasized are the  $\text{FeP}_6$  octahedra (in the middle of the drawing) and the environment of a  $\text{P}_4$  ring (bottom of the drawing).

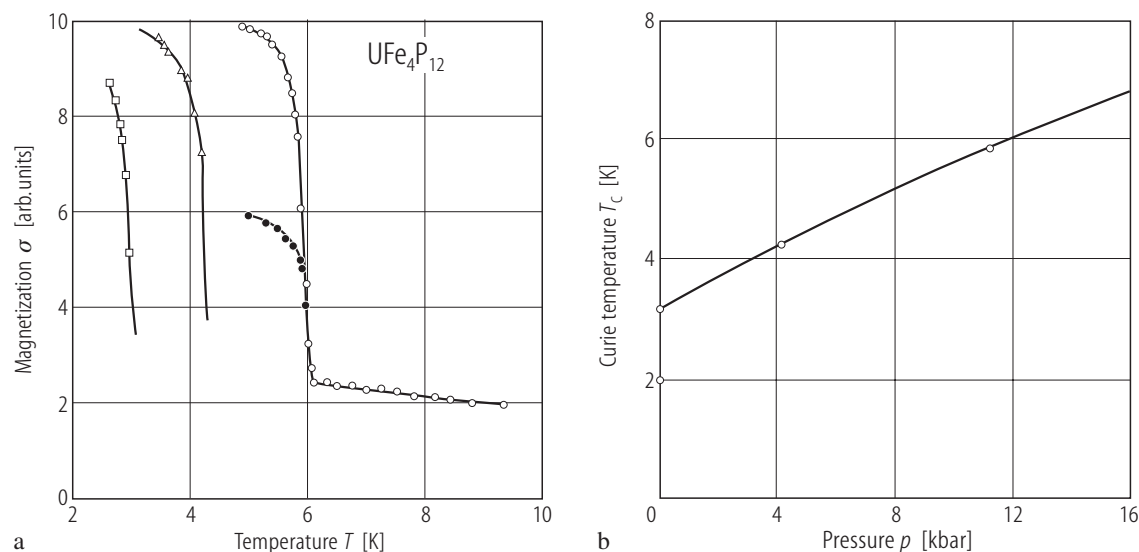


**Fig. 99.**  $\text{UFe}_4\text{P}_{12}$ . (a) Low-field magnetization,  $\sigma$ , vs. temperature,  $T$ , measured on a single crystal under hydrostatic pressure  $p = 0$  (squares), 4.2 (triangles) and 11.3 kbar (circles) in a field of 20 (closed circles) and 50 G (open symbols) [87GRTM]. Note that for  $p = 11.3$  kbar the data taken at 20 and 50 G give the same Curie temperature of 6 K. (b) Curie temperature,  $T_C$ , vs. pressure,  $p$

[87GRTM]. Note a sharp increase of  $T_C$  with the rate  $dT_C/dp = 0.26$  K/kbar. Assuming a model of the competition between the Kondo effect and RKKY interactions the authors predicted that at higher pressures  $T_C$  should start to decrease because of quenching of the uranium magnetic moment in the extreme Kondo limit.

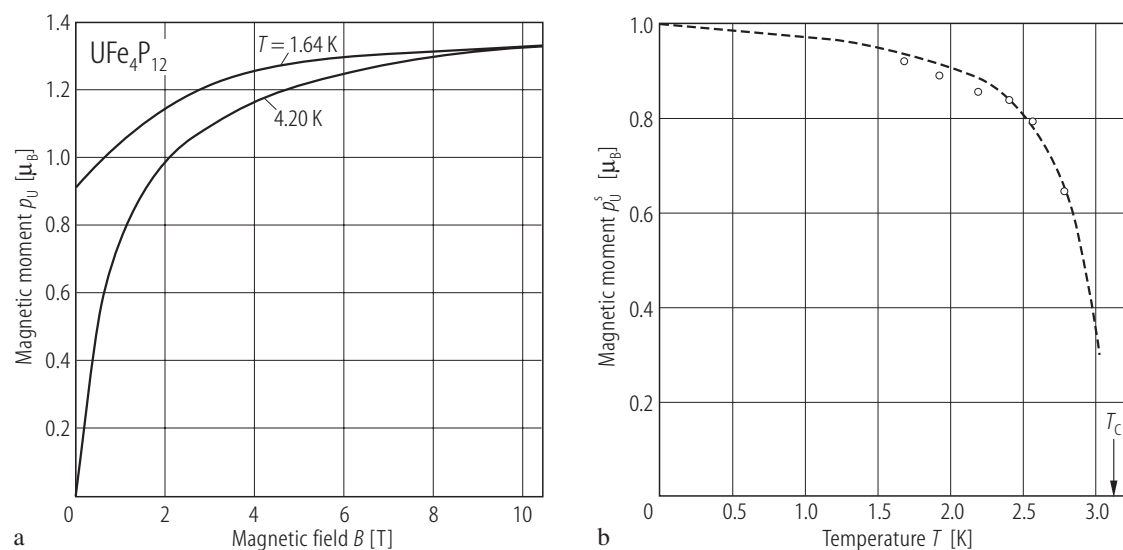


**Fig. 100.**  $\text{UFe}_4\text{P}_{12}$ . (a) Magnetic moment per U atom,  $p_U$ , vs. magnetic field,  $B$ , measured on a single crystal at 1.64 and 4.2 K [87GRTM]. (b) Spontaneous magnetic moment,  $p_U^s$ , vs. temperature,  $T$  [87GRTM]. The compound is a

ferromagnet with the Curie temperature of 3.15 K. Magnetic saturation is reached in fields  $B > 15$  T yielding the uranium moment of about  $1.3 \mu_B$  (not shown).

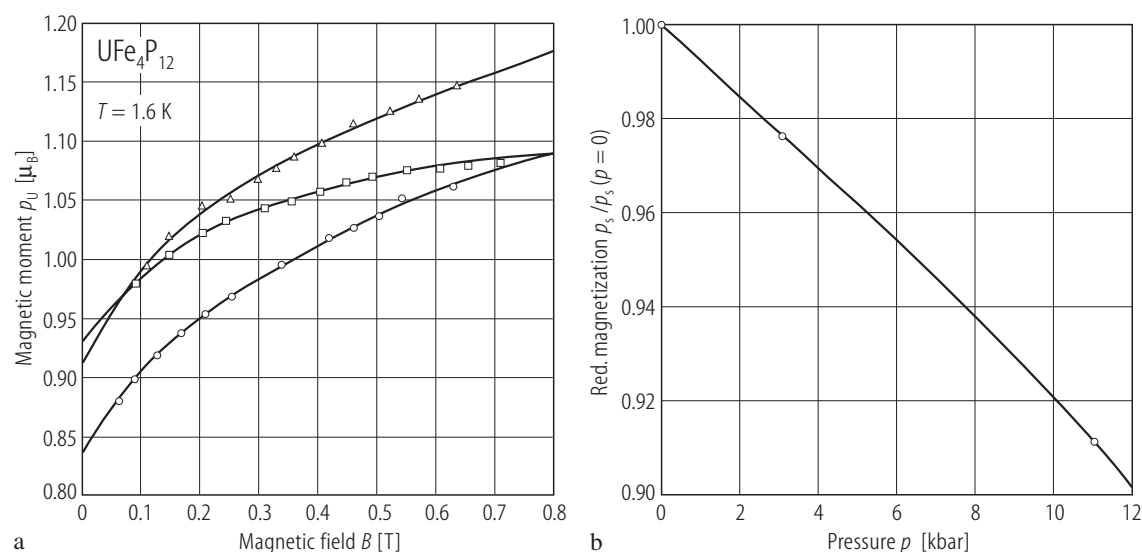


**Fig. 101.**  $\text{UFe}_4\text{P}_{12}$ . (a) Magnetic moment per U atom,  $\mu_U$ , vs. magnetic field,  $B$ , measured at 1.6 K on a single crystal under hydrostatic pressure  $p = 1$  bar (squares), 3.1 (triangles) and 11 kbar (circles) [87GRTM]. (b) Spontaneous magnetic moment normalized to the ambient

pressure value,  $\mu_s/\mu_s(0)$ , vs. pressure,  $p$  [87GRTM]. Note a decrease of  $\mu_s$  with the rate  $[1/\mu_s(0)](d\mu_s/dp) = -0.007 \text{ kbar}^{-1}$ . The authors interpret the observed effect as an indication of some weakening of the magnetic moment with increased f-ligand (mainly f-d) hybridisation.

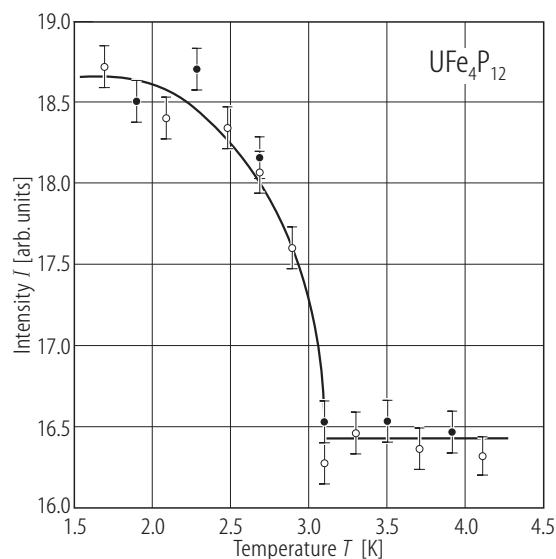


**Fig. 102.**  $\text{UFe}_4\text{P}_{12}$ . Neutron diffraction intensity of the magnetic reflection (220),  $I$ , vs. temperature,  $T$ , taken on a single crystal using a triple-axis spectrometer [99NDTB]. Open and closed symbols denote measurements taken on heating and cooling, respectively. The solid line is a guide to the eye. The compound orders ferromagnetically at  $T_C = 3.1$  K. An upper limit for the uranium magnetic moment is  $0.5 \mu_B$  (at 2.8 K). No magnetic moment was found on the iron sites. Because of domain effect the direction of the moments could not be determined (cubic system).

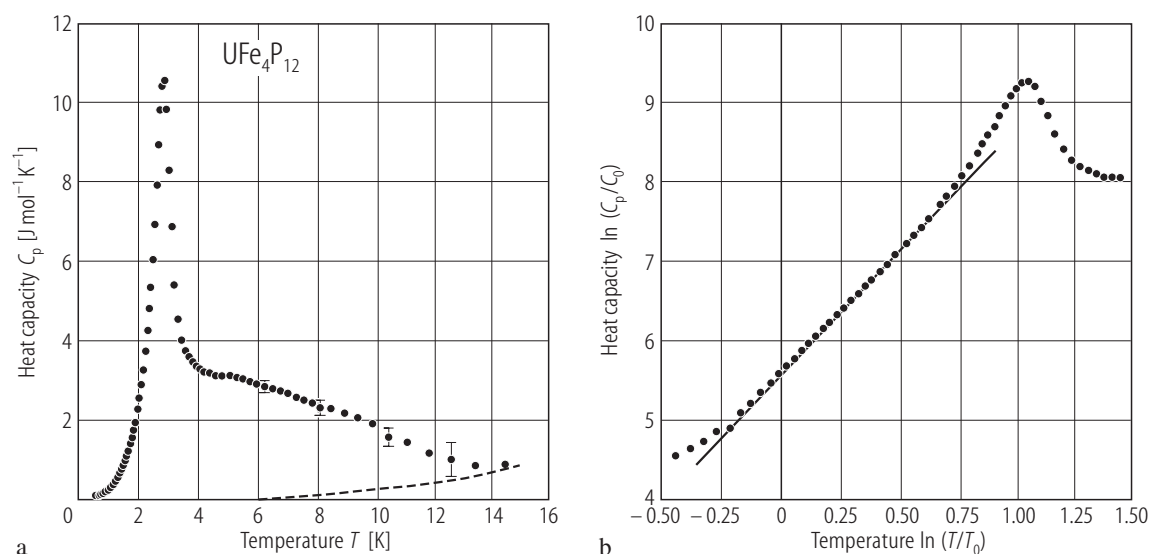


**Fig. 103.**  $\text{UFe}_4\text{P}_{12}$ . **(a)** Heat capacity,  $C_p$ , vs. temperature,  $T$ , below 15 K, measured on a collection of several single crystals [86TRMM]. The dashed line represents the lattice contribution, estimated from the heat capacity of  $\text{LaFe}_4\text{P}_{12}$ . A pronounced peak with a maximum at 2.86 K is associated with the ferromagnetic phase transition at  $T_C = 3.15$  K. A broad background comes from the Schottky contribution

due to crystalline electric field splitting of the uranium  $^3\text{H}_4$  ground multiplet. **(b)** Heat capacity plotted as  $\ln(C/C_0)$  vs.  $\ln(T/T_0)$  ( $C_0 = 1 \text{ J mol}^{-1} \text{ K}^{-1}$ ,  $T_0 = 1 \text{ K}$ ) [86TRMM]. The solid line marks a  $T^3$  behaviour of  $C(T)$  in the range 0.8...1.9 K. Note that for ferromagnetic magnons a  $T^{3/2}$  dependence has been predicted and not a  $T^3$  one, which is characteristic of antiferromagnetic spin waves.

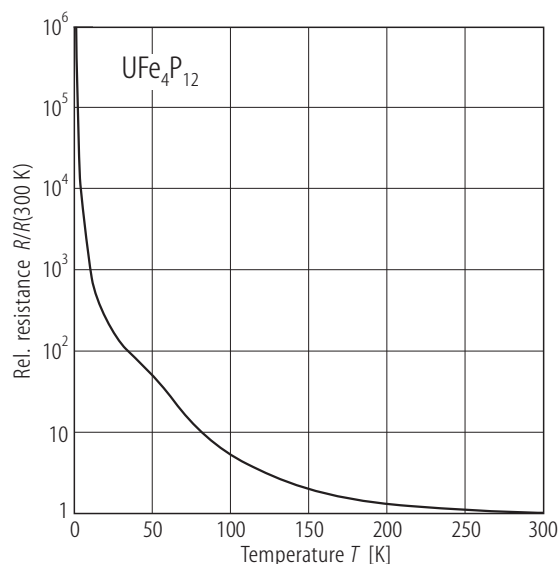


**Fig. 104.**  $\text{UFe}_4\text{P}_{12}$ . Electrical resistance normalized to the room-temperature value,  $R/R(300 \text{ K})$ , vs. temperature,  $T$  [85MTYM]. The room temperature resistivity is larger than  $1000 \mu\Omega\text{cm}$ . Note a semiconducting behaviour, which however cannot be described by a simple activation conduction.

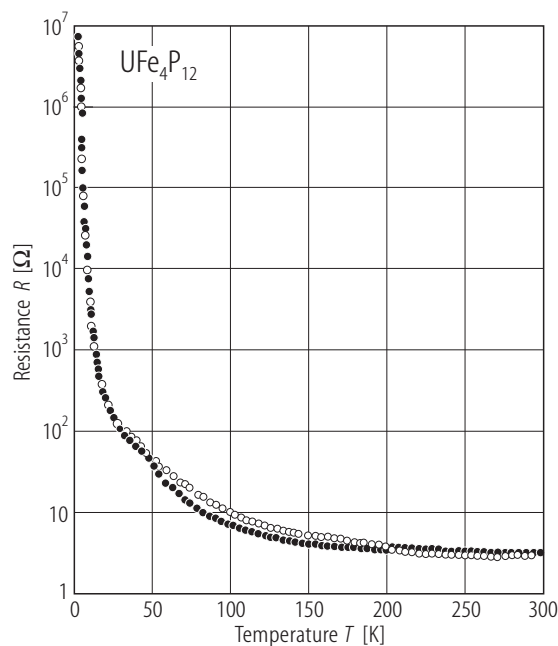


**Fig. 105.**  $\text{UFe}_4\text{P}_{12}$ . Electrical resistance,  $R$ , vs. temperature,  $T$ , under hydrostatic pressure  $p = 0$  (open circles) and 15.5 kbar (closed circles) [87GRTM]. The compound is a semiconductor ( $\text{RRR} \approx 10^7$ ) but no single excitation energy can be ascribed to  $R(T)$  over the entire temperature range, nor the observed behaviour can be attributed to hopping conductivity [no  $R \sim \exp(T^{-1/4})$  dependence]. Note that pressure has little effect on  $R(T)$  in contrast to substantial effect of pressure on the magnetism (see Figs. 99 and 101). Decoupling of the magnetic and electrical properties strongly suggests that the ferromagnetism of this compound is a result of superexchange interactions via phosphorus ions rather than of RKKY interactions mediated by conduction electrons.

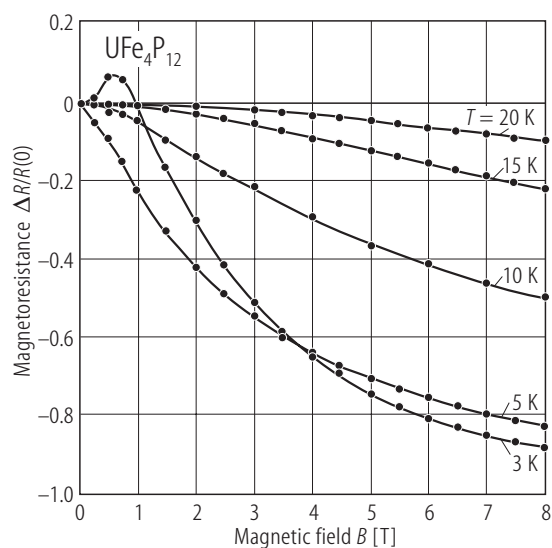


**Fig. 106.**  $\text{UFe}_4\text{P}_{12}$ . Magnetoresistance,  $\Delta R(B)/R(0)$ , vs. applied magnetic field,  $B$ , up to 8 T, measured at various temperatures specified in the figure [86TRMM]. Negative magnetoresistance found above  $T_C = 3.15$  K the authors attributed to spin-flip scattering due to the alignment of the uranium magnetic moments with increasing field, delocalisation of electrons with increasing field and/or Zeeman band splitting. A positive maximum in  $\Delta R(B)/R(0)$  taken near  $T_C$  may be associated with the onset of ferromagnetic order.

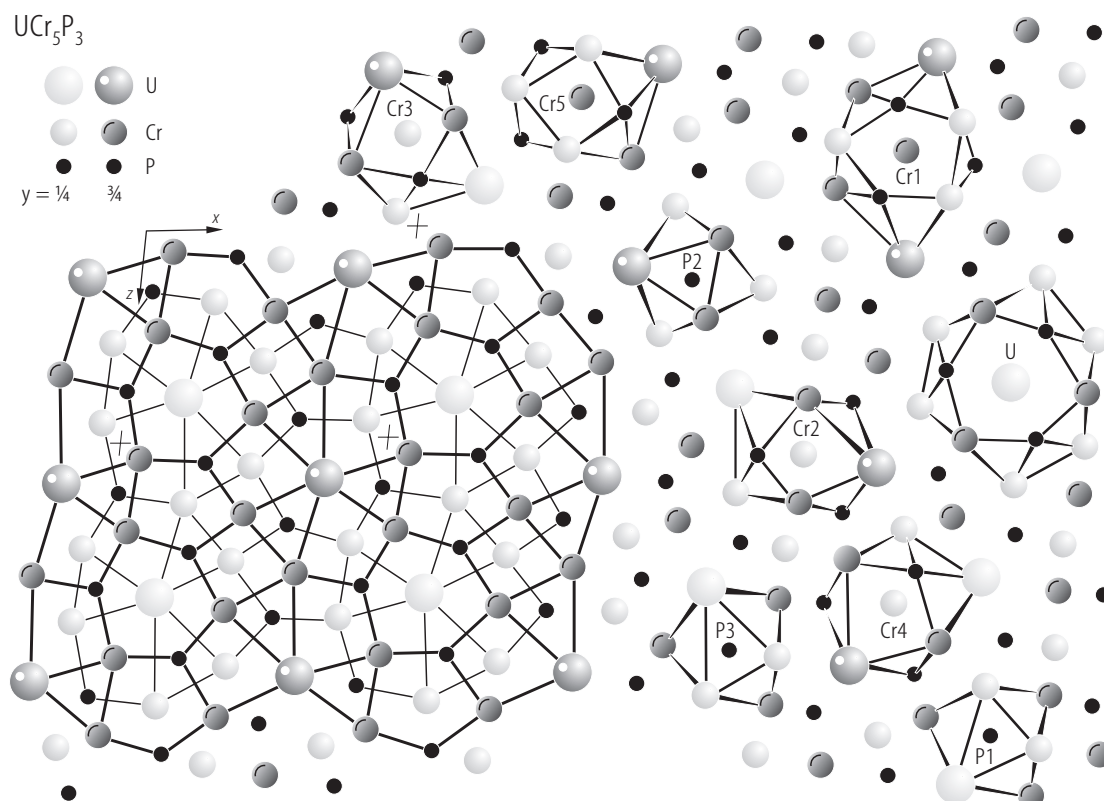


**Fig. 107.**  $\text{UCr}_5\text{P}_3$ . Crystal structures and coordination polyhedra projected on the  $xz$  plane [93JBP]. The atoms connected by thin and thick lines are situated at  $y = 1/4$  and  $3/4$ , respectively.

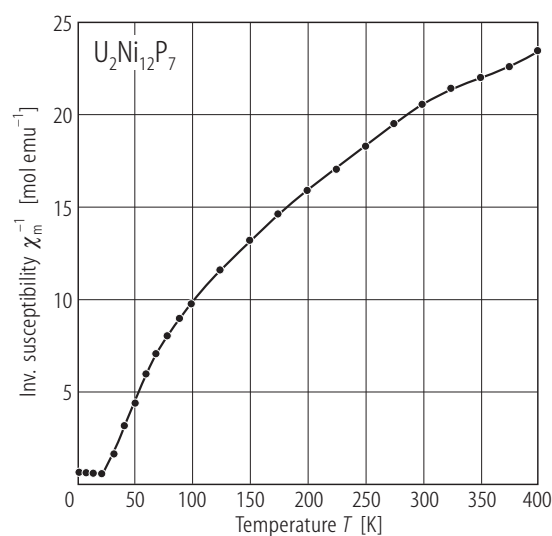


**Fig. 109.**  $\text{U}_2\text{Ni}_{12}\text{P}_7$ . Reciprocal molar magnetic susceptibility,  $\chi_m^{-1}$ , vs. temperature,  $T$ , measured in a field of 1 T [98EAI]. The compound orders ferromagnetically at  $T_C = 29(3)$  K. See the modified Curie-Weiss fit parameters given in Table B.

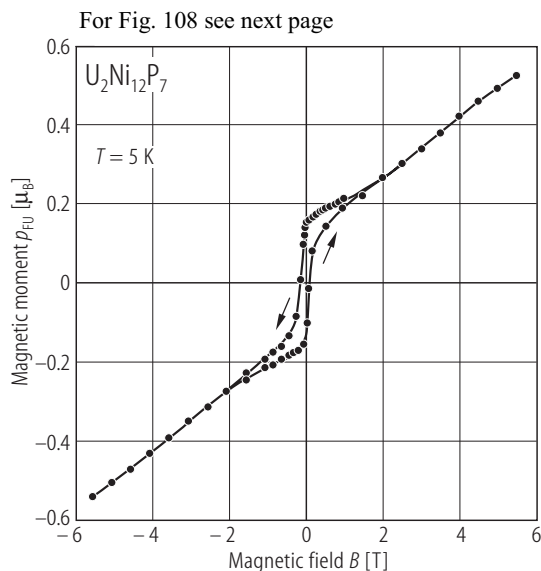


**Fig. 110.**  $\text{U}_2\text{Ni}_{12}\text{P}_7$ . Hysteresis loop,  $p_{\text{FU}}(B)$ , taken at 5 K [98EAI]. The arrows represent increasing and decreasing magnetic field. Note an unusual shape of the loop with a linear field dependence of the magnetization at higher fields. On this basis the authors proposed that the compound is a canted antiferromagnet.



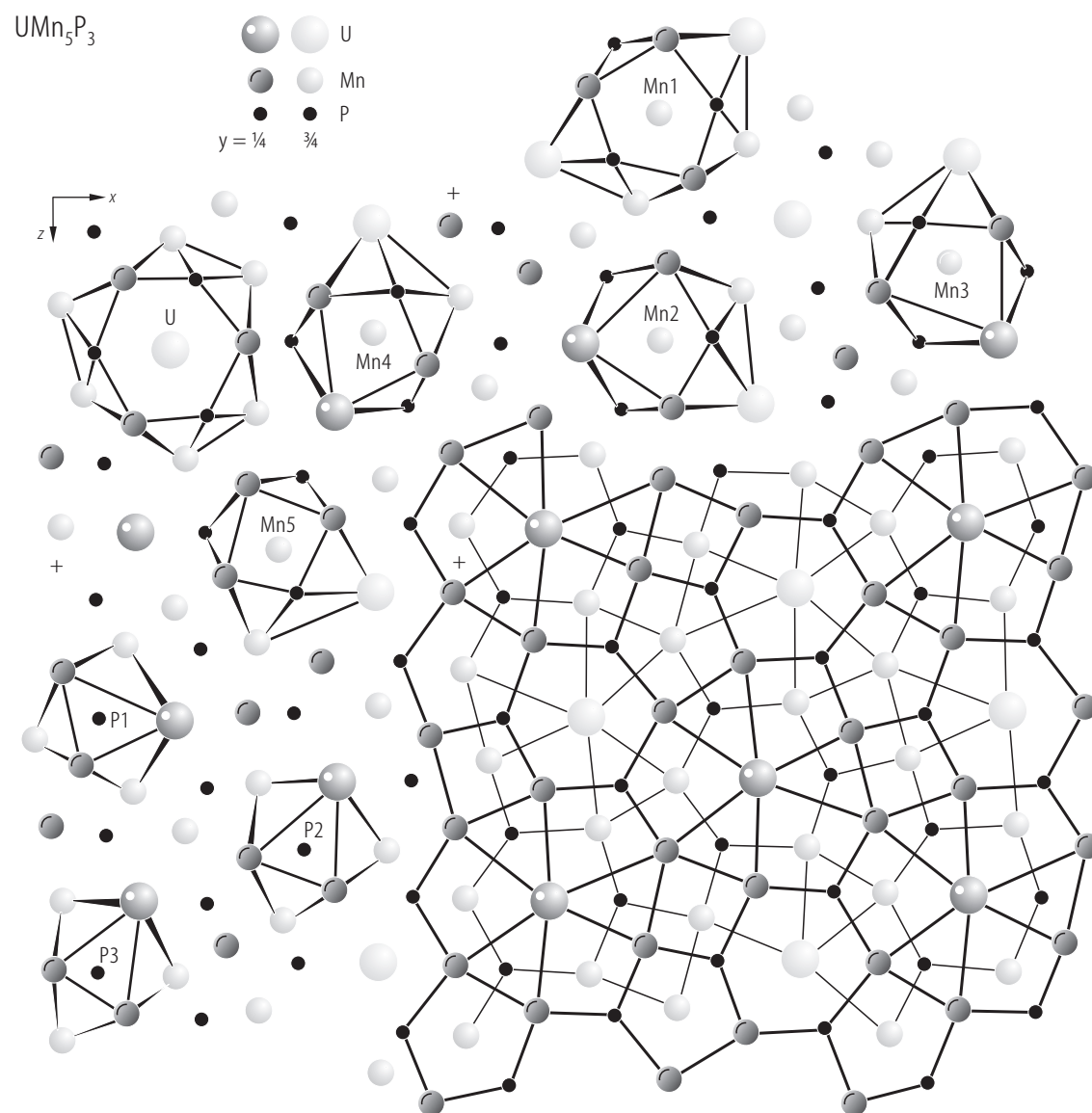


**Fig. 108.**  $\text{UMn}_5\text{P}_3$ . Crystal structures and coordination polyhedra projected on the  $xz$  plane [93JBP]. The atoms connected by thin and thick lines are situated at  $y = \frac{1}{4}$  and  $\frac{3}{4}$ , respectively.

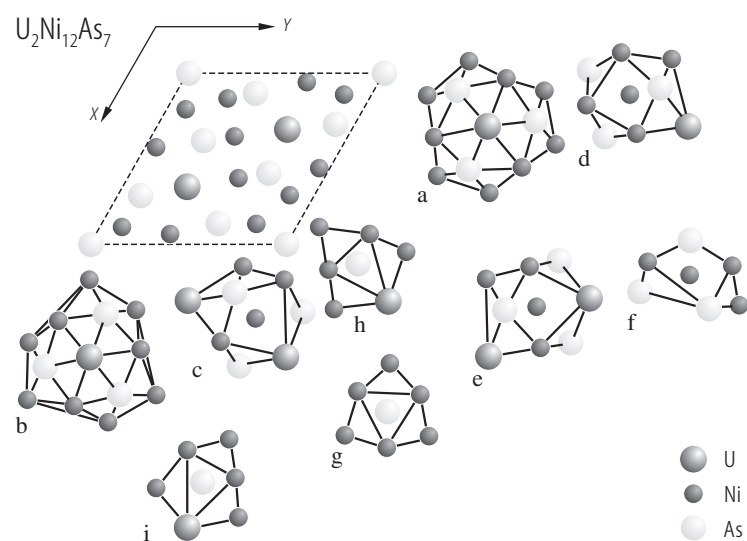


**Fig. 111.**  $\text{U}_2\text{Ni}_{12}\text{As}_7$ . Crystal structure projected on the (010) plane and the coordination polyhedra of all atoms [01SKW]. (a), (b): U(1) and U(2); (c) – (f): Ni(1)–Ni(4); (g) – (i): As(1)–As(3).

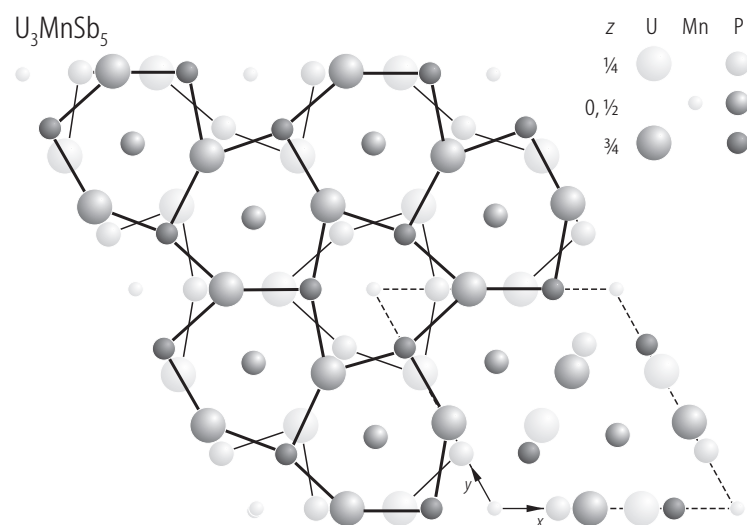


**Fig. 112.**  $\text{U}_3\text{MnSb}_5$ . Crystal structure projected on the xy plane [94BJ]. The atoms connected by thin and thick lines are situated at  $z = \frac{1}{4}$  and  $\frac{3}{4}$ , respectively; unconnected atoms are superimposed at  $z = 0$  and  $z = \frac{1}{2}$ .

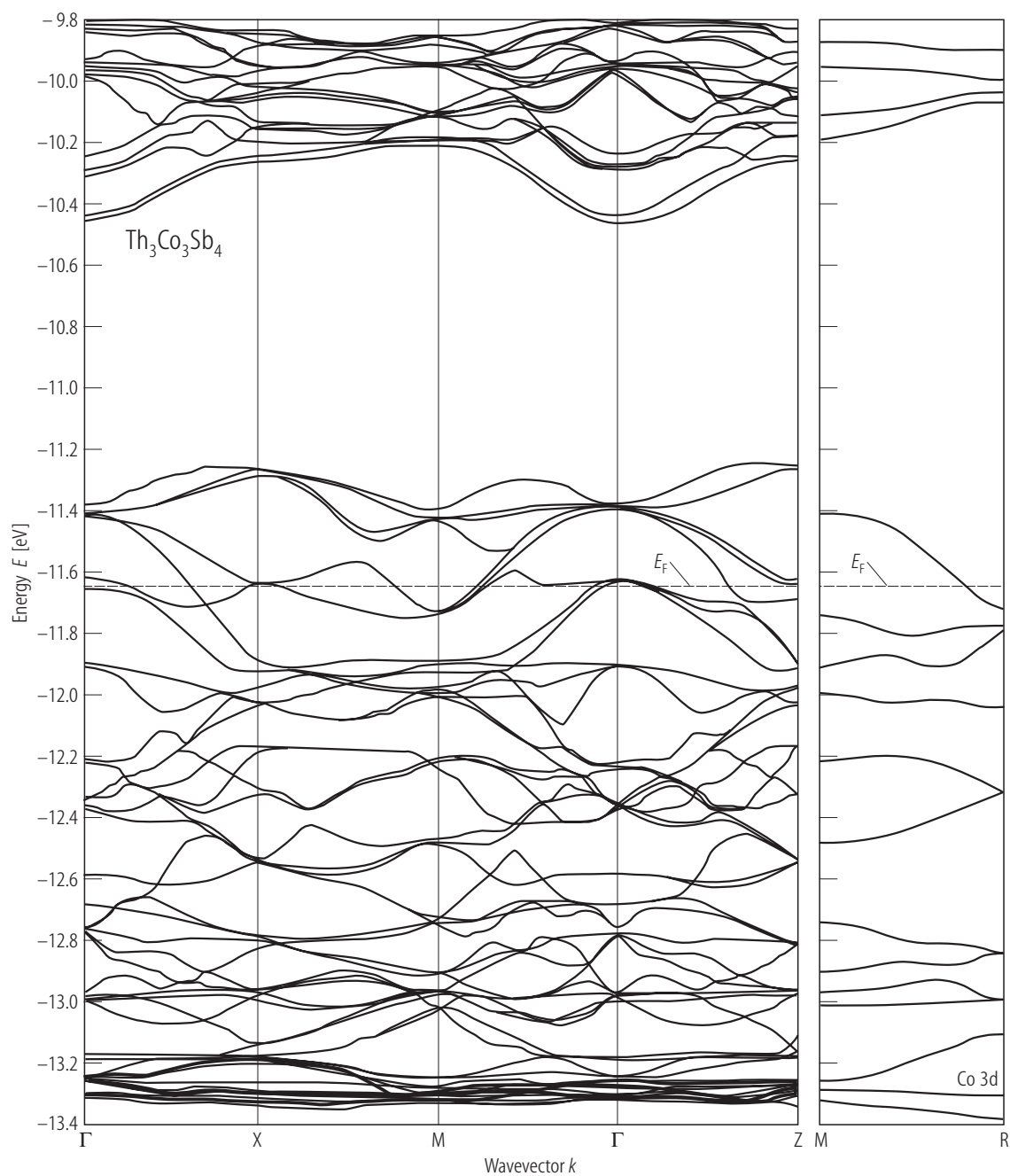


**Fig. 113.**  $\text{Th}_3\text{Co}_3\text{Sb}_4$ . Energy band structure calculated by the extended Hückel method [01SK]. The compound is a metal unlike the parent phase  $\text{Th}_3\text{Sb}_4$ , which is a semiconductor. The Fermi level is marked by the dashed line. A set of weakly dispersed bands lying around -13.3 eV has predominantly Co 3d character (see Fig. 114).

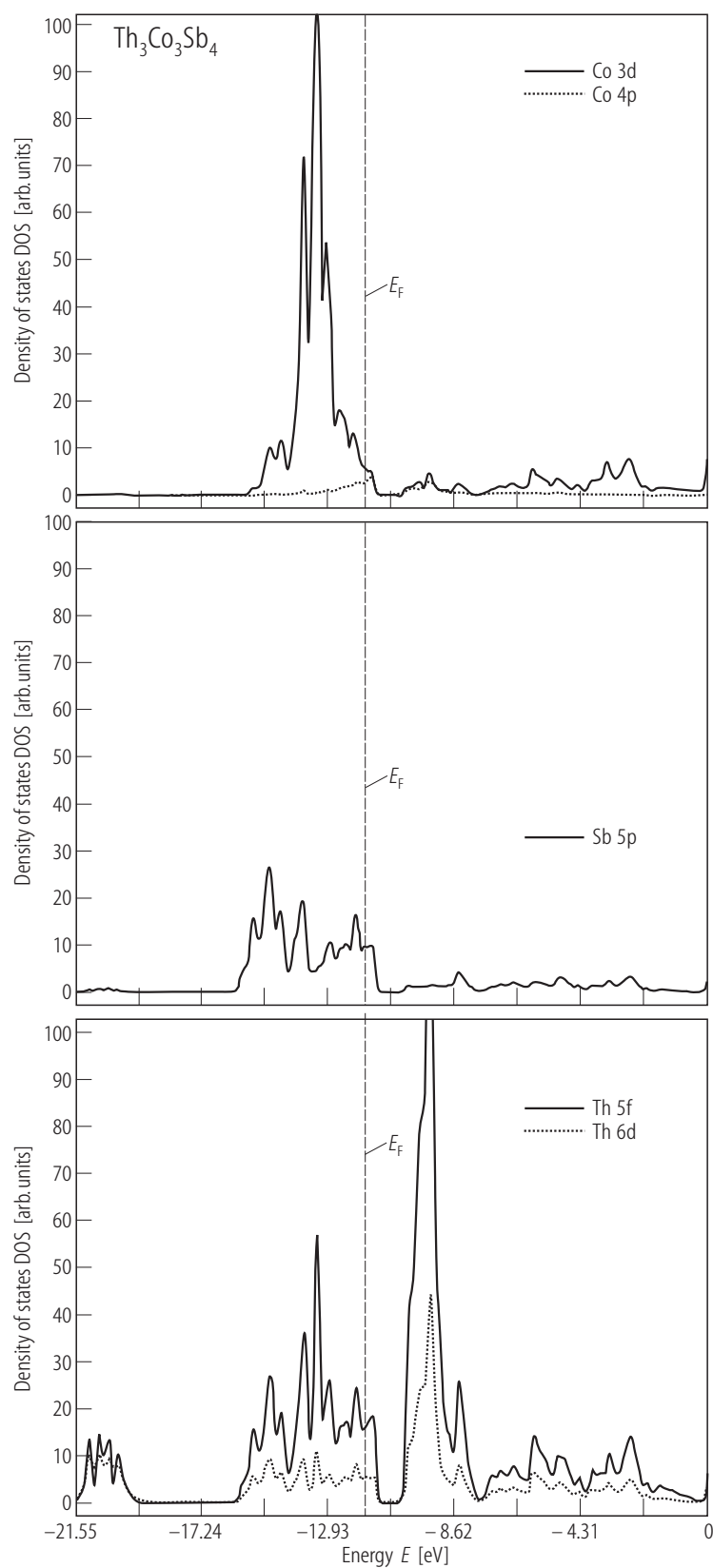


**Fig. 114.**  $\text{Th}_3\text{Co}_3\text{Sb}_4$ . Partial DOS calculated by the extended Hückel method [01SK]. The Fermi level is marked by the vertical dashed line. The band centered at -13.3 eV is formed by Co 3d states hybridized over 20% with Th 5f, 6d orbitals and less strongly with Sb 5p orbitals. The bands above  $E_F$  consists of empty Th 5f, 6d and 7p states with some admixture of Sb 5p and Co 3d and 4p states.

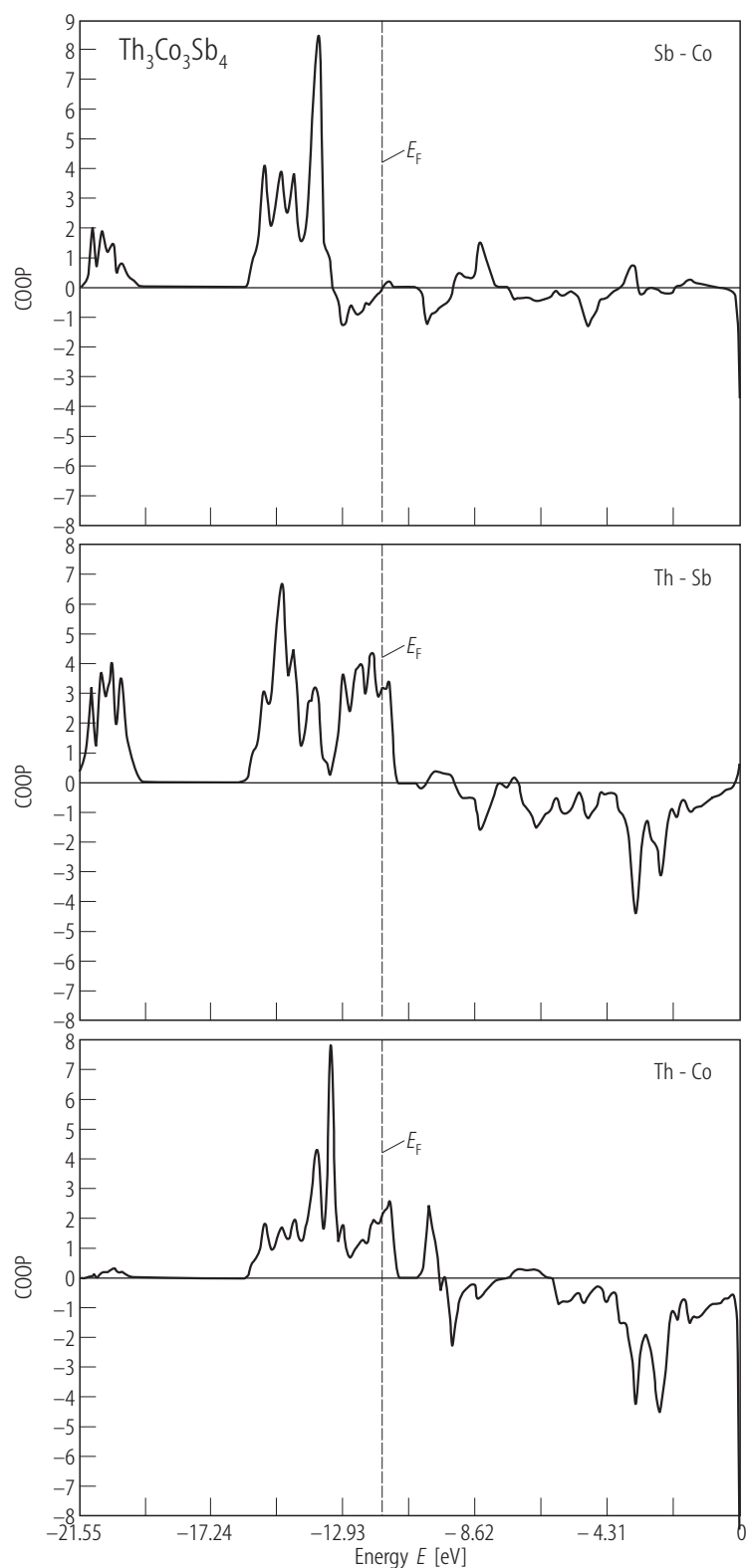


**Fig. 115.**  $\text{Th}_3\text{Co}_3\text{Sb}_4$ . Crystal orbital overlap population (COOP) curves corresponding to Sb-Co, Th-Sb and Th-Co bonds (panels from the top to the bottom) [01SK]. The Fermi level is marked by the vertical dashed line. Positive COOP indicates bonding levels and negative COOP indicates antibonding levels. All the bonds have a strong covalent character. The Th-Co bonds are the strongest and determine the physical behaviour of the compound. For further details see the original paper.

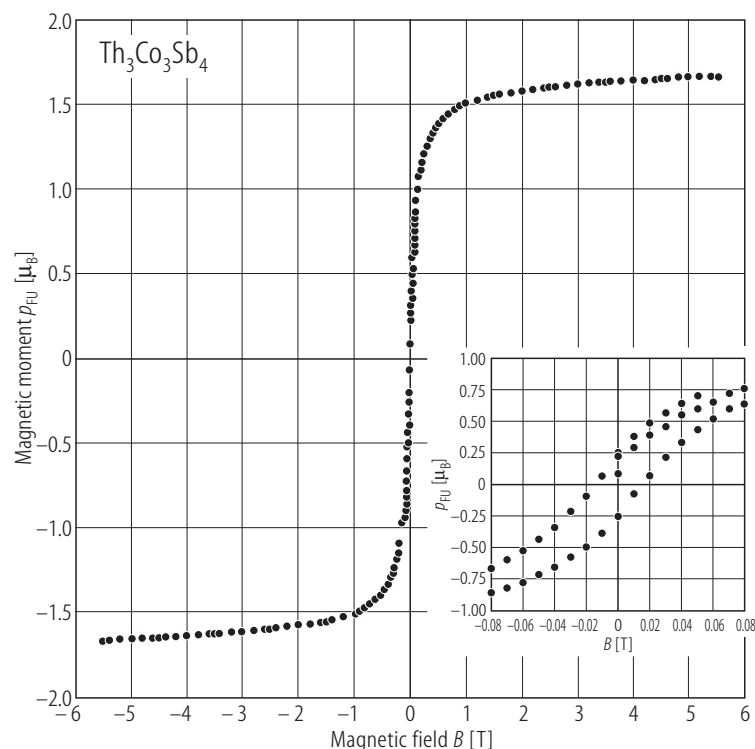


**Fig. 116.**  $\text{Th}_3\text{Co}_3\text{Sb}_4$ . Magnetization hysteresis loop,  $p_{\text{FU}}$  vs.  $B$ , taken at  $T = 300$  K [01SK]. The compound is a strong ferromagnet with  $T_C$  lying much above room temperature (see also Fig. 117). The saturation moment is only  $0.99 \mu_B$  per Co atom. This strong reduction of the magnetic moment with respect to the expected value of  $1.72 \mu_B/\text{Co}$  atom arises probably because of the hybridization of Co 3d orbitals with Th and Sb orbitals (see Fig. 114). Inset:  $p_{\text{FU}}(B)$  in low fields. Note a small coercive field of 0.0169 T, characteristic of soft ferromagnets.

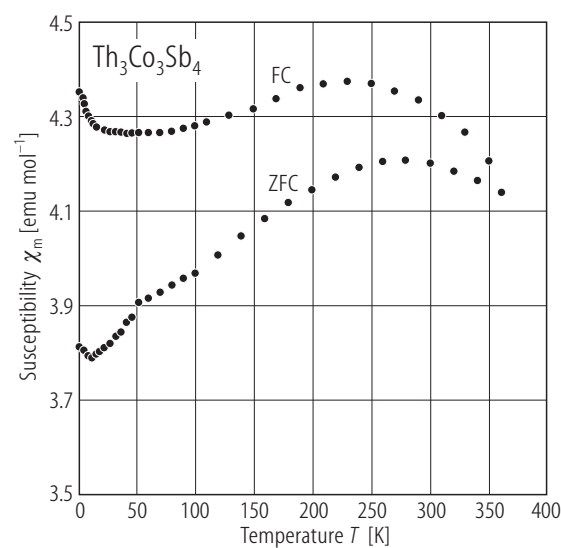


**Fig. 117.**  $\text{Th}_3\text{Co}_3\text{Sb}_4$ . Molar magnetic susceptibility,  $\chi_m$ , vs. temperature,  $T$ , in the range 2...370 K taken in a field of 0.1 T upon cooling the sample without (ZFC) and with (FC) an applied field [01SK]. The irreversibility in  $\chi_m(T)$  indicates that the compound is in a ferromagnetically ordered state. The Curie temperature lies above the upper limit of the measurement.

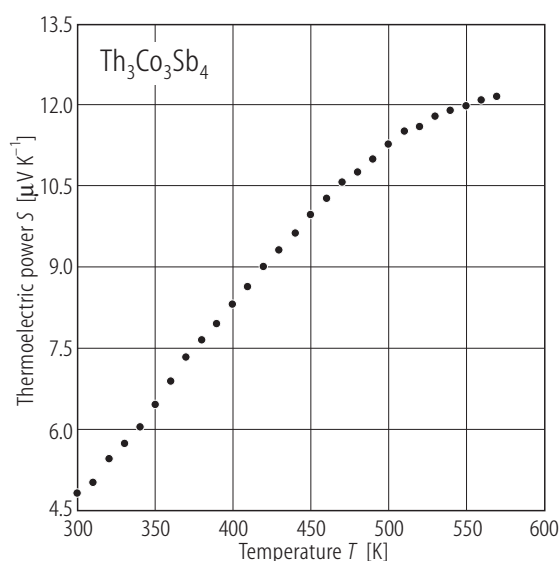


**Fig. 118.**  $\text{Th}_3\text{Co}_3\text{Sb}_4$ . Thermoelectric power,  $S$ , vs. temperature,  $T$ , in the range 300...570 K [01SK]. Positive and small Seebeck coefficient implies that the compound is a metallic conductor with holes being the dominant charge carriers.

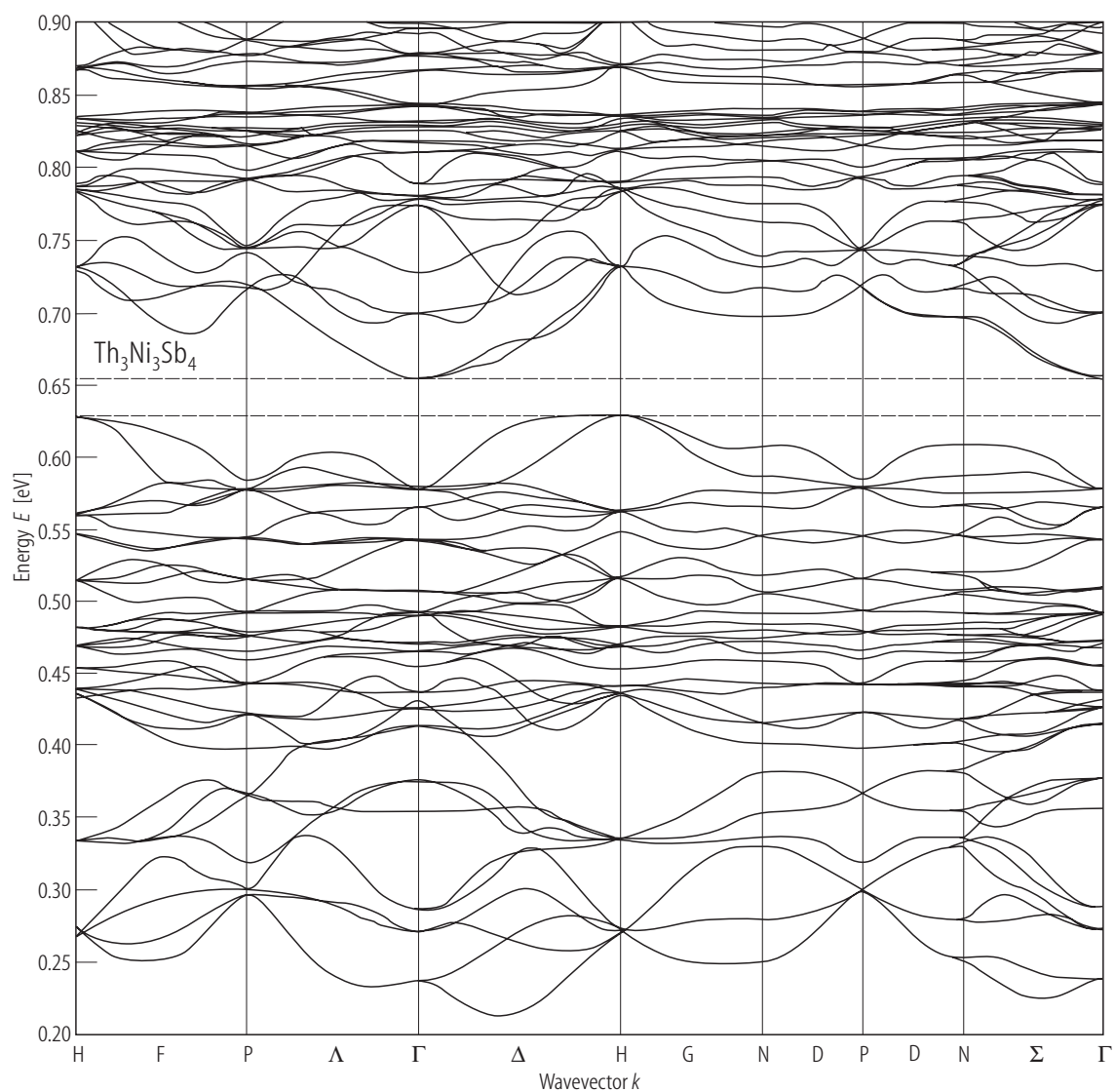


**Fig. 119.**  $\text{Th}_3\text{Ni}_3\text{Sb}_4$ . Energy band structure calculated by the self-consistent APW method with the local density approximation [90TKK]. For the details on the method used and comprehensive description of the results refer to the original paper. See also Fig. 120.

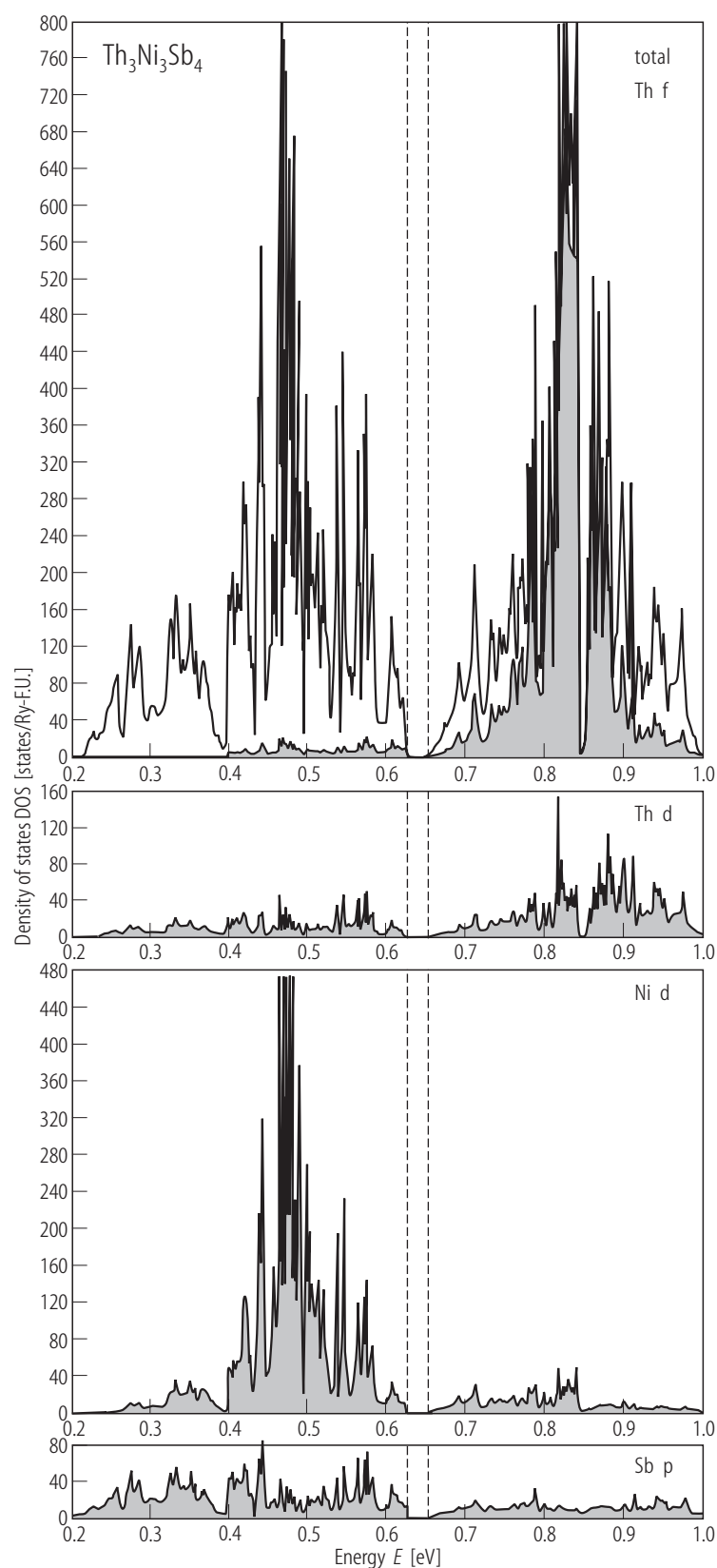


**Fig. 120.**  $\text{Th}_3\text{Ni}_3\text{Sb}_4$ . Total (light areas) and partial (shaded areas) density of states calculated by the self-consistent APW method with the local density approximation [90TKK]. The compound is a semiconductor and the valence bands consist of the Ni 3d and Sb 5p states. Due to the mixing between the Ni 3d and Th 6d states, the empty Th 6d conduction band is pushed up resulting in a gap of 0.36 eV. For further details see the original paper.



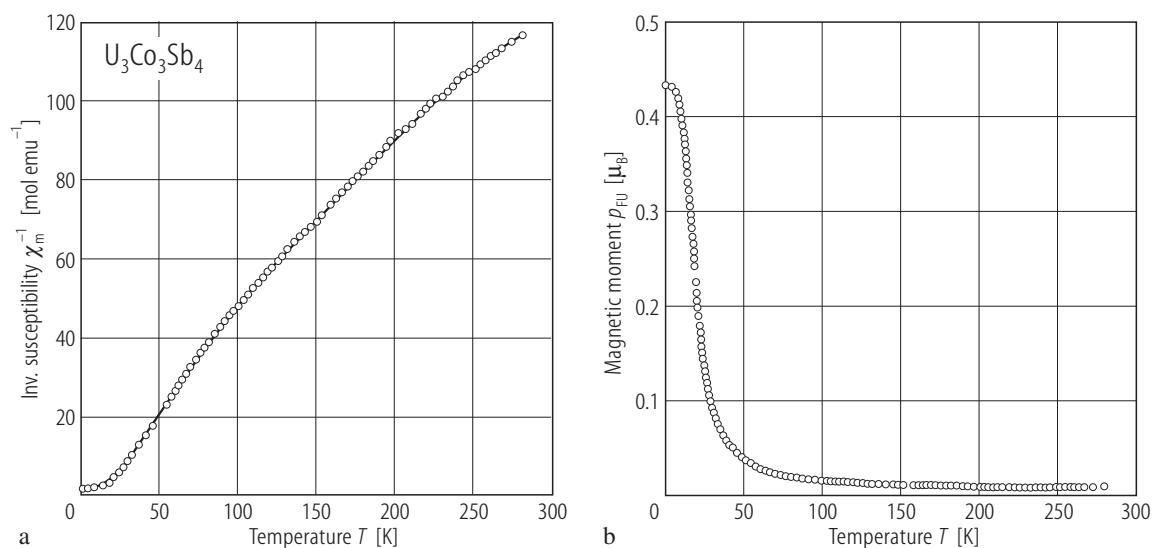


**Fig. 121.**  $\text{U}_3\text{Co}_3\text{Sb}_4$ . **(a)** Reciprocal molar magnetic susceptibility,  $\chi_m^{-1}$ , vs.  $T$  [90ENMB]. The solid line is a modified Curie-Weiss fit with the parameters given in Table B. **(b)** Magnetic moment,  $p_{\text{FU}}$ , vs. temperature,  $T$ , measured in a field of 0.4 T [90ENMB]. The compound orders ferromagnetically at  $T_C = 10$  K.

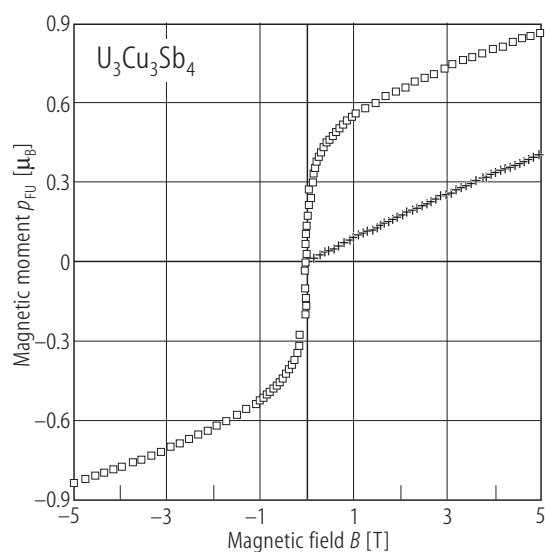


**Fig. 122.**  $\text{U}_3\text{Co}_3\text{Sb}_4$ . Hysteresis loop,  $p_{\text{FU}}(B)$ , taken at  $T = 4.4$  K (squares) and  $T = 50$  K (crosses) [90ENMB]. Note a very narrow hysteresis observed at 4.4 K, with a lack of saturation and rather low moment in 5 T.

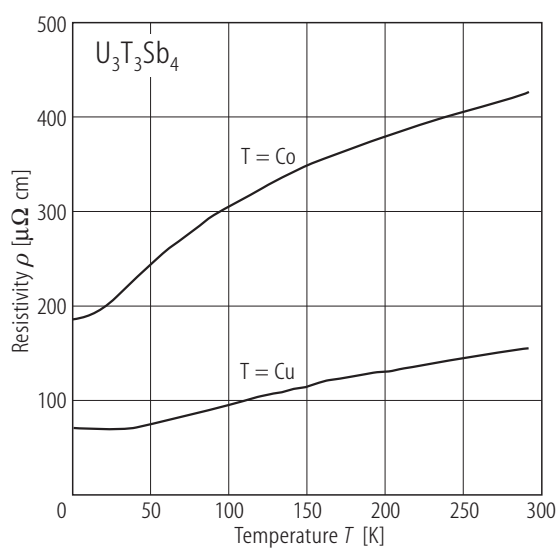


**Fig. 123.**  $\text{U}_3\text{T}_3\text{Sb}_4$ ,  $T = \text{Co}, \text{Cu}$ . Electrical resistivity,  $\rho$ , vs. temperature,  $T$  [90ENMB]. The compounds are ferromagnets with  $T_C$  of 10 and 88 K for  $\text{U}_3\text{Co}_3\text{Sb}_4$  and  $\text{U}_3\text{Cu}_3\text{Sb}_4$ , respectively (see Figs. 121 and 129) but do not show any anomalies in both  $\rho(T)$  and  $d\rho/dT(T)$  at the onset of the magnetic order. This feature signals a weak coupling between the uranium 5f electrons and the conduction band.

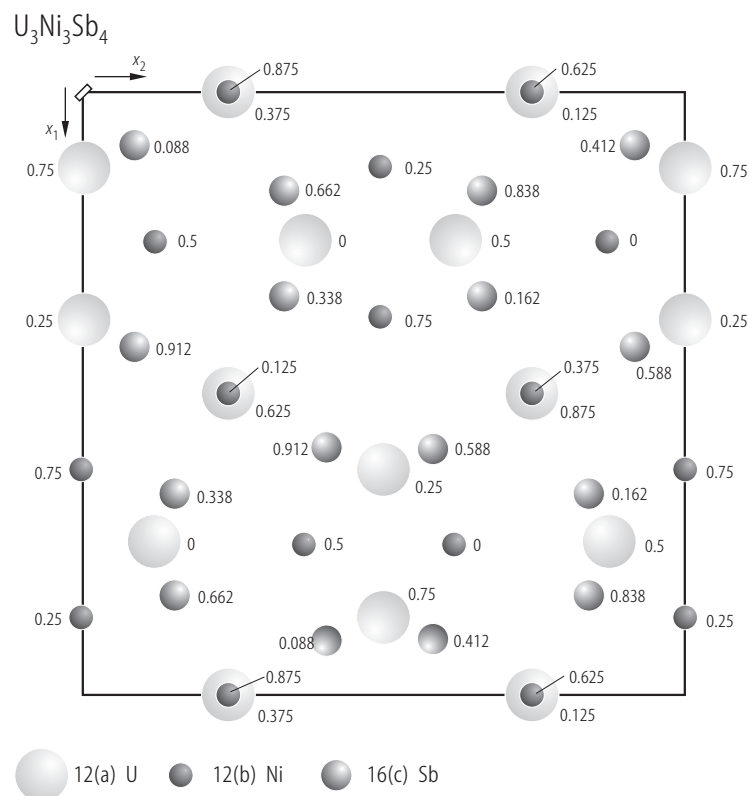


**Fig. 124.**  $\text{U}_3\text{Ni}_3\text{Sb}_4$ . Crystal structure projected on the (100) plane [79D]. The numbers represent the positional parameters.

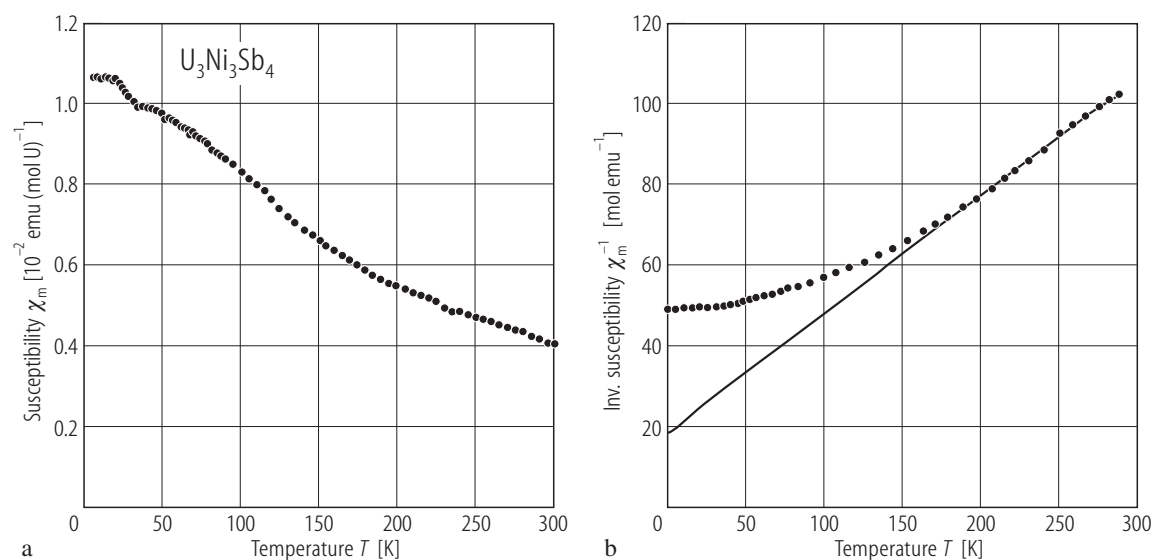


**Fig. 125.**  $\text{U}_3\text{Ni}_3\text{Sb}_4$ . **(a)** Molar magnetic susceptibility,  $\chi_m$ , vs. temperature,  $T$  [90TMFA1]. The compound remains paramagnetic down to 4.2 K. Note a tendency to saturation below 50 K indicating a singlet ground state. See the Curie-

Weiss fit parameters given in Table B. **(b)** Reciprocal molar magnetic susceptibility,  $\chi_m^{-1}$ , vs.  $T$ , measured in a field of 2 T [90ENMB]. The solid line is a Curie-Weiss fit with the parameters given in Table B.

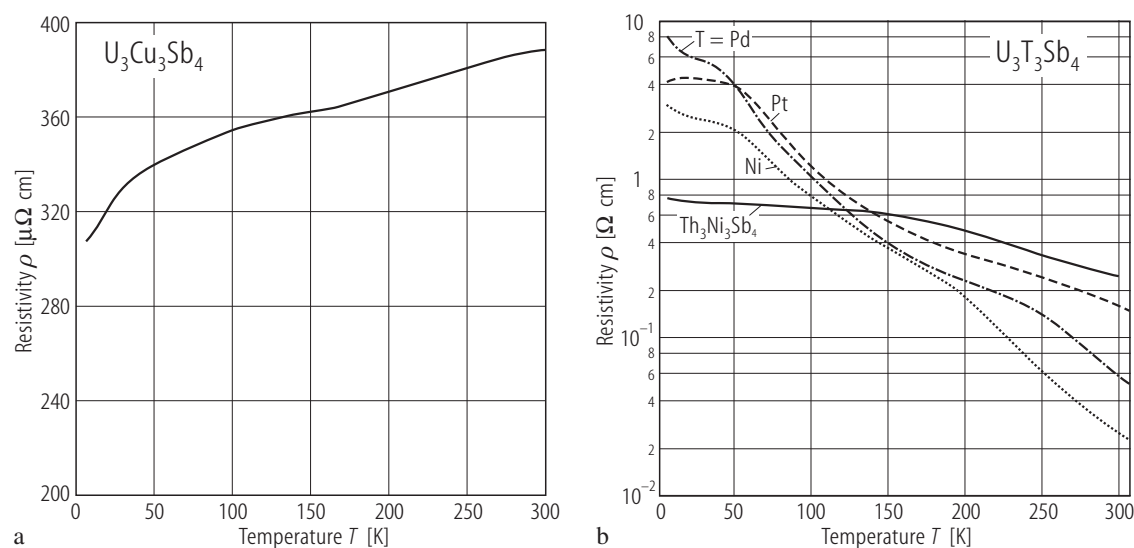


**Fig. 126.**  $\text{U}_3\text{T}_3\text{Sb}_4$ ,  $\text{T} = \text{Ni}, \text{Cu}, \text{Pd}, \text{Pt}$ . Electrical resistivity,  $\rho$ , vs. temperature,  $T$ , for (a)  $\text{T} = \text{Cu}$  and (b)  $\text{T} = \text{Ni}, \text{Pd}, \text{Pt}$  as compared to  $\text{Th}_3\text{Ni}_3\text{Sb}_4$  [90TMFA2]. Note a negative slope in  $\rho(T)$  and huge resistivities of several ten  $\text{m}\Omega\text{cm}$  at room temperature for all the compounds but  $\text{U}_3\text{Cu}_3\text{Sb}_4$ , indicating their semiconducting behaviour. Above 250 K the resistivity of  $\text{U}_3\text{Ni}_3\text{Sb}_4$ ,  $\text{U}_3\text{Pd}_3\text{Sb}_4$  and  $\text{U}_3\text{Pt}_3\text{Sb}_4$  follows a simple activation law  $\rho(T) \propto \exp(E_g/2k_B T)$  with  $E_g$  of

0.20, 0.23 and 0.15 eV, respectively. Note that the formation of a band gap is not related to the 5f electrons because also  $\text{Th}_3\text{Ni}_3\text{Sb}_4$  is a semiconductor with a rather small energy gap of 0.07 eV. In contrast, the resistivity of  $\text{U}_3\text{Cu}_3\text{Sb}_4$  has a metallic character. Only a very tiny anomaly on  $\rho(T)$  is seen at the ferromagnetic phase transition at  $T_C = 91$  K.

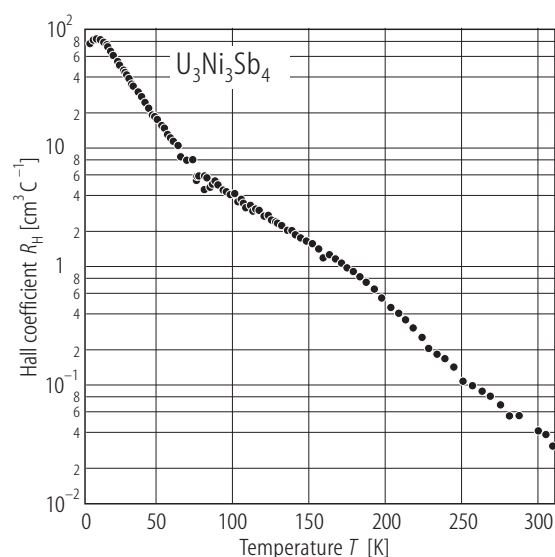


**Fig. 127.**  $\text{U}_3\text{Ni}_3\text{Sb}_4$ . Hall coefficient,  $R_H$ , vs. temperature,  $T$  [90TMFA2]. Note an increase in  $R_H$  by four orders of magnitude as temperature decreases from room temperature down to 4.2 K. Assuming the presence of carriers of one type one obtains in this temperature range a decrease in the carrier concentration from  $1.5 \cdot 10^{20}$  to  $7.7 \cdot 10^{16} \text{ cm}^{-3}$ . Between 210 and 320 K  $R_H(T)$  follows a simple activation law with  $E_g = 0.27$  eV, which is in agreement with the gap deduced from the resistivity data (see Fig. 126).

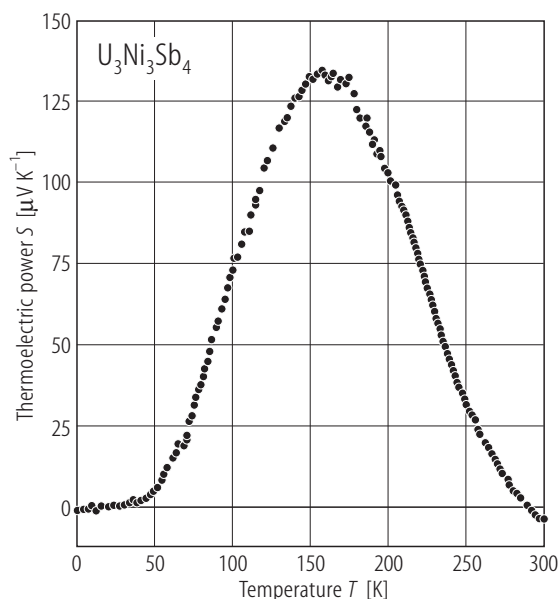


**Fig. 128.**  $\text{U}_3\text{Ni}_3\text{Sb}_4$ . Thermoelectric power,  $S$ , vs. temperature,  $T$  [90TMFA2]. Above 250 K the thermopower is inversely proportional to  $T$ , as characteristic of intrinsic semiconductors. The temperature dependence of  $S$  below 160 K suggests the presence of impurity states in the band gap. The dominant carriers are probably holes as indicated by a positive sign of both  $S(T)$  and  $R_H(T)$  (see Fig. 127).

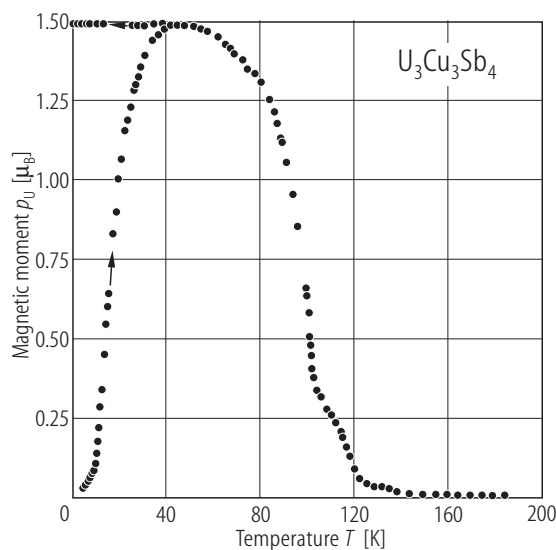


**Fig. 130.**  $\text{U}_3\text{Cu}_3\text{Sb}_4$ . Magnetic moment per U atom,  $p_U$ , vs. temperature,  $T$ , measured in a field of 0.24 T on heating and cooling (as marked by the arrows) [90TMFA2]. The compound orders ferromagnetically at  $T_C = 91$  K. Note a significant difference between the ZFC and FC curves, characteristic of narrow domain-wall ferromagnets. At 4.2 K the FC magnetization attains  $1.5 \mu_B/\text{U-atom}$ .

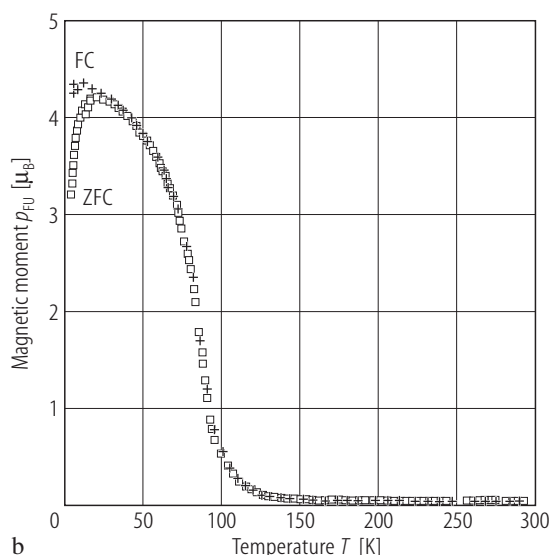
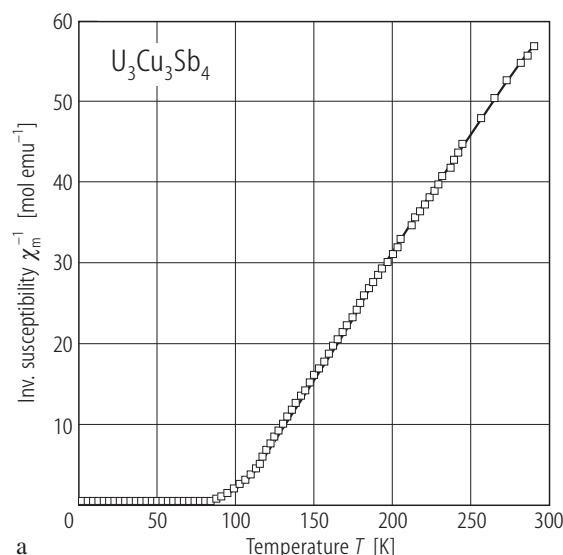


**Fig. 129.**  $\text{U}_3\text{Cu}_3\text{Sb}_4$ . (a) Reciprocal molar magnetic susceptibility,  $\chi_m^{-1}$ , vs.  $T$  [90ENMB]. The solid line is a Curie-Weiss fit with the parameters given in Table B. (b) Magnetic moment,  $p_U$ , vs. temperature,  $T$ , measured in a

field of 0.6 T upon cooling the sample in zero (ZFC; squares) and non-zero (FC; crosses) magnetic field [90ENMB]. The compound orders ferromagnetically at  $T_C = 88$  K. Compare Fig. 130.

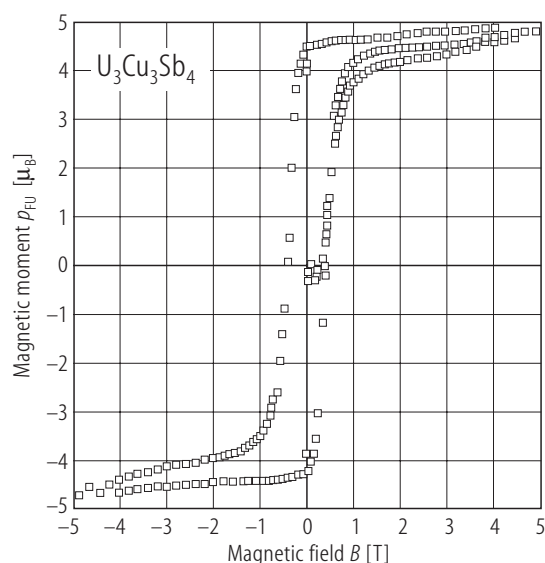


**Fig. 131.**  $\text{U}_3\text{Cu}_3\text{Sb}_4$ . Hysteresis loop,  $p_{\text{FU}}(B)$ , taken at  $T = 4.5$  K [90ENMB]. Note a rectangular hysteresis observed at 4.4 K with the saturation magnetic moment of  $4.8 \mu_{\text{B}}/\text{f.u.}$

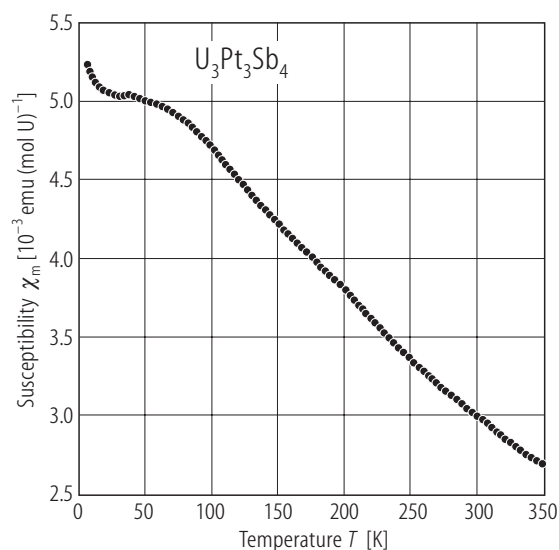


**Fig. 132.**  $\text{U}_3\text{Pt}_3\text{Sb}_4$ . Molar magnetic susceptibility,  $\chi_{\text{m}}$ , vs. temperature,  $T$  [92CLTS]. Above 200 K, the susceptibility follows a Curie-Weiss law with the effective magnetic moment of  $3.3 \mu_{\text{B}}/\text{U}$  atom and the paramagnetic Curie temperature of  $-160$  K (see also Table B).

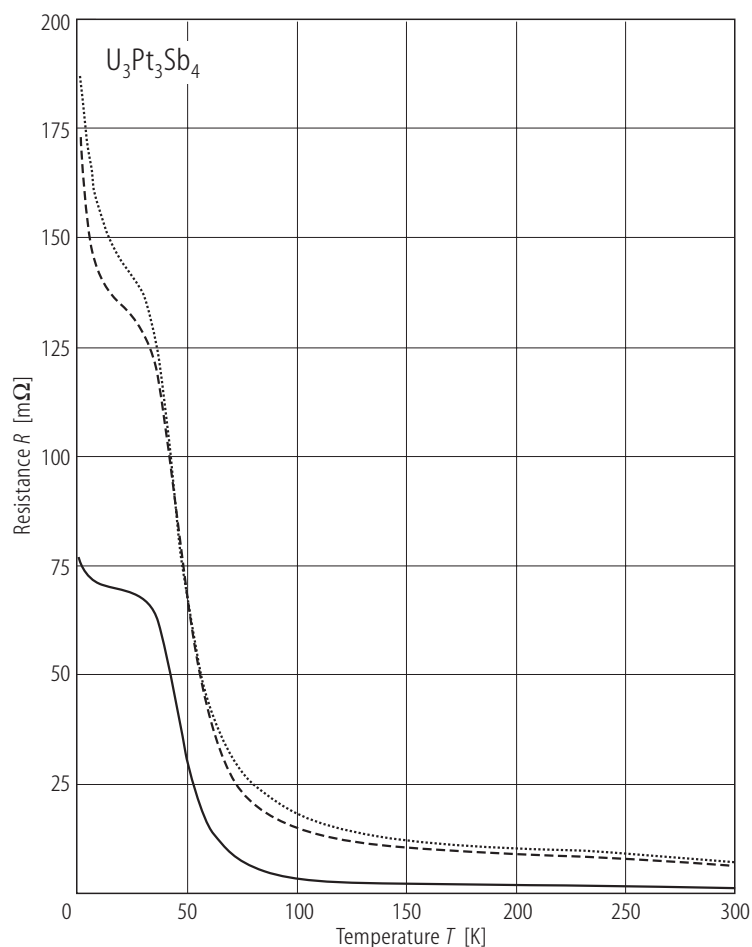


**Fig. 133.**  $\text{U}_3\text{Pt}_3\text{Sb}_4$ . Electrical resistance,  $R$ , vs. temperature,  $T$ , measured on a single crystal at atmospheric pressure (solid curve) and under hydrostatic pressure of 10.5 kbar (dashed curve) and 16.5 kbar (dotted curve) [92CLTS]. Note a semiconducting behaviour. Above 250 K,  $\rho(T)$  measured at 1 bar can be described by an activation law with the gap energy of about 500 K, while within the range 50...150 K the gap is approximately 200 K. Upon applying pressure the resistance increases at all temperatures but the gap does not change significantly.

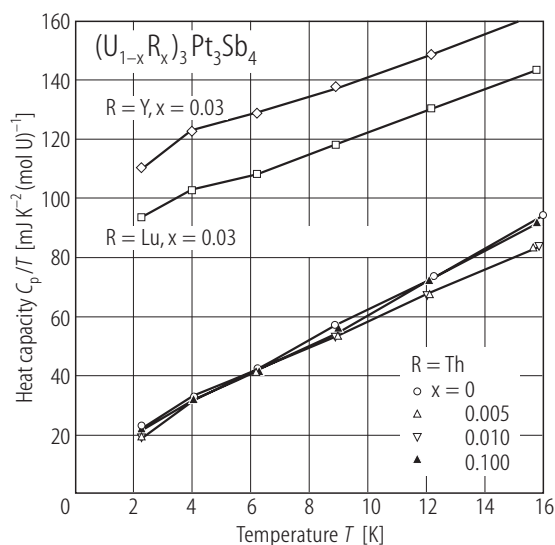


**Fig. 134.**  $(U_{1-x}R_x)_3Pt_3Sb_4$ ,  $R = Th, Lu, Y$ . Heat capacity divided by temperature,  $C_p/T$ , vs. temperature,  $T$ , measured on single crystals of  $U_3Pt_3Sb_4$  (circles),  $(U_{0.995}Th_{0.005})_3Pt_3Sb_4$  (open triangles-up),  $(U_{0.99}Th_{0.01})_3Pt_3Sb_4$  (open triangles-down),  $(U_{0.90}Th_{0.10})_3Pt_3Sb_4$  (filled triangles),  $(U_{0.97}Lu_{0.03})_3Pt_3Sb_4$  (squares) and  $(U_{0.97}Y_{0.03})_3Pt_3Sb_4$  (diamonds) [92CLTS]. Note that the pure and three Th-doped materials show the same behaviour, whereas the Lu- and Y-doped compounds exhibit an enhancement of the electronic heat capacity. This difference in the behaviour of  $C_p$  comes from the fact that Th is a tetravalent ion, while Lu and Y are trivalent ions.

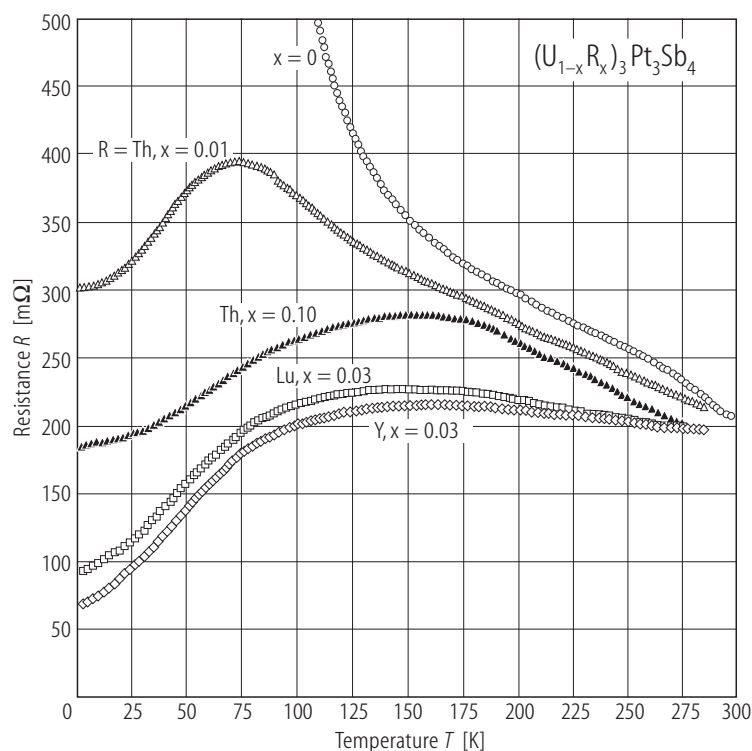


**Fig. 135.**  $(U_{1-x}R_x)_3Pt_3Sb_4$ ,  $R = Th, Lu, Y$ . Electrical resistance,  $R$ , vs. temperature,  $T$ , measured on single crystals of  $U_3Pt_3Sb_4$  (circles),  $(U_{0.99}Th_{0.01})_3Pt_3Sb_4$  (open triangles),  $(U_{0.90}Th_{0.10})_3Pt_3Sb_4$  (filled triangles),  $(U_{0.97}Lu_{0.03})_3Pt_3Sb_4$  (squares) and  $(U_{0.97}Y_{0.03})_3Pt_3Sb_4$  (diamonds) [92CLTS]. Note that even 1% substitution for uranium depress the low temperature semiconducting-like rise in  $R(T)$  and results in the formation of a resistance maximum. The temperature of this maximum increases with higher doping concentrations. All the samples studied have roughly the same room temperature resistivity of 25 mΩcm.

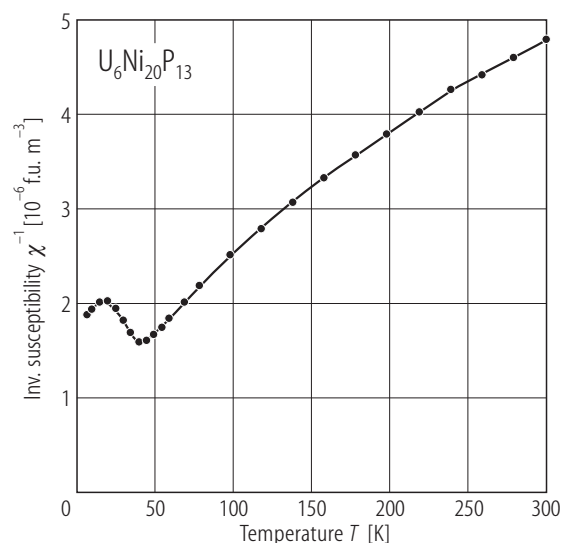


**Fig. 136.**  $\text{U}_6\text{Ni}_{20}\text{P}_{13}$ . Reciprocal magnetic susceptibility,  $\chi^{-1}$  (SI units), vs. temperature,  $T$ , measured in a field of 1 T [98EAJ]. The compound orders antiferromagnetically at  $T_N = 41(4)$  K. The anomalous increase in the susceptibility at the lowest temperatures is not caused by ferromagnetic impurities as the magnetization at 5 K is a linear function of magnetic field (not shown). The solid line is a guide for the eye. See the modified Curie-Weiss fit parameters given in Table B.

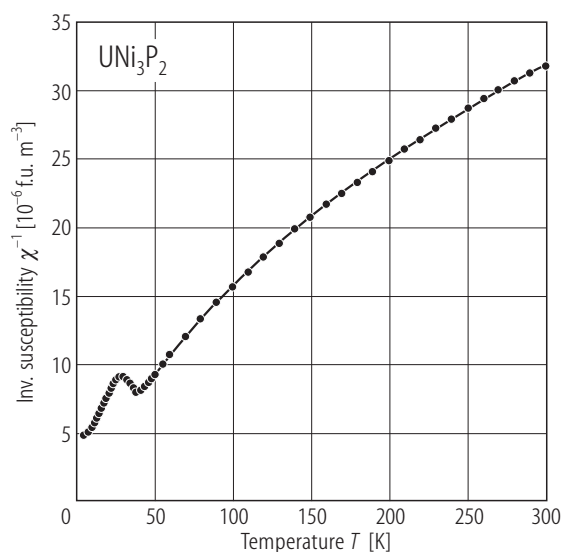


**Fig. 138.**  $\text{UNi}_3\text{P}_2$ . Reciprocal magnetic susceptibility,  $\chi^{-1}$  (SI units), vs. temperature,  $T$ , measured in a field of 1 T [98EAJ]. The compound orders antiferromagnetically at  $T_N = 39(3)$  K. The solid line denotes a modified Curie-Weiss fit with the parameters given in Table B. The anomalous increase in the susceptibility at the lowest temperatures is not caused by ferromagnetic impurities as the magnetization at 5 K is a linear function of magnetic field (not shown).

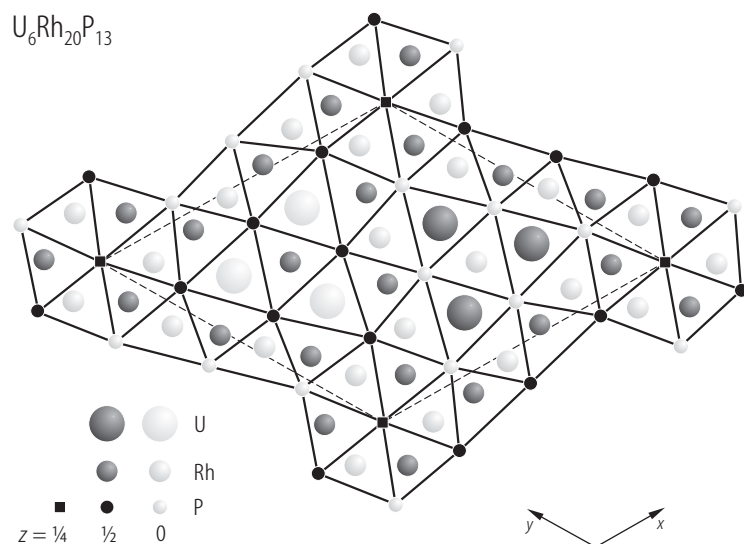


**Fig. 137.**  $\text{U}_6\text{Rh}_{20}\text{P}_{13}$ . Crystal structure projected along the  $[001]$  axis [87GCMS]. The dashed lines outline the unit cell.

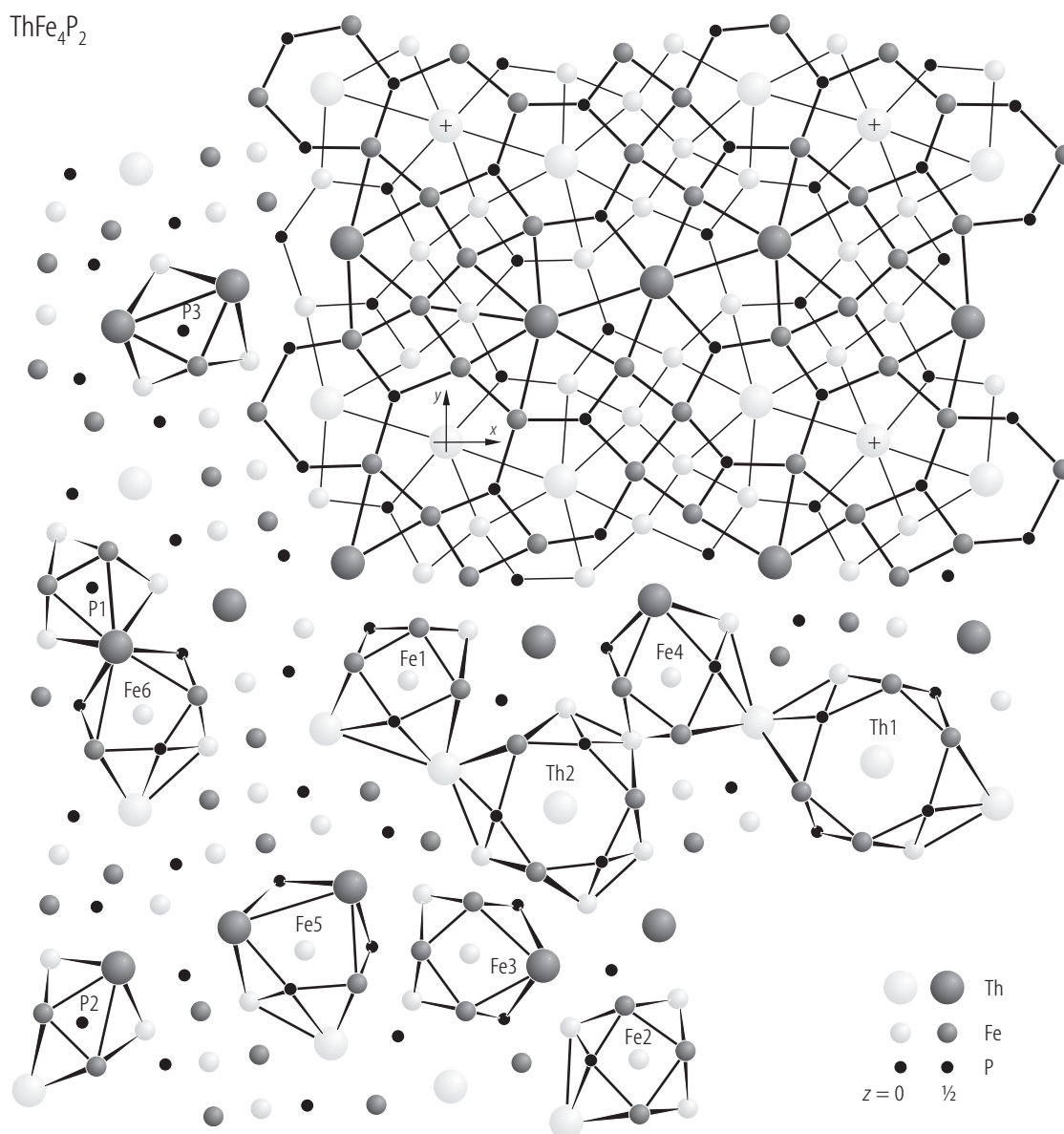


**Fig. 139.**  $\text{ThFe}_4\text{P}_2$ . Crystal structure and coordination polyhedra projected on the  $xy$  plane [92AJ1]. The atoms connected by the thin and thick lines are at  $z = 0$  and  $1/2$ , respectively.



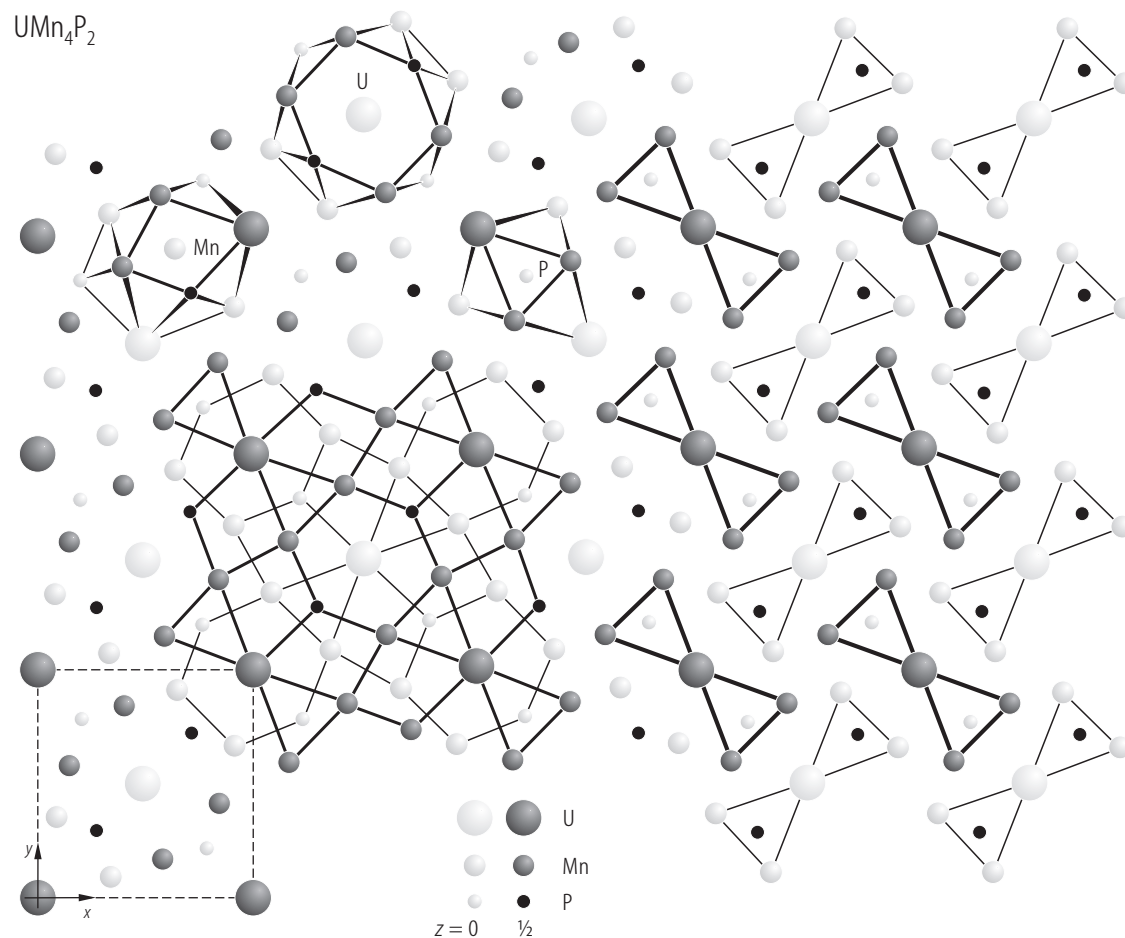


**Fig. 140.** UMn<sub>4</sub>P<sub>2</sub>. Crystal structure projected on the (*a*,*b*) plane [90JTRP]. The arrangement of the metal prisms around the phosphorus atoms is shown (right-hand side). All coordination polyhedra have mirror planes perpendicular to the projection direction.

For Fig. 141 see next page

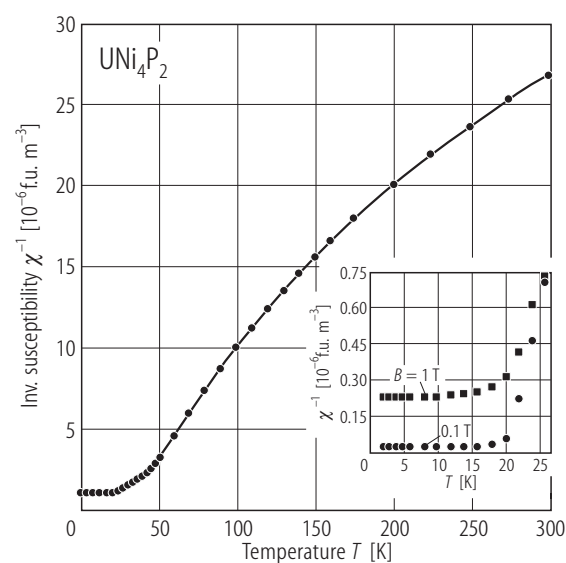


**Fig. 142.** UNi<sub>4</sub>P<sub>2</sub>. Reciprocal magnetic susceptibility,  $\chi^{-1}$  (SI units), vs. temperature, *T*, measured in a field of 1 T [98EAI]. Inset:  $\chi^{-1}(T)$  below 25 K taken at 0.1 T (circles) and 1 T (squares). The compound orders ferromagnetically at  $T_C = 21(1)$  K. A tiny anomaly on  $\chi^{-1}(T)$  at about 40 K the authors ascribed to an unknown ferromagnetic impurity. See the modified Curie-Weiss fit parameters given in Table B.

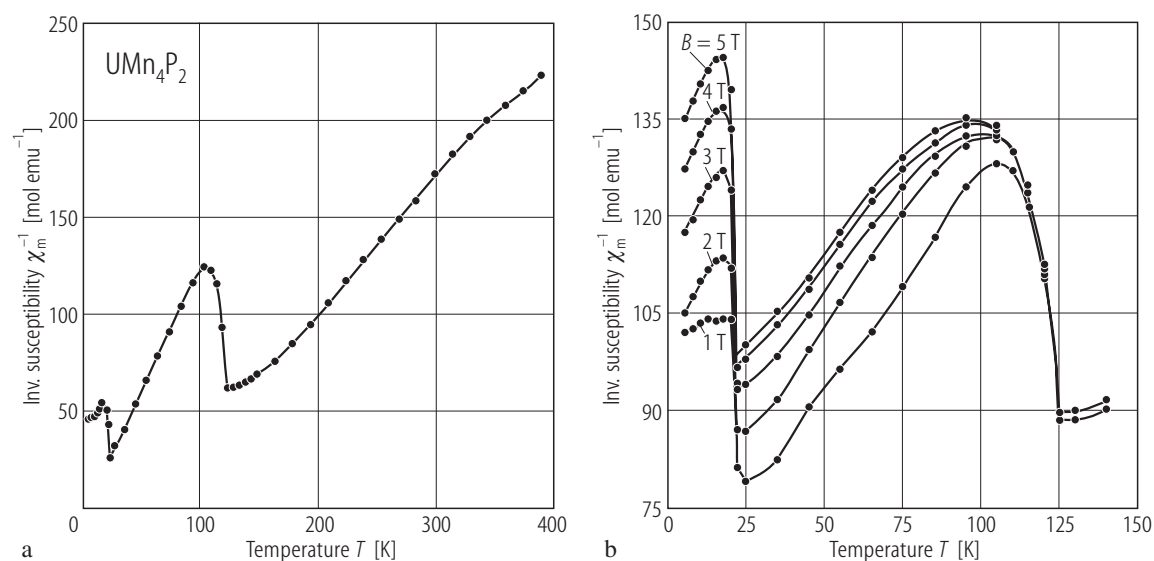


**Fig. 141.**  $\text{UMn}_4\text{P}_2$ . (a) Reciprocal molar magnetic susceptibility,  $\chi_m^{-1}$ , vs. temperature,  $T$ , taken in a field of 1 T [90JTRP]. (b) Low-temperature  $\chi_m^{-1}(T)$  measured at  $B = 1, 2, 3, 4$  and 5 T [90JTRP]. Note that only above 125 K the susceptibility is independent of the magnetic field. The

authors ascribed the transitions at  $T_N = 125$  K and  $T_I = 22$  K to the antiferromagnetic ordering of the manganese and uranium magnetic moments, respectively. See the Curie-Weiss fit parameters given in Table B.

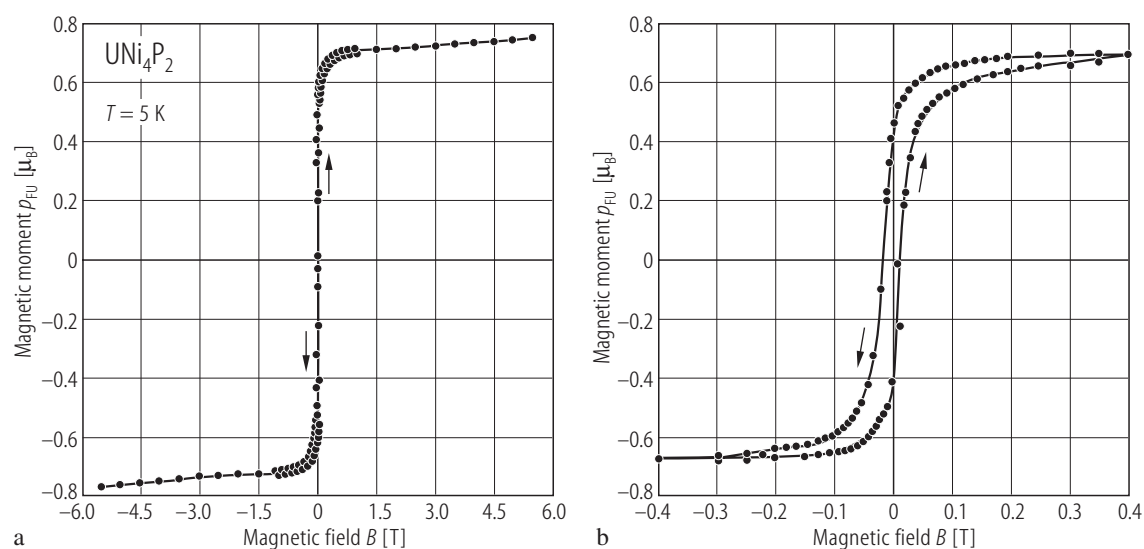


**Fig. 143.**  $\text{UNi}_4\text{P}_2$ . (a) Hysteresis loop,  $\rho_{\text{FU}}(B)$ , taken at 5 K [98EAJ]. The arrows represent increasing and decreasing magnetic field. (b)  $\rho_{\text{FU}}(B)$  measured in weak fields [98EAJ]. Note a small coercivity.

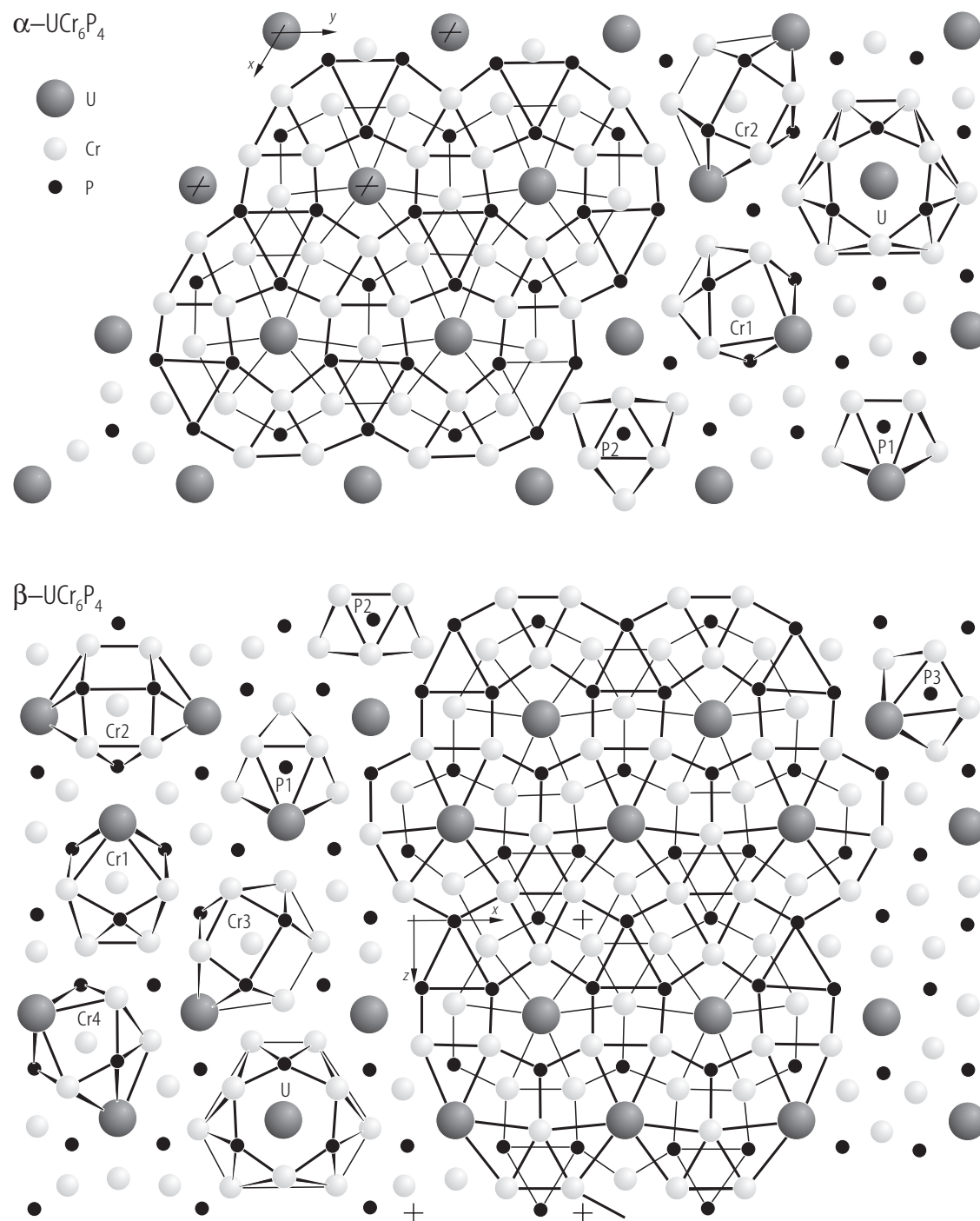


**Fig. 144.**  $\alpha\text{-UCr}_6\text{P}_4$ ,  $\beta\text{-UCr}_6\text{P}_4$ . Crystal structures and coordination polyhedra projected on the  $xy$  ( $\alpha$  modification) or  $xz$  ( $\beta$  modification) plane [92JB]. The atoms connected by thick and thin lines are separated from each other by half a translation period of the projection direction.

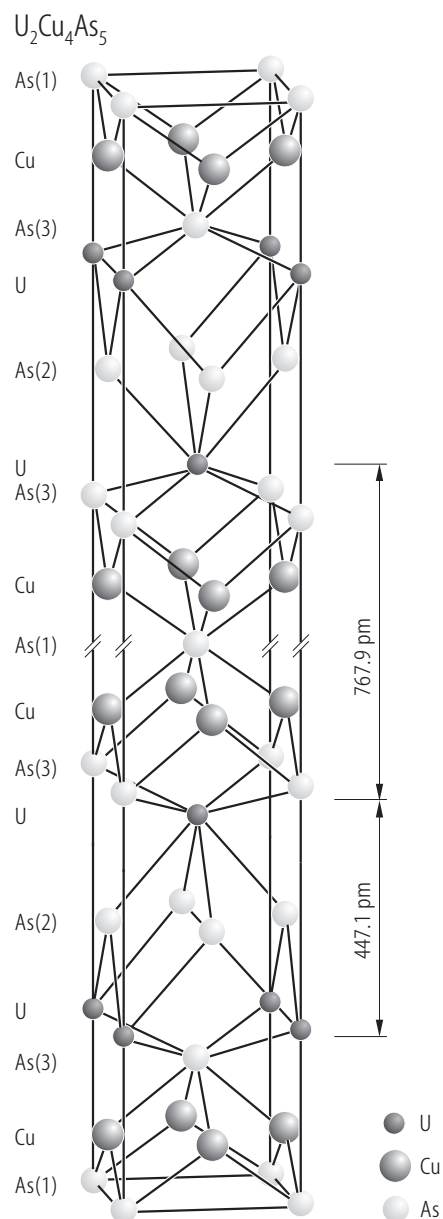


**Fig. 145.**  $\text{U}_2\text{Cu}_4\text{As}_5$ . Crystal structure [91KNT].

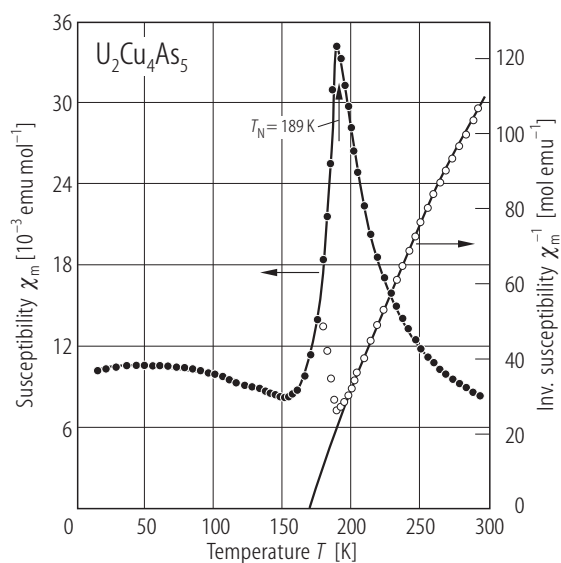


**Fig. 146.**  $\text{U}_2\text{Cu}_4\text{As}_5$ . Molar magnetic susceptibility,  $\chi_m$ , vs. temperature,  $T$ , (left-hand scale) and reciprocal molar magnetic susceptibility,  $\chi_m^{-1}$ , vs.  $T$ , (right-hand scale) [91KNT]. The vertical arrow marks an antiferromagnetic phase transition at 189 K. The solid line is a modified Curie-Weiss fit with the parameters given in Table B.

For Figs. 147, 148 see next page

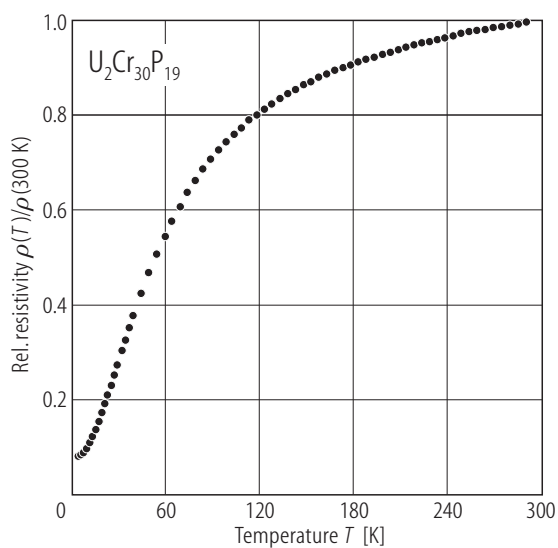


**Fig. 149.**  $\text{U}_2\text{Cr}_{30}\text{P}_{19}$ . Normalised electrical resistivity,  $\rho/\rho(300\text{ K})$ , vs. temperature,  $T$ , [98LPDG].  $\rho(300\text{ K}) = 372\text{ }\mu\Omega\text{ cm}$ . Note a metallic behaviour.

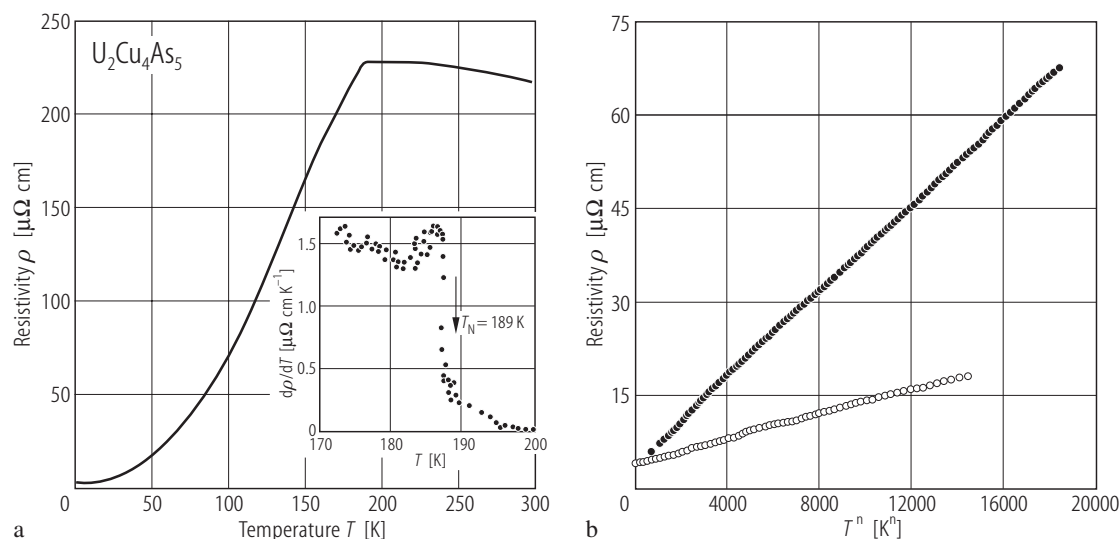


**Fig. 147.**  $\text{U}_2\text{Cu}_4\text{As}_5$ . **(a)** Electrical resistivity,  $\rho$ , vs. temperature,  $T$ , measured on a single crystal with  $i \perp c$ -axis [91KNT]. Inset: temperature derivative of the resistivity,  $d\rho/dT$ , vs.  $T$  in the vicinity of  $T_N$  (compare Fig. 146). Note a negative slope in  $\rho(T)$  in the paramagnetic region. **(b)** Low-temperature resistivity plotted against  $T^n$  with  $n = 2.46$

(open circles) and 2.14 (filled circles) [91KNT]. A linear dependence is observed in the regions 4.2...100 and 4.2...50 K, respectively. The proportionality  $\rho \sim T^{2.5}$  characterizes also the low-temperature resistivity of  $\text{USb}_2$  [72HK] but the reason of its occurrence is not yet clear.

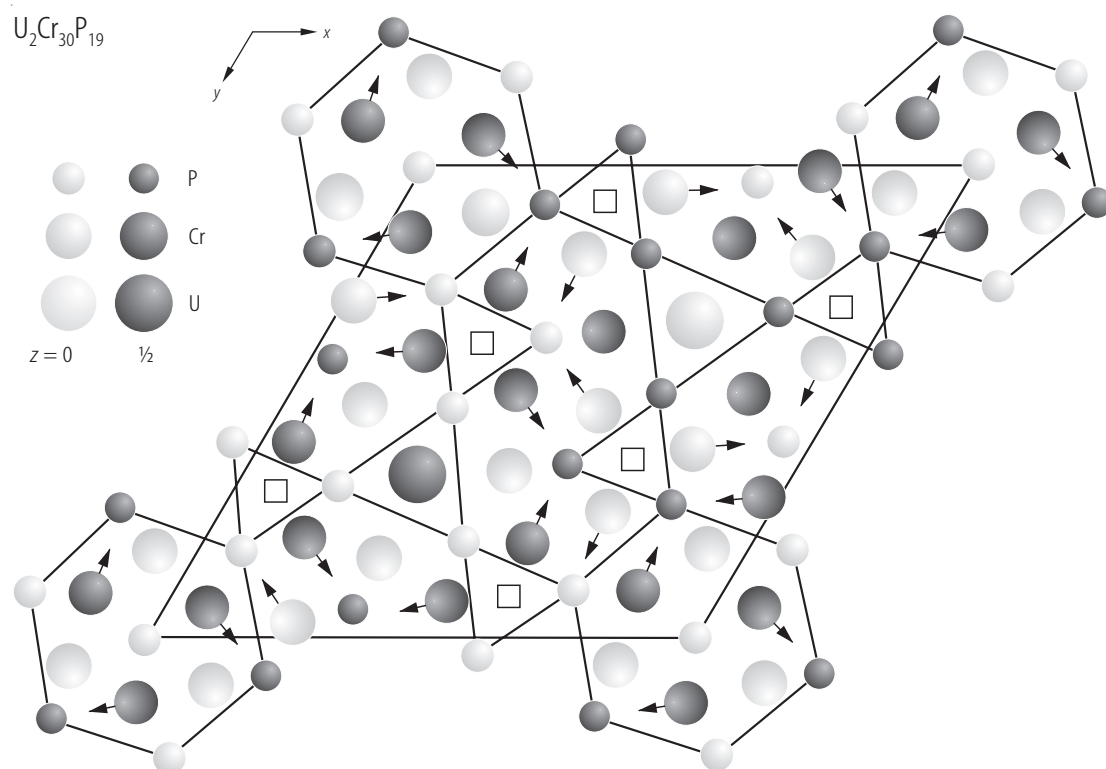


**Fig. 148.**  $\text{U}_2\text{Cr}_{30}\text{P}_{19}$ . Crystal structure projected on the (001) plane [98LPDG]. Light and dark gray circles are translated from each other by half a period of the projection direction. Solid lines denote the phosphorus channels and

the hexagonal framework around the origin. Arrows mark the apex of the  $[\text{CrP}_5]$  pyramids. The squares denote trigonal prismatic phosphorus vacancies (for discussion see original paper).

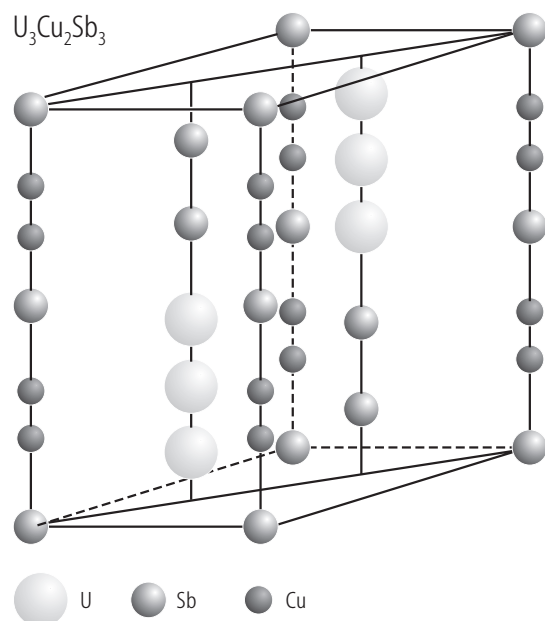


**Fig. 150.**  $\text{U}_3\text{Cu}_2\text{Sb}_3$ . Crystal structure [86DB].

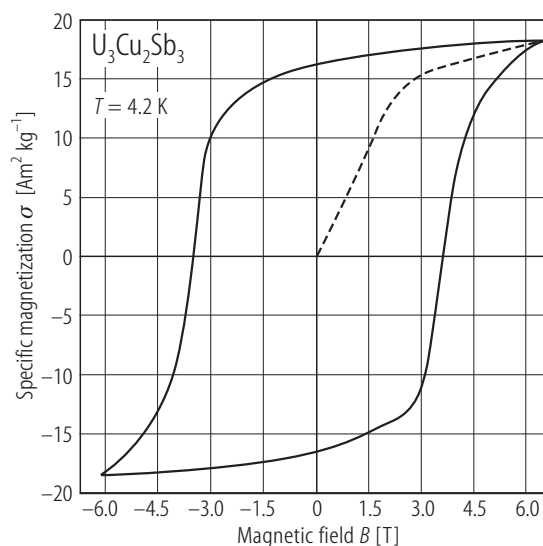
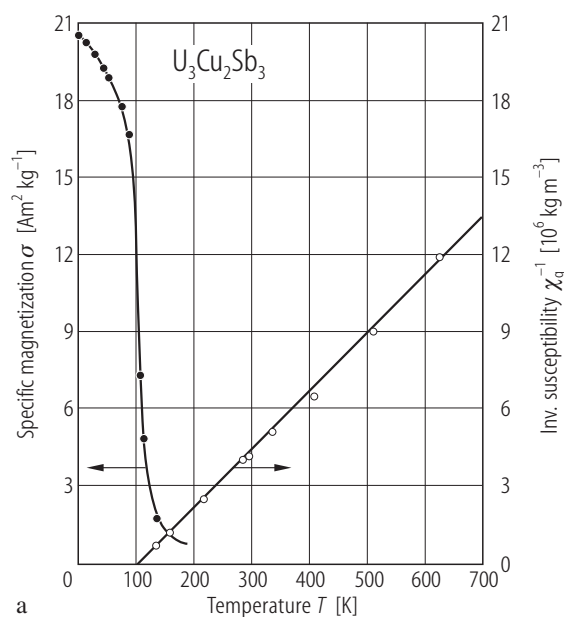
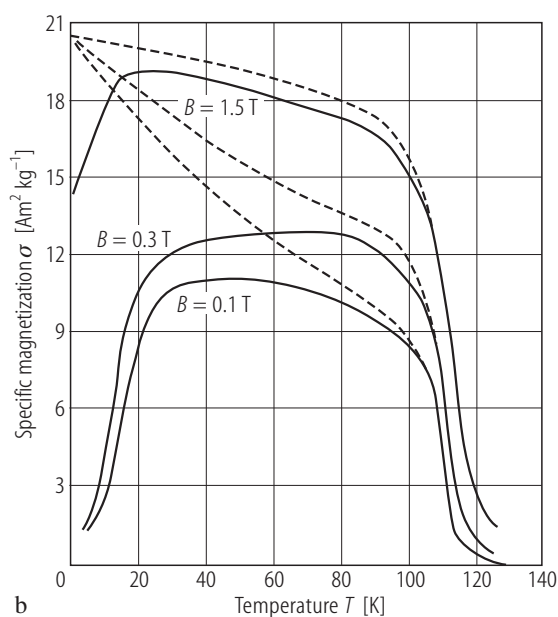


**Fig. 152.**  $\text{U}_3\text{Cu}_2\text{Sb}_3$ . Hysteresis loop,  $\sigma(B)$ , taken at  $T = 4.2$  K on a zero-field cooled sample (SI units) [86DB]. Note a strongly rectangular shape of  $\sigma(B)$  with a large remanence and a large coercive force.



a



b

**Fig. 151.**  $\text{U}_3\text{Cu}_2\text{Sb}_3$ . (a) Specific magnetization,  $\sigma$ , measured in a field of 1.5 T upon cooling the sample in a field of 0.3 T (filled circles, left-hand side scale) and reciprocal mass magnetic susceptibility,  $\chi_g^{-1}$ , (open circles, right-hand side scale) vs. temperature,  $T$ , up to 700 K (SI units) [86DB]. The compound orders ferromagnetically at  $T_C = 110$  K. The straight line marks a Curie-Weiss

behaviour of the susceptibility with the parameters given in Table B. (b)  $\sigma$  vs.  $T$ , measured in different magnetic fields (specified in the figure) upon cooling the sample in zero (full curves) and non-zero (broken curves) magnetic field [86DB]. Note a pronounced thermomagnetic history effect, reflecting strong magnetocrystalline anisotropy. The spontaneous magnetic moment at 4.2 K is  $1.48 \mu_B/\text{U atom}$ .

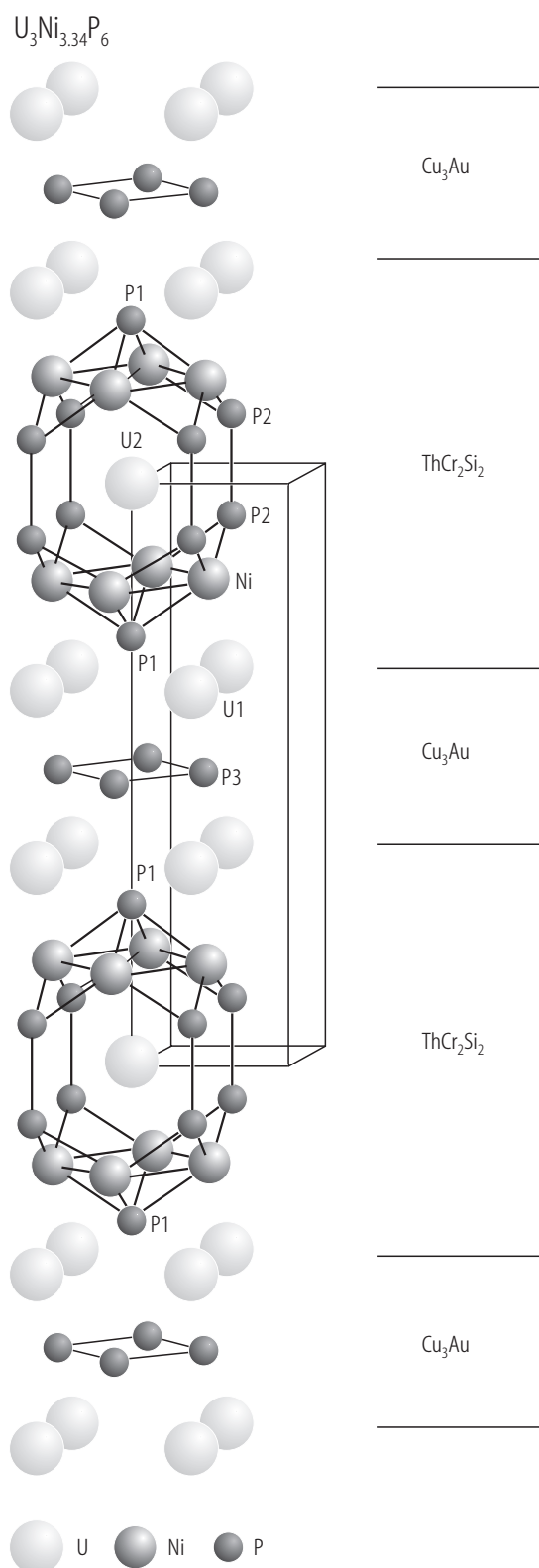


**Fig. 153.**  $\text{U}_3\text{Ni}_{3.34}\text{P}_6$ . Crystal structure [95EJ]. Short Ni-Ni, Ni-P and P-P distances are outlined to show characteristic polyanionic building elements. Emphasized are the  $\text{Cu}_3\text{Au}$ - and  $\text{ThCr}_2\text{Si}_2$ -type building blocks.

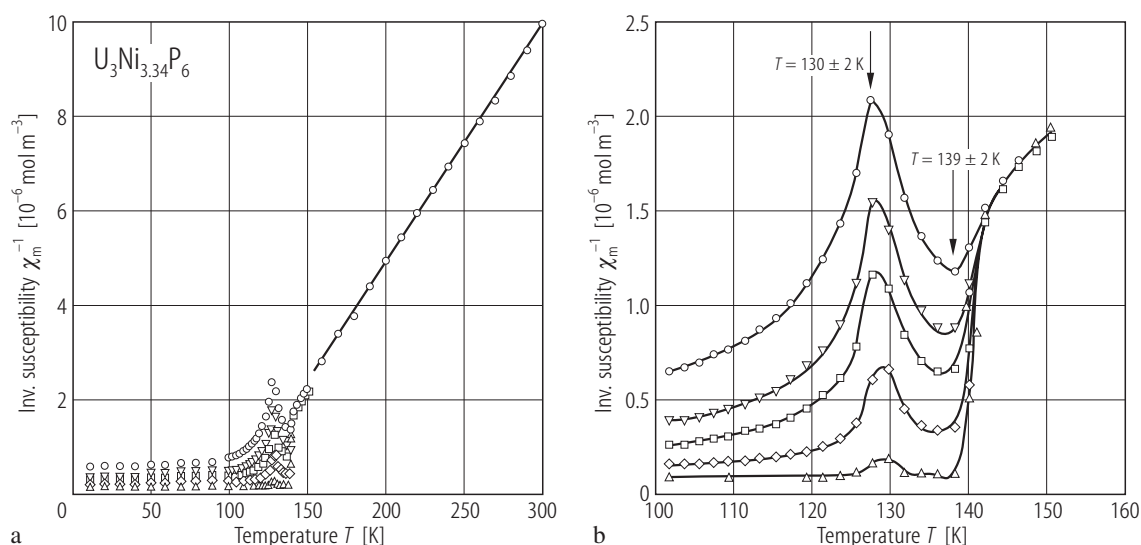


**Fig. 154.**  $\text{U}_3\text{Ni}_{3.34}\text{P}_6$ . (a) Reciprocal molar magnetic susceptibility,  $\chi_m^{-1}$  (SI units), vs. temperature,  $T$ , measured in several magnetic fields [95EJ]. Triangles up: 0.005 T; diamonds: 0.1 T; squares: 0.3 T; triangles down: 0.5 T; circles: 1 T. The solid line denotes a Curie-Weiss fit with the parameters given in Table B. (b)  $\chi_m^{-1}(T)$  as in panel (a),

in the vicinity of the magnetic phase transition [95EJ]. The compound is ferrimagnetic below  $T_C = 139(2) \text{ K}$  (see Fig. 157). The maximum in  $\chi_m^{-1}(T)$  occurring at  $130(2) \text{ K}$  the authors interpreted as a compensation point (for discussion refer to the caption of Fig. 155).

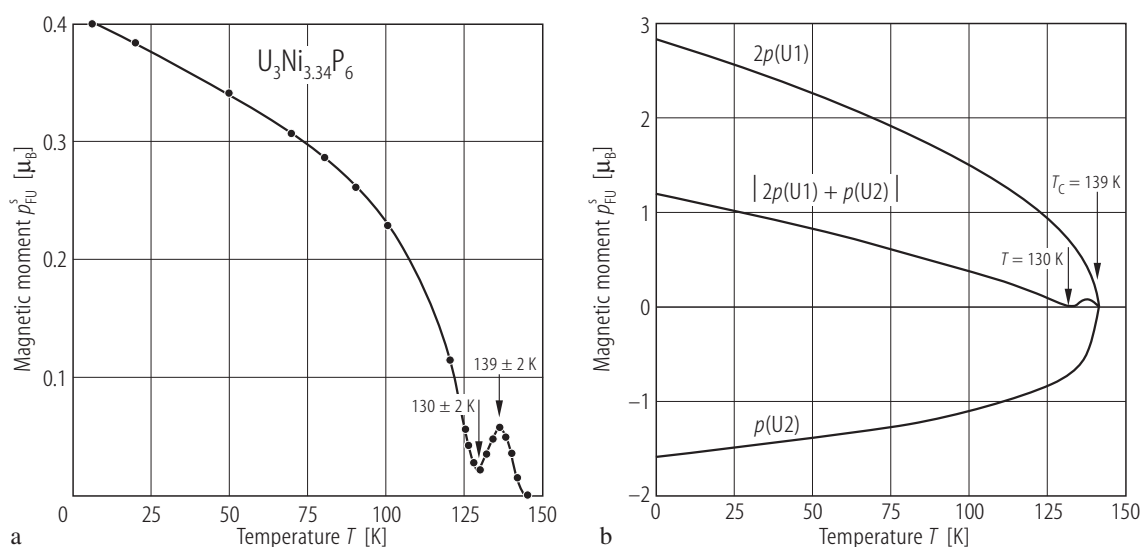


**Fig. 155.**  $\text{U}_3\text{Ni}_{3.34}\text{P}_6$ . (a) Spontaneous magnetic moment,  $p_{\text{FU}}^s$ , vs. temperature,  $T$ , obtained by extrapolation to zero magnetic field of high-field parts of several magnetization curves  $p_{\text{FU}}(B)$ , taken at the temperatures marked by the black circles [96REJS]. The compound orders ferrimagnetically below  $T_C = 139(2) \text{ K}$  (see Fig. 157) and exhibits a compensation point at  $130(2) \text{ K}$ . (b) Model calculation of  $p_{\text{FU}}^s(T)$  showing the formation of a

compensation point in a ferrimagnet [96REJS]. Magnetic structure and values of the two uranium magnetic moments were assumed as shown in Fig. 158. The temperature variations of  $p(\text{U1})$  and  $p(\text{U2})$  were taken as given by the Brillouin function  $p \propto (1 - T/T_C)^\beta$  with the critical exponent  $\beta = 0.5$  and  $0.3$  for U1 and U2, respectively. The difference curve has a minimum at  $130 \text{ K}$ , which is the compensation point in this compound.



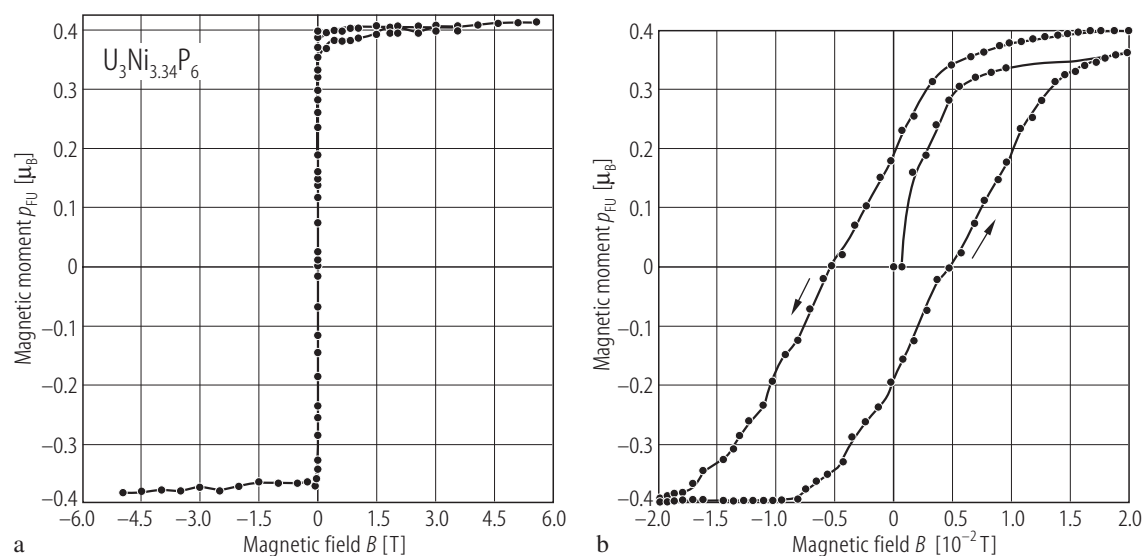


**Fig. 156.**  $\text{U}_3\text{Ni}_{3.34}\text{P}_6$ . (a) Hysteresis loop: magnetic moment,  $p_{\text{FU}}$ , vs. magnetic field,  $B$ , taken at 5 K [96REJS]. (b)  $\alpha(B)$  measured in weak fields [96REJS]. The arrows indicate increasing and decreasing field. The loop is very

small with the remanence of  $0.19(1) \mu_{\text{B}}$  and the coercivity of about  $0.005(1) \text{ T}$ . The saturation moment is only  $0.41(1) \mu_{\text{B}}$ , i.e. much smaller than the value obtained by neutron diffraction (see Fig. 158).

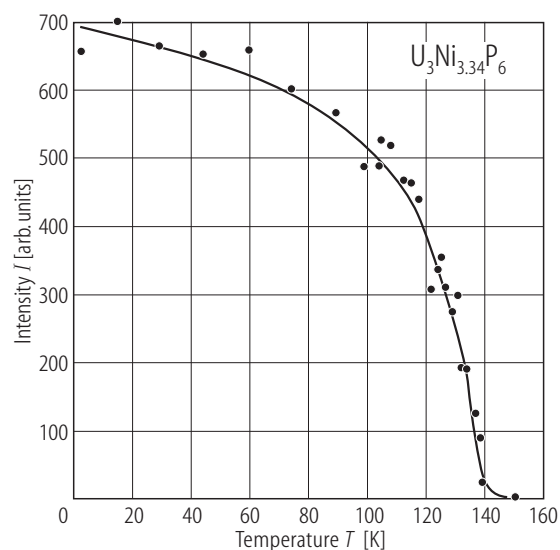


**Fig. 157.**  $\text{U}_3\text{Ni}_{3.34}\text{P}_6$ . Neutron diffraction intensity of the magnetic reflection (100),  $I$ , vs. temperature,  $T$  [96REJS]. The compound orders ferrimagnetically at  $T_{\text{C}} = 139 \text{ K}$  (see Fig. 155).

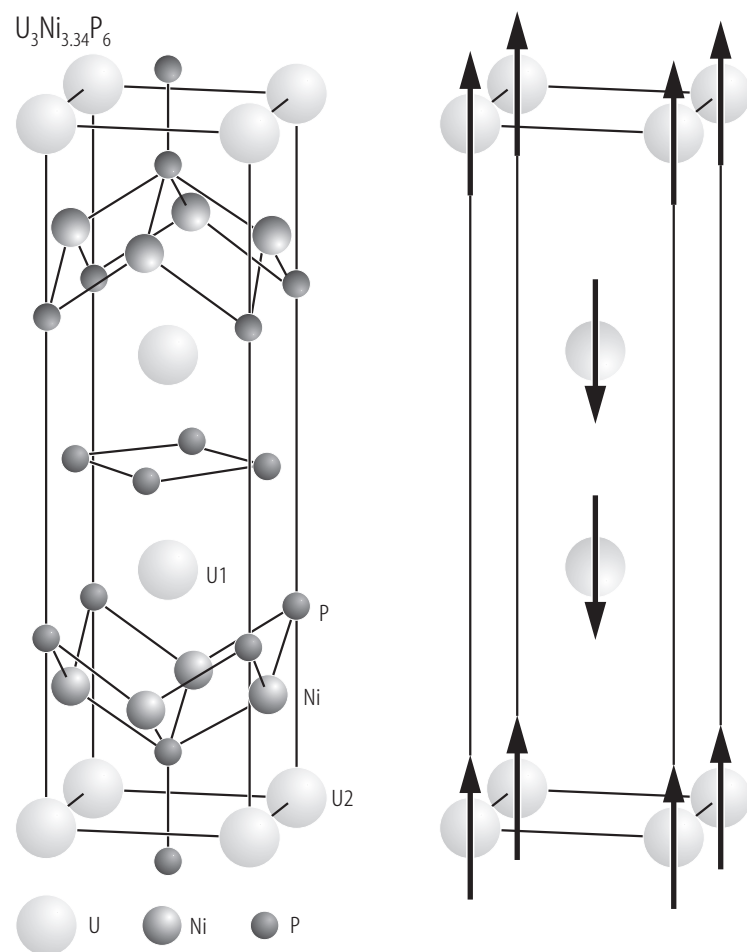


**Fig. 158.**  $\text{U}_3\text{Ni}_{3.34}\text{P}_6$ . Magnetic structure [96REJS]. For clarity the crystal structure determined in [95EJ] (see Fig. 153) is also shown. The compound is a ferrimagnet with the uranium magnetic moments  $p(\text{U1}) = 1.4(1) \mu_{\text{B}}$  and  $p(\text{U2}) = 1.6(2) \mu_{\text{B}}$ . The nickel atoms do not carry magnetic moments. Accordingly, the net magnetic moment is  $p = 2p(\text{U1}) - p(\text{U2}) = 1.2(3) \mu_{\text{B}}$  being much larger than that found in the magnetization studies (compare Fig. 156).

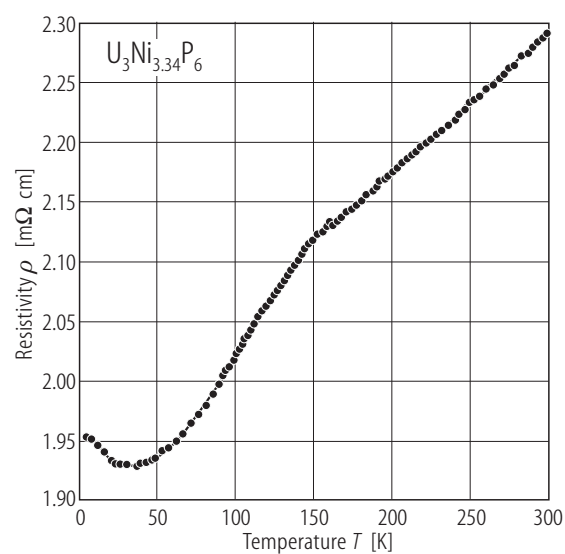


**Fig. 159.**  $\text{U}_3\text{Ni}_{3.34}\text{P}_6$ . Electrical resistivity,  $\rho$ , vs. temperature,  $T$  [95EJ]. Note high values of the resistivity. The authors describe the compound as a semimetal (zero-gap semiconductor): at low temperatures the material behaves as a semiconductor, while with increasing temperature the conduction band becomes gradually populated and the carriers are scattered like in a metal. The kink at about 150 K they attributed to the magnetic ordering, which sets in at 139(2) K (see Fig. 154).

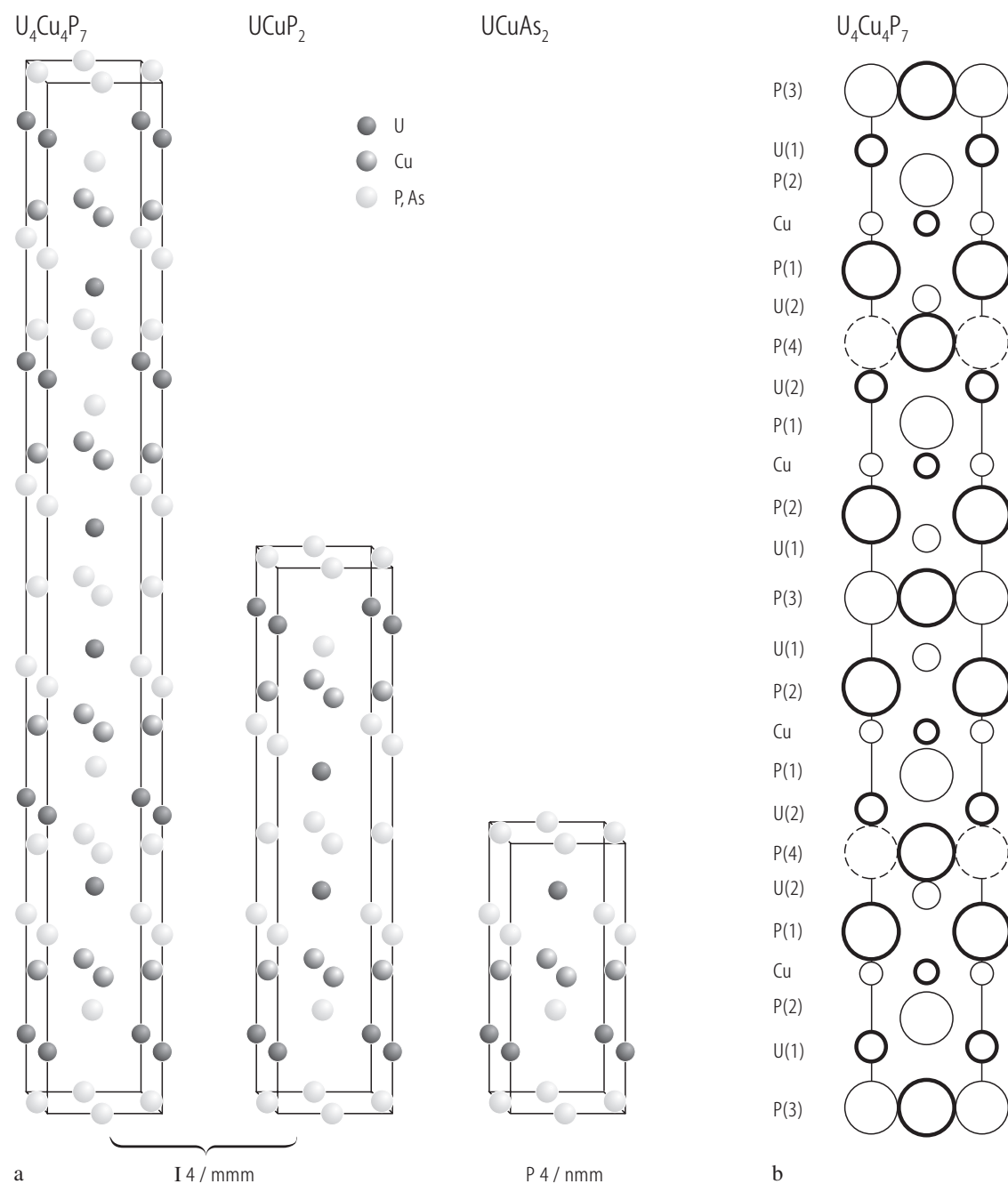


**Fig. 160.**  $U_4Cu_4P_7$ . (a) Crystal structure as compared to that of  $UCuP_2$  and  $UCuAs_2$  [87NZKT2]. Note similar building blocks. (b) Projection of the structure on the  $xz$  plane showing details of the atom arrangement [92SKB]. Atoms

at  $y = 0$  are drawn with thick lines, atoms at  $y = \frac{1}{2}$  are drawn with narrow lines. The P(4) sites are only half filled and two possible positions of this atom are shown by full-line circles and dashed-line circles, respectively.

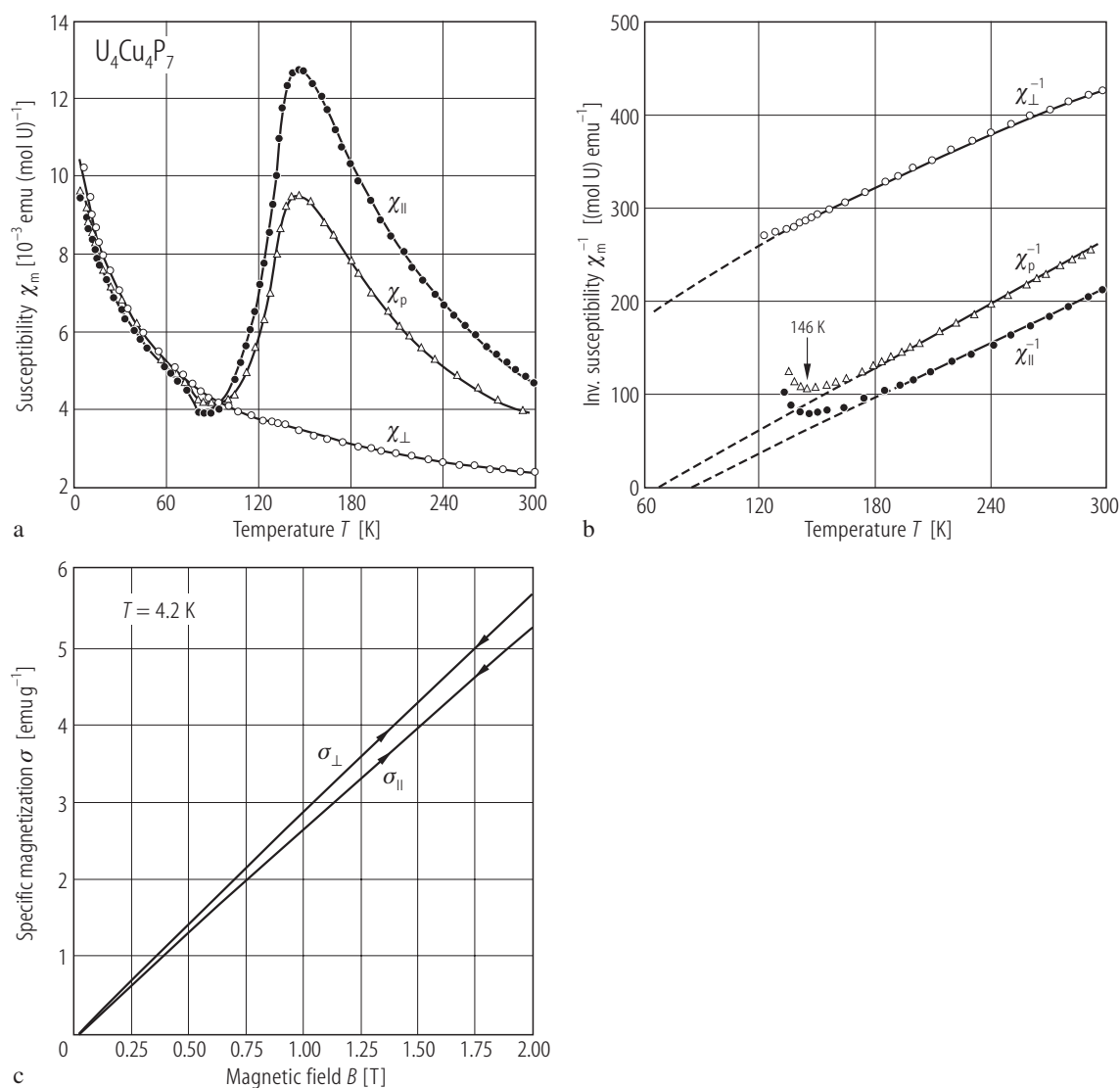


**Fig. 161.**  $\text{U}_4\text{Cu}_4\text{P}_7$ . (a) Longitudinal,  $\chi_{||}$ , (full circles), transversal,  $\chi_{\perp}$ , (open circles) and powder,  $\chi_p$ , (triangles) molar magnetic susceptibility vs. temperature,  $T$  [90KTN]. The solid lines are guides to the eye. The compound orders antiferromagnetically at 146 K. Note an anomalous increase of the susceptibility at low temperatures which may originate in crystal field interactions (see the original paper). (b) Reciprocal molar magnetic susceptibilities as in

panel (a) vs.  $T$ , in the paramagnetic region [90KTN]. The dashed lines are Curie-Weiss (for  $\chi_{||}^{-1}$  and  $\chi_p^{-1}$ ) and modified Curie-Weiss (for  $\chi_{\perp}^{-1}$ ) fits with the parameters given in Table B. (c) Specific magnetization,  $\sigma_{||}$  and  $\sigma_{\perp}$ , vs. magnetic field,  $B$ , measured at 4.2 K on a single crystal with  $B \parallel c$ -axis and  $B \perp c$ -axis [90KTN]. The small arrows mark increasing and decreasing magnetic field. Note that no metamagnetic transition occurs up to 2 T.

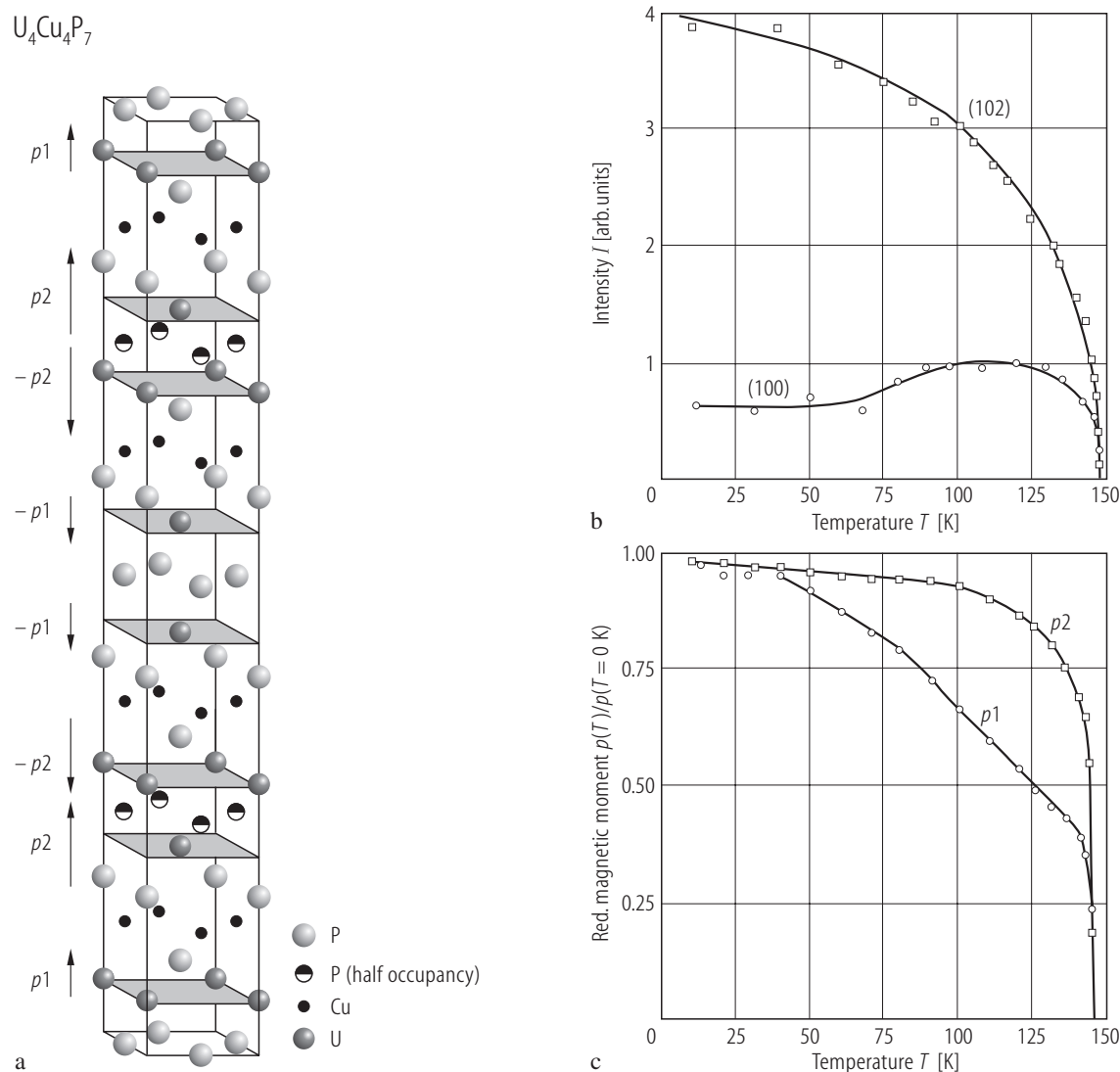


**Fig. 162.**  $U_4Cu_4P_7$ . **(a)** Magnetic structure [94BTKN]. There are two inequivalent crystallographic positions for the uranium atoms (see also Fig. 160) which carry different magnetic moments  $p_1$  and  $p_2$ , both directed along the tetragonal  $c$ -axis. The magnetic ordering corresponds to a stacking of ferromagnetic (001) planes in the sequence shown schematically in the figure. The wave vector  $\mathbf{k} = [001]$ . **(b)** Neutron diffraction intensities of the magnetic reflections (100) and (102),  $I$ , vs. temperature,  $T$  [94BTKN]. The Néel temperature is 146 K. The unusual

behaviour of (100) indicates that  $p_1$  and  $p_2$  have different temperature dependencies. **(c)** Normalized magnetic moments,  $p(T)/p(T = 0 \text{ K})$ , vs.  $T$  for the two inequivalent uranium sites [94BTKN]. Note different temperature variations. At 4.2 K  $p_1 = 1.1(1) \mu_B$  and  $p_2 = 2.2(1) \mu_B$ . The occurrence of the different uranium magnetic moments with different temperature dependencies the authors attributed to different valence of uranium atoms carrying the moments  $p_1$  and  $p_2$ :  $4^+$  and  $3^+$ , respectively.

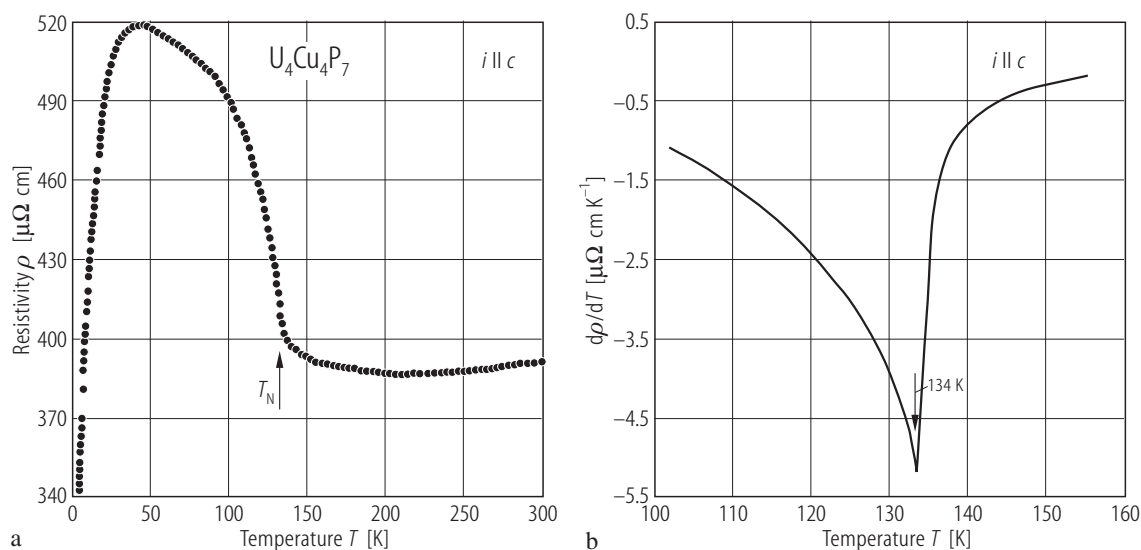


**Fig. 163.**  $\text{U}_4\text{Cu}_4\text{P}_7$ . (a) Electrical resistivity,  $\rho$ , vs. temperature,  $T$ , measured on a single crystal with  $i \parallel c$ -axis [90KTN]. The arrow marks the antiferromagnetic phase transition (see Fig. 161). Note a large broad hump below  $T_N$ , which may originate in the specific semimetal-like Fermi surface of the compound. For the resistivity

measured with  $i \perp c$ -axis see Fig. 164. (b) Temperature derivative of the resistivity [90KTN]. Note a sharp anomaly at  $T_N = 134$  K. This ordering temperature is considerably lower than that derived from magnetic data (compare Figs. 161, 162).

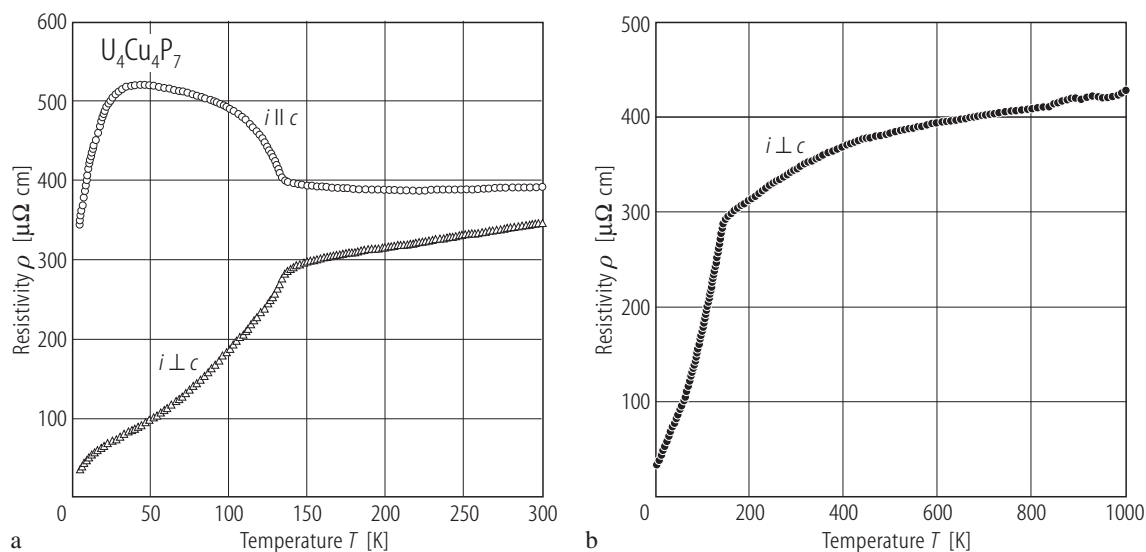


**Fig. 164.**  $\text{U}_4\text{Cu}_4\text{P}_7$ . (a) Electrical resistivity,  $\rho$ , vs. temperature,  $T$ , measured on single crystals with  $i \parallel c$ -axis (circles) and  $i \perp c$ -axis (triangles) [92SKB]. Note a different behaviour of  $\rho(T)$  near the antiferromagnetic phase transition at 146 K, which arises due to a specific magnetic

structure of the compound (see Fig. 162). (b) Electrical resistivity,  $\rho$ , vs.  $T$  up to 1000 K, measured on a single crystal with  $i \perp c$ -axis [92SKB]. The linear part in  $\rho(T)$  between 500 and 1000 K is attributed to the phonon contribution  $c_{\text{ph}}T$  with  $c_{\text{ph}} = 0.075 \mu\Omega\text{cm/K}$ .

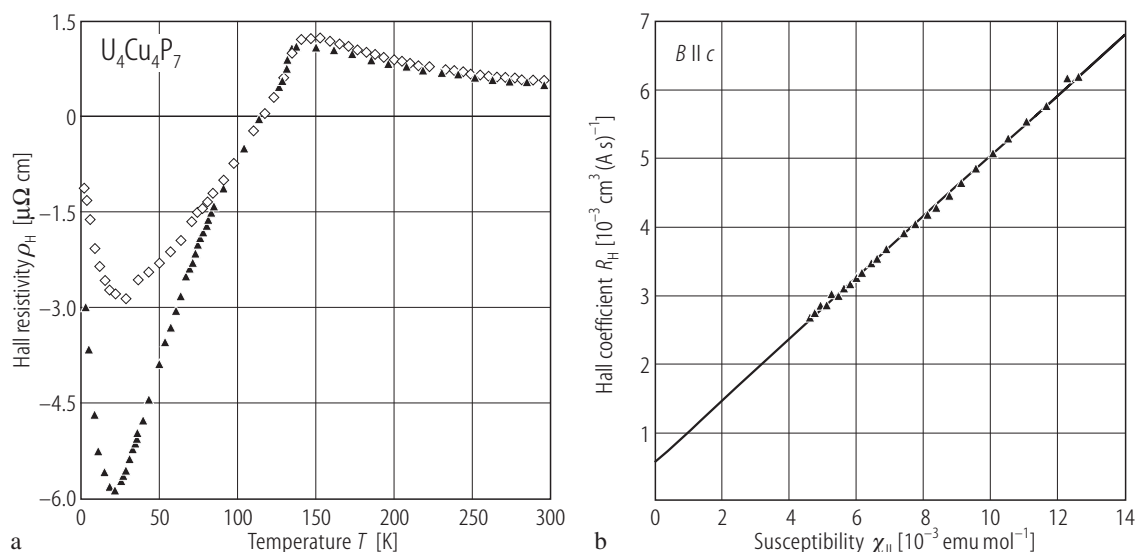


**Fig. 165.**  $\text{U}_4\text{Cu}_4\text{P}_7$ . **(a)** Hall resistivity,  $\rho_H$ , vs. temperature,  $T$ , measured on two single crystals with  $i \perp c$ -axis in a magnetic field of 2 T applied parallel to the easy magnetization  $c$ -axis [92SKB]. Note quantitative differences in  $\rho_H(T)$  for the two samples below 100 K which are related to some structural properties (for discussion see the original paper). **(b)** Hall effect,  $R_H = \rho_H/B$ , derived from the data shown in panel (a), vs. longitudinal molar magnetic susceptibility,  $\chi_{||}$ , as shown in Fig. 161, in the temperature range 150...300 K [92SKB].

The solid line is a fit of the data to the relation  $\rho(B, T) = R_0 B + 4\pi R_s M(B, T)$ , which assumes that the normal,  $R_0$ , and spontaneous,  $R_s$ , Hall coefficients are temperature independent in the paramagnetic region. The least-squares fit gives:  $R_0 = 0.56 \cdot 10^{-3} \text{ cm}^3/\text{As}$  and  $R_s = 0.036 \text{ cm}^3/\text{As}$ . Note that a positive ordinary Hall effect is quite unique in uranium compounds. The concentration of free carriers estimated from  $R_0$  within a single parabolic band model amounts to 0.7 holes per uranium atom.

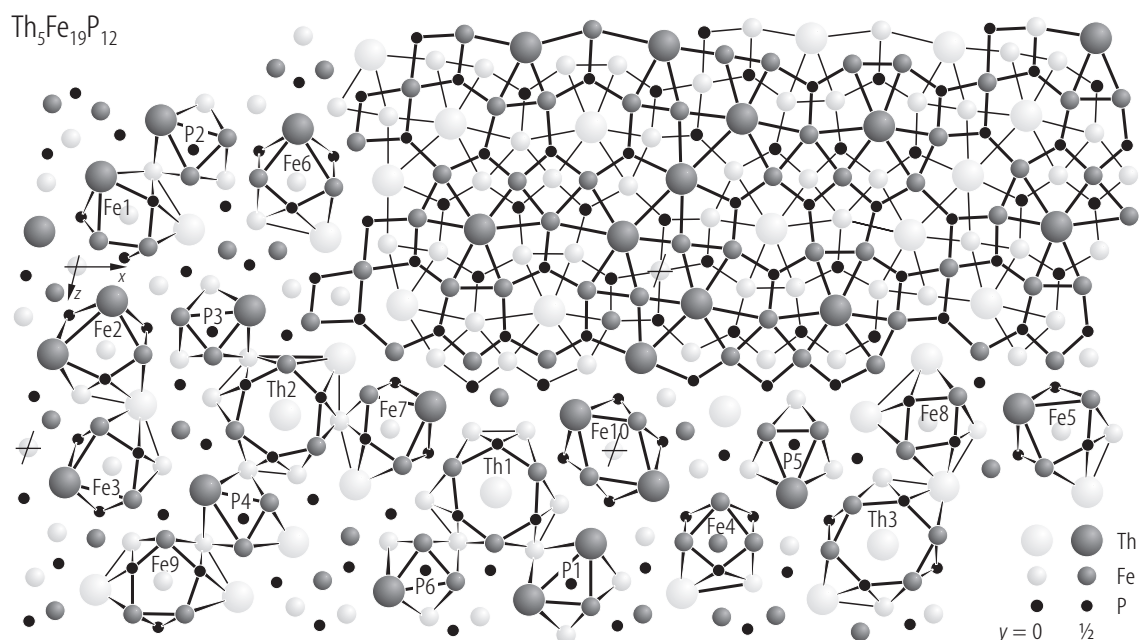


**Fig. 166.**  $\text{Th}_5\text{Fe}_{19}\text{P}_{12}$ . Crystal structure and coordination polyhedra [92AJ1]. All the atoms are situated on mirror planes perpendicular to the projection direction. The thin and thick lines connect the atoms having the positional parameter  $y = 0$  and  $1/2$ , respectively.

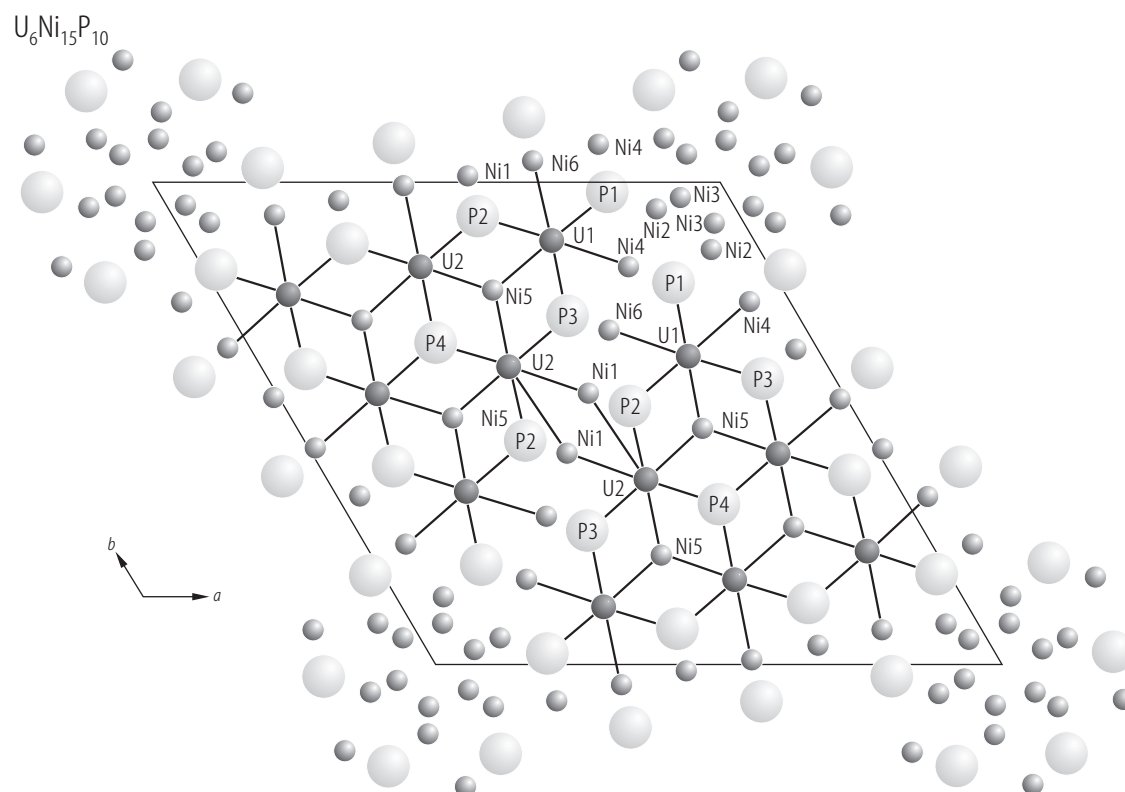
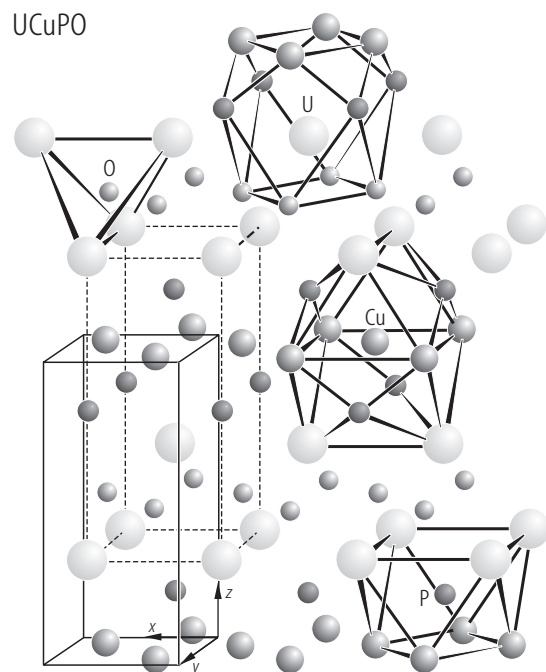


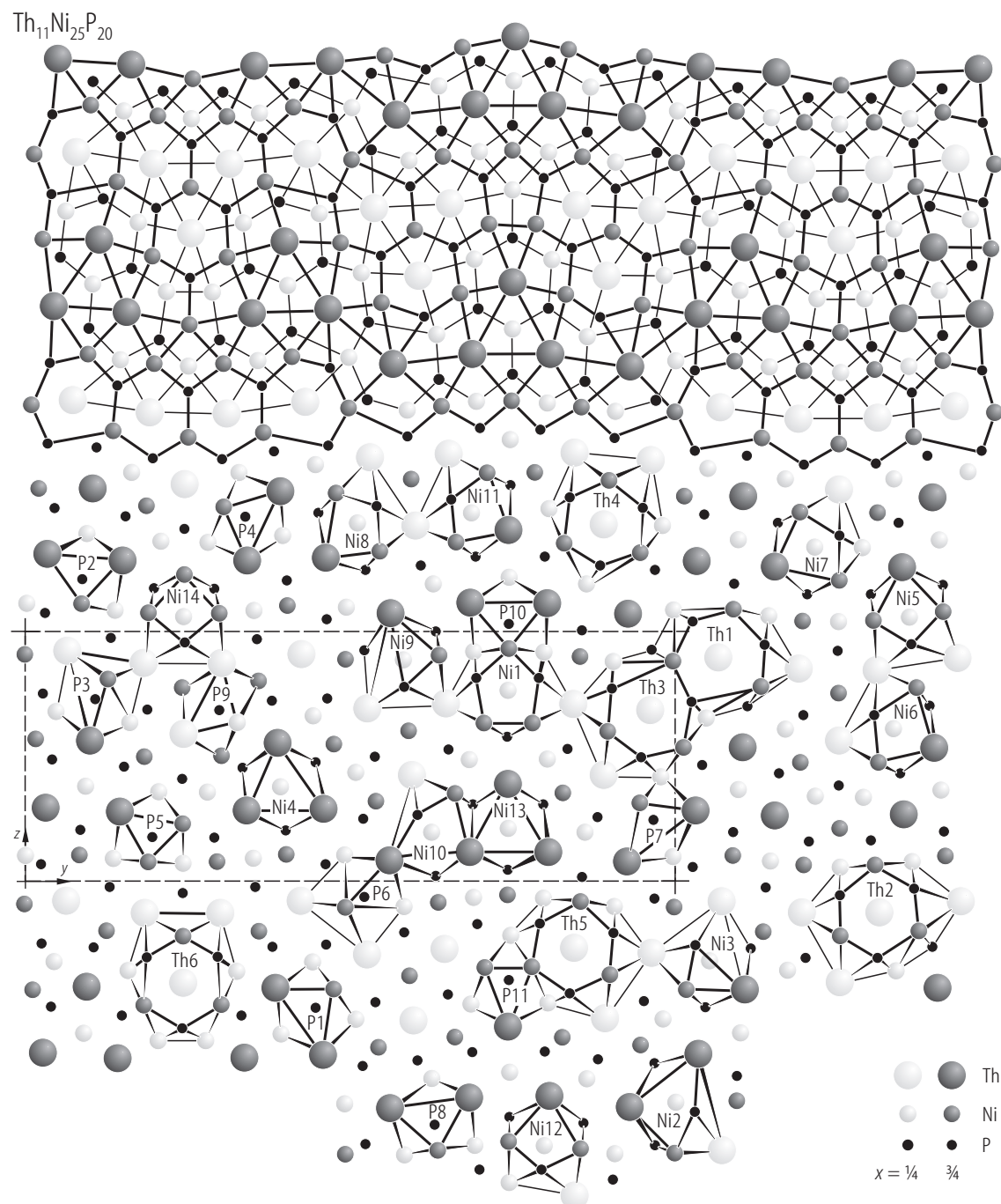
**Fig. 167.**  $U_6Ni_{15}P_{10}$ . Crystal structure projected onto the (001) plane [02KPN]. Dark gray circles: U (two nonequivalent sites); small gray circles: Ni (six sites); large light gray circles: P (four sites). Ni(2) and Ni(3) sites have partial occupancy (77% and 23%, respectively)..



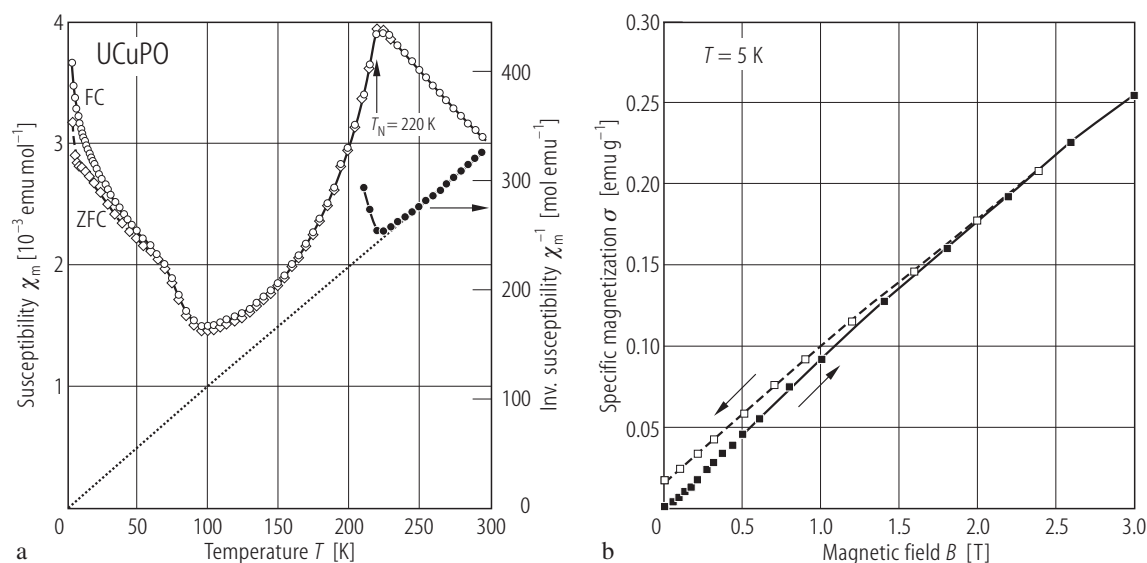
For Fig. 168 see next page

**Fig. 169.**  $UCuPO$ . Crystal structure and coordination polyhedra [94KANJ]. The solid and dashed lines outline the unit cell with two different settings.



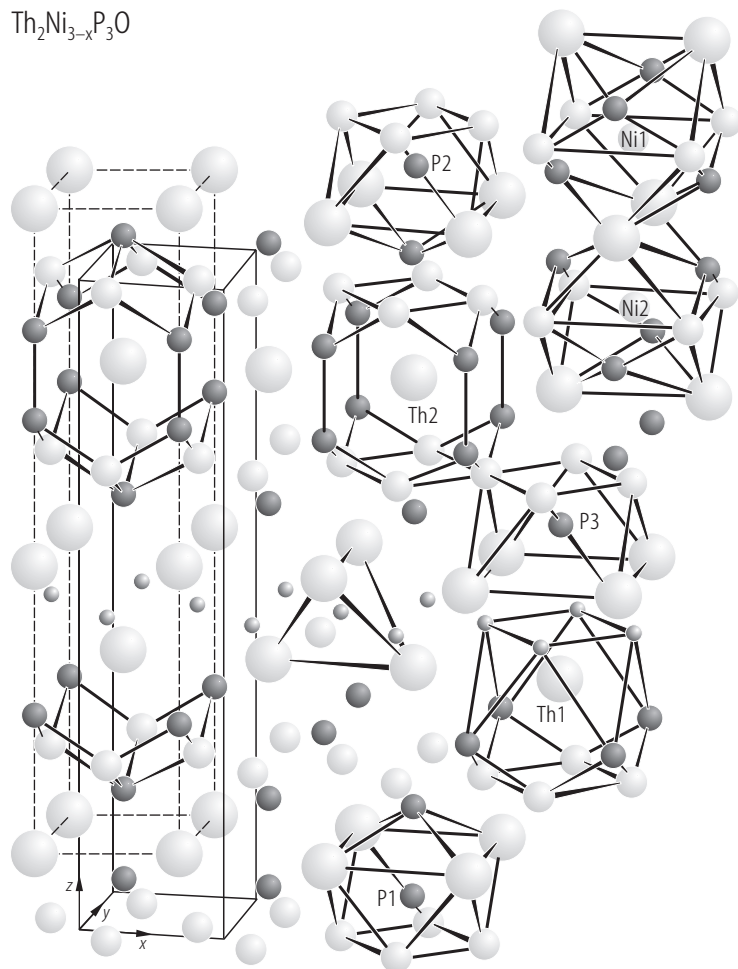
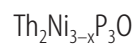


**Fig. 168.**  $\text{Th}_{11}\text{Ni}_{25}\text{P}_{20}$ . Crystal structure and coordination polyhedra [96AJ2]. Thin and thick lines connect atoms situated on mirror planes at  $x = 1/4$  and  $3/4$ , respectively.

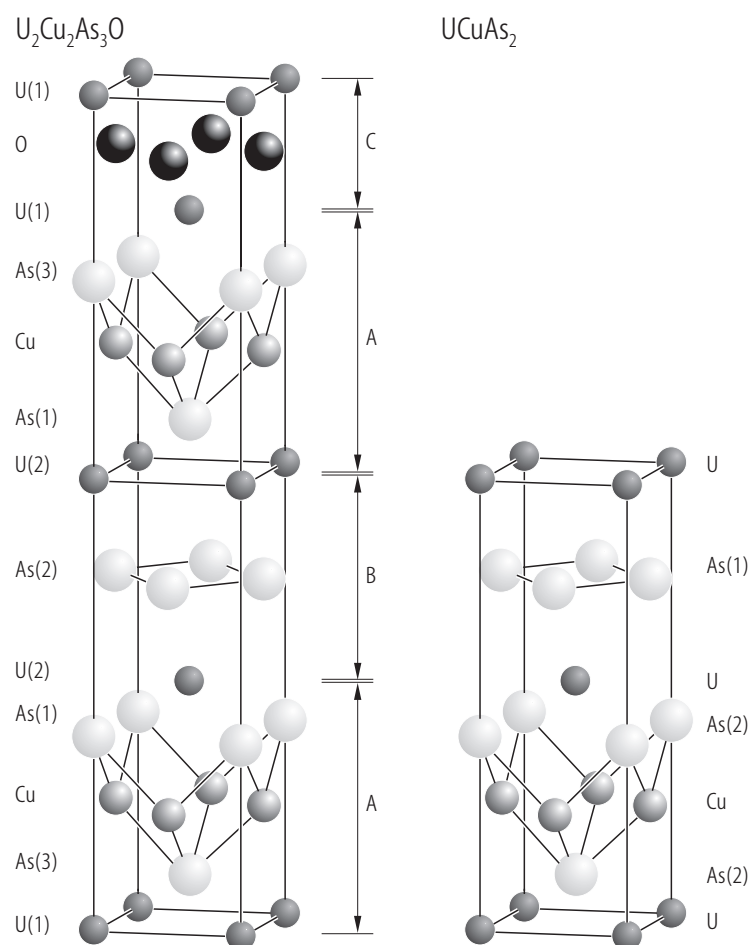


**Fig. 170.** UCuPO. **(a)** Molar magnetic susceptibility,  $\chi_m$ , (left-hand scale) and reciprocal molar magnetic susceptibility,  $\chi_m^{-1}$ , (right-hand scale) vs. temperature,  $T$  [94KANJ]. The arrow marks an antiferromagnetic phase transition at 220 K. The dotted line is a Curie-Weiss fit with the parameters given in Table B. In the ordered region the susceptibility was measured with cooling the sample with (FC, circles) and without (ZFC, diamonds) an applied magnetic field of 0.5 T. Note a strong rise in  $\chi_m(T)$  below 80 K which may result from crystal field interactions (for

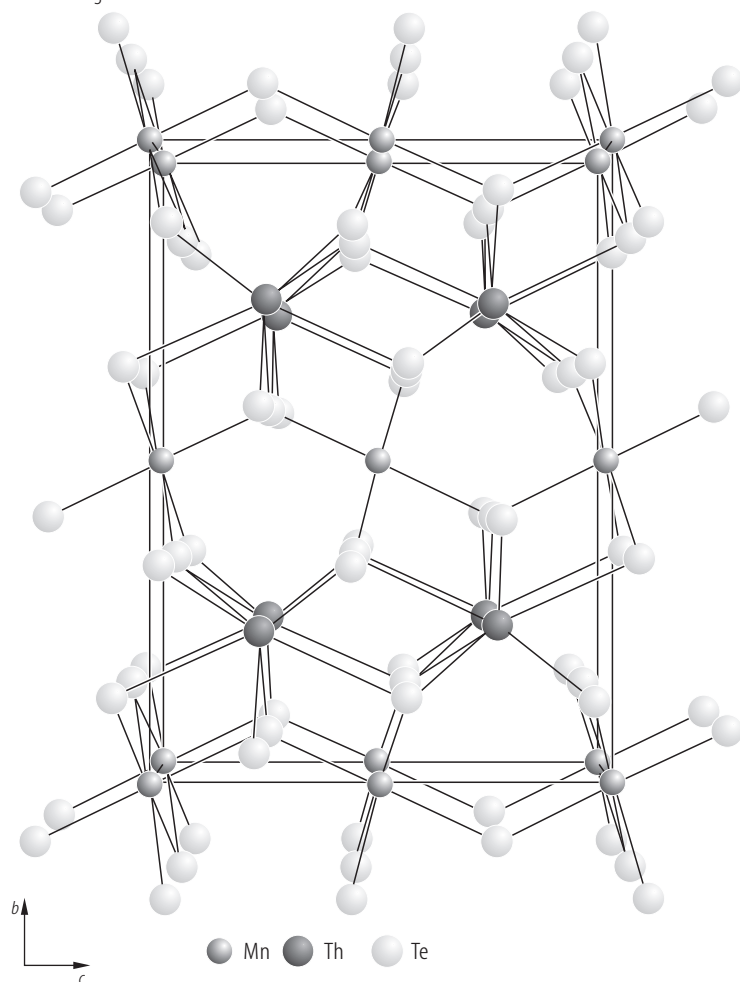
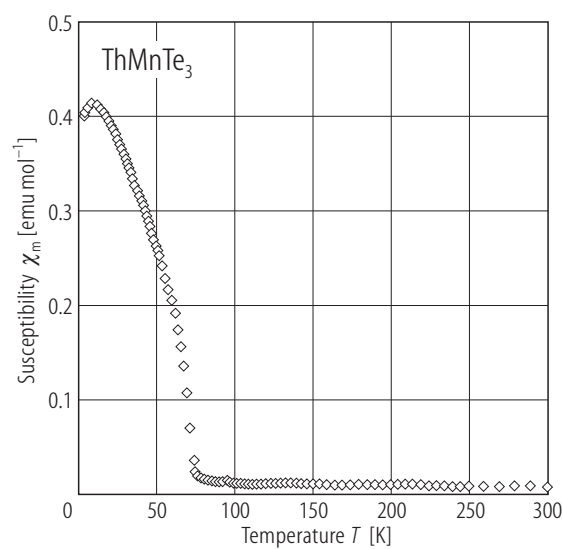
discussion see the original paper). The pronounced inflection around 75 K and the difference between the ZFC and FC curves were interpreted as being due to a tiny admixture of UCuP<sub>2</sub> that orders ferromagnetically at this temperature (see Fig. 19). **(b)** Specific magnetization,  $\sigma$ , vs. magnetic field,  $B$ , taken at 5 K with increasing (filled squares) and decreasing (open squares) magnetic field [94KANJ]. The small hysteresis results probably from an admixture of 0.1 % of ferromagnetic UCuP<sub>2</sub>.

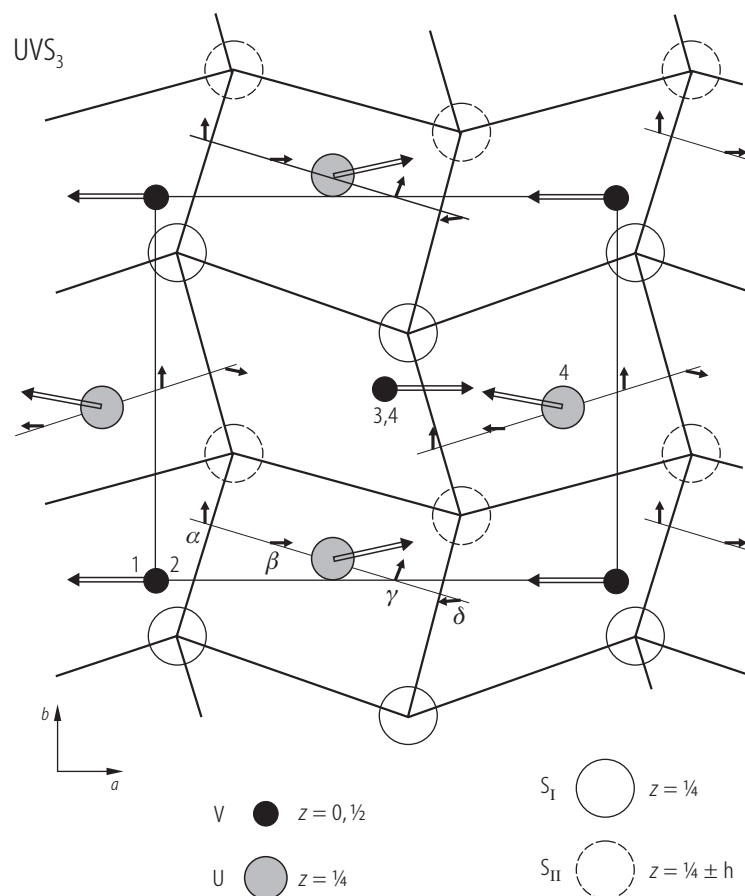


**Fig. 171.**  $\text{Th}_2\text{Ni}_{3-x}\text{P}_3\text{O}$ . Crystal structure and coordination polyhedra [96AJ1]. The refinement from the single-crystal X-ray data revealed significant deviation from the ideal value of the occupancy parameters for the Ni sites yielding the exact composition  $\text{Th}_2\text{Ni}_{2.45(1)}\text{P}_3\text{O}$ . The solid and dashed lines outline the unit cell with different settings of the origin.

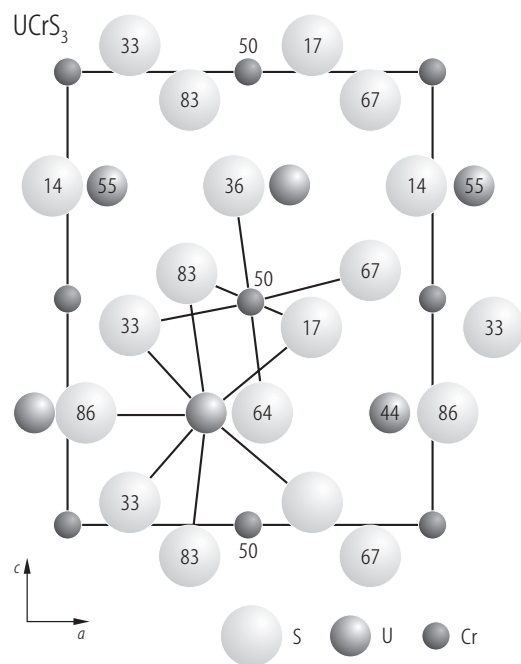


**Fig. 172.**  $U_2Cu_2As_3O$ . Crystal structure compared to that of  $UCuAs_2$  [94KPN]. Thin solid lines show a pyramidal arrangement of Cu, As(1) and As(3) atoms and a planar arrangement of As(2) atoms. Letters A, B and C denote characteristic blocks in the structures of both compounds.

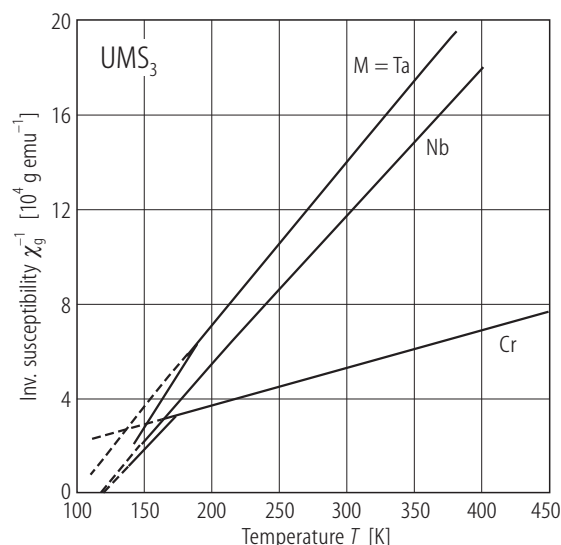
ThMnTe<sub>3</sub>**Fig. 173.** ThMnTe<sub>3</sub>. Crystal structure viewed along the [100] axis [00NI].**Fig. 174.** ThMnTe<sub>3</sub>. Molar magnetic susceptibility,  $\chi_m$ , vs. temperature,  $T$  [00NI]. The compound orders ferromagnetically at about 70 K due to the magnetic moments carried by Mn<sup>2+</sup> ions. Above 210 K the susceptibility follows a Curie-Weiss behaviour with the parameters given in Table B.



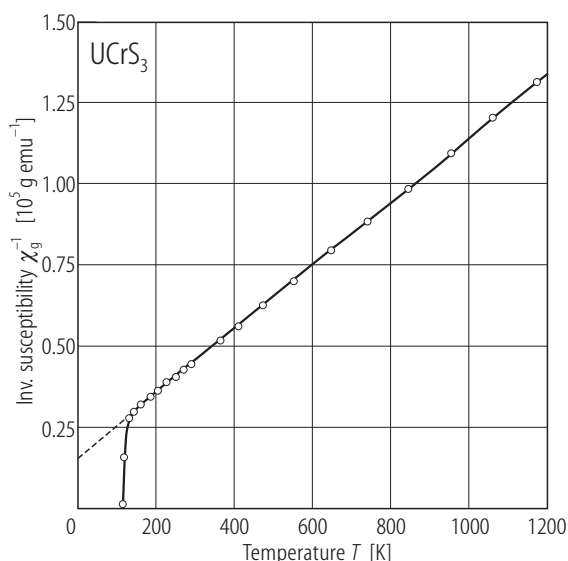
**Fig. 175.** UVS<sub>3</sub>. Magnetic structure projected on the *ab* plane [77WF]. The numbers label U and V atoms at different sites. There are magnetic moments localized on the U and V sites and additional moments (denoted as  $\alpha$ ,  $\beta$ ,  $\gamma$  and  $\delta$ ) located more than 2 Å away from any atom along the US<sub>6</sub> prism axis, which can be attributed to an extended 6d<sub>2</sub><sup>2</sup> orbital of uranium. The components of magnetic moments:  $p(U) = (2.1, 0.5, 0) \mu_B$ ,  $p(V) = (-2.1, 0, 0) \mu_B$ ,  $p_\alpha = (0, 0.3, 0) \mu_B$ ,  $p_\beta = (0.3, 0, 0) \mu_B$ ,  $p_\gamma = (0.1, 0, 0) \mu_B$ ,  $p_\delta = (-0.1, 0, 0) \mu_B$ . Similar magnetic structure was also found for UCrSe<sub>3</sub> and UCrS<sub>3</sub>. In UCrSe<sub>3</sub> the components are as follows:  $p(U) = (2.3, 0.8, -1.4) \mu_B$ ,  $p(Cr) = (-2.1, -1.7, 0.5) \mu_B$ ,  $p_\alpha = (0, 0.4, -0.5) \mu_B$ ,  $p_\beta = (0, 0.1, 0) \mu_B$ ,  $p_\gamma = (-0.1, 0, 0) \mu_B$ ,  $p_\delta = (0.2, 0.2, -0.3) \mu_B$ . For the components in UCrS<sub>3</sub> see the caption of Fig. 181.



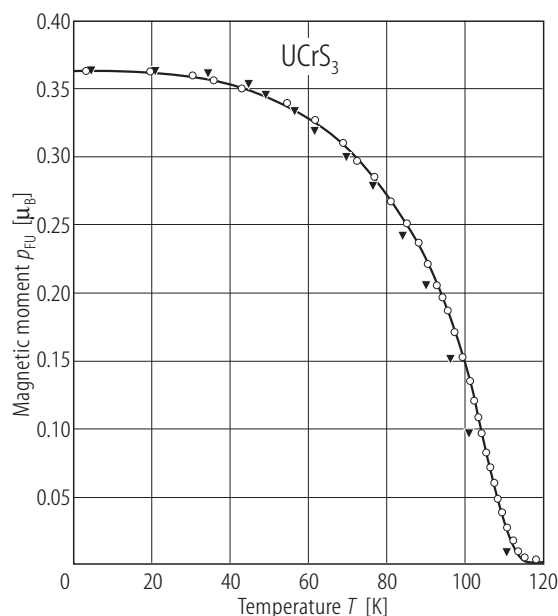
**Fig. 176.** UCrS<sub>3</sub>. Crystal structure projected on the (010) plane [75NPP2]. The numbers are the positions  $y \cdot 100$  of the relevant atoms.



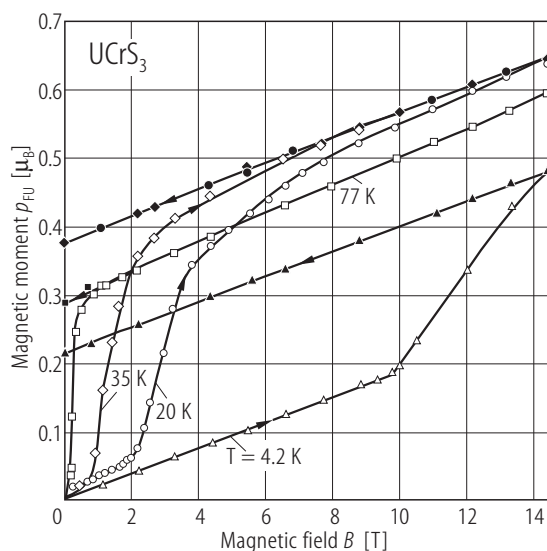
**Fig. 177.**  $\text{UMS}_3$ ,  $M = \text{Ta}, \text{Nb}, \text{Cr}$ . Reciprocal mass magnetic susceptibility,  $\chi_g^{-1}$ , vs. temperature,  $T$ , in the paramagnetic region up to 450 K [85NCKS]. The dashed lines are Curie-Weiss fits with the parameters given in Table B.



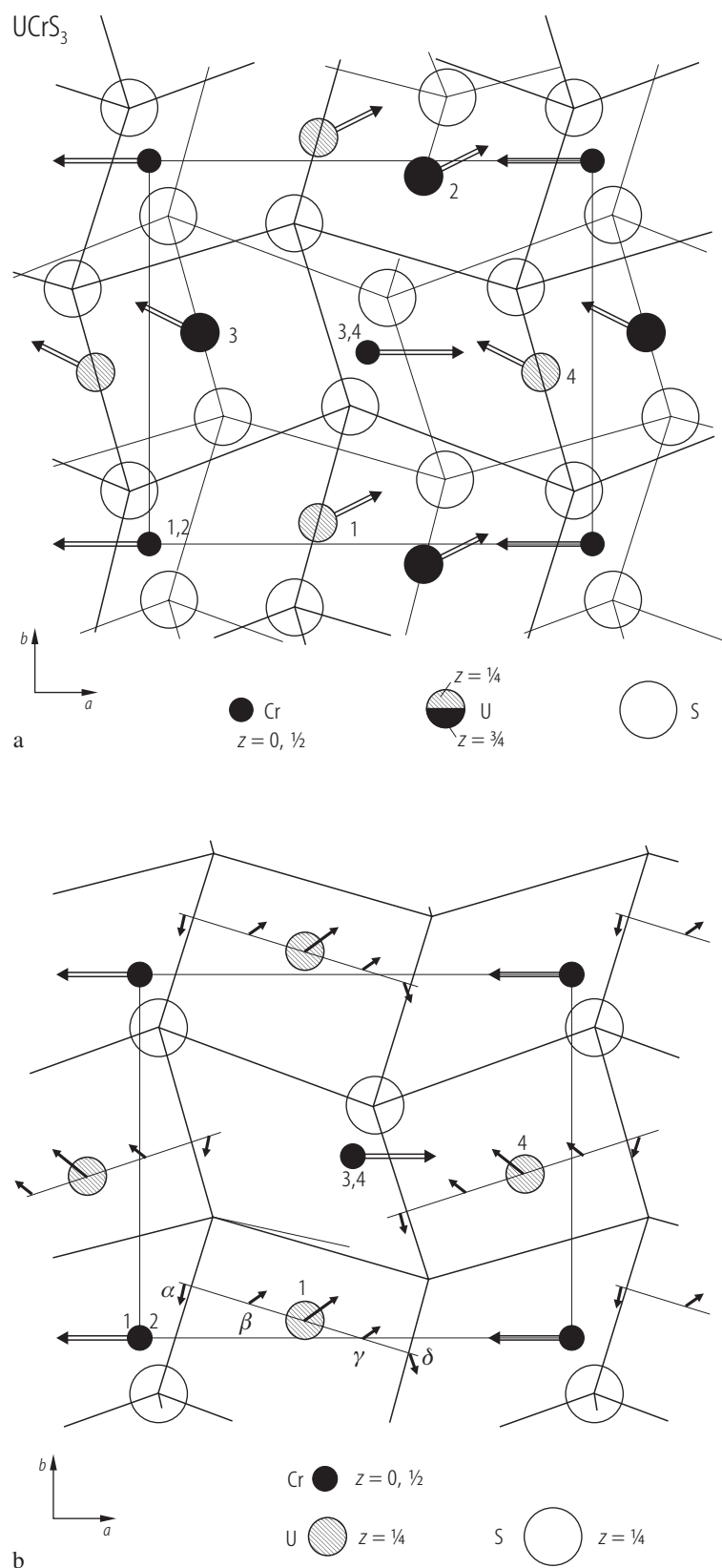
**Fig. 178.**  $\text{UCrS}_3$ . Reciprocal mass magnetic susceptibility,  $\chi_g^{-1}$ , vs. temperature,  $T$ , in the paramagnetic region up to 1200 K [76WFBN]. The dashed line marks a Curie-Weiss fit with the parameters given in Table B. The compound orders ferromagnetically at  $T_C = 110$  K.



**Fig. 179.**  $\text{UCrS}_3$ . Magnetic moment,  $p_{\text{FU}}$ , vs. temperature,  $T$ , measured in a magnetic field of 0.05 T (triangles) on cooling the specimen and remanent magnetic moment,  $p_{\text{FU}}^{\text{R}}$ , vs.  $T$  (circles) [76WFBN]. The compound is ferromagnetic below  $T_C = 110$  K. At 4.2 K the magnetic moment is  $0.36 \mu_B/\text{f.u.}$

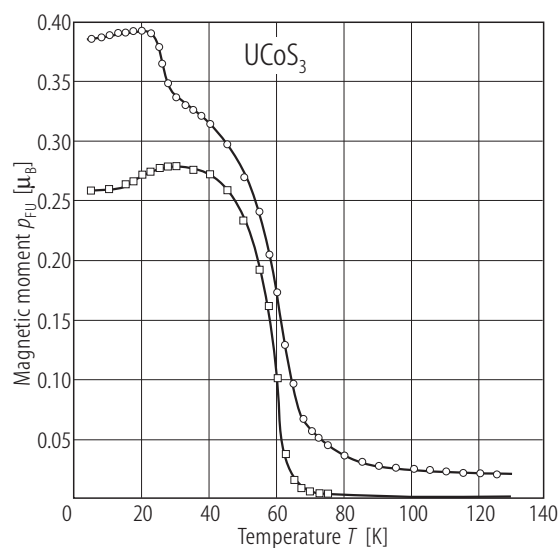


**Fig. 180.**  $\text{UCrS}_3$ . Magnetic moment,  $p_{\text{FU}}$ , vs. magnetic field,  $B$ , measured at several different temperatures [76WFBN]. Triangles:  $T = 4.2$  K; circles:  $T = 20$  K; diamonds:  $T = 35$  K; squares:  $T = 77$  K. Open and filled symbols correspond to the data taken with increasing and decreasing field, respectively. Note a large magnetocrystalline anisotropy, which manifests itself at 4.2 and 20 K as pronounced reversible linear increase of the initial magnetization. A large constant susceptibility superimposed on  $p_{\text{FU}}(B)$  in strong magnetic fields indicates the presence of an antiferromagnetic component (see Fig. 181).

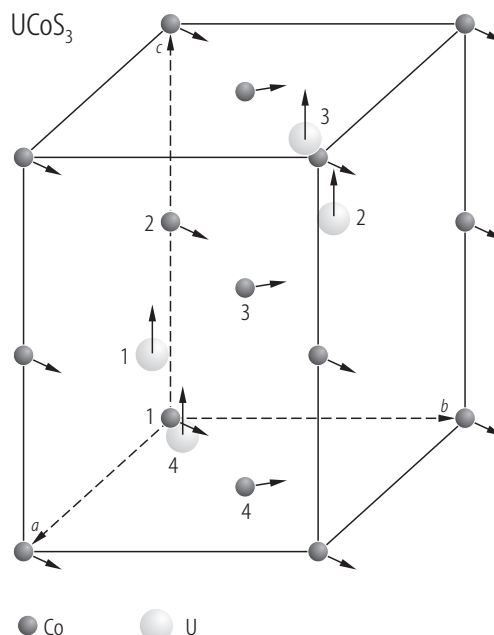


**Fig. 181.** UCrS<sub>3</sub>. Magnetic structure, projected on the  $(a,b)$  plane [76WFBN]. The numbers label U and Cr atoms at different sites. Both uranium and chromium atoms contribute to the magnetism. **(a)** Localized model. The Cr moments form a collinear antiferromagnetic structure along the  $a$ -axis, while the U moments are arranged in a canted antiferromagnetic manner in the  $(a,b)$  plane. At 60 K:  $p(\text{Cr}) = (-2.08, 0, 0) \mu_{\text{B}}$ ,  $p(\text{U}) = (1.41, 0.68, 0) \mu_{\text{B}}$ . **(b)** Delocalised model. The Cr moments are arranged as in the localized model, whereas the U moments are strongly delocalised and besides the 5f-component at the U atom site there are some additional moments in the  $(a,b)$  plane, denoted as  $\alpha$ ,  $\beta$ ,  $\gamma$  and  $\delta$ , which can be attributed to extended  $6d_{5/2}^2$  orbitals of the uranium atoms. At 60 K:  $p(\text{Cr}) = (-2.10, 0, 0) \mu_{\text{B}}$ ,  $p(\text{U}) = (0.80, 0.60, 0) \mu_{\text{B}}$ ,  $p_{\alpha} = (-0.14, -0.54, 0) \mu_{\text{B}}$ ,  $p_{\beta} = (0.32, 0.24, 0) \mu_{\text{B}}$ ,  $p_{\gamma} = (0.38, 0.29, 0) \mu_{\text{B}}$ ,  $p_{\delta} = (0.07, -0.13, 0) \mu_{\text{B}}$ . At 4.2 K:  $p(\text{Cr}) = (-2.42, 0, 0) \mu_{\text{B}}$ ,  $p(\text{U}) = (0.86, 0.71, 0) \mu_{\text{B}}$ ,  $p_{\alpha} = (-0.08, -0.50, 0) \mu_{\text{B}}$ ,  $p_{\beta} = (0.46, 0.37, 0) \mu_{\text{B}}$ ,  $p_{\gamma} = (0.46, 0.37, 0) \mu_{\text{B}}$ ,  $p_{\delta} = (0.21, -0.03, 0) \mu_{\text{B}}$ . Note that with decreasing temperature the U moments become more delocalised.

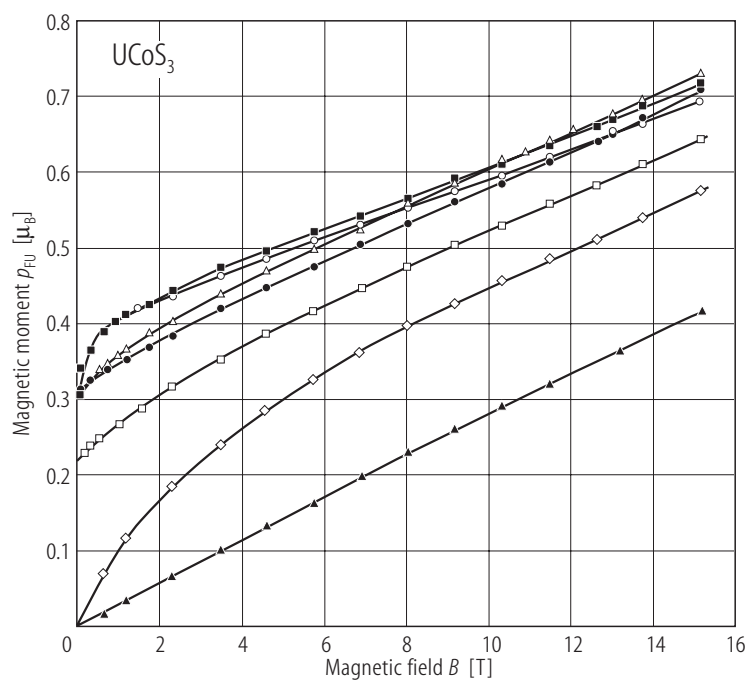




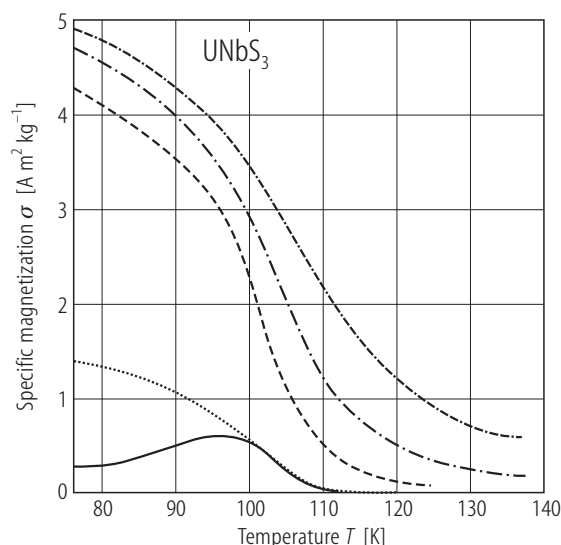
**Fig. 182.**  $\text{UCoS}_3$ . Magnetic moment,  $p_{\text{FU}}$ , vs. temperature,  $T$ , measured in a field of 0.05 T (squares) and 10 T (circles) [81CWBN]. The compound orders ferromagnetically at  $T_C = 60$  K. At 4.2 K the magnetic moment is  $0.4 \mu_B/\text{f.u.}$



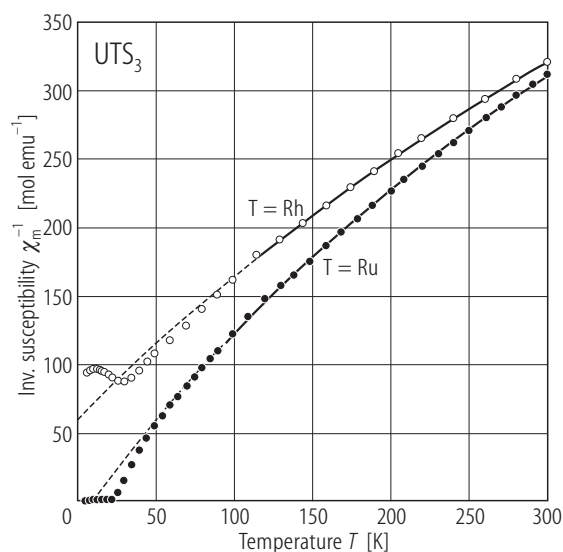
**Fig. 184.**  $\text{UCoS}_3$ . Magnetic structure [81CWBN]. The U moments form a collinear ferromagnetic structure along the  $c$ -axis, while the Co atoms are arranged in a canted antiferromagnetic manner in the  $(a,b)$  plane. The numbers denote different magnetic sublattices.



**Fig. 183.**  $\text{UCoS}_3$ . Magnetic moment,  $p_{\text{FU}}$ , vs. magnetic field,  $B$ , measured at several different temperatures [81CWBN]. Open circles:  $T = 4.2$  K; full squares:  $T = 20$  K; open triangles:  $T = 30$  K; full circles:  $T = 40$  K; open squares:  $T = 55$  K; open diamonds:  $T = 65$  K; full triangles:  $T = 88$  K. Note a large constant susceptibility superimposed on  $p_{\text{FU}}(B)$  in strong magnetic fields, which indicates the presence of a non-compensated antiferromagnetic component (see Fig. 184).

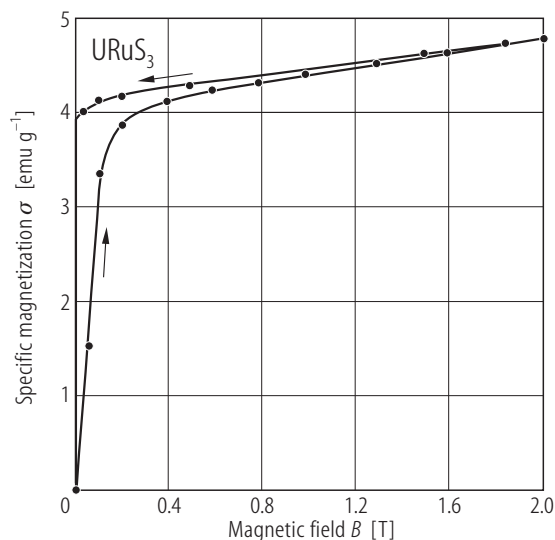


**Fig. 185.**  $\text{UNbS}_3$ . Specific magnetization,  $\sigma$ , vs. temperature,  $T$ , measured on cooling in a magnetic field of 0.06 (dotted curve), 0.15 (dashed curve), 0.34 (dash-dotted curve), and 0.87 T (dash-dash-dotted curve) [85NCKS]. The solid curve corresponds to the data obtained on heating in a field of 0.06 T, upon cooling the sample in zero field (ZFC). The compound orders ferromagnetically at  $T_C = 107$  K. A characteristic maximum in  $\sigma(T)$  obtained in the ZFC regime is due to strong magnetic anisotropy (domain effect).

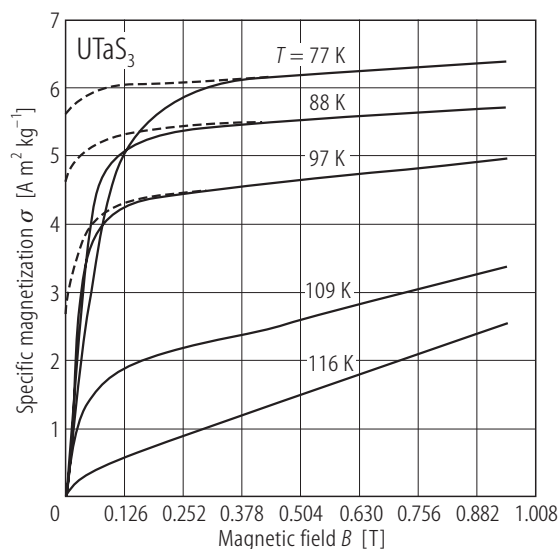


**Fig. 186.**  $\text{UTS}_3$ ,  $T = \text{Ru, Rh}$ . Reciprocal molar magnetic susceptibility,  $\chi_m^{-1}$ , vs. temperature,  $T$  [87DN]. Filled circles:  $T = \text{Ru}$ ; open circles:  $T = \text{Rh}$ . The dashed lines denote a modified Curie-Weiss fits with the parameters given in Table B.  $\text{URuS}_3$  orders ferromagnetically at  $T_C = 26$  K (see also Fig. 187).  $\text{URhS}_3$  orders antiferromagnetically at  $T_N = 30$  K.

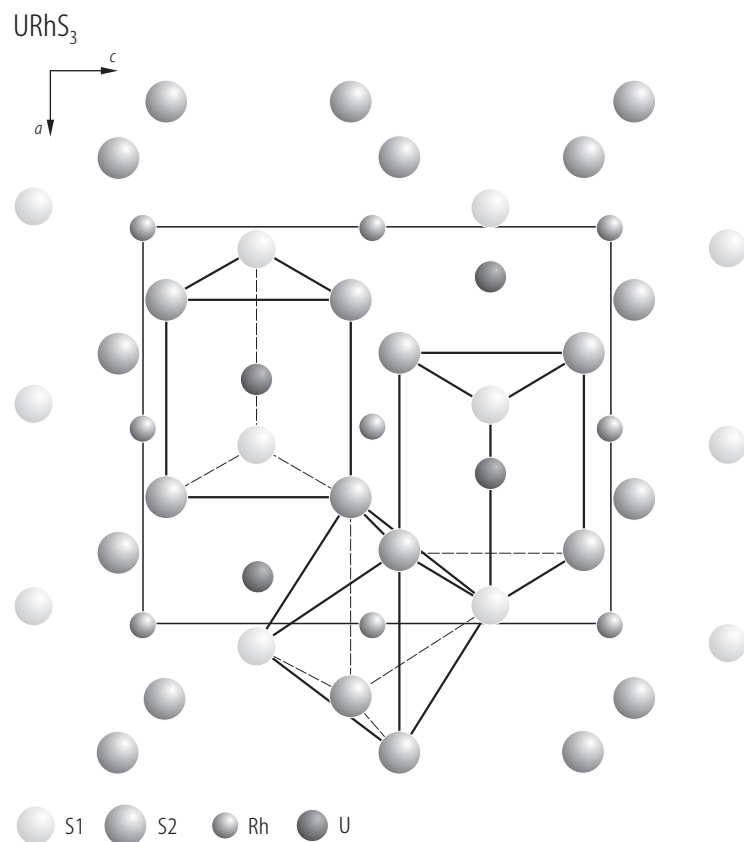
For Fig. 188 see next page



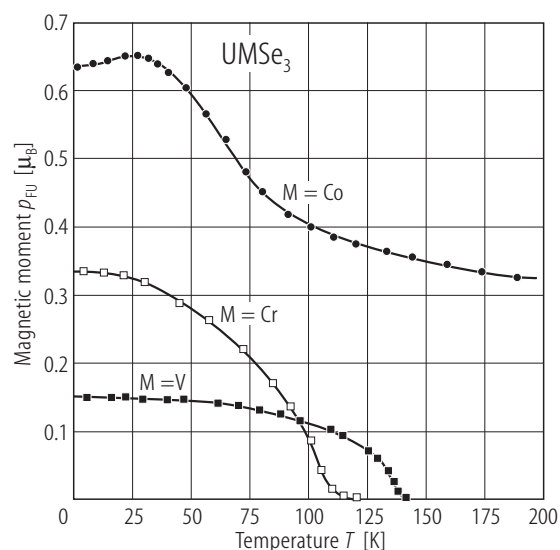
**Fig. 187.**  $\text{URuS}_3$ . Specific magnetization,  $\sigma$ , vs. magnetic field,  $B$ , taken at 5 K [87DN]. The arrows indicate measurements taken with increasing and decreasing field. At 2 T  $\sigma_0$  is only  $0.31 \mu_B$ , suggesting a canted structure of the uranium magnetic moments, like in  $\text{UCrS}_3$  [76WFBN] (compare Fig. 180).



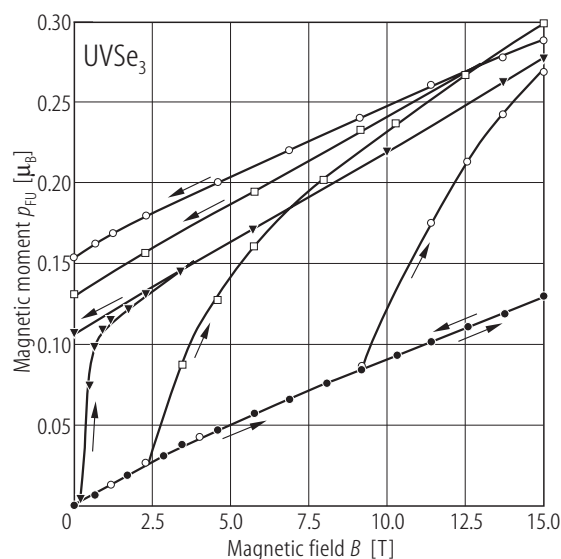
**Fig. 189.**  $\text{UTaS}_3$ . Specific magnetization,  $\sigma$ , vs. magnetic field,  $B$ , measured at various temperatures specified in the figure [85NCKS]. The solid and dashed lines denote the data taken with increasing and decreasing magnetic field, respectively. The compound is ferromagnetic below  $T_C = 113$  K. See also Table B.



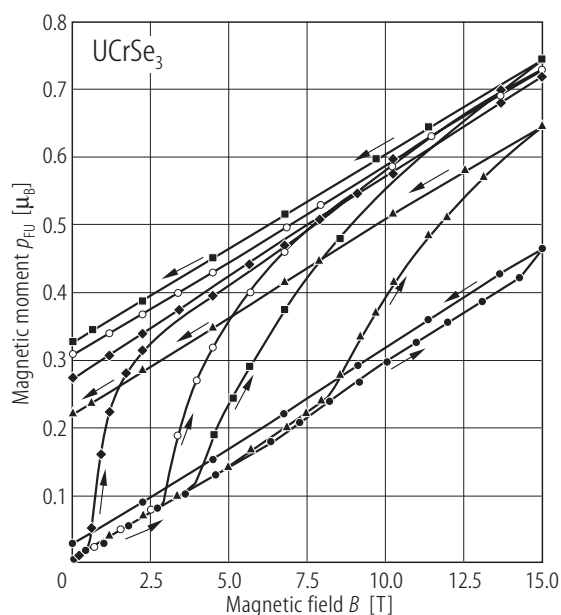
**Fig. 188.** URhS<sub>3</sub>. Crystal structure projected on the (*a*,*c*) plane [87DN].



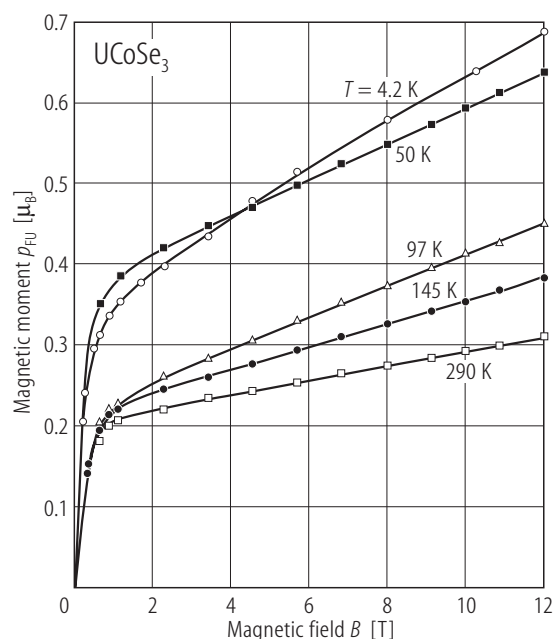
**Fig. 190.** UMSe<sub>3</sub>, M = V, Cr, Co. Magnetic moment,  $p_{\text{FU}}$ , vs. temperature,  $T$ , taken in a magnetic field of 0.05 T (squares) or 10 T (circles) [77NWF]. The solid lines serve as guides for the eye. USe<sub>3</sub> and UCrSe<sub>3</sub> are weak ferromagnets below  $T_C$  of 140 and 110 K, respectively (see also Figs. 191 and 192). Also UCoSe<sub>3</sub> orders ferromagnetically but with a very high Curie temperature  $700 < T_C < 1100$  K (sample dependent). For this compound note an anomalous behaviour of  $p_{\text{FU}}(T)$  below 30 K, which may indicate changes in the magnetic structure, similar to those observed in U<sub>2</sub>FeS<sub>5</sub> (compare Fig. 201).



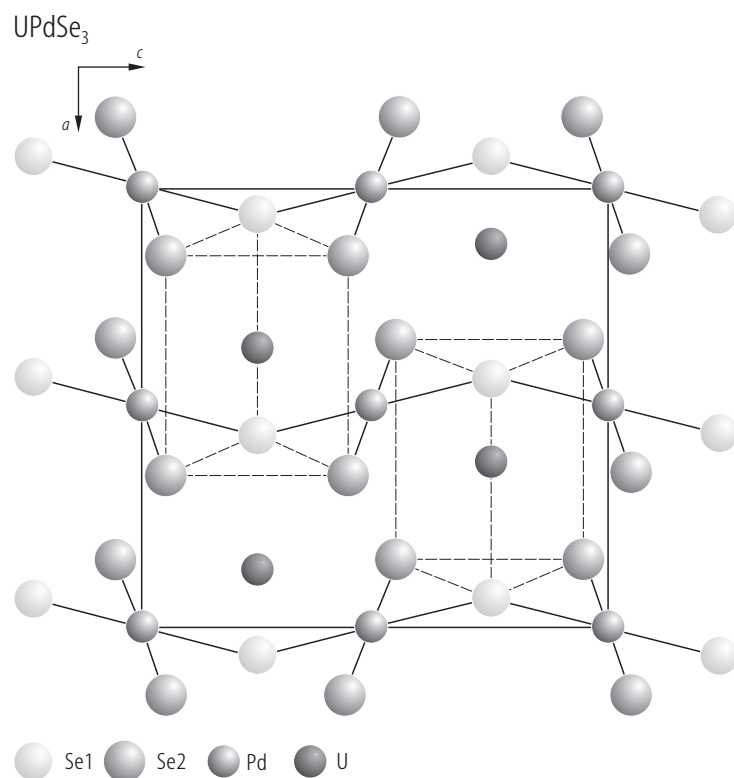
**Fig. 191.**  $\text{UVSe}_3$ . Magnetic moment,  $p_{\text{FU}}$ , vs. magnetic field,  $B$ , up to 15 T, measured at several different temperatures [77NWF]. Full circles:  $T = 4.2\text{--}20$  K; open circles:  $T = 44$  K; open squares:  $T = 67$  K; full triangles:  $T = 107$  K. The arrows denote measurements done with increasing and decreasing magnetic field. The compound orders ferromagnetically at 140 K (see also Fig. 190). Large, nearly temperature independent, superimposed constant susceptibility, seen at high fields, the authors interpreted as a sign of canted magnetic structure. Note extremely high values of the threshold field (larger than 15 T below 20 K) for the appearance of irreversible ferromagnetic component. This feature is characteristic of systems with large magnetocrystalline anisotropy, resulting in the formation of narrow Bloch walls.



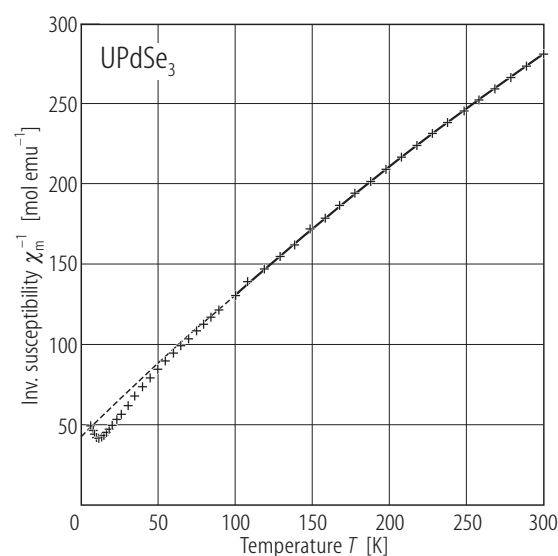
**Fig. 192.**  $\text{UCrSe}_3$ . Magnetic moment,  $p_{\text{FU}}$ , vs. magnetic field,  $B$ , up to 15 T, measured at several different temperatures [77NWF]. Full circles:  $T = 4.2$  K; full triangles:  $T = 8$  K; full squares:  $T = 15$  K; open circles:  $T = 20$  K; full diamonds:  $T = 60$  K. The arrows denote measurements done with increasing and decreasing magnetic field. The compound orders ferromagnetically at 110 K (see also Fig. 190). Large, nearly temperature independent, superimposed constant susceptibility, seen at high fields, the authors interpreted as a sign of canted magnetic structure. Note extremely high values of the threshold field (14 T at 4.2 K) for the appearance of irreversible ferromagnetic component. This feature is characteristic of systems with large magnetocrystalline anisotropy, resulting in the formation of narrow Bloch walls.



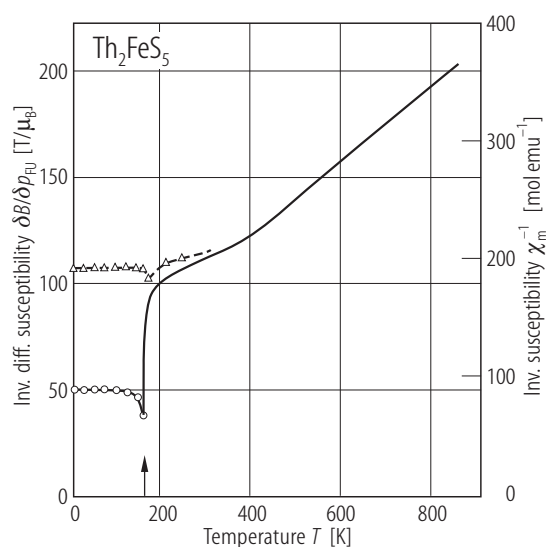
**Fig. 193.**  $\text{UCoSe}_3$ . Magnetic moment,  $p_{\text{FU}}$ , vs. magnetic field,  $B$ , up to 12 T, measured at different temperatures [77NWF]. Open circles:  $T = 4.2$  K; full squares:  $T = 50$  K; open triangles:  $T = 97$  K; full circles:  $T = 145$  K; open squares:  $T = 290$  K. The compound is in a ferromagnetic state at the highest temperature measured (see also Fig. 190). Note a superimposed constant susceptibility, which indicates the presence of a strong antiferromagnetic contribution.



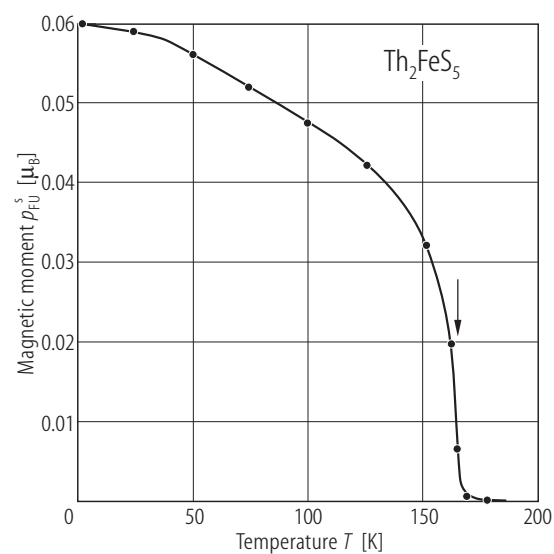
**Fig. 194.** UPdSe<sub>3</sub>. Crystal structure projected on the  $(a,c)$  plane [89DN].



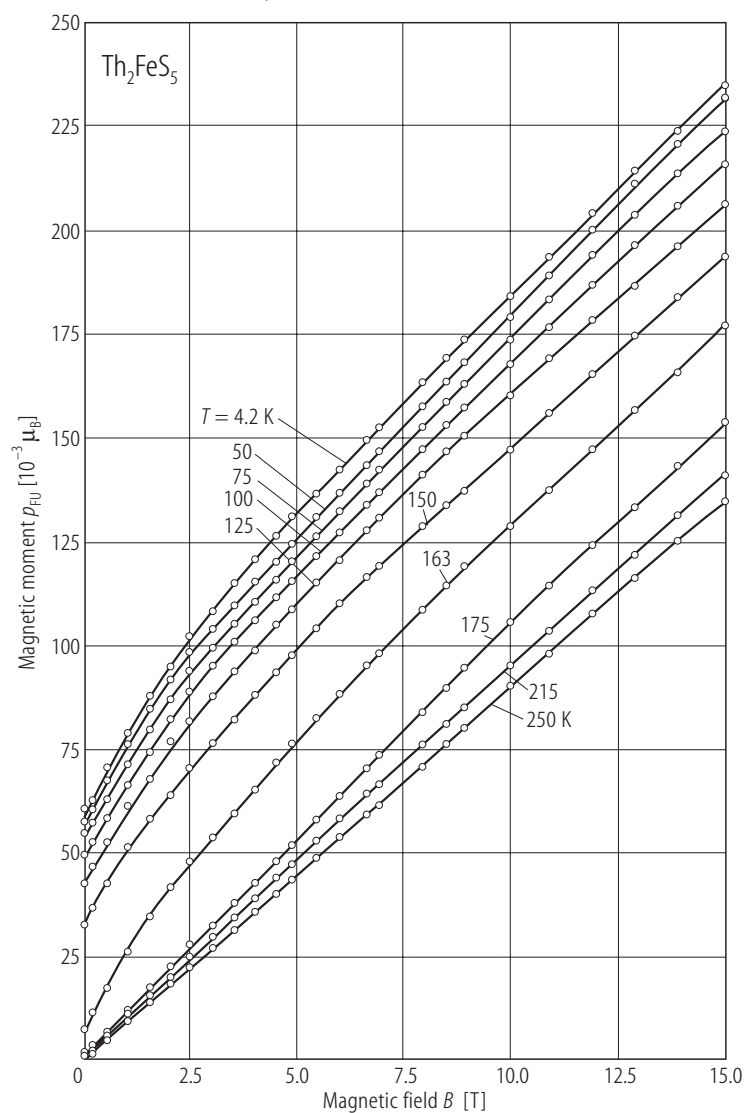
**Fig. 195.** UPdSe<sub>3</sub>. Reciprocal molar magnetic susceptibility,  $\chi_m^{-1}$ , vs. temperature,  $T$  [89DN]. The dashed line denotes a modified Curie-Weiss fit with the parameters given in Table B. The compound orders antiferromagnetically at  $T_N = 11$  K.



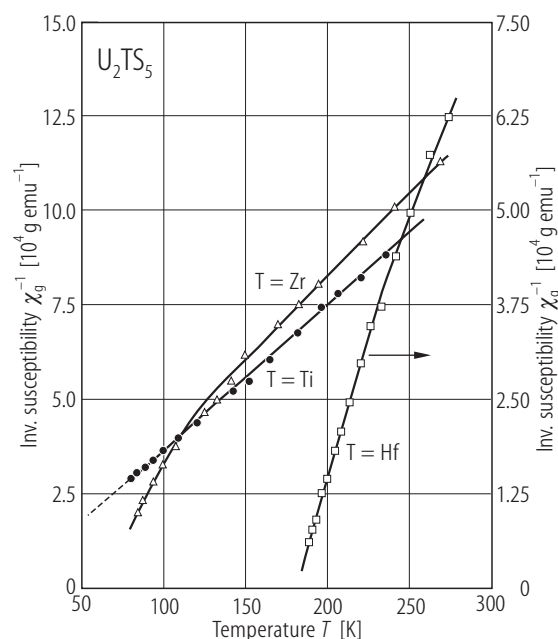
**Fig. 196.** Th<sub>2</sub>FeS<sub>5</sub>. Reciprocal molar magnetic susceptibility,  $\chi_m^{-1}$ , vs. temperature,  $T$ , up to 900 K, measured at 0.4 T (solid line, right-hand side scale) and reciprocal differential molar susceptibility,  $\delta B/\delta p_{FU}$ , vs.  $T$  (left-hand side scale) taken at 15 T (triangles) and 0.1 T (circles) [80BFNW]. Above 440 K a Curie-Weiss law is followed with the parameters:  $p_{\text{eff}} = 5 \mu_B$  and  $\Theta = -240$  K. Note a closeness of  $p_{\text{eff}}$  to the spin only Fe<sup>2+</sup> moment. The arrow marks a ferromagnetic phase transition at  $T_C = 163$  K.



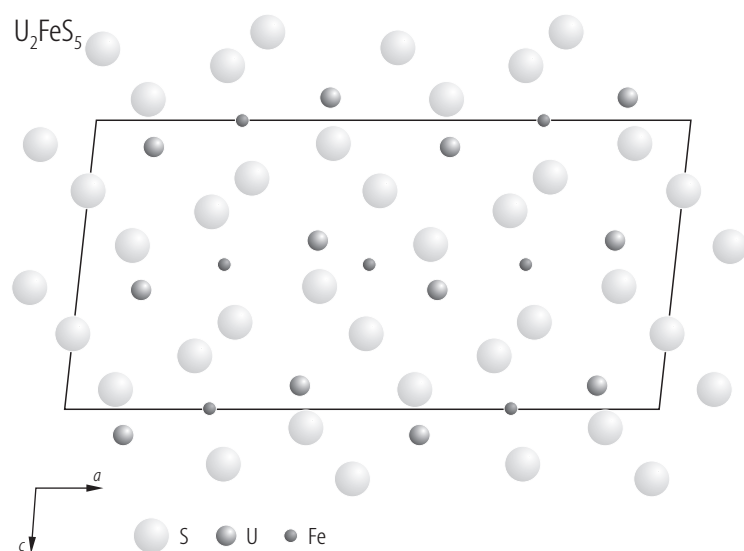
**Fig. 197.**  $\text{Th}_2\text{FeS}_5$ . Spontaneous magnetic moment,  $p_{\text{FU}}^s$ , vs. temperature,  $T$  [80BFNW]. The arrow marks a ferromagnetic phase transition at  $T_C = 163$  K.



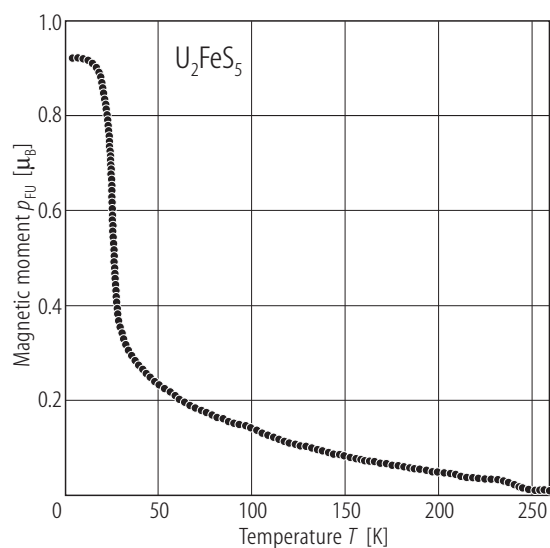
**Fig. 198.**  $\text{Th}_2\text{FeS}_5$ . Magnetic moment,  $p_{\text{FU}}$ , vs. field,  $B$ , taken at several different temperatures specified in the figure [80BFNW].



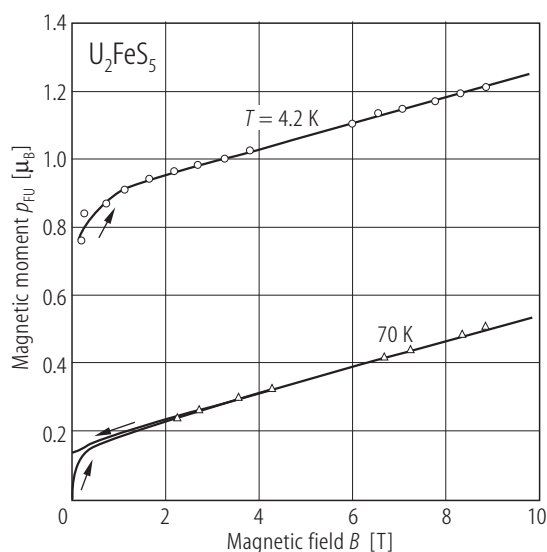
**Fig. 199.**  $U_2TS_5$ ,  $T = Ti, Zr, Hf$ . Reciprocal mass magnetic susceptibility,  $\chi_g^{-1}$ , vs. temperature,  $T$ , in the range 80... 280 K [84NCKS2]. Circles:  $U_2TiS_5$ ; triangles:  $U_2ZrS_5$ ; squares:  $U_2HfS_5$ . Note a different (right-hand side) vertical scale for  $U_2HfS_5$ . The solid lines serve as a guide for the eye.  $U_2TiS_5$  and  $U_2ZrS_5$  are paramagnetic down to 80 K. At high temperatures their susceptibility follows a Curie-Weiss law with the uranium effective magnetic moment of 2.70...2.80  $\mu_B$ . In the case of  $U_2ZrS_5$  some deviation of  $\chi_g^{-1}(T)$  from a straight-line behaviour is observed, which may suggest the occurrence of magnetic ordering at temperatures below 80 K.  $U_2HfS_5$  orders ferromagnetically at  $T_C = 180$  K (see Fig. 207). Its  $\chi_g^{-1}(T)$  exhibits a Curie-Weiss behaviour with the uranium effective magnetic moment of only 1.91  $\mu_B$ .



**Fig. 200.**  $U_2FeS_5$ . Crystal structure projected on the (010) plane [76NPP].

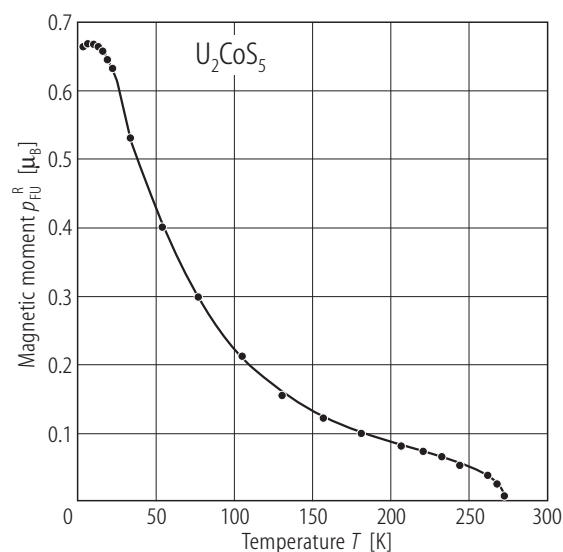


**Fig. 201.**  $\text{U}_2\text{FeS}_5$ . Magnetic moment,  $p_{\text{FU}}$ , vs. temperature,  $T$ , measured in a field of 0.57 T [77WB]. The compound exhibits a ferromagnetic-like order below  $T_C = 250$  K with a moment reorientation near 22 K. At 4.2 K the magnetic moment reaches a value of  $0.885 \mu_{\text{B}}/\text{f.u.}$  As found in neutron diffraction study [77WB], down to 25 K the Fe magnetic moments form a collinear antiferromagnetic structure along the  $b$ -axis. At 100 K the Fe moment is  $3.6 \mu_{\text{B}}$  and the U moment is  $0.13 \mu_{\text{B}}$ . The U-U exchange interaction is too weak to set ordering of the U moments. Between 25 and 18 K there occurs a rotation of the Fe moments while their antiferromagnetic arrangement is kept unaltered. At 12 K the Fe moments point along the  $[277]$  crystallographic direction and are equal to  $4.50 \mu_{\text{B}}$ . The U magnetic moments also increase with decreasing temperature and reach  $0.99 \mu_{\text{B}}$  at 4.2 K. Their arrangement gives a ferromagnetic component along the  $a$ -axis, and two different antiferromagnetic configurations along the other axes.



**Fig. 202.**  $\text{U}_2\text{FeS}_5$ . Magnetic moment,  $p_{\text{FU}}$ , vs. magnetic field,  $B$ , measured at  $T = 4.2$  K (circles) and  $T = 70$  K (triangles) with increasing and decreasing magnetic field (marked by the arrows) [77WB]. Note that  $p_{\text{FU}}(B)$  does not saturate in high fields and instead shows a large constant susceptibility superimposed, suggesting a non-compensated antiferromagnetic structure. See the description of the magnetic structure in the caption of Fig. 201.

**Fig. 203.**  $\text{U}_2\text{CoS}_5$ . Remanent magnetization,  $p_{\text{FU}}^{\text{R}}$ , vs. temperature,  $T$  [79WBFN]. The value of  $p_{\text{FU}}^{\text{R}}$ , measured at 4.2 K is  $0.65 \mu_{\text{B}}/\text{f.u.}$





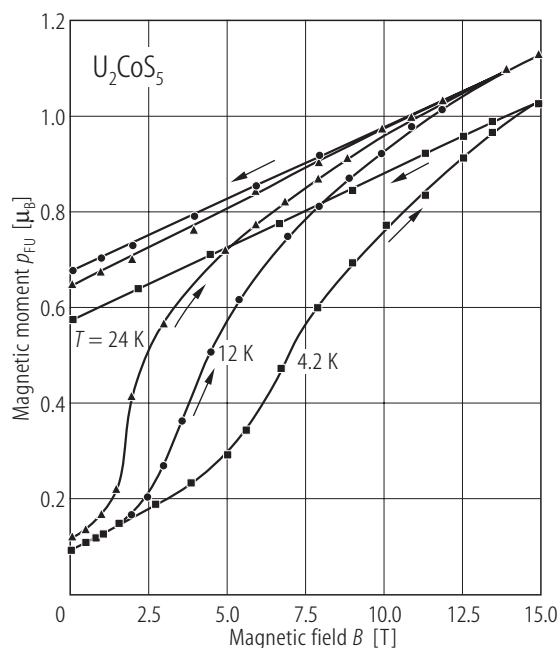
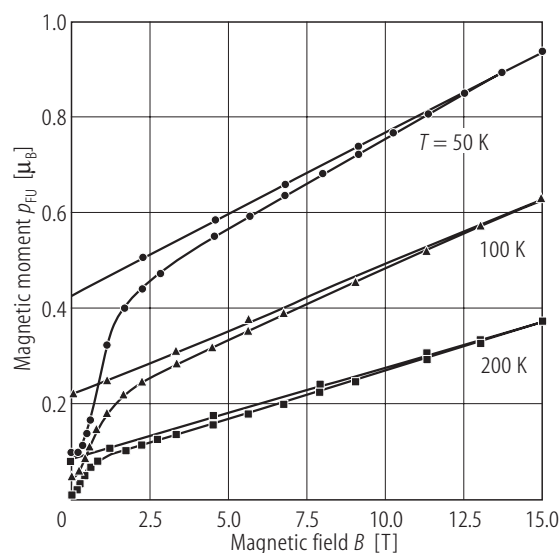


**Fig. 204.**  $\text{U}_2\text{CoS}_5$ . Magnetic moment,  $p_{\text{FU}}$ , vs. magnetic field,  $B$ , measured at several temperatures below  $T_C = 270$  K specified in the figure [79WBFN]. Note large critical fields for the irreversible rise of the magnetization, characteristic of systems with large magnetocrystalline



anisotropy. The compound exhibits a collinear antiferromagnetic arrangement of the Co moments and a canted one of the U moments. For details on the magnetic structure see Fig. 205.

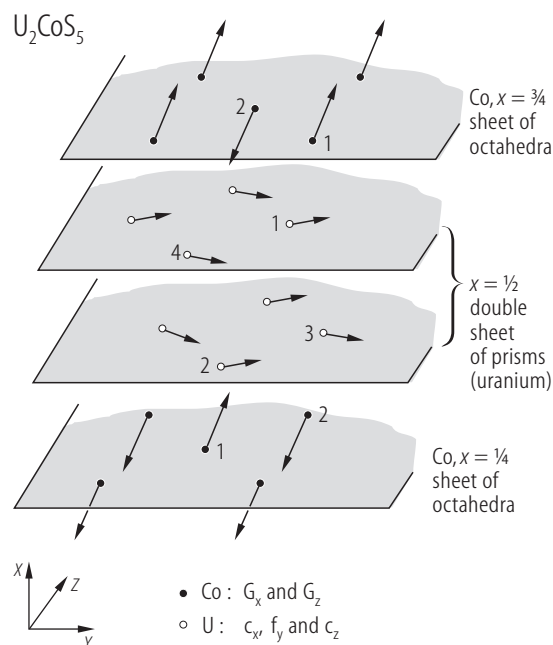


**Fig. 205.**  $\text{U}_2\text{CoS}_5$ . Schematic representation of the magnetic structure [79WBFN]. The magnetic unit cell consists of a pure collinear sublattice of the Co moments ( $G_x$  and  $G_z$  modes) and a canted sublattice of the U moments ( $c_x$ ,  $c_z$  and  $f_y$  modes). The latter can be described by two Ising-like systems with inequivalent easy directions, which are only weakly coupled to the Co sublattice. The refined values of the particular components of the Co and U moments at 125 and 4.2 K:  $p_{\text{Co}}(125\text{K}) = (2.3, 0, 1.9) \mu_B$ ,  $p_{\text{Co}}(4.2\text{K}) = (2.4, 0, 1.7) \mu_B$ ,  $p_{\text{U}}(125\text{K}) = (-0.1, 0.1, 0.2) \mu_B$  and  $p_{\text{U}}(4.2\text{K}) = (-0.4, 0.6, 1.5) \mu_B$ . Note that there is almost no change in the direction of the Co moments with decreasing temperature, in contrast to the case of  $\text{U}_2\text{FeS}_5$  (compare Fig. 201).

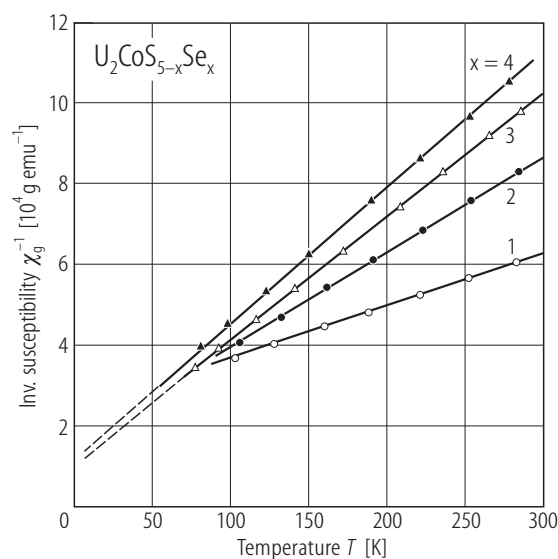


**Fig. 206.**  $\text{U}_2\text{CoS}_{5-x}\text{Se}_x$ ,  $x = 1, 2, 3, 4$ . Reciprocal mass magnetic susceptibility,  $\chi_g^{-1}$ , vs. temperature,  $T$ , in the range 80...300 K [93CSKM]. Open circles:  $\text{U}_2\text{CoS}_4\text{Se}$ ; filled circles:  $\text{U}_2\text{CoS}_3\text{Se}_2$ ; open triangles:  $\text{U}_2\text{CoS}_2\text{Se}_3$ ; filled triangles:  $\text{U}_2\text{CoSSe}_4$ . The lines are Curie-Weiss fits with the parameters given in Table B.

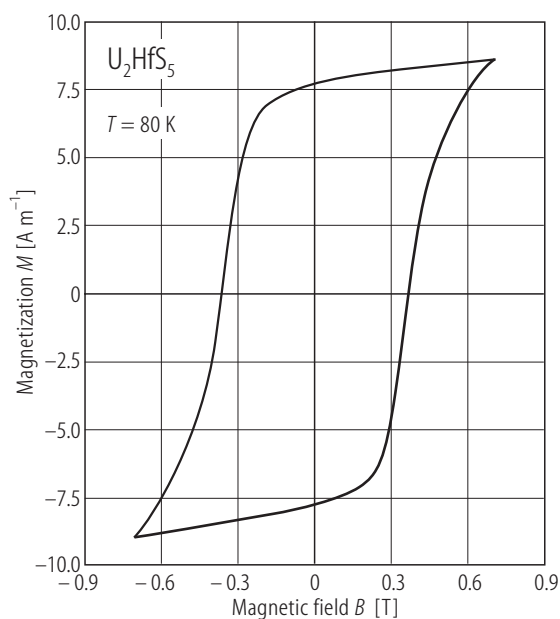
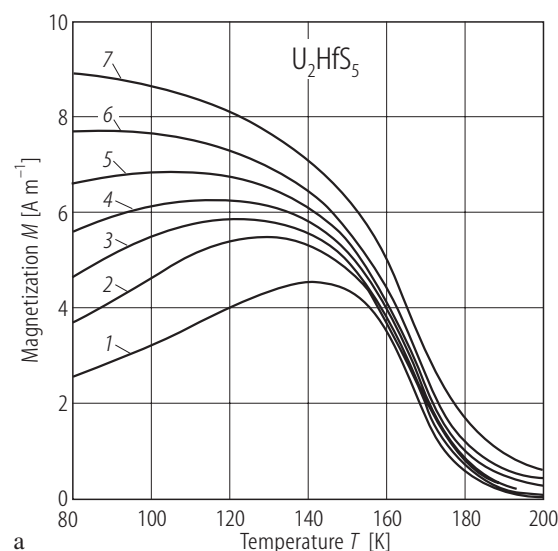
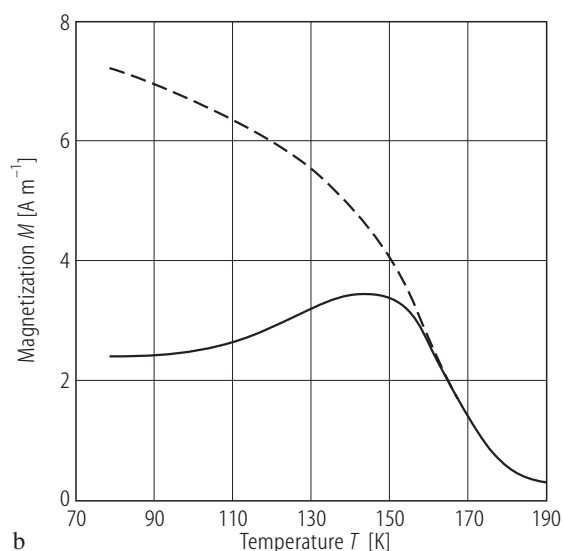


**Fig. 208.**  $\text{U}_2\text{HfS}_5$ . Hysteresis loop,  $M(B)$  (SI units), measured at  $T = 80$  K [84NCKS2].



a



b

**Fig. 207.**  $\text{U}_2\text{HfS}_5$ . (a) Magnetization,  $M$  (SI units), vs. temperature,  $T$ , in the range 80...200 K measured in several different magnetic fields upon cooling the sample in zero field [84NCKS2]. 1) 0.10 T; 2) 0.16 T; 3) 0.20 T; 4) 0.26 T;

5) 0.36 T; 6) 0.90 T. (b)  $M(T)$  taken in a field of 0.05 T taken on heating (solid curve) and cooling (dashed curve) [84NCKS2]. The compound orders ferromagnetically at  $T_C = 180$  K.

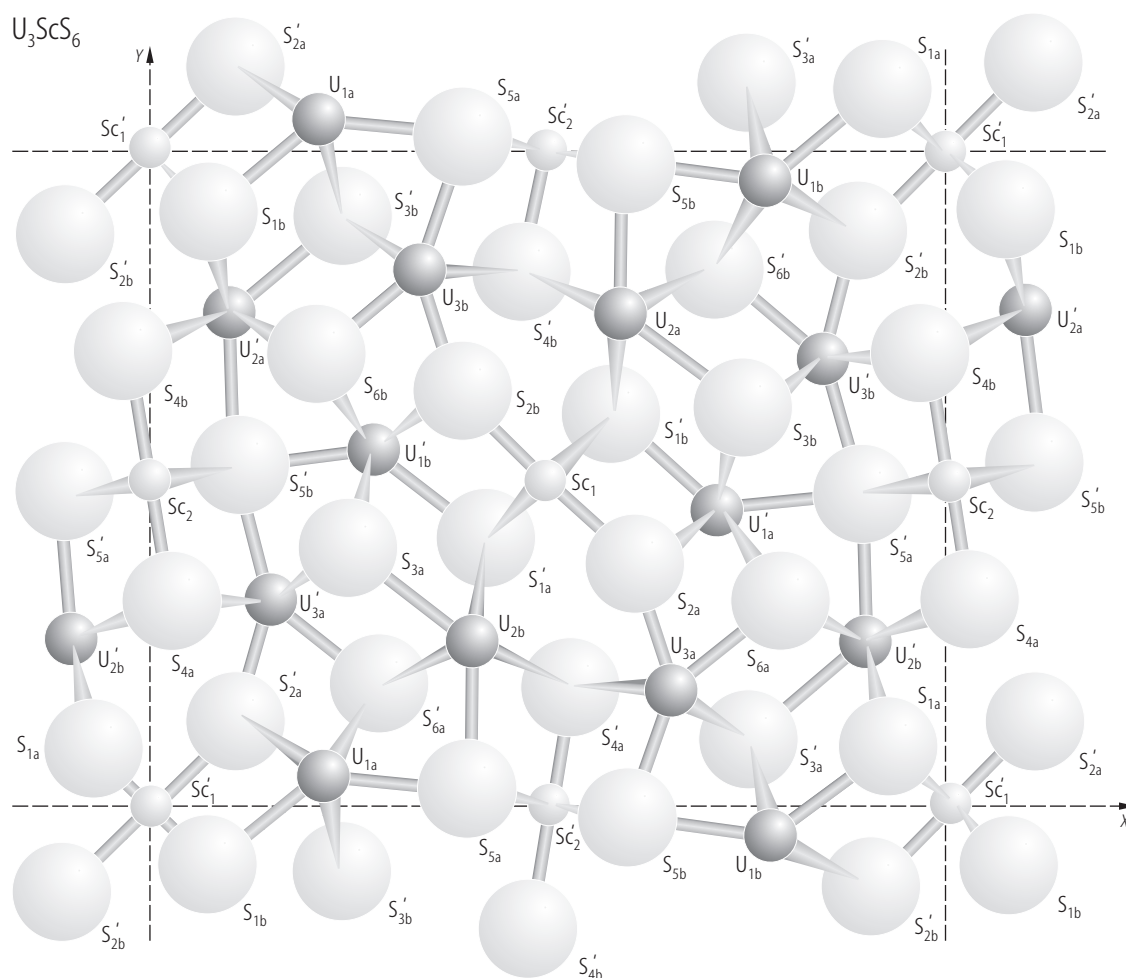


**Fig. 209.**  $\text{U}_3\text{ScS}_6$ . Crystal structure [76RT]. There are three nonequivalent positions for U atoms, two positions for Sc atoms and six positions for S atoms. Labels  $E_{na}$ ,  $E_{nb}$ ,  $E'_{na}$  and  $E'_{nb}$  refer to the atoms located at  $(x,y,0)$ ,  $(-x,-y,0)$ ,  $(\frac{1}{2}+x, \frac{1}{2}-y, \frac{1}{2})$  and  $(\frac{1}{2}-x, \frac{1}{2}+y, \frac{1}{2})$ , respectively.

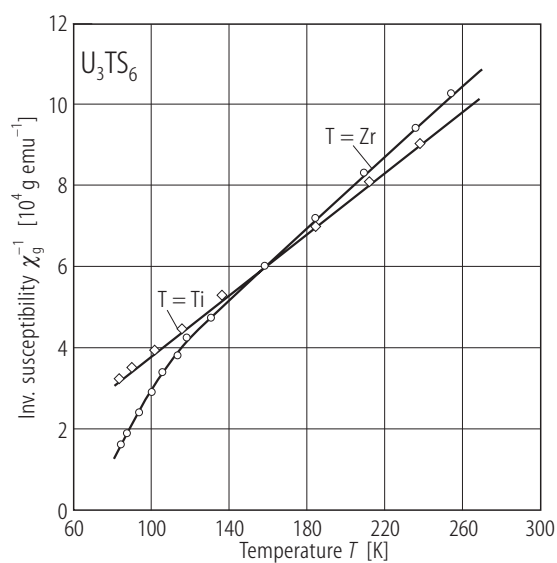


**Fig. 210.**  $\text{U}_3\text{TS}_6$ ,  $T = \text{Ti, Zr}$ . Reciprocal mass magnetic susceptibility,  $\chi_g^{-1}$ , vs. temperature,  $T$ , in the range 80... 300 K [84NCKS2]. Diamonds:  $\text{U}_3\text{TiS}_6$ ; circles:  $\text{U}_3\text{ZrS}_6$ . The solid lines serve as a guide for the eye. Both compounds are paramagnetic down to 80 K. At high temperatures their susceptibility follows a Curie-Weiss law with the uranium effective magnetic moment of 2.70... 2.80  $\mu_B$ . For  $\text{U}_3\text{ZrS}_6$  some deviation of  $\chi_g^{-1}(T)$  from a straight-line behaviour is observed, suggesting the occurrence of magnetic ordering at temperatures below 80 K.

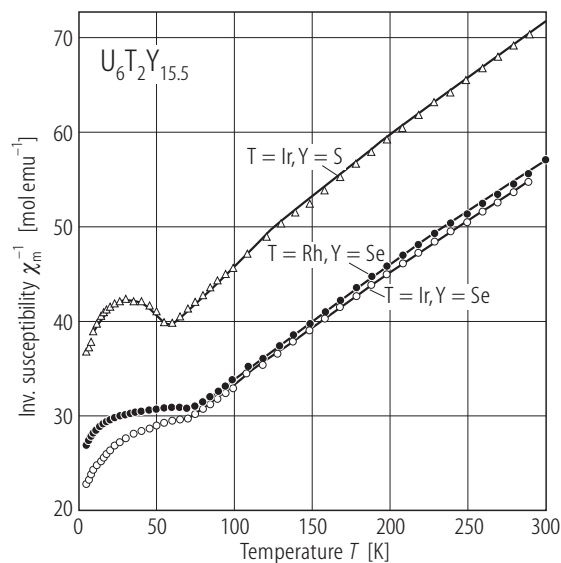


**Fig. 211.**  $U_6Rh_2Se_{15.5}$ ,  $U_6Ir_2Y_{15.5}$ ,  $Y = \text{S, Se}$ . Reciprocal molar magnetic susceptibility,  $\chi_m^{-1}$ , vs. temperature,  $T$  [96DN]. Filled circles:  $U_6Rh_2Se_{15.5}$ ; triangles:  $U_6Ir_2S_{15.5}$ ; open circles:  $U_6Rh_2S_{15.5}$ . The compounds order antiferromagnetically at  $T_N = 70, 57$  and  $75$  K for  $U_6Rh_2Se_{15.5}$ ,  $U_6Ir_2S_{15.5}$  and  $U_6Ir_2Se_{15.5}$ , respectively. The low-temperature upturn in  $\chi_m(T)$ , the authors interpreted as being caused by undefined paramagnetic impurities. The modified Curie-Weiss fit parameters are given in Table B.

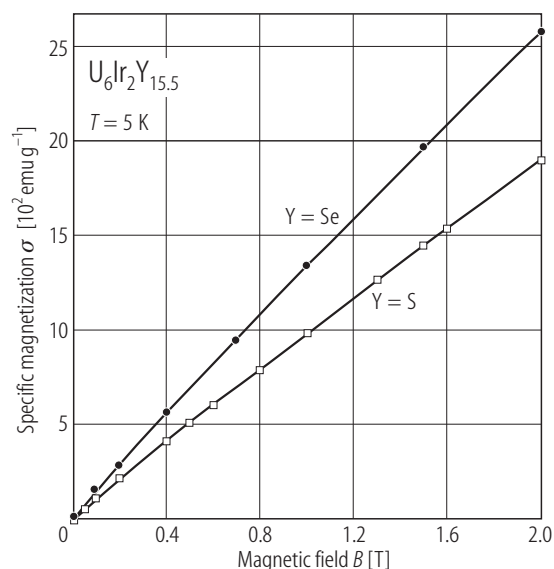


**Fig. 212.**  $U_6Ir_2Y_{15.5}$ ,  $Y = \text{S, Se}$ . Specific magnetization,  $\sigma$ , vs. magnetic field,  $B$ , taken at 5 K [96DN]. Squares:  $U_6Ir_2S_{15.5}$ ; circles:  $U_6Ir_2Se_{15.5}$ . Both compounds are antiferromagnetic at low temperatures (see Fig. 211).

For Fig. 213 see next page

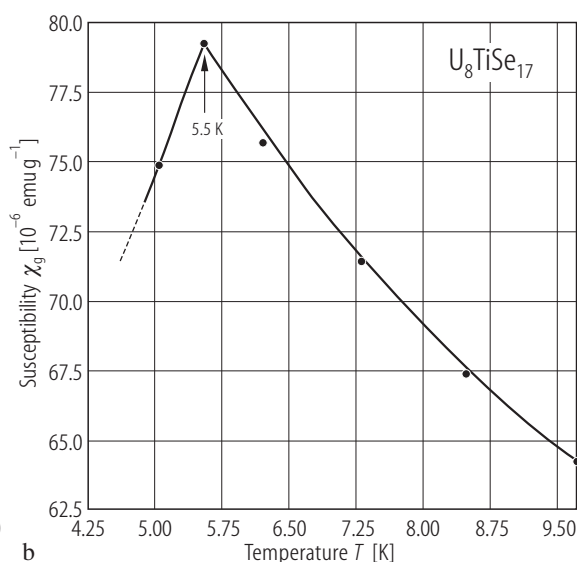
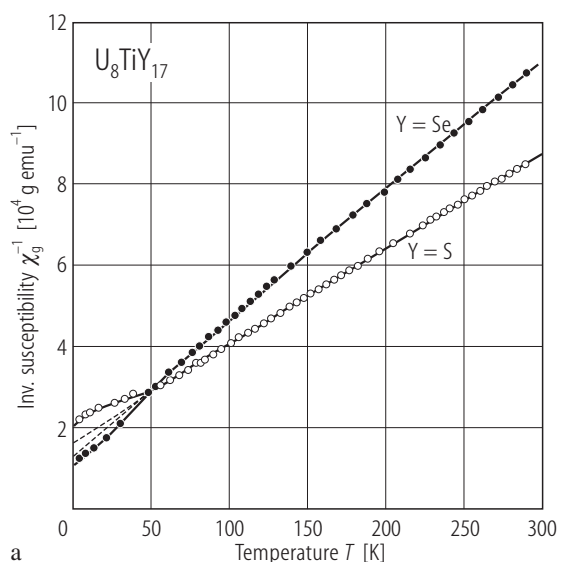


**Fig. 214.**  $U_8TiY_{17}$ ,  $Y = \text{S, Se}$ . (a) Reciprocal mass magnetic susceptibility,  $\chi_g^{-1}$ , vs. temperature,  $T$  [79NT]. Open circles:  $U_8TiS_{17}$ ; full circles:  $U_8TiSe_{17}$ . The dashed lines mark a Curie-Weiss behaviour with the parameters given in Table F. (b) Mass magnetic susceptibility,  $\chi_g$ , vs.  $T$  below 10 K for  $U_8TiSe_{17}$  [79NT]. The compound orders antiferromagnetically at  $T_N = 5.5$  K.

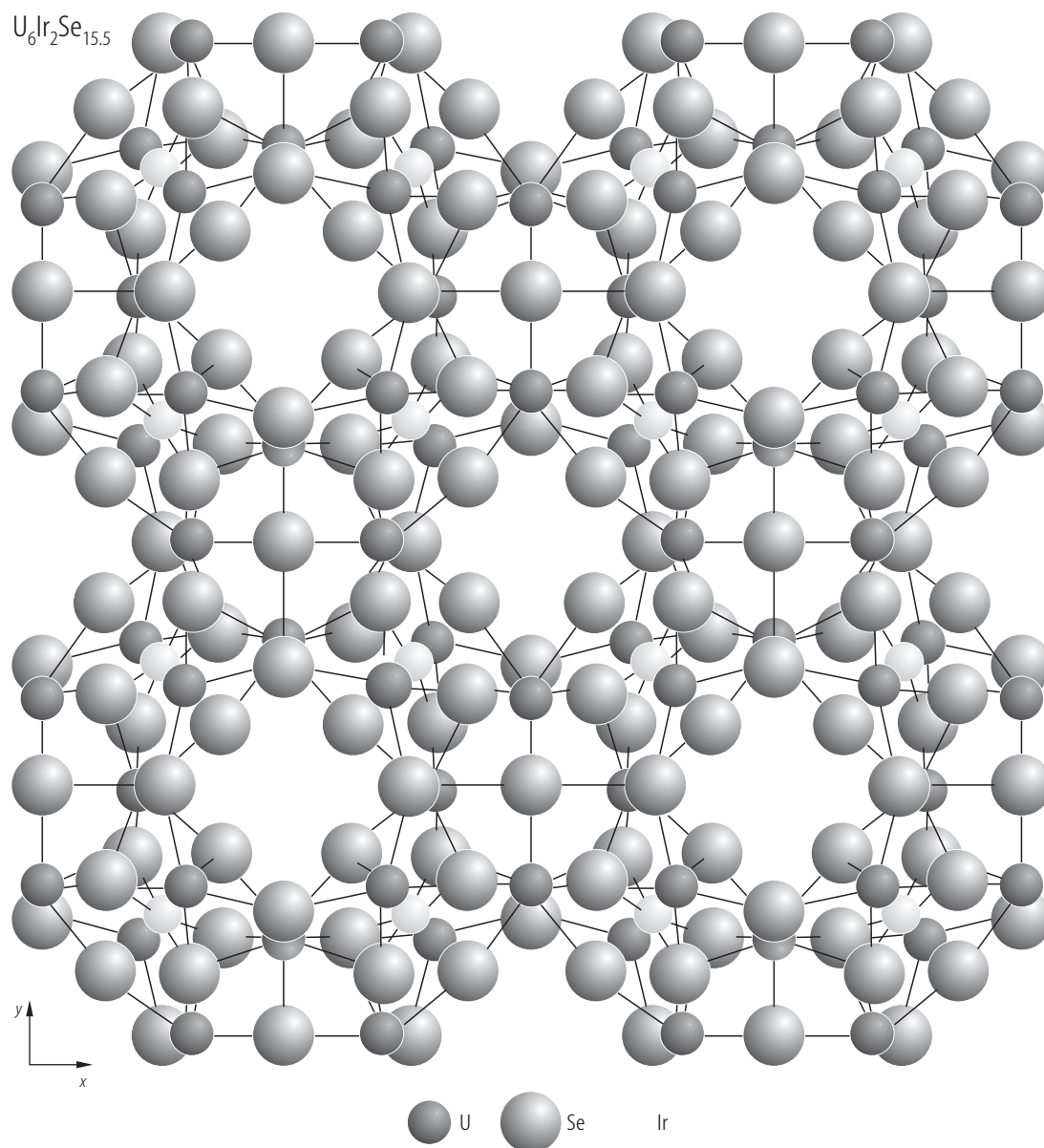


**Fig. 213.** Crystal structure of  $\text{U}_6\text{Ir}_2\text{Se}_{15.5}$  [96DN].

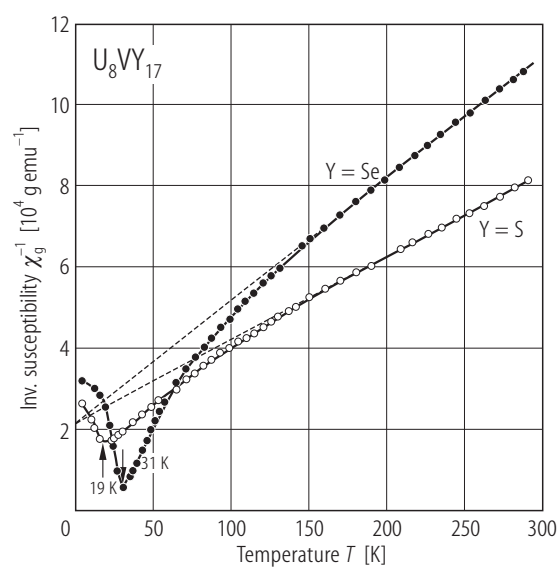


**Fig. 215.**  $\text{U}_8\text{VY}_{17}$ ,  $\text{Y} = \text{S, Se}$ . Reciprocal mass magnetic susceptibility,  $\chi_g^{-1}$ , vs. temperature,  $T$  [79NT]. Open circles:  $\text{U}_8\text{VS}_{17}$ ; full circles:  $\text{U}_8\text{VSe}_{17}$ . The dashed lines mark a Curie-Weiss behaviour with the parameters given in Table F. Both compounds are antiferromagnets, and  $T_N = 19$  and 31 K for the sulphide and the selenide, respectively.

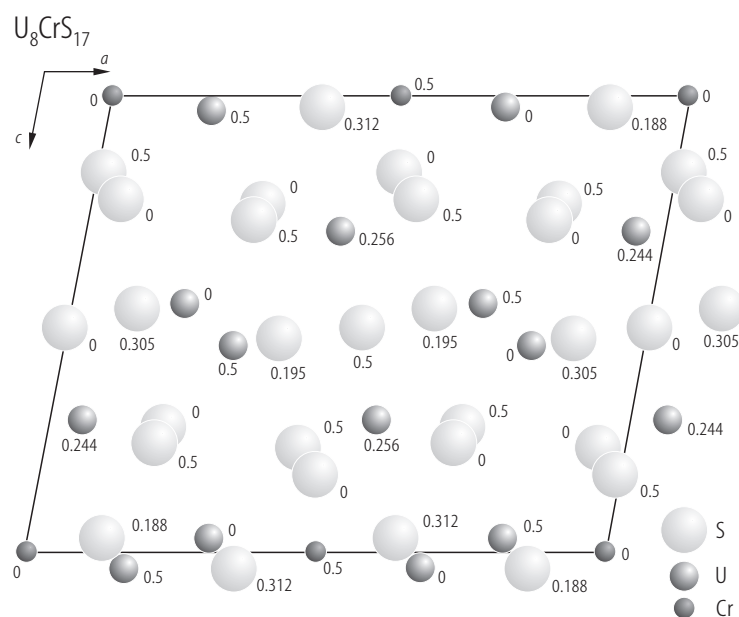


**Fig. 216.**  $\text{U}_8\text{CrS}_{17}$ . Crystal structure projected on the (010) plane [75NPP1]. The numbers denote the values of the positional parameter  $y$ .

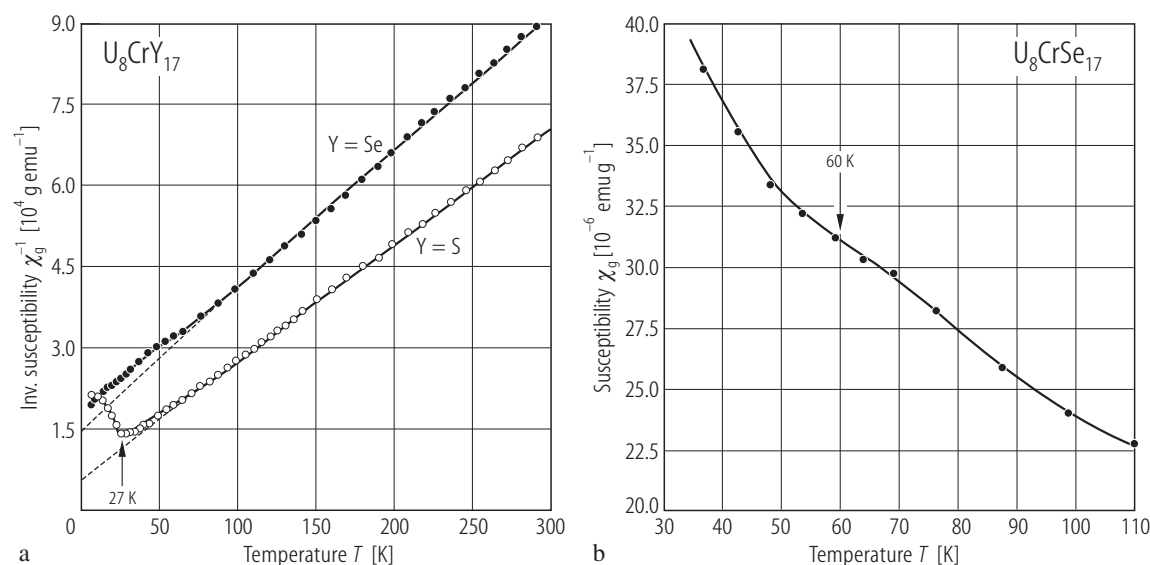


**Fig. 217.**  $\text{U}_8\text{CrY}_{17}$ ,  $\text{Y} = \text{S}, \text{Se}$ . **(a)** Reciprocal mass magnetic susceptibility,  $\chi_g^{-1}$ , vs. temperature,  $T$  [79NT]. Open circles:  $\text{U}_8\text{CrS}_{17}$ ; full circles:  $\text{U}_8\text{CrSe}_{17}$ . The dashed lines mark a Curie-Weiss behaviour with the parameters given in Table E. **(b)** Mass magnetic susceptibility,  $\chi_g$ , vs.  $T$  below 120 K for  $\text{U}_8\text{CrSe}_{17}$  [79NT]. Whereas for the sulphide there

occurs a well pronounced minimum in  $\chi_g^{-1}(T)$  at the antiferromagnetic phase transition at  $T_N = 27 \text{ K}$ , for the selenide only an inflection point in  $\chi_g(T)$  at 60 K is observed, which may manifest the onset of antiferromagnetic state.

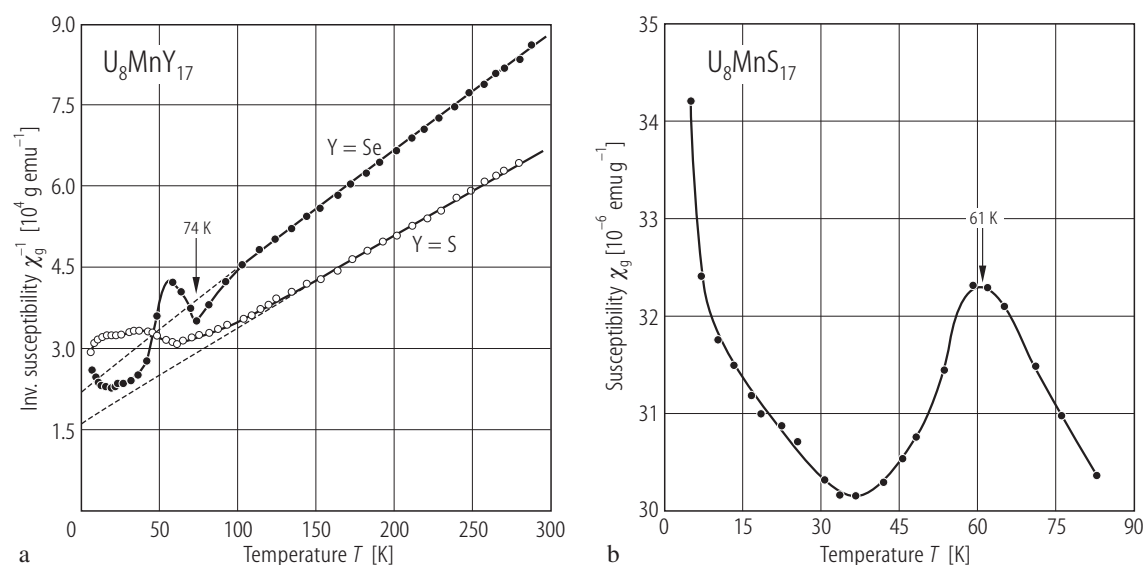


**Fig. 218.**  $\text{U}_8\text{MnY}_{17}$ ,  $\text{Y} = \text{S}, \text{Se}$ . **(a)** Reciprocal mass magnetic susceptibility,  $\chi_g^{-1}$ , vs. temperature,  $T$  [79NT]. Open circles:  $\text{U}_8\text{MnS}_{17}$ ; full circles:  $\text{U}_8\text{MnSe}_{17}$ . The dashed lines mark a Curie-Weiss behaviour with the parameters given in Table E. The compounds order antiferromagnetically at  $T_N = 61$  and  $74 \text{ K}$  for the sulphide and the selenide, respectively. Note that in the ordered

region the  $\chi_g^{-1}(T)$  curves of both phases show complex features. As no field dependence of the susceptibility was found at  $4.2 \text{ K}$  the authors suggested that the observed properties result from the fact that not all paramagnetic ions participate in the magnetic order. **(b)** Mass magnetic susceptibility,  $\chi_g$ , vs.  $T$  below 80 K for  $\text{U}_8\text{MnS}_{17}$  [79NT].

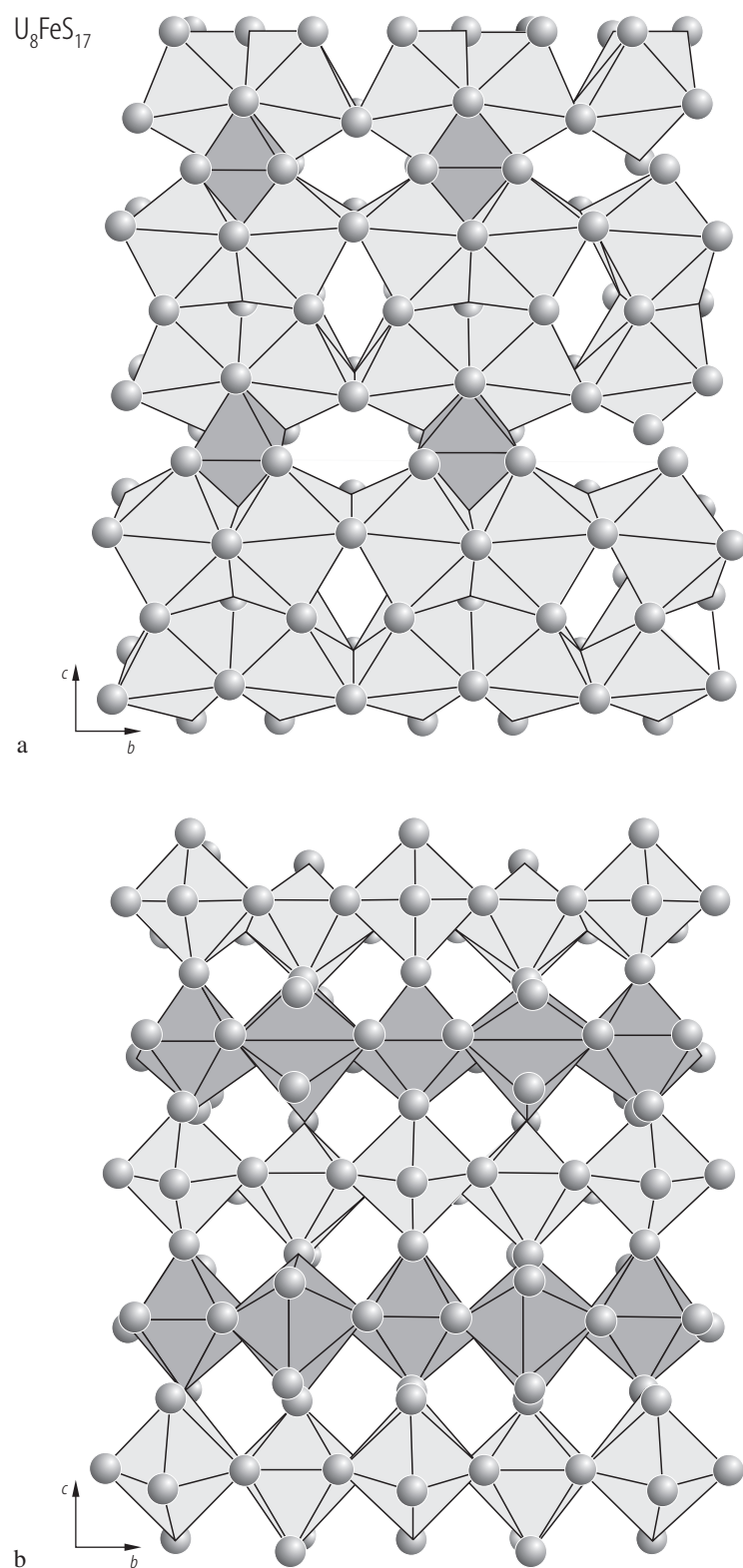


**Fig. 219.**  $U_8FeS_{17}$ . Crystal structure viewed along the  $[100]$  axis (the  $[010]$  axis goes from left to right side) [97KSB]. Marked polyhedra: **(a)** Fe: dark grey, U(1): light grey; **(b)** U(2): light grey, U(3): dark grey.



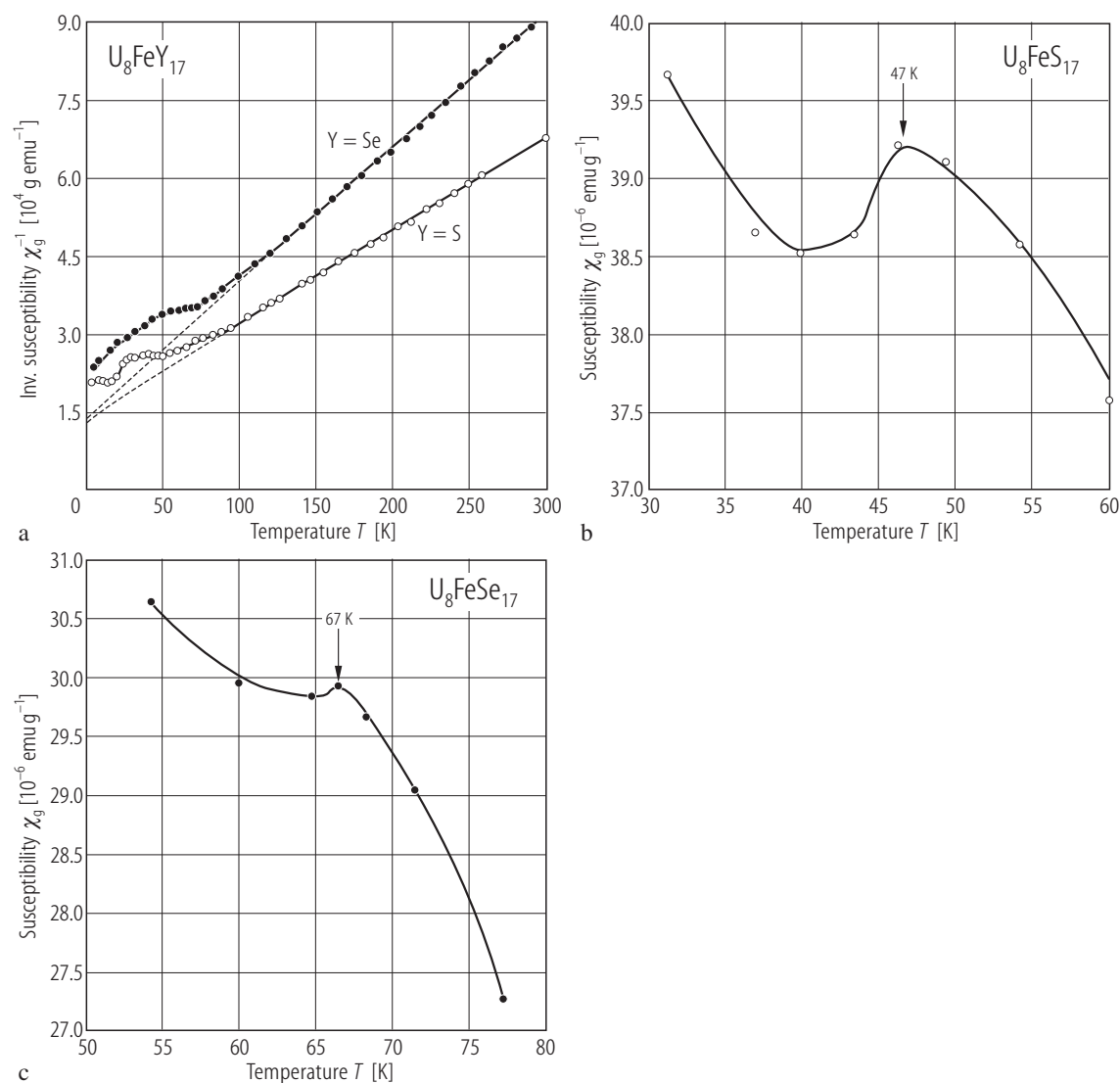


**Fig. 220.**  $U_8FeY_{17}$ ,  $Y = S, Se$ . (a) Reciprocal mass magnetic susceptibility,  $\chi_g^{-1}$ , vs. temperature,  $T$  [79NT]. Open circles:  $U_8FeS_{17}$ ; full circles:  $U_8FeSe_{17}$ . The dashed lines mark a Curie-Weiss behaviour with the parameters given in Table E. (b) Mass magnetic susceptibility,  $\chi_g$ , vs.  $T$  below 60 K for  $U_8FeS_{17}$  [79NT]. (c) Mass magnetic susceptibility,

$\chi_g$ , vs.  $T$  below 80 K for  $U_8FeSe_{17}$  [79NT]. The compounds are antiferromagnets with the Néel temperatures of 47 and 67 K for the sulphide and the selenide, respectively. Note anomalous tails in both  $\chi_g(T)$  curves below the respective  $T_N$ . See the original paper for discussion on this problem.

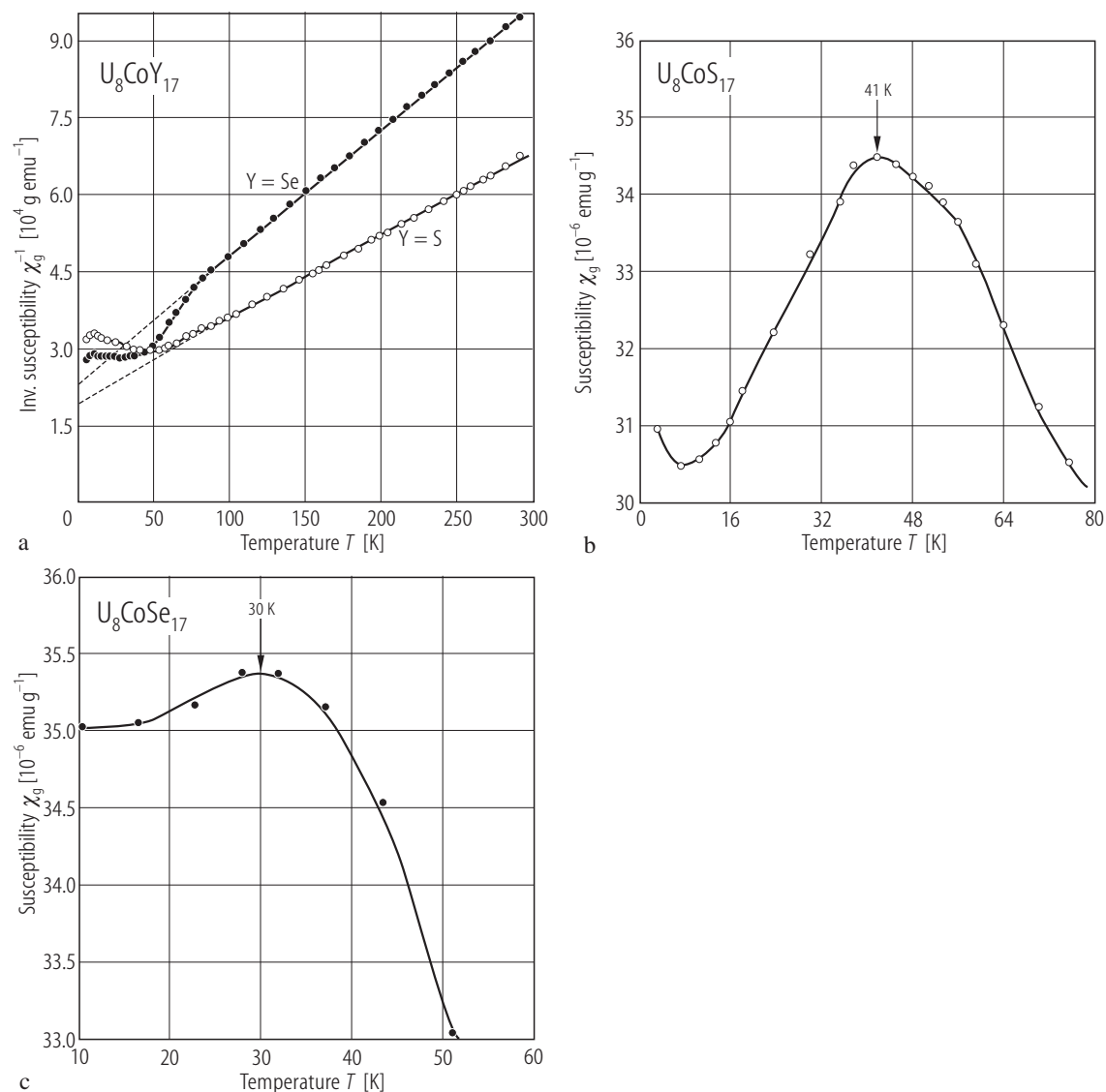


**Fig. 221.**  $U_8CoY_{17}$ ,  $Y = S, Se$ . (a) Reciprocal mass magnetic susceptibility,  $\chi_g^{-1}$ , vs. temperature,  $T$  [79NT]. Open circles:  $U_8CoS_{17}$ ; full circles:  $U_8CoSe_{17}$ . The dashed lines mark a Curie-Weiss behaviour with the parameters given in Table E. (b) Mass magnetic susceptibility,  $\chi_g$ , vs.  $T$  below

80 K for  $U_8CoS_{17}$  [79NT]. (c) Mass magnetic susceptibility,  $\chi_g$ , vs.  $T$  below 60 K for  $U_8CoSe_{17}$  [79NT]. The compounds order antiferromagnetically at  $T_N$  of 41 and 30 K for the sulphide and the selenide, respectively.

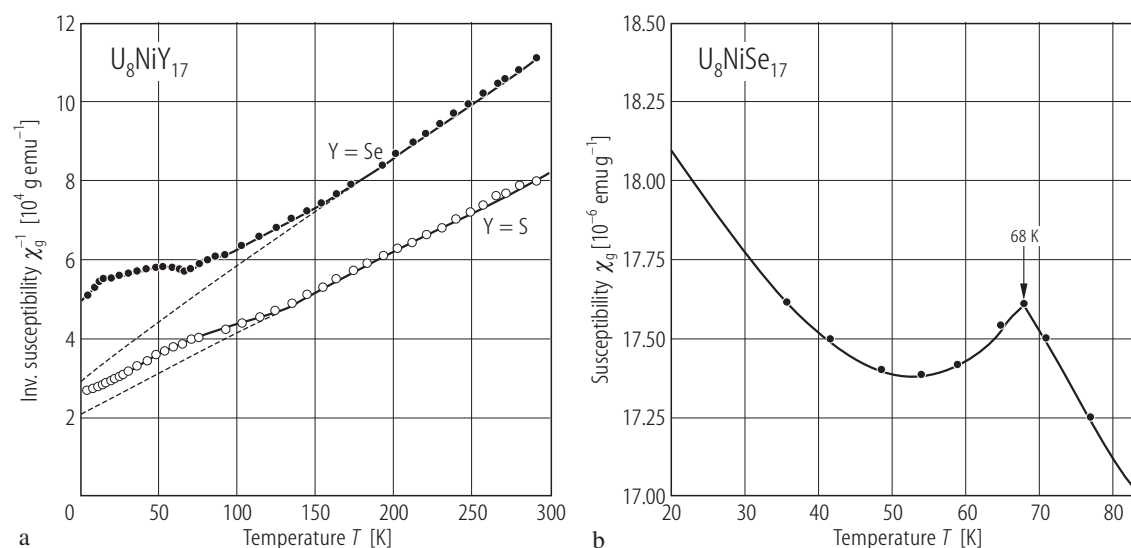


**Fig. 222.**  $\text{U}_8\text{NiY}_{17}$ ,  $\text{Y} = \text{S, Se}$ . **(a)** Reciprocal mass magnetic susceptibility,  $\chi_g^{-1}$ , vs. temperature,  $T$  [79NT]. Open circles:  $\text{U}_8\text{NiS}_{17}$ ; full circles:  $\text{U}_8\text{NiSe}_{17}$ . The dashed lines mark a Curie-Weiss behaviour with the parameters given in Table F. **(b)** Mass magnetic susceptibility,  $\chi_g$ , vs.  $T$  below 90 K for  $\text{U}_8\text{NiSe}_{17}$  [79NT]. The latter compound is

antiferromagnetic below  $T_N = 68$  K.  $\text{U}_8\text{NiS}_{17}$  is probably also an antiferromagnet but the onset of the ordered state does not manifest itself as a minimum in  $\chi_g^{-1}(T)$  but only as an inflection point at 40 K. Note also an anomalous rise of the susceptibility with decreasing temperature below  $T_N$ , observed for both phases.

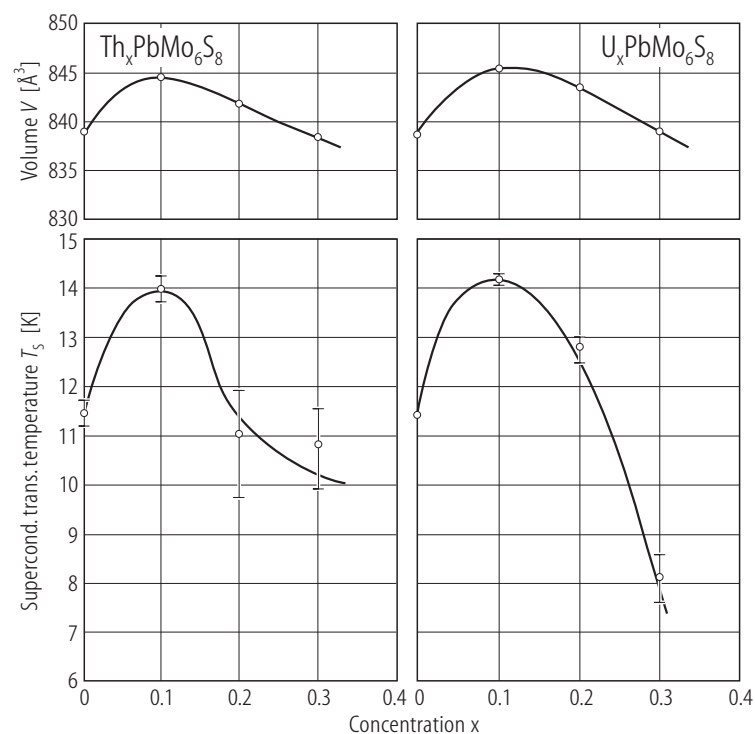


**Fig. 223.**  $\text{Th}_x\text{PbMo}_6\text{S}_8$ ,  $\text{U}_x\text{PbMo}_6\text{S}_8$ . Volume,  $V$ , (upper panels) and superconducting transition temperature,  $T_s$ , (bottom panels) vs. Th- (left-hand side panels) and U- concentration (right-hand side panels),  $x$  [78SCRF]. Note maxima in  $V(x)$  and  $T_s(x)$  near  $x = 0.1$ . The decrease of  $T_s$  and  $V$  at higher concentrations the authors interpreted as a result of substitution of Pb by Th or U.

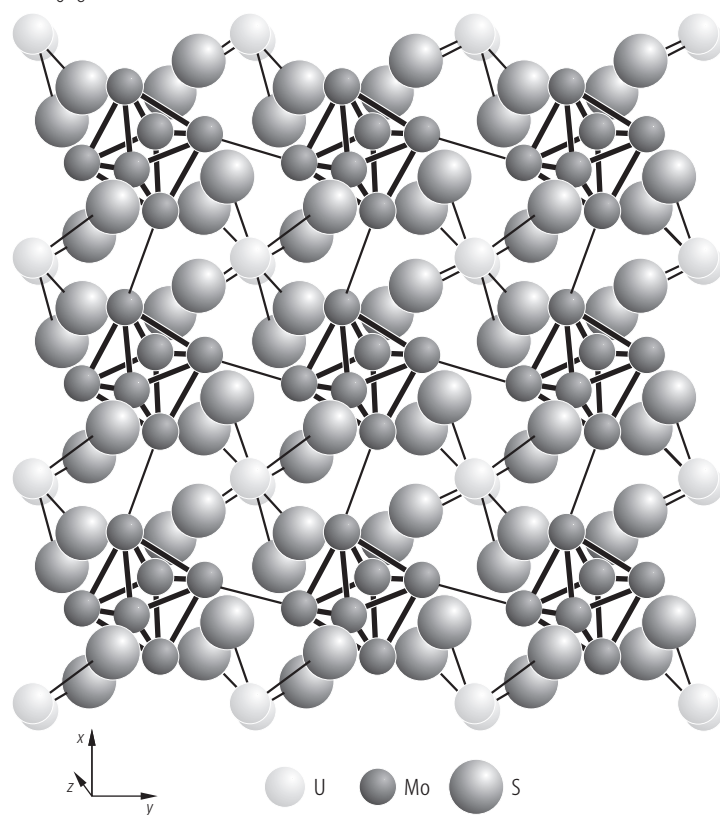


**Fig. 224.**  $\text{UMo}_6\text{S}_8$ . Crystal structure [96DPN].

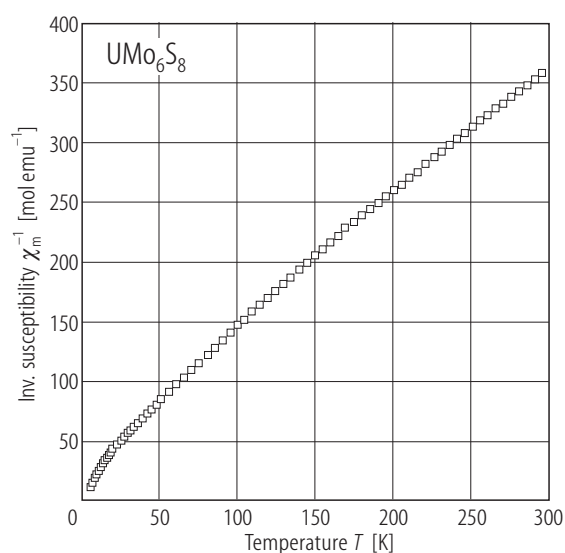


**Fig. 225.**  $\text{UMo}_6\text{S}_8$ . Reciprocal molar magnetic susceptibility,  $\chi_m^{-1}$ , vs. temperature,  $T$  [96DPN]. The compound remains paramagnetic down to 2 K. See the Curie-Weiss fit parameters given in Table B.

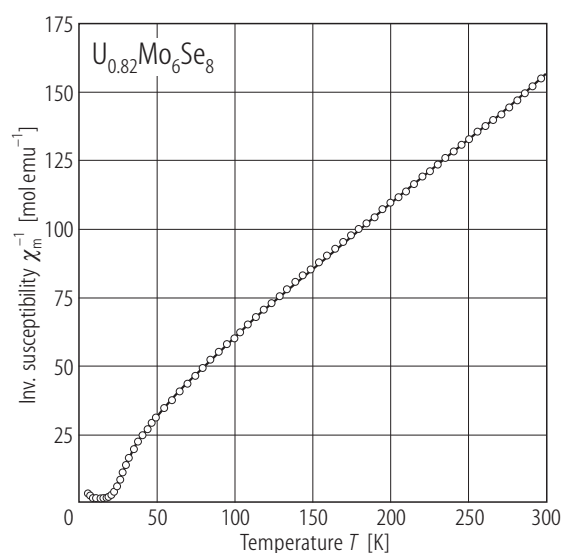


**Fig. 226.**  $\text{U}_{0.82}\text{Mo}_6\text{Se}_8$ . Reciprocal molar magnetic susceptibility,  $\chi_m^{-1}$ , vs. temperature,  $T$  [96DPN]. A weak ferromagnetism is observed below 25 K. See the Curie-Weiss fit parameters given in Table B.

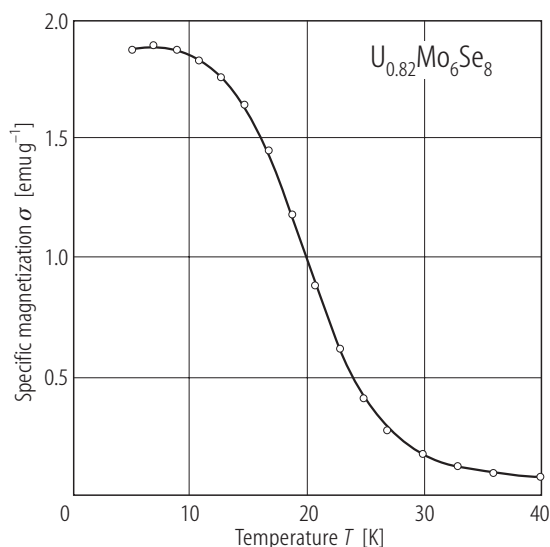


**Fig. 227.**  $\text{U}_{0.82}\text{Mo}_6\text{Se}_8$ . Specific magnetization,  $\sigma$ , vs. temperature,  $T$  [96DPN]. The compound orders ferromagnetically below  $T_C = 25$  K.

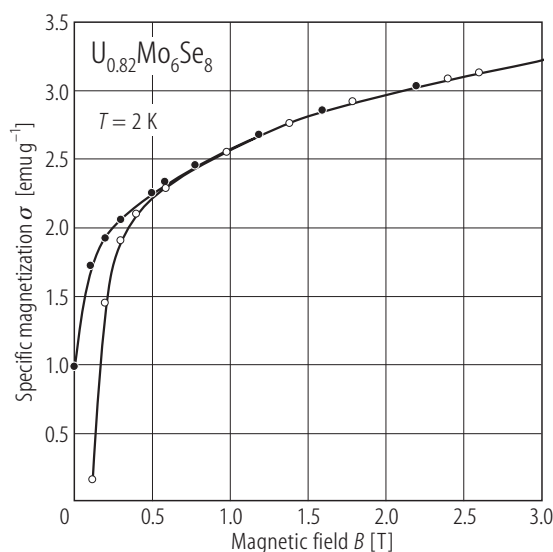
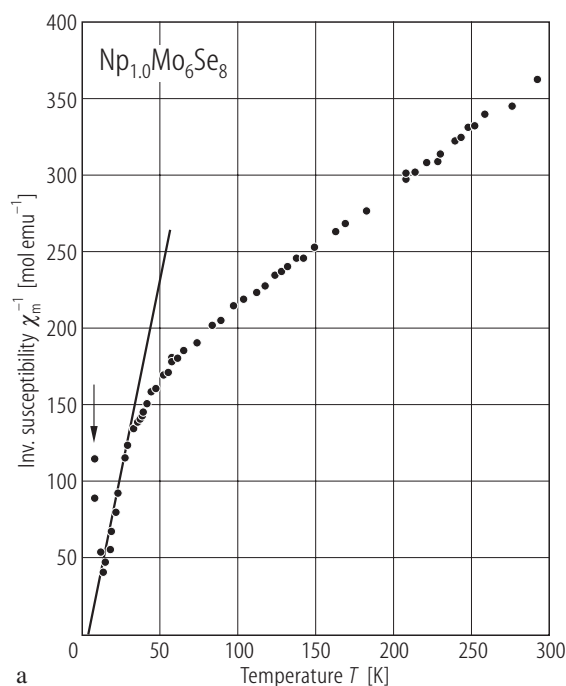
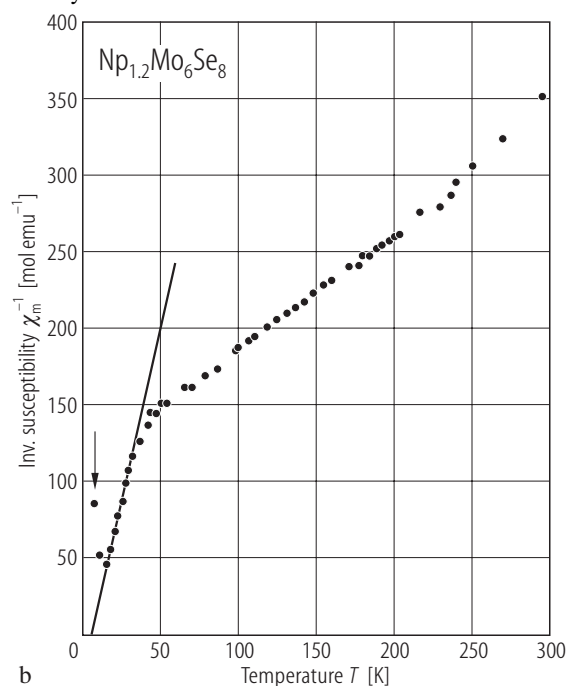


**Fig. 228.**  $\text{U}_{0.82}\text{Mo}_6\text{Se}_8$ . Specific magnetization,  $\sigma$ , vs. field,  $B$ , taken at 2 K with increasing (open circles) and decreasing (closed circles) magnetic field [96DPN]. Note a hysteretic behaviour.



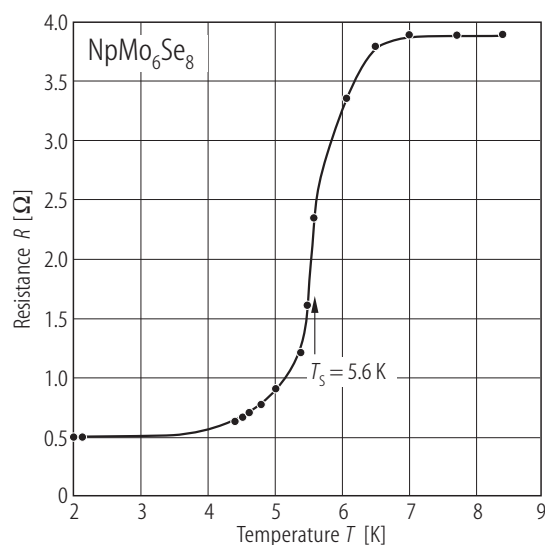
a



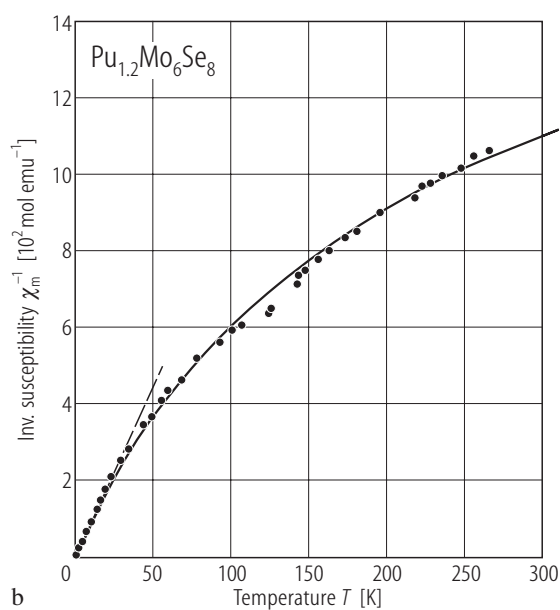
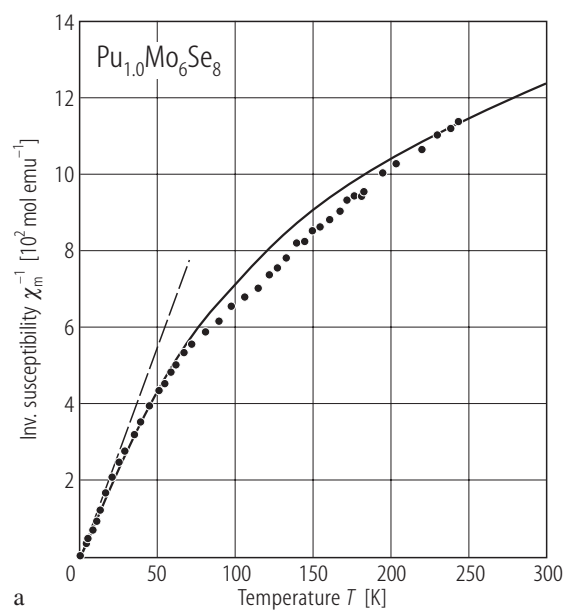
b

**Fig. 229.**  $\text{Np}_{1+x}\text{Mo}_6\text{Se}_8$ ,  $x = 0.0$  and  $0.2$ . Reciprocal molar magnetic susceptibility,  $\chi_m^{-1}$ , vs. temperature,  $T$ , for (a)  $x = 0.0$ , (b)  $x = 0.2$  [81DDG]. The solid lines are Curie-Weiss fits with the parameters given in Table B. Both samples show a sharp diamagnetic transition at about 6 K (marked by the arrows), suggesting superconductivity (compare Fig. 230). At higher temperatures the compounds are paramagnetic. A minimum observed around 14 K the authors ascribed to a

lattice distortion, a crystal field effect or/and magnetic ordering. The change in slope of  $\chi_m^{-1}(T)$  they attributed to crystal field effects, with an important non-cubic component, arising from some distortion of the selenium cube. The neptunium effective moment,  $p_{\text{eff}}$ , calculated in a manner described in the caption of Fig. 232 approaches at room temperature a free  $\text{Np}^{3+}$  ion value of  $2.8 \mu_B$  ( $p_{\text{eff}} = 1.87, 2.25$  and  $2.44 \mu_B$  at 100, 200 and 300 K, respectively).

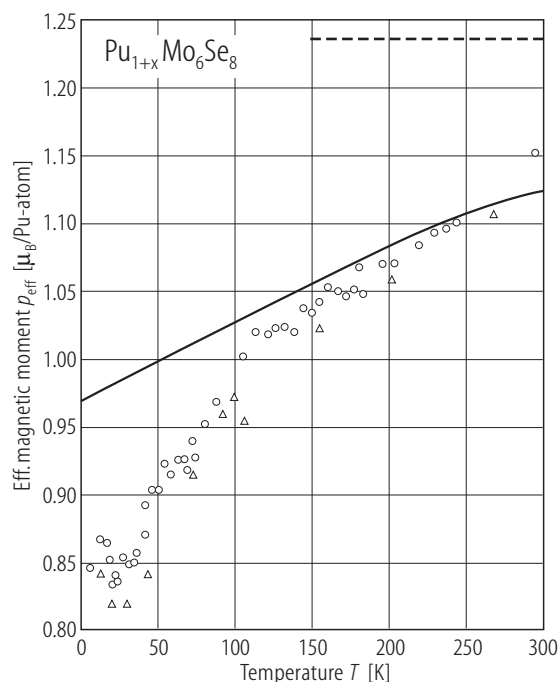


**Fig. 230.**  $\text{NpMo}_6\text{Se}_8$ . Electrical resistance,  $R$ , vs. temperature,  $T$ , in the range 2...9 K [81DDG]. From 7 to 300 K the resistance is almost temperature independent (not shown). At 6 K the resistance drops by an order of magnitude due to a superconducting transition at 5.6(1) K (see also Fig. 229).



**Fig. 231.**  $\text{Pu}_{1+x}\text{Mo}_6\text{Se}_8$ ,  $x = 0.0$  and  $0.2$ . Reciprocal molar magnetic susceptibility,  $\chi_m^{-1}$ , vs. temperature,  $T$ , for (a)  $x = 0.0$ , (b)  $x = 0.2$  [81DDH]. Both samples are paramagnetic with no field dependence of the susceptibility. Superconductivity and/or long-range magnetic order were

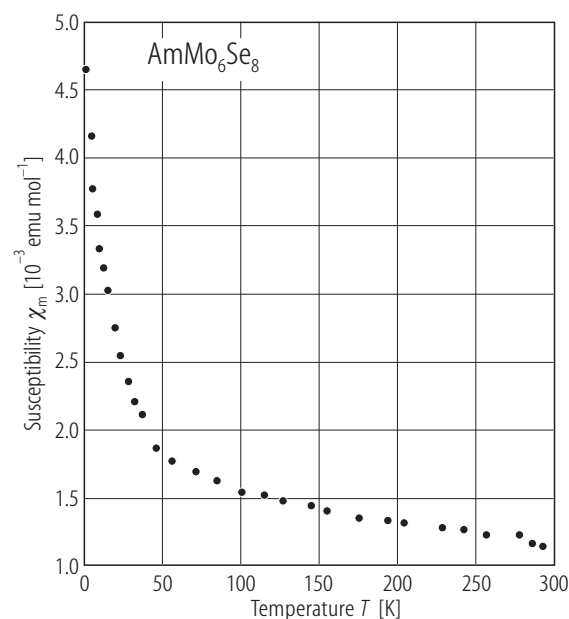
not found down to 2.5 K. The dashed and solid lines are Curie-Weiss and modified Curie-Weiss fits, respectively, with the parameters given in Table B. A strong negative curvature of  $\chi_m^{-1}(T)$  the authors ascribed to thermal population of excited crystal field levels (see Fig. 232).



**Fig. 232.**  $\text{Pu}_{1+x}\text{Mo}_6\text{Se}_8$ ,  $x = 0.0$  and  $0.2$ . Plutonium effective magnetic moment,  $p_{\text{eff}}$ , vs. temperature,  $T$ , as derived from the formula

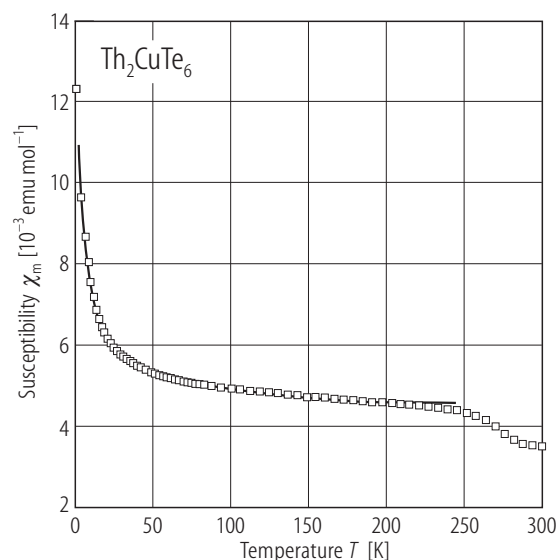
$$p_{\text{eff}} = \left\{ \frac{3k_B T [\chi_m(\text{Pu}_{1+x}\text{Mo}_6\text{Se}_8) - \chi_m(\text{LaMo}_6\text{Se}_8)]}{N} \right\},$$

where  $\chi_m(\text{Pu}_{1+x}\text{Mo}_6\text{Se}_8)$  is the susceptibility measured for  $\text{Pu}_{1+x}\text{Mo}_6\text{Se}_8$  (see Fig. 231) and  $\chi_m(\text{LaMo}_6\text{Se}_8) = (345 - 0.363T) \cdot 10^{-6} \text{ emu/mol}$  ( $T$  in K) [81DDH]. Circles:  $x = 0.0$ ; triangles:  $x = 0.2$ . The horizontal dashed line marks a free  $\text{Pu}^{3+}$  ion magnetic moment value ( $1.23 \mu_B$ ). The solid line is a theoretical curve derived for a  $\text{Pu}^{3+}$  ion placed in a cubic crystal field potential, which gives the energy difference between the ground state  $\Gamma_8$  and the excited state  $\Gamma_7$  of 1000 K. The agreement with  $p_{\text{eff}}(T)$  is rather good above 150 K. The discrepancy seen at lower temperatures the authors attributed to the splitting of  $\Gamma_8$  by a non-cubic crystal field component due to some distortion of the selenium cube.

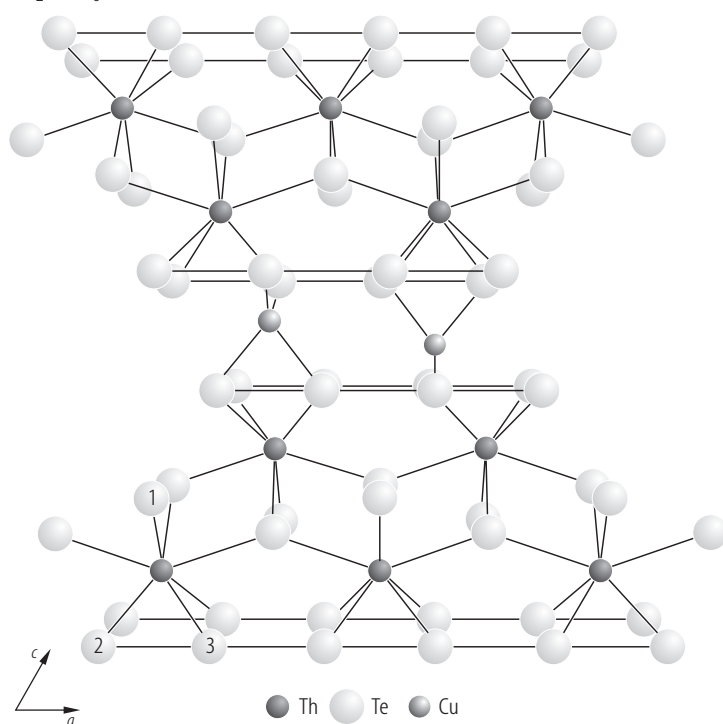


**Fig. 233.**  $\text{AmMo}_6\text{Se}_8$ . Molar magnetic susceptibility,  $\chi_m$ , vs. temperature,  $T$  measured in a field of 0.5 T [81DDH]. The susceptibility is weakly temperature dependent above 150 K. The low-temperature upturn the authors attributed to paramagnetic impurities, either  $\text{Cm}^{3+}$  or  $\text{Am}^{2+}$  in an atomic concentration of  $2 \cdot 10^{-3}$ . The intrinsic susceptibility of the compound is  $(942 - 0.843T) \cdot 10^{-6} \text{ emu/mol}$ , suggesting a trivalent state of Am ions (singlet ground state).

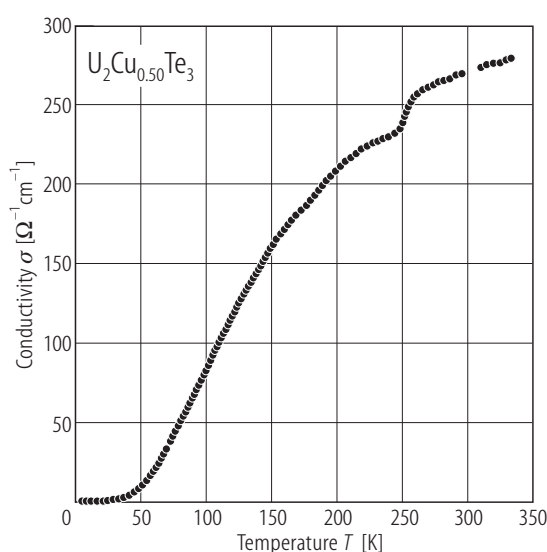
For Fig. 234 see next page



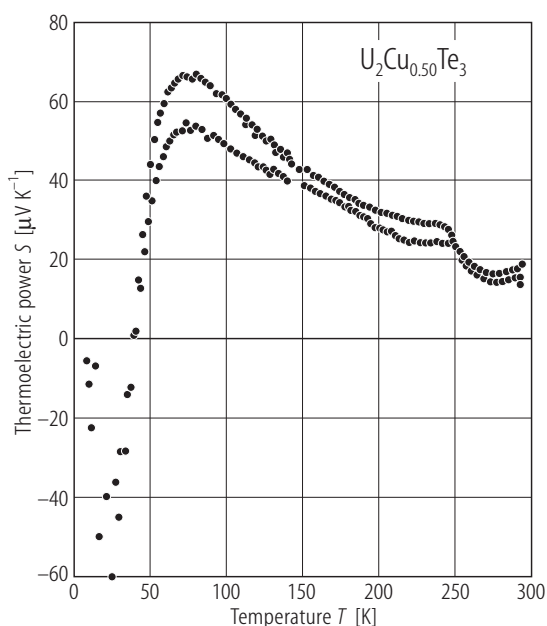
**Fig. 235.**  $\text{Th}_2\text{CuTe}_6$ . Molar magnetic susceptibility,  $\chi_m$ , vs. temperature,  $T$  [98NI]. The solid line is a modified Curie-Weiss fit with the parameters  $p_{\text{eff}} = 0.63 \mu_B/\text{f.u.}$ ,  $\Theta_{\text{CW}} = -5.5 \text{ K}$  and  $\chi_0 = 4.38 \cdot 10^{-3} \text{ emu/mol}$ . The anomaly at about 250 K has unknown origin.

$\text{Th}_2\text{CuTe}_6$ 

**Fig. 234.**  $\text{Th}_2\text{CuTe}_6$ . Crystal structure [98NI]. There are three crystallographically nonequivalent Te atom sites (labels 1-3). The unit cell consists of two-dimensional  $[\text{Th}_2\text{Te}_6]$  slabs stacked along the  $c$ -axis and connected by  $\text{Cu}^+$  cations. In a slab the Th atom is coordinated by a bicapped trigonal prism of eight Te atoms. Isostructural to  $\text{Th}_2\text{CuTe}_6$  are the compounds  $\text{U}_2\text{Cu}_x\text{Te}_6$  with  $x = 0.50, 0.66$  [01PBBK] and  $x = 0.78$  [01HI].

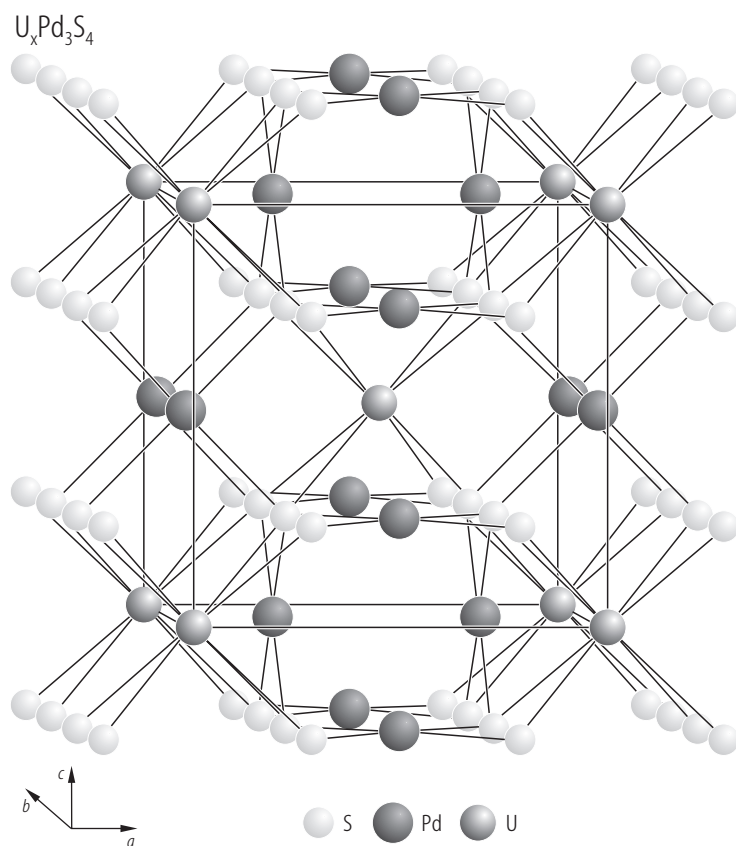


**Fig. 236.**  $\text{U}_2\text{Cu}_{0.50}\text{Te}_6$ . Electrical conductivity,  $\sigma$ , vs. temperature,  $T$ , measured on a single crystal in the range 5...330 K [01PBBK]. The compound is a narrow-gap semiconductor. The anomaly at 250 K has unknown origin yet structural transition can be excluded on the basis of the low-temperature X-ray diffraction data. Interestingly, pronounced anomalies at this temperature occur also in the thermopower of  $\text{U}_2\text{Cu}_{0.50}\text{Te}_6$  (see Fig. 237) and in the magnetic susceptibility of  $\text{Th}_2\text{CuTe}_6$  (see Fig. 235).

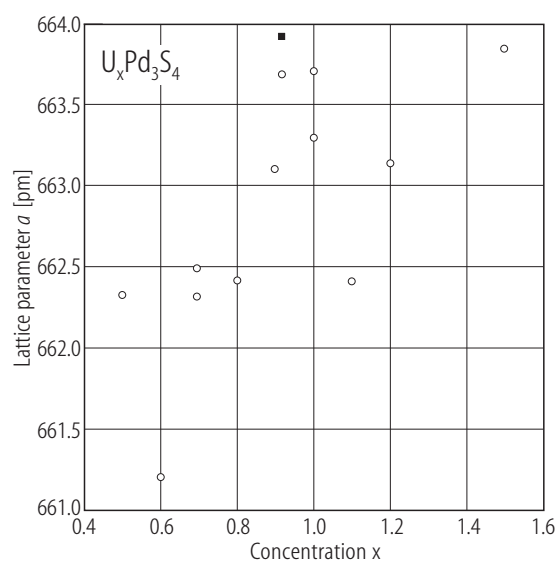


**Fig. 237.**  $\text{U}_2\text{Cu}_{0.50}\text{Te}_6$ . Thermoelectric power,  $S$ , vs. temperature,  $T$ , measured on two different single crystal in the range 5...300 K [01PBBK]. The compound is a p-type semiconductor down to 40 K. Below this temperature a p-n transition takes place due to a two-component dielectric polaron conduction mechanism. The anomaly at 250 K corresponds to a dip in the temperature-dependent electrical resistivity (see Fig. 236).

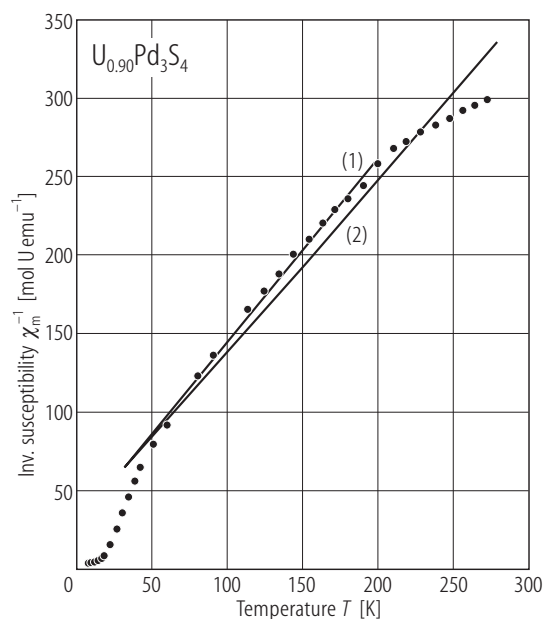




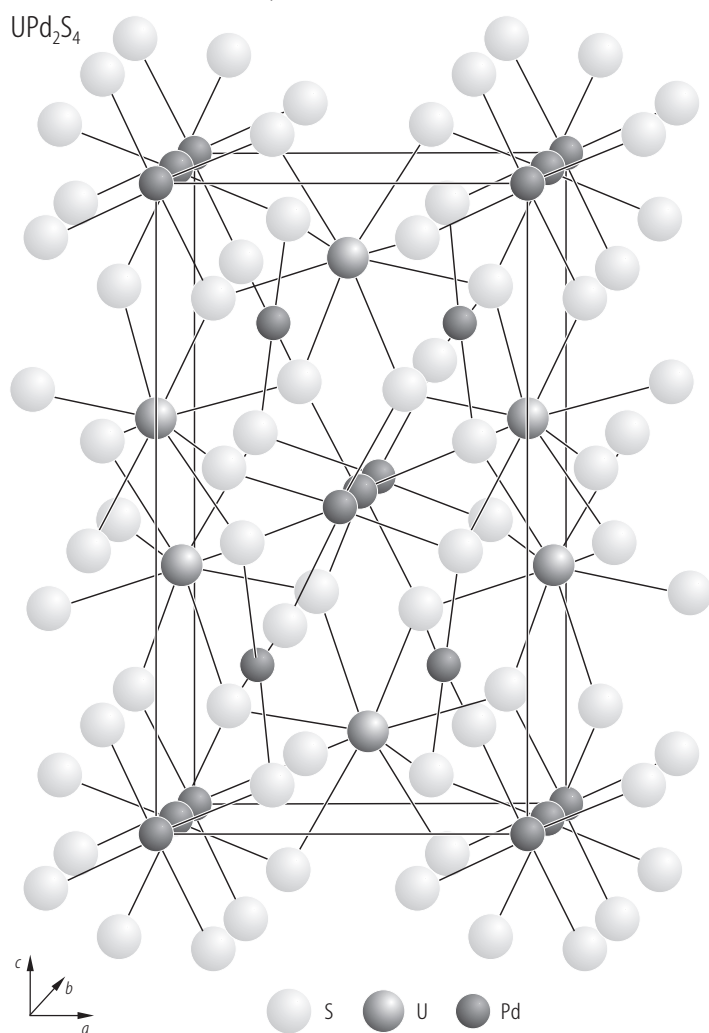
**Fig. 238.**  $U_xPd_3S_4$ . Crystal structure [86DN1].



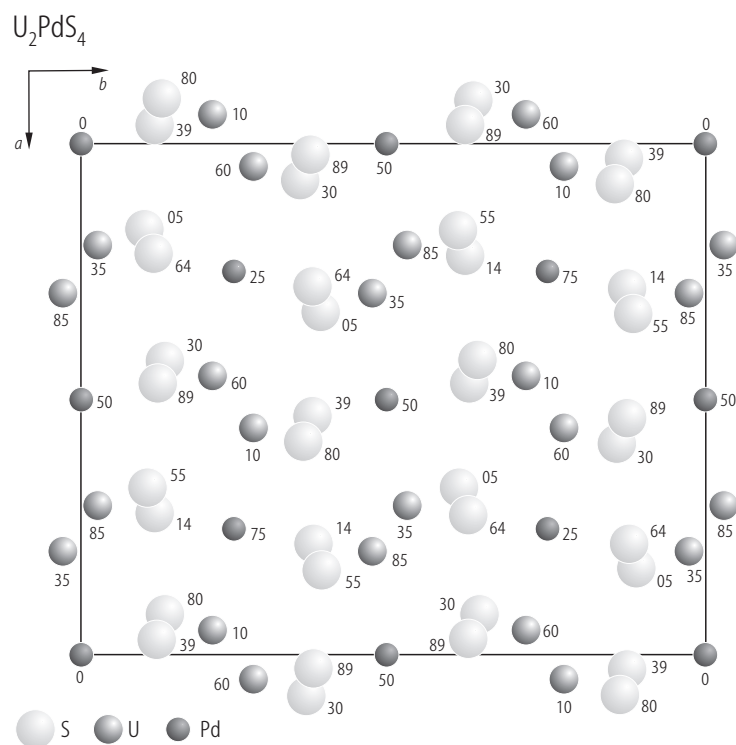
**Fig. 239.**  $U_xPd_3S_4$ . Lattice parameter,  $a$ , vs.  $x$  value [98FSYM]. The closed square corresponds to the value reported in [86DN1].



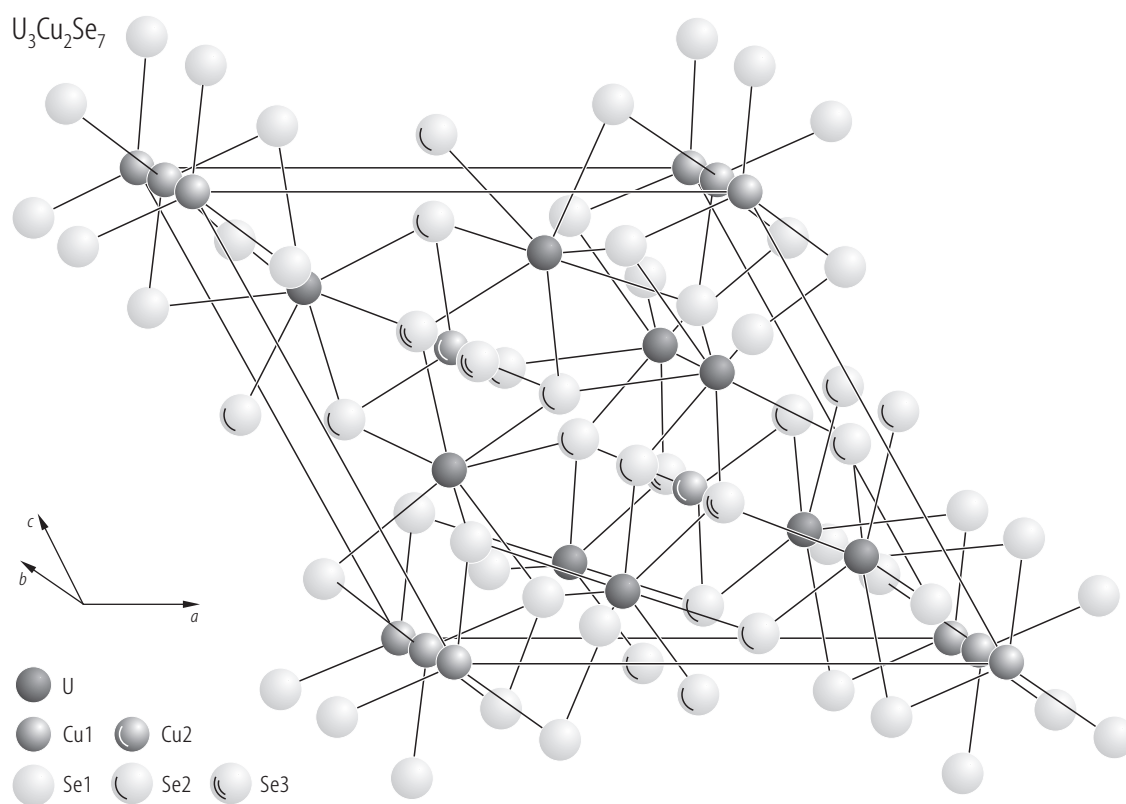
**Fig. 240.**  $U_xPd_3S_4$ ,  $x = 0.90$ . Reciprocal molar magnetic susceptibility,  $\chi_m^{-1}$ , vs. temperature,  $T$  [98FSYM]. Line (1): Curie-Weiss fit in the range 50...200 K ; line (2): Curie-Weiss fit in the range 30...270 K. For the CW fit parameters see Table B. The curvature of  $\chi_m^{-1}(T)$  seen above 200 K is ascribed by the authors to the manifestation of additional temperature independent susceptibility of unknown origin. The slope of line (1) gives the effective moment of  $2.60 \mu_B$  suggesting that the  $U^{4+}$  and  $U^{3+}$  ions are present in the compound in nearly the same amounts: 53 % and 47 % of  $U^{4+}$  and  $U^{3+}$ , respectively (assuming that the triplet  $\Gamma_5$  with  $p_{eff} = 2.83 \mu_B$  is the ground state level for  $U^{4+}$  ions and the Kramer's doublet  $\Gamma_6$  with  $p_{eff} = 2.31 \mu_B$  is the ground state level for  $U^{3+}$ ). The mixed valence state of uranium in  $U_xPd_3S_4$  is postulated also in [86DN1] on the basis of the bonding length being intermediate between those expected for  $U^{4+}-S^{2-}$  and  $U^{3+}-S^{2-}$  bonds.



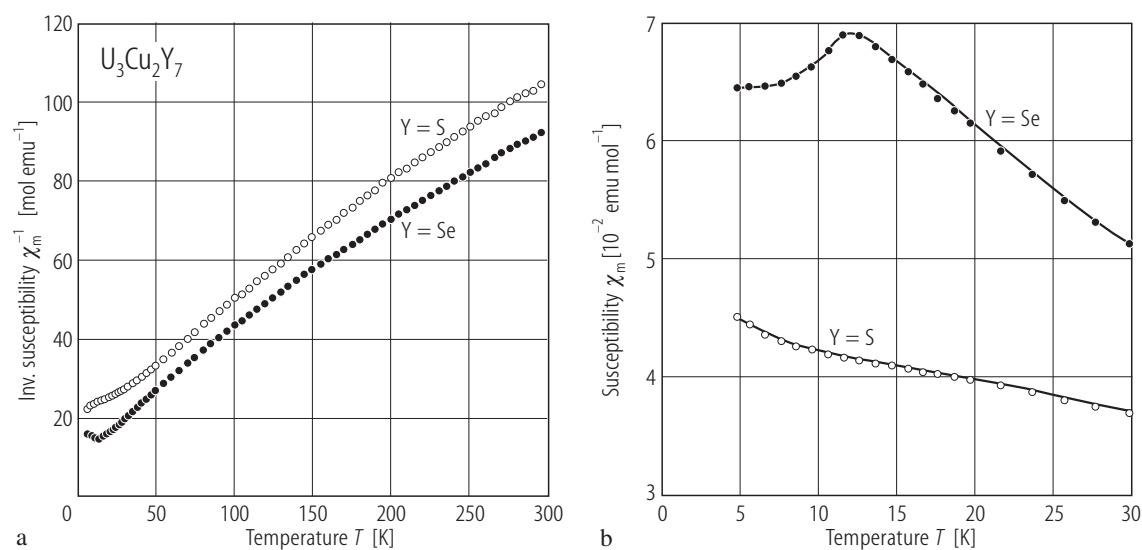
**Fig. 241.**  $UPd_2S_4$ . Crystal structure [85DN].



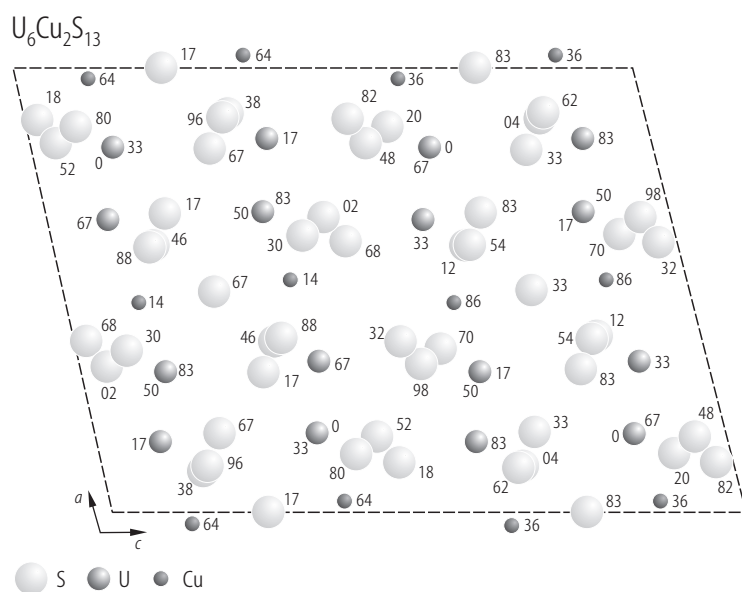
**Fig. 242.**  $\text{U}_2\text{PdS}_4$ . Crystal structure projected along the [001] axis [86DN2]. The numbers are the positions  $z$  ( $\cdot 10^2$ ) of the relevant atoms.



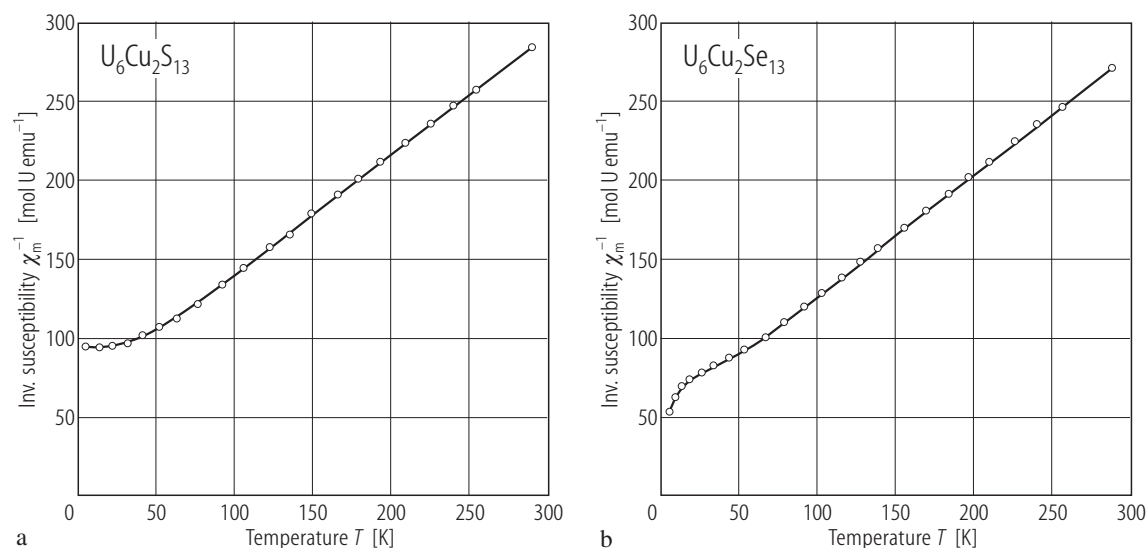
**Fig. 243.**  $\text{U}_3\text{Cu}_2\text{Se}_7$ . Crystal structure [96DLLN].



**Fig. 244.**  $U_3Cu_2Y_7$ ,  $Y = S, Se$ . **(a)** Reciprocal molar magnetic susceptibility,  $\chi_m^{-1}$ , vs. temperature,  $T$  [96DLLN]. Open circles:  $Y = S$ ; filled circles:  $Y = Se$ . **(b)** Low temperature molar magnetic susceptibility,  $\chi_m$ , vs.  $T$  [96DLLN].  $U_3Cu_2S_7$  is paramagnetic down to 5 K.  $U_3Cu_2Se_7$  orders antiferromagnetically at  $T_N = 13$  K. See also Table B.



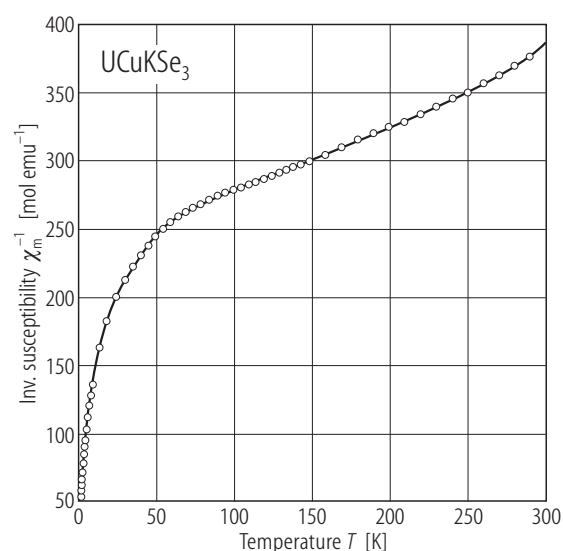
**Fig. 245.**  $U_6Cu_2S_{13}$ . Crystal structure projected on the  $(a,c)$  plane [85NP]. The numbers are the positions  $y$  ( $\times 10^2$ ) of the relevant atoms.



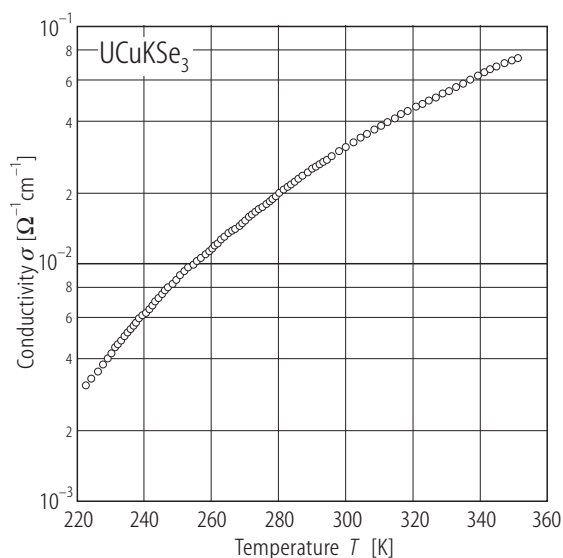
**Fig. 246.**  $\text{U}_6\text{Cu}_2\text{Y}_{13}$ , Y = S, Se. Reciprocal molar magnetic susceptibility,  $\chi_m^{-1}$ , vs. temperature,  $T$  for (a)  $\text{U}_6\text{Cu}_2\text{S}_{13}$  and (b)  $\text{U}_6\text{Cu}_2\text{Se}_{13}$  [80N]. Both compounds do not exhibit magnetic ordering down to 4.2 K. From the characteristic behavior of  $\chi_m^{-1}(T)$  at the lowest temperatures the author

suggested the presence of a singlet and a doublet crystal field ground state in the sulphide and the selenide, respectively. See the Curie-Weiss fit parameters given in Table B

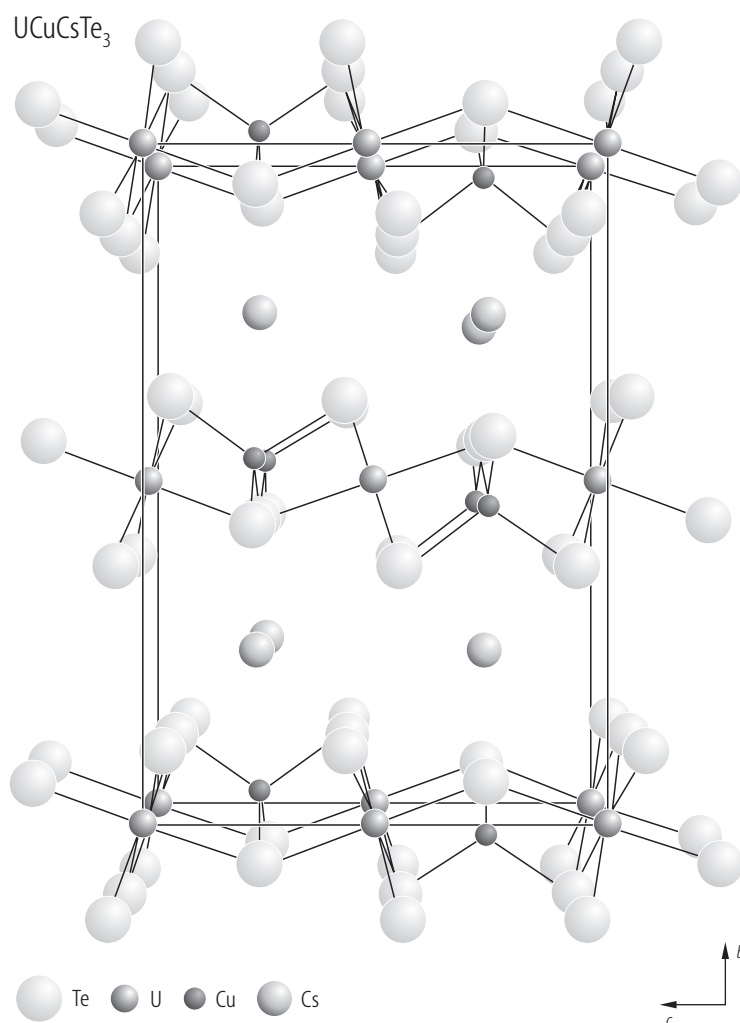
For Fig. 247 see next page



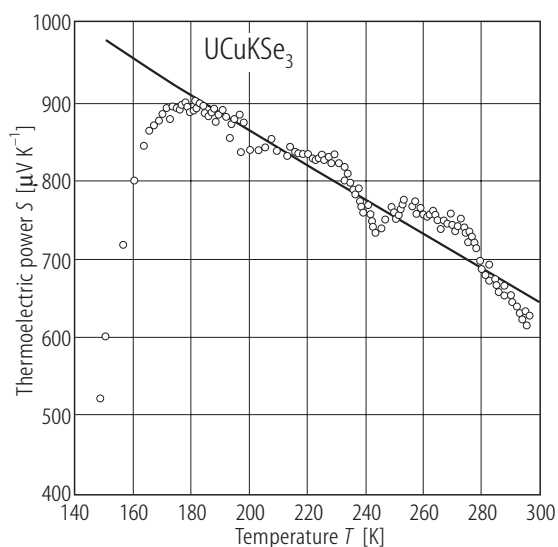
**Fig. 248.**  $\text{UCuKSe}_3$ . Reciprocal molar magnetic susceptibility,  $\chi_m^{-1}$ , vs. temperature,  $T$ , in the range 2...300 K [96SAHK]. The solid line serves as a guide for the eye. Fitting the data above 150 K to a Curie-Weiss law yields  $\mu_{\text{eff}} = 3.65 \mu_B$  and  $\theta_{\text{CW}} = -378$  K.



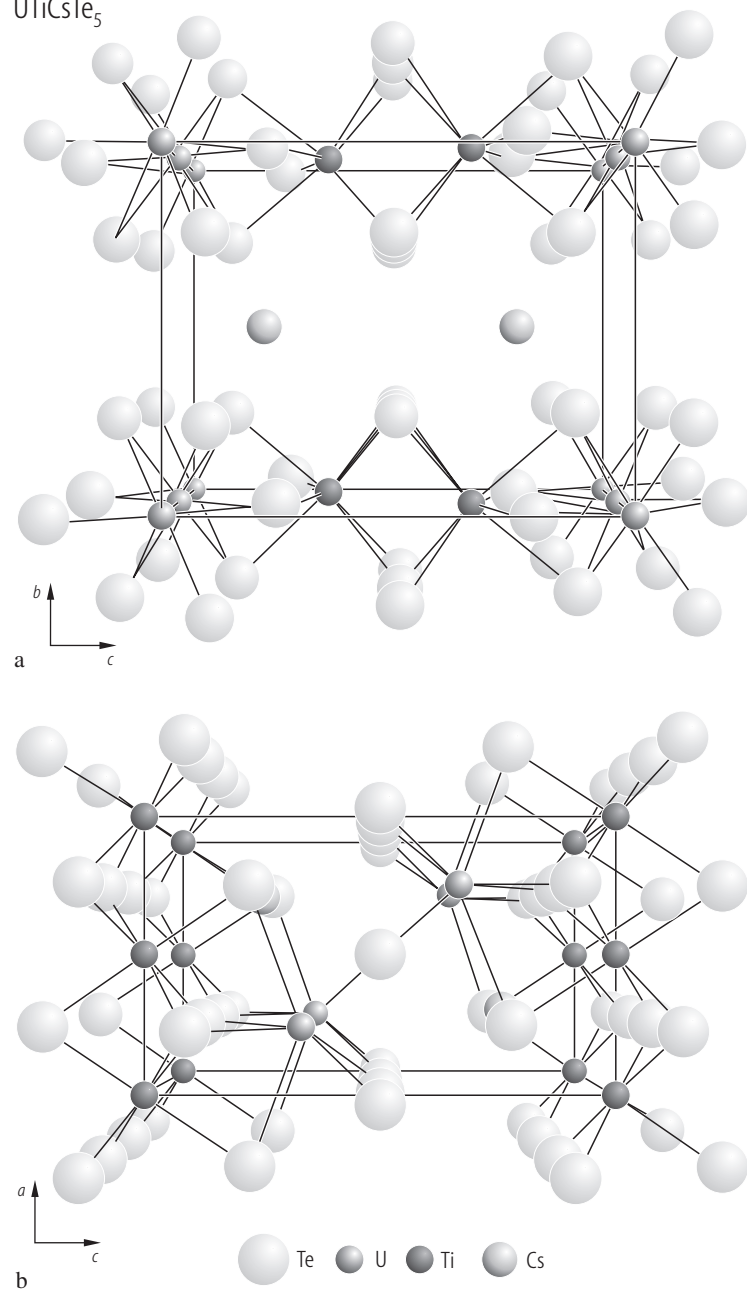
**Fig. 249.**  $\text{UCuKSe}_3$ . Electrical conductivity,  $\sigma$ , vs. temperature,  $T$ , measured on a single crystal in the range 220...350 K [96SAHK]. The compound is a semiconductor with the activation energy being in the range 0.164...0.167 eV.



**Fig. 247.** UCuCsTe<sub>3</sub>. Unit cell viewed down the [100] direction [95CI]. The structure has a two-dimensional layered character. Isostructural to UCuCsTe<sub>3</sub> are the thorium compounds ThCuKSe<sub>3</sub> and ThCuCsSe<sub>3</sub> [00NI] as well as the uranium compounds UCuKSe<sub>3</sub> [96SAHK] and UCuCsSe<sub>3</sub> [01HMI].



**Fig. 250.** UCuKSe<sub>3</sub>. Thermoelectric power,  $S$ , vs. temperature,  $T$ , measured on a single crystal in the range 150...300 K [96SAHK]. The solid line emphasizes a negative temperature coefficient, which together with large absolute values of  $S$  is characteristic of semiconductors. Positive Seebeck coefficient indicates the dominance of p-type carriers.

$\text{UTiCsTe}_5$ 

**Fig. 251.**  $\text{UTiCsTe}_5$ . Unit cell viewed down (a)  $[100]$  and (b)  $[010]$  directions [95Cl].

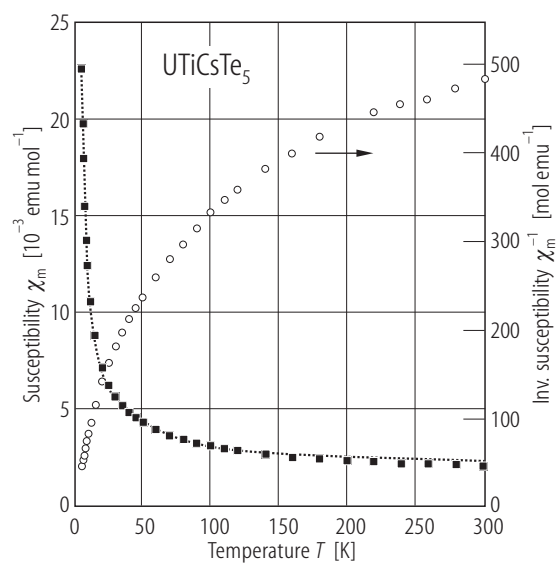


**Fig. 252.**  $\text{UTiCsTe}_5$ . Molar magnetic susceptibility,  $\chi_m$ , (squares; left-hand side scale) and reciprocal molar magnetic susceptibility,  $\chi_m^{-1}$ , (circles; right-hand side scale) vs. temperature,  $T$  [95CI]. The compound remains paramagnetic at least down to 6 K. The modified Curie-Weiss parameters are given in Table B.

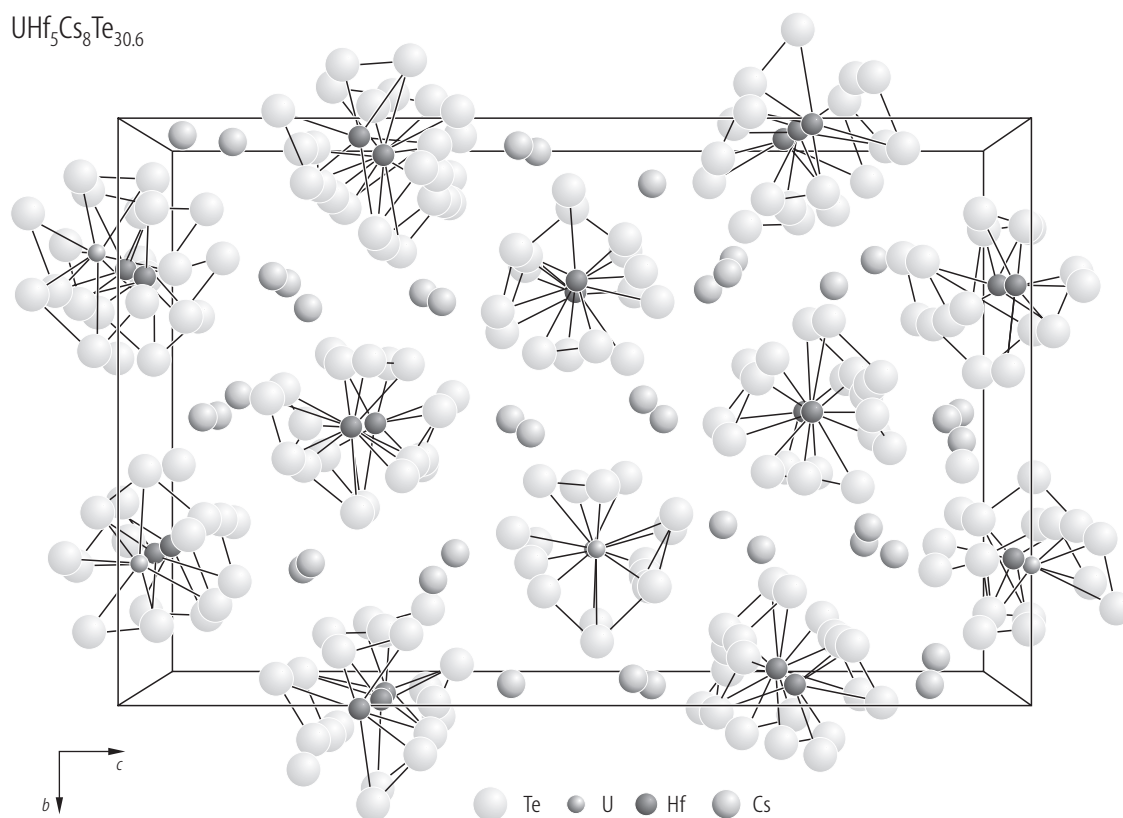


**Fig. 253.**  $\text{UHf}_5\text{Cs}_8\text{Te}_{30.6}$ . Crystal structure [95CI].



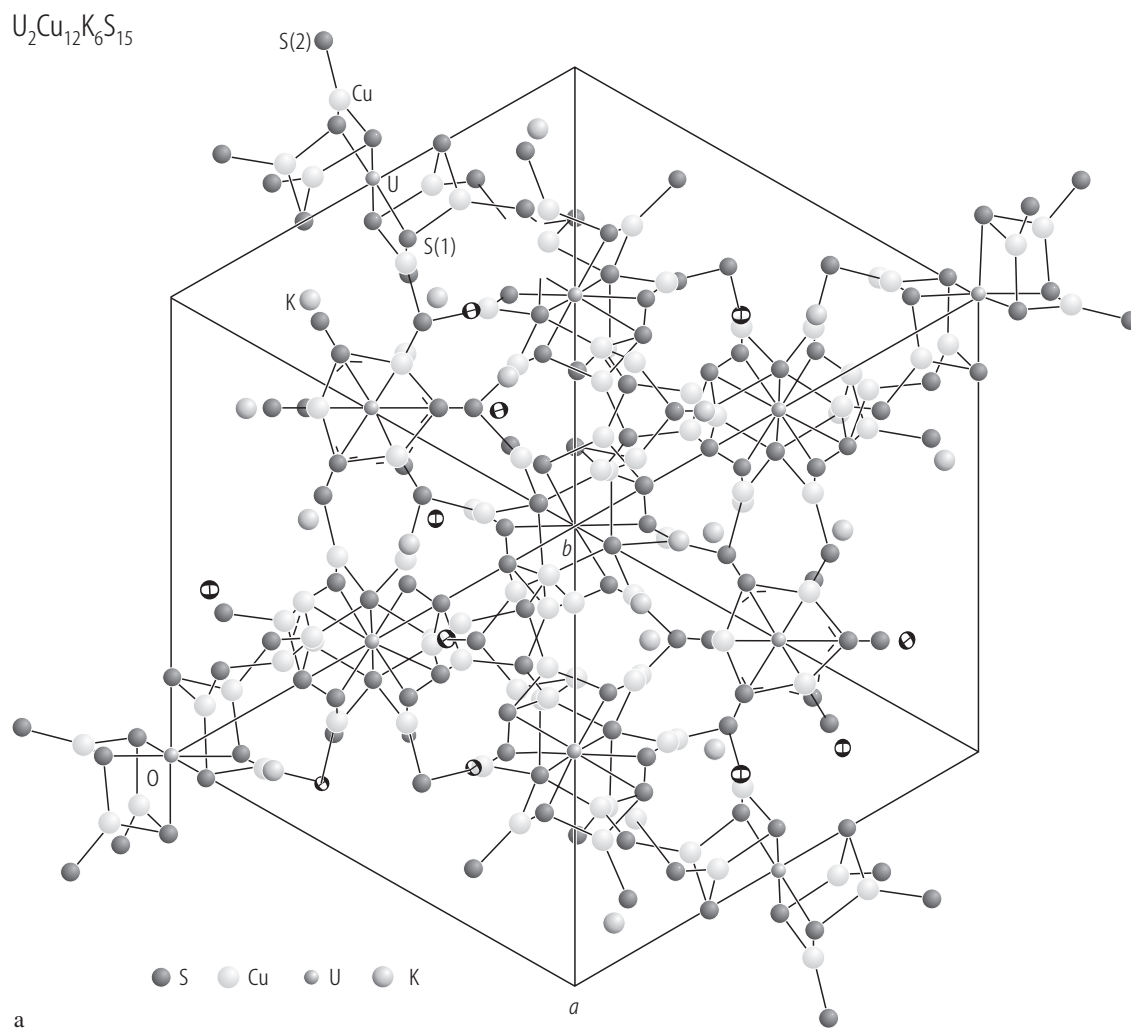
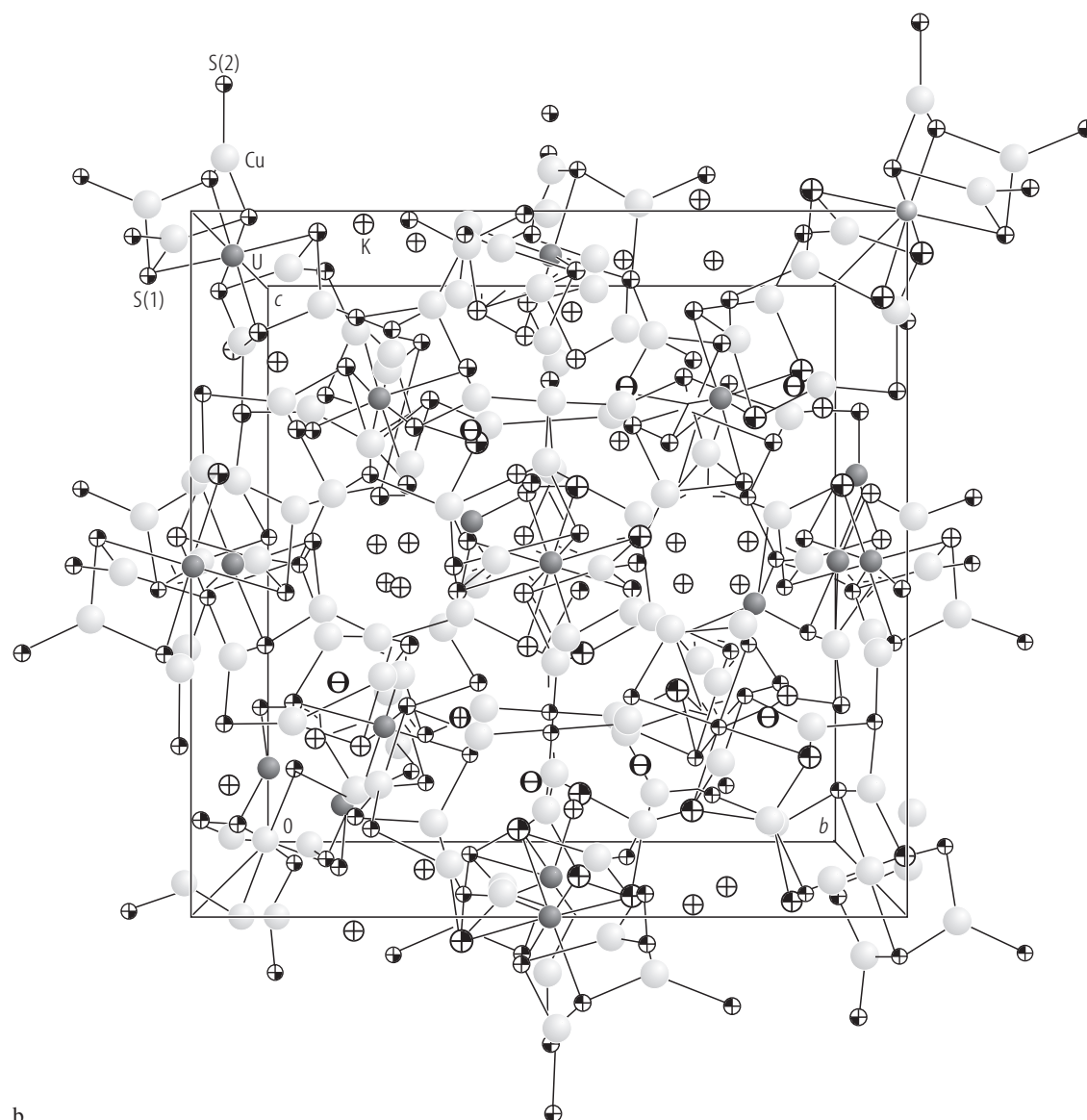


**Fig. 254.**  $\text{U}_2\text{Cu}_{12}\text{K}_6\text{S}_{15}$ . Unit cell viewed parallel to (a) the  $[100]$  axis; (b) the  $[1\bar{1}1]$  axis and (c) the  $[1\bar{1}0]$  axis [00SPSK]. The structure is built from  $[\text{US}_6]$  octahedra connected into one-dimensional columns with  $[\text{CuS}_3]$  trigonal planar units.

For Figs. 254(b) and (c) see next pages



b

**Fig. 254(b).**

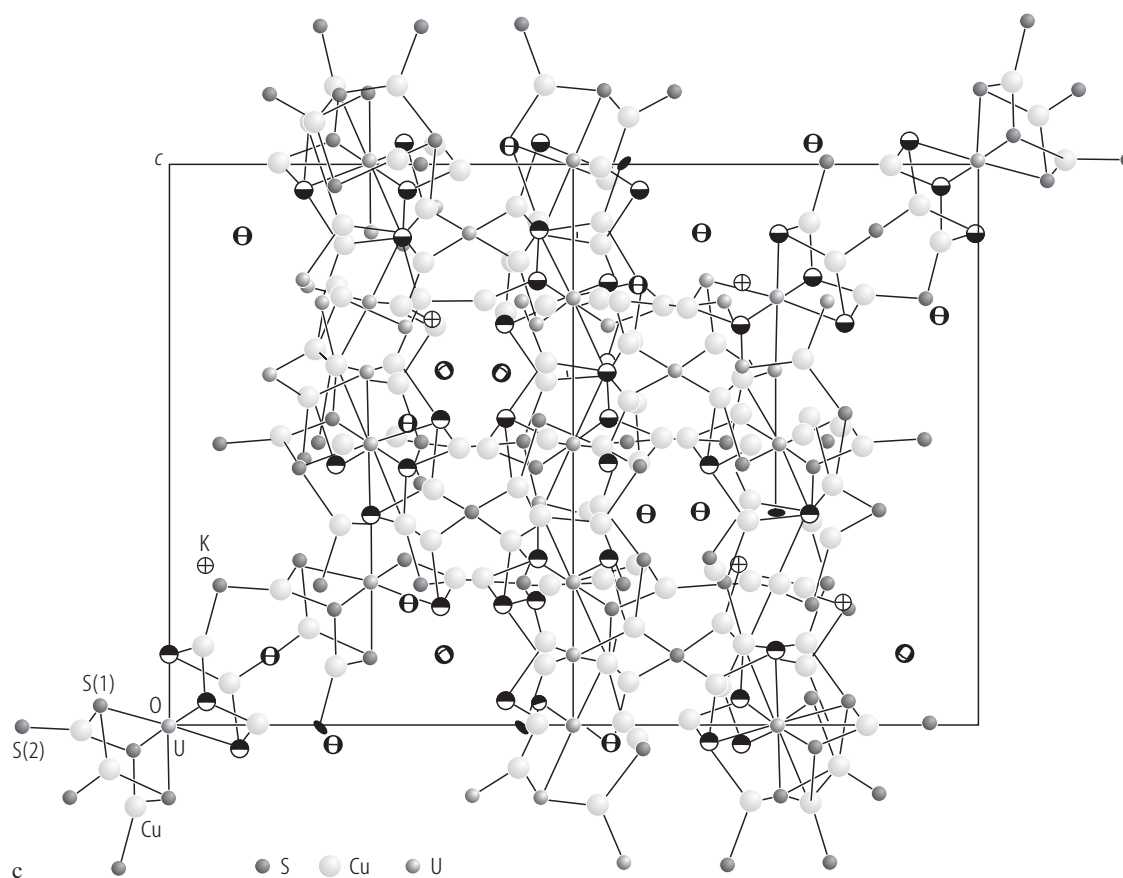
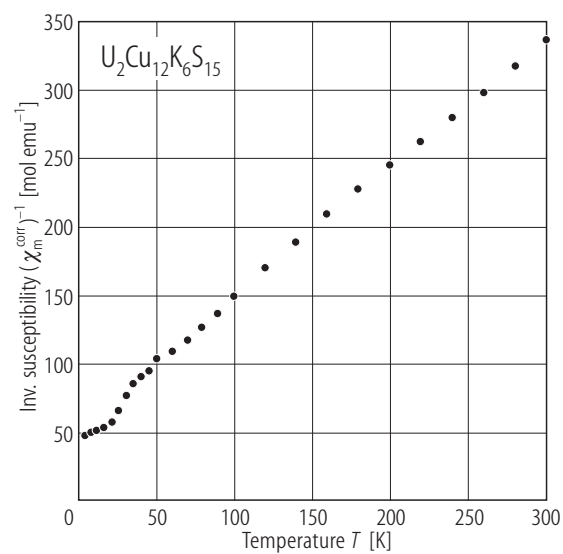
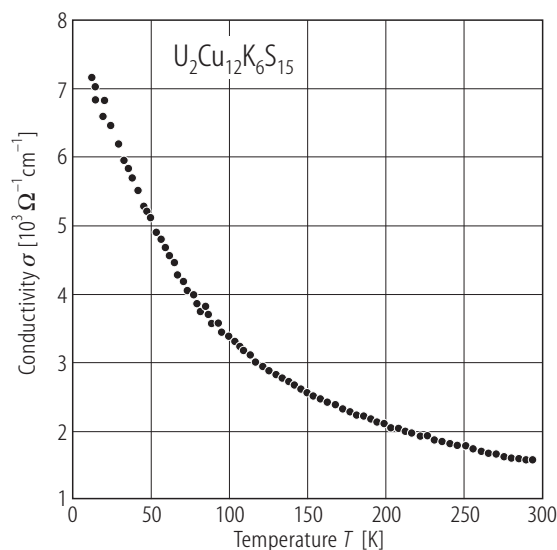


Fig. 254(c)



**Fig. 255.**  $\text{U}_2\text{Cu}_{12}\text{K}_6\text{S}_{15}$ . Reciprocal molar magnetic susceptibility,  $\chi_m^{-1}$ , vs. temperature,  $T$ , in the range 5...300 K [00SPSK]. The data were corrected for Pauli paramagnetism  $\chi_{\text{TIP}} = 0.0008$  emu/mol. Above 100 K, a Curie-Weiss behaviour is observed with the parameters  $p_{\text{eff}} = 2.96(2) \mu_B/\text{f.u.}$  and  $\Theta_{\text{CW}} = -69(4)$  K.



**Fig. 256.**  $\text{U}_2\text{Cu}_{12}\text{K}_6\text{S}_{15}$ . Electrical conductivity,  $\sigma$ , vs. temperature,  $T$ , in the range 6...300 K measured on a polycrystalline pellet compacted at 270 °C [00SPSK]. Note a metallic behaviour.

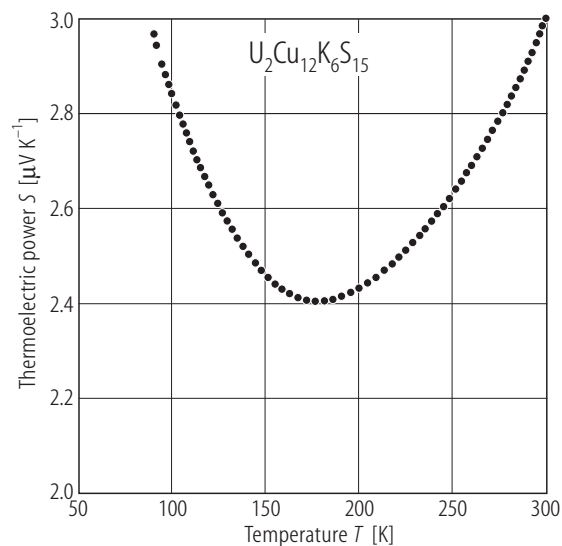


**Fig. 257.**  $\text{U}_2\text{Cu}_{12}\text{K}_6\text{S}_{15}$ . Thermoelectric power,  $S$ , vs. temperature,  $T$ , in the range 90...300 K measured on a polycrystalline pellet compacted at 270 °C [00SPSK]. Small absolute values of  $S$  and a positive slope of  $S(T)$  above 200 K are characteristic of good metals. The upturn at lower temperatures results probably from a phonon-drag. The positive thermopower indicates the dominance of p-type charge carriers.

**Table A.** Crystallographic data for actinide pnictides and chalcogenides containing d-electron transition metals.

Compound	Sym- metry	Point group (structure type)	Lattice parameters				Ref.
			<i>a</i> [pm]	<i>b</i> [pm]	<i>c</i> [pm]	$\beta$	
<b>AnTX</b>							
ThRhSb	cub.	F43m (MgAgAs)	666				<a href="#">87PNVV</a>
UNiAs	hex.	P6 <sub>3</sub> /mmc	404.8(1)		1532.5(5)		<a href="#">01JTR</a>
URhSb	cub.	F43m (MgAgAs)	653.4				<a href="#">85BDPN</a> , <a href="#">87PNVV</a>
UPdSb	hex.	P6 <sub>3</sub> /mmc (CaIn <sub>2</sub> )	458.7		721.5		<a href="#">85BDPN</a> , <a href="#">87PNVV</a>
<b>AnTX<sub>2</sub></b>							
UCoP <sub>2</sub>	tetr.	P4/nmm (HfCuSi <sub>2</sub> )	381.2		929.3		<a href="#">92K</a>
UCuP <sub>2</sub>	tetr.	I4/mmm (SrZnBi <sub>2</sub> )	380.3(1)		1852.3(9)		<a href="#">87NZKT1</a>
UFeAs <sub>2</sub>	tetr.	P4/nmm (HfCuSi <sub>2</sub> )	395.8		917.6		<a href="#">92K</a>
UCoAs <sub>2</sub>	tetr.	P4/nmm (HfCuSi <sub>2</sub> )	395.3		903.7		<a href="#">92K</a>
			396.15(6)		914.9(2)		<a href="#">00KNP</a>
UNiAs <sub>2</sub>	tetr.	P4/nmm (HfCuSi <sub>2</sub> )	395.1(1)		913.8(2)		<a href="#">89FMKT</a>
UCuAs <sub>2</sub>	tetr.	P4/nmm (HfCuSi <sub>2</sub> )	395.1(1)		955.8(3)		<a href="#">87SKT</a>
UPdAs <sub>2</sub>	tetr.	P4/nmm (HfCuSi <sub>2</sub> )	398.7(1)		949.3(3)		<a href="#">90MFK</a>
UFeSb <sub>2</sub>	tetr.	P4/nmm (HfCuSi <sub>2</sub> )	433.2(1)		932.0(3)		<a href="#">98KKSM</a>
URuSb <sub>2</sub>	tetr.	P4/nmm (HfCuSi <sub>2</sub> )	434.2(2)		924.9(2)		<a href="#">98KKSM</a>
UCoSb <sub>2</sub>	tetr.	P4/nmm (HfCuSi <sub>2</sub> )	431.1(2)		907.5(4)		<a href="#">98KKSM</a>
UNiSb <sub>2</sub>	tetr.	P4/nmm (HfCuSi <sub>2</sub> )	431.6		910.4		<a href="#">92K</a>
			432.2(1)		908.1(1)		<a href="#">98KKSM</a>
UPdSb <sub>2</sub>	tetr.	P4/nmm (HfCuSi <sub>2</sub> )	433.2(1)		952.0(2)		<a href="#">98KKSM</a>
UCuSb <sub>2</sub>	tetr.	P4/nmm (HfCuSi <sub>2</sub> )	431.2		964.0		<a href="#">92K</a>
			429.7(1)		964.3(2)		<a href="#">98KKSM</a>
UAgSb <sub>2</sub>	tetr.	P4/nmm (HfCuSi <sub>2</sub> )	432.40(6)		1031.8(2)		<a href="#">95BMJ</a>
			432.2(2)		1028.1(1)		<a href="#">98KKSM</a>
UAuSb <sub>2</sub>	tetr.	P4/nmm (HfCuSi <sub>2</sub> )	434.2(1)		979.5(1)		<a href="#">98KKSM</a>
UNiBi <sub>2</sub>	tetr.	P4/nmm (HfCuSi <sub>2</sub> )	447.0		907.3		<a href="#">92K</a>
UCuBi <sub>2</sub>	tetr.	P4/nmm (HfCuSi <sub>2</sub> )	452.6		937.6		<a href="#">92K</a>

Compound	Sym- metry	Point group (structure type)	Lattice parameters				Ref.
			<i>a</i> [pm]	<i>b</i> [pm]	<i>c</i> [pm]	$\beta$	
<b>AnT<sub>2</sub>X<sub>2</sub></b>							
ThCo <sub>2</sub> P <sub>2</sub>	tetr.	P4/nmm (CaBe <sub>2</sub> Ge <sub>2</sub> )	403.45(4)		912.5(1)		<a href="#">85JMMR</a>
ThCu <sub>2</sub> P <sub>2</sub>	hex.	P $\bar{3}$ m1 (CaAl <sub>2</sub> Si <sub>2</sub> )	402.8(1)		646.9(1)		<a href="#">79KMS</a>
$\alpha$ ThNi <sub>2</sub> P <sub>2</sub>	orth.	Pnma (BaCu <sub>2</sub> S <sub>2</sub> )	819.69(5)	394.28(3)	981.54(7)		<a href="#">94AJ</a>
$\beta$ ThNi <sub>2</sub> P <sub>2</sub>	tetr.	P4/nmm (CaBe <sub>2</sub> Ge <sub>2</sub> )	408.5(1)		908.0(3)		<a href="#">94AJ</a>
ThRu <sub>2</sub> P <sub>2</sub>	orth.	Pnma	753.15(5) 752.4(3)	413.95(4) 413.2(1)	1047.80(8) 1046.3(2)		<a href="#">87GJ</a> <a href="#">92GAJB</a>
ThCo <sub>2</sub> As <sub>2</sub>	tetr.	P4/nmm (CaBe <sub>2</sub> Ge <sub>2</sub> )	396.38(8)		894.6(3)		<a href="#">85JMMR</a>
UFe <sub>2</sub> P <sub>2</sub>	tetr.	I4/mmm (ThCr <sub>2</sub> Si <sub>2</sub> )	383.16(5)		941.0(2)		<a href="#">85JMMR</a>
UCo <sub>2</sub> P <sub>2</sub>	tetr.	P4/nmm (CaBe <sub>2</sub> Ge <sub>2</sub> )	396.38(8) 396.1(2) 395.5(5)		894.6(3) 894.6(3) 897.1(3)		<a href="#">85JMMR</a> <a href="#">88ZVLM</a> <a href="#">91RVJ</a>
UNi <sub>2</sub> P <sub>2</sub>	tetr.	I4/mmm (ThCr <sub>2</sub> Si <sub>2</sub> )	388.5(1)		940.4(3)		<a href="#">84HJ</a>
UNi <sub>1.56</sub> P <sub>2</sub>	tetr.	I4/mmm (ThCr <sub>2</sub> Si <sub>2</sub> )	382.8(1)		943.1(2)		<a href="#">89FMKT</a>
UCu <sub>2</sub> P <sub>2</sub>	hex.	P $\bar{3}$ m1 (CaAl <sub>2</sub> Si <sub>2</sub> )	394.1(1) 395.3(1)		636.6(2) 638.9(1)		<a href="#">87ZNK</a> <a href="#">94DZTK</a>
URu <sub>2</sub> P <sub>1.894(5)</sub>	orth.	Pnma	737.5(1)	406.20(4)	1028.9(1)		<a href="#">92GAJB</a>
UCo <sub>2</sub> As <sub>2</sub>	tetr.	P4/nmm (CaBe <sub>2</sub> Ge <sub>2</sub> )	399.2(2)		927.0(3)		<a href="#">88ZVLM</a>
UNi <sub>2</sub> As <sub>2</sub>	tetr.	P4/nmm (CaBe <sub>2</sub> Ge <sub>2</sub> )	403.06(6)		934.6(2)		<a href="#">88JHT</a>
UNi <sub>1.6</sub> As <sub>2</sub>	tetr.	P4/nmm (def. CaBe <sub>2</sub> Ge <sub>2</sub> )	399.4(1)		928.1(11)		<a href="#">90TKNG2</a>
URh <sub>1.6</sub> As <sub>1.9</sub>	tetr.	I4cm	1155.4(4)		1935.9(9)		<a href="#">88ZVLM</a>
<b>AnT<sub>4</sub>X<sub>12</sub></b>							
ThFe <sub>4</sub> P <sub>12</sub>	cub.	Im $\bar{3}$ (LaFe <sub>4</sub> P <sub>12</sub> )	779.99(6)				<a href="#">80BJ,95EJBB</a>
ThRu <sub>4</sub> P <sub>12</sub>	cub.	Im $\bar{3}$ (LaFe <sub>4</sub> P <sub>12</sub> )	804.61(4)				<a href="#">80BJ</a>
ThOs <sub>4</sub> As <sub>12</sub>	cub.	Im $\bar{3}$ (LaFe <sub>4</sub> P <sub>12</sub> )	851.83(6)				<a href="#">80BJ</a>
UFe <sub>4</sub> P <sub>12</sub>	cub.	Im $\bar{3}$ (LaFe <sub>4</sub> P <sub>12</sub> )	777.29 777.09(7) 722.28(5) (at 15 K)				<a href="#">85MTYM</a> <a href="#">95EJBB</a> <a href="#">99NDTB</a>

Compound	Sym- metry	Point group (structure type)	Lattice parameters				Ref.
			<i>a</i> [pm]	<i>b</i> [pm]	<i>c</i> [pm]	<i>β</i>	
<b>AnT<sub>5</sub>X<sub>3</sub></b>							
UV <sub>5</sub> P <sub>3</sub>	mon.	P2 <sub>1</sub> m	1018.0(3)	341.0(1)	748.8(2)	100.36(3)°	<a href="#">93JBP</a>
UCr <sub>5</sub> P <sub>3</sub>	mon.	P2 <sub>1</sub> m	959.1(2)	370.95(6)	696.7(1)	100.05(3)°	<a href="#">89BJ</a> , <a href="#">93JBP</a>
UMn <sub>5</sub> P <sub>3</sub>	orth.	Pnma (YCo <sub>5</sub> P <sub>3</sub> )	1225.0(3)	369.3(1)	1072.6(3)		<a href="#">87PJ</a> , <a href="#">93JBP</a>
<b>An<sub>2</sub>T<sub>12</sub>X<sub>7</sub></b>							
Th <sub>2</sub> Mn <sub>12</sub> P <sub>7</sub>	hex.	P $\bar{6}$ (Zr <sub>2</sub> Fe <sub>12</sub> P <sub>7</sub> )	951.1(2)		373.8(1)		<a href="#">93JPM</a>
U <sub>2</sub> Mn <sub>12</sub> P <sub>7</sub>	hex.	P $\bar{6}$ (Zr <sub>2</sub> Fe <sub>12</sub> P <sub>7</sub> )	937.70(8)		364.42(4)		<a href="#">87PJ</a>
U <sub>2</sub> Fe <sub>12</sub> P <sub>7</sub>	hex.	P $\bar{6}$ (Zr <sub>2</sub> Fe <sub>12</sub> P <sub>7</sub> )	938.3(2)		364.8(1)		<a href="#">93JPM</a>
U <sub>2</sub> Co <sub>12</sub> P <sub>7</sub>	hex.	P $\bar{6}$ (Zr <sub>2</sub> Fe <sub>12</sub> P <sub>7</sub> )	908.4(1)		364.3(1)		<a href="#">93JPM</a>
U <sub>2</sub> Ni <sub>12</sub> P <sub>7</sub>	hex.	P $\bar{6}$ (Zr <sub>2</sub> Fe <sub>12</sub> P <sub>7</sub> )	904.7(1)		359.2(1)		<a href="#">93JPM</a>
U <sub>2</sub> Rh <sub>12</sub> P <sub>7</sub>	hex.	P $\bar{6}$	907.7(2)		369.4(1)		<a href="#">91PM</a>
U <sub>2</sub> Ni <sub>12</sub> As <sub>7</sub>	hex.	P $\bar{6}$ (Zr <sub>2</sub> Fe <sub>12</sub> P <sub>7</sub> )	907.9(1)		369.5(1)		<a href="#">93JPM</a>
			907.2(3)		369.4(1)		<a href="#">98EAJ</a>
			956		385		<a href="#">87GCMS</a>
			937.8(1)		383.8(1)		<a href="#">01SKW</a>
<b>An<sub>3</sub>TX<sub>5</sub></b>							
U <sub>3</sub> TiSb <sub>5</sub>	hex.	P6 <sub>3</sub> /mcm (anti- Hf <sub>5</sub> CuSn <sub>3</sub> )	913.9(2)		611.2(2)		<a href="#">94BJ</a>
U <sub>3</sub> VSb <sub>5</sub>	hex.	P6 <sub>3</sub> /mcm (anti- Hf <sub>5</sub> CuSn <sub>3</sub> )	908.2(2)		608.3(2)		<a href="#">94BJ</a>
U <sub>3</sub> CrSb <sub>5</sub>	hex.	P6 <sub>3</sub> /mcm (anti- Hf <sub>5</sub> CuSn <sub>3</sub> )	911.0(1)		611.5(1)		<a href="#">94BJ</a>
U <sub>3</sub> MnSb <sub>5</sub>	hex.	P6 <sub>3</sub> /mcm (anti- Hf <sub>5</sub> CuSn <sub>3</sub> )	916.8(2)		613.2(1)		<a href="#">94BJ</a>
<b>An<sub>3</sub>T<sub>3</sub>X<sub>4</sub></b>							
Th <sub>3</sub> Co <sub>3</sub> Sb <sub>4</sub>	cub.	I $\bar{4}$ 3d (Y <sub>3</sub> Au <sub>3</sub> Sb <sub>4</sub> )	957.2(2)				<a href="#">01SK</a>
U <sub>3</sub> Co <sub>3</sub> Sb <sub>4</sub>	cub.	I $\bar{4}$ 3d (Y <sub>3</sub> Au <sub>3</sub> Sb <sub>4</sub> )	930.3(2)				<a href="#">79D</a>
			930.3				<a href="#">85BDPN</a>
			928.4				<a href="#">90ENMB</a>
U <sub>3</sub> Ni <sub>3</sub> Sb <sub>4</sub>	cub.	I $\bar{4}$ 3d (Y <sub>3</sub> Au <sub>3</sub> Sb <sub>4</sub> )	938.6(2)				<a href="#">79D</a>
			937.7				<a href="#">85BDPN</a> ,
							<a href="#">90ENMB</a>
			939.3				<a href="#">90TMFA2</a>

Compound	Sym- metry	Point group (structure type)	Lattice parameters				Ref.
			<i>a</i> [pm]	<i>b</i> [pm]	<i>c</i> [pm]	$\beta$	
U <sub>3</sub> Cu <sub>3</sub> Sb <sub>4</sub>	cub.	I $\bar{4}$ 3d (Y <sub>3</sub> Au <sub>3</sub> Sb <sub>4</sub> )	944.5 945.1				<a href="#">90ENMB</a> <a href="#">90TMFA2</a>
U <sub>3</sub> Rh <sub>3</sub> Sb <sub>4</sub>	cub.	I $\bar{4}$ 3d (Y <sub>3</sub> Au <sub>3</sub> Sb <sub>4</sub> )	953.1(2)				<a href="#">79D</a>
U <sub>3</sub> Pd <sub>3</sub> Sb <sub>4</sub>	cub.	I $\bar{4}$ 3d (Y <sub>3</sub> Au <sub>3</sub> Sb <sub>4</sub> )	967.2(2) 968.4				<a href="#">79D</a> <a href="#">90TMFA2</a>
U <sub>3</sub> Ir <sub>3</sub> Sb <sub>4</sub>	cub.	I $\bar{4}$ 3d (Y <sub>3</sub> Au <sub>3</sub> Sb <sub>4</sub> )	957.2(2)				<a href="#">79D</a>
U <sub>3</sub> Pt <sub>3</sub> Sb <sub>4</sub>	cub.	I $\bar{4}$ 3d (Y <sub>3</sub> Au <sub>3</sub> Sb <sub>4</sub> )	966.1(2) 968.3				<a href="#">79D</a> <a href="#">90TMFA2</a>
<b>An<sub>6</sub>T<sub>20</sub>X<sub>13</sub></b>							
U <sub>6</sub> Ni <sub>20</sub> P <sub>13</sub>	hex.	P6 <sub>3</sub> /m (Ho <sub>6</sub> Ni <sub>20</sub> P <sub>13</sub> )	1266.4(4)		378.9(2)		<a href="#">92TKNL</a>
		P $\bar{6}$ (Zr <sub>6</sub> Ni <sub>20</sub> P <sub>13</sub> )	1267.6(2)		377.31(4)		<a href="#">98EAJ</a>
U <sub>6</sub> Rh <sub>20</sub> P <sub>13</sub>	hex.	P $\bar{6}$ (Zr <sub>6</sub> Ni <sub>20</sub> P <sub>13</sub> )	1325.9(7)		389.6(7)		<a href="#">87GCMS</a>
U <sub>6</sub> Ni <sub>20</sub> As <sub>13</sub>	hex.	P6 <sub>3</sub> /m (Ho <sub>6</sub> Ni <sub>20</sub> P <sub>13</sub> )	1304.4(4)		388.8(2)		<a href="#">92TKNL</a>
<b>other pnictides</b>							
U <sub>0.87</sub> Mo <sub>13</sub> P <sub>9</sub>	hex.	P $\bar{6}$ m2	1080.7(1)		331.12(5)		<a href="#">87BJ</a>
UNi <sub>3</sub> P <sub>2</sub>	orth.	Pmmm (HoCo <sub>3</sub> P <sub>2</sub> )	1047.5(2)	379.40(4)	1238.2(2)		<a href="#">98EAJ</a>
ThFe <sub>4</sub> P <sub>2</sub>	orth.	Pnnm (SmNi <sub>4</sub> P <sub>2</sub> )	1448.9(2)	1074.7(2)	376.98(4)		<a href="#">92AJ1</a>
UMn <sub>4</sub> P <sub>2</sub>	tetr.	P4 <sub>2</sub> /mnm (ZrFe <sub>4</sub> Si <sub>2</sub> )	719.93(5) 720.1(1)		370.18(4) 370.1(1)		<a href="#">87PJ</a> <a href="#">90JTRP</a>
UNi <sub>4</sub> P <sub>2</sub>	tetr.	P4 <sub>2</sub> /mnm (ZrFe <sub>4</sub> Si <sub>2</sub> )	707.67(1)		365.58(1)		<a href="#">98EAJ</a>
$\alpha$ -UCr <sub>6</sub> P <sub>4</sub>	hex.	P $\bar{6}$ m2	698.5(3)		350.8(1)		<a href="#">86BJ,92JB</a>
$\beta$ -UCr <sub>6</sub> P <sub>4</sub>	orth.	Pmmn	698.6(1)	350.85(4)	1196.1(2)		<a href="#">87BJ,92JB</a>
U <sub>2</sub> Cu <sub>4</sub> As <sub>5</sub>	tetr.	I4/mmm	399.0(1)		2429.9(15)		<a href="#">91KNT</a>
U <sub>2</sub> Cr <sub>30</sub> P <sub>19</sub>	hex.	P $\bar{6}$ (Zr <sub>2</sub> Cr <sub>30</sub> P <sub>19</sub> )	1482.4(4) 1481.4(2)		337.88(8) 337.6(1)		<a href="#">87BJ</a> <a href="#">98LPDG</a>
U <sub>3</sub> NiAs <sub>4</sub>	cub.	I $\bar{4}$ 3d (def. Y <sub>3</sub> Au <sub>3</sub> Sb <sub>4</sub> )	867.2(1)				<a href="#">90TKNG1</a>
U <sub>3</sub> Cu <sub>2</sub> Sb <sub>3</sub>	hex.	P6 <sub>3</sub> /mmc	439.3		2301.1		<a href="#">86DB</a>
U <sub>3</sub> Ni <sub>3.34</sub> P <sub>6</sub>	tetr.	P4/mmm	381.8(1) 381.5(1)		1350.1(4) 1350.2(3)		<a href="#">95EJ</a> <a href="#">96REJS</a>
U <sub>4</sub> Cu <sub>4</sub> P <sub>7</sub>	tetr.	I4/mmm	380.3(1)		3495.4(7)		<a href="#">87NZKT2</a>
U <sub>4</sub> Ru <sub>7</sub> As <sub>6</sub>	cub.	Im $\bar{3}$ m	830.48(7)				<a href="#">00NPK</a>
Th <sub>5</sub> Fe <sub>19</sub> P <sub>12</sub>	mon.	C2/m	2920.3(3)	379.18(3)	931.48(8)	103.36(1)°	<a href="#">92AJ1</a>
U <sub>5</sub> Rh <sub>19</sub> P <sub>12</sub>	hex.		1207		371		<a href="#">87GCMS</a>



Compound	Sym- metry	Point group (structure type)	Lattice parameters				Ref.
			<i>a</i> [pm]	<i>b</i> [pm]	<i>c</i> [pm]	$\beta$	
U <sub>6</sub> Ni <sub>15</sub> P <sub>10</sub>	hex.	P6 <sub>3</sub> /m (Ce <sub>6</sub> Ni <sub>15</sub> P <sub>10</sub> )	1641.04(8)		380.90(6)		<a href="#">02KPN</a>
U <sub>6</sub> Mo <sub>74</sub> P <sub>49</sub>	hex.	P $\bar{6}$	2556.1(5)		333.38(6)		<a href="#">88BJ</a>
Th <sub>11</sub> Ni <sub>25</sub> P <sub>20</sub>	orth.	Pmmn	392.57(2)	3508.7(2)	1247.9(2)		<a href="#">96AJ2</a>
U <sub>11</sub> Ni <sub>25</sub> P <sub>20</sub>	orth.	Pmmn	380.38(3)	3480.4(3)	1226.4(1)		<a href="#">96AJ2</a>
ThCu <sub>0.938(4)</sub> PO	tetr.	P4/nmm (ZrCuSiAs)	389.43(4)		828.3(1)		<a href="#">96AJ1</a>
ThCuAsO	tetr.	P4/nmm (ZrCuSiAs)	396.14(5)		844.0(2)		<a href="#">96AJ1</a>
UCuPO	tetr.	P4/nmm (ZrCuSiAs)	379.3(1)		823.3(2)		<a href="#">94KANJ</a>
UMnAsO	tetr.	P4/nmm (ZrCuSiAs)	386.9(1)		852.5(2)		<a href="#">97NJPB</a>
Th <sub>2</sub> Ni <sub>2.45(1)</sub> P <sub>3</sub> O	tetr.	P4/nmm	394.62(4)		1723.2(3)		<a href="#">96AJ1</a>
U <sub>2</sub> Cu <sub>2</sub> As <sub>3</sub> O	tetr.	P4/nmm	391.11(2)		1791.6(4)		<a href="#">94KPN</a>
<b>AnTY<sub>3</sub></b>							
ThMnTe <sub>3</sub>	orth.	Cmcm	427.83(6)	1386.18(11)	995.68(15)		<a href="#">00NI</a>
UScS <sub>3</sub>	orth.	Cmcm	376.5(2)	1213.4(6)	917.6(5)		<a href="#">78JRT</a>
UVS <sub>3</sub>	orth.	Pna2 <sub>1</sub>	697.4(2)	612.4(2)	900.1(4)		<a href="#">73N</a>
			697	612	900		<a href="#">85NCKS</a>
UCrS <sub>3</sub>	orth.	Pna2 <sub>1</sub>	716.3(3)	609.5(2)	885.1(3)		<a href="#">73N,75NPP2</a>
		Pnam	712	610	880		<a href="#">85NCKS</a>
UFeS <sub>3</sub>	orth.	Cmc2 <sub>1</sub>	379.5(5)	1162.6(9)	871.7(9)		<a href="#">71NPP</a>
		Cmcm	379.5(3)	1162.6(5)	871.7(4)		<a href="#">76NP</a>
UCoS <sub>3</sub>	orth.	Pna2 <sub>1</sub>	699.0(5)	591.4(5)	862.5(8)		<a href="#">71NPP,81C</a>
		or Pnam					<a href="#">WBN</a>
UNiS <sub>3</sub>	orth.	Pna2 <sub>1</sub>	689.6(6)	607.6(6)	879.3(8)		<a href="#">71NPP</a>
UNbS <sub>3</sub>	orth.	Pnmm	665	612	899		<a href="#">85NCKS</a>
URuS <sub>3</sub>	orth.	Pnam	693.9(2)	589.6(2)	877.0(3)		<a href="#">87DN</a>
URhS <sub>3</sub>	orth.	Pnam	711.9(2)	597.8(2)	861.8(2)		<a href="#">87DN</a>
UTaS <sub>3</sub>	orth.	Pna2 <sub>1</sub>	664	610	898		<a href="#">85NCKS</a>
UVSe <sub>3</sub>	orth.	Pnam	727.8(3)	638.0(3)	940.5(4)		<a href="#">74N</a>
UCrSe <sub>3</sub>	orth.	Pnam	748.4(4)	638.2(2)	927.6(4)		<a href="#">74N</a>
UMnSe <sub>3</sub>	orth.	Cmcm	392.9(3)	1277.1(5)	919.4(3)		<a href="#">74N</a>
UFeSe <sub>3</sub>	orth.	Cmcm	394.2(3)	1220.6(5)	911.7(4)		<a href="#">74N</a>
UCoSe <sub>2.7</sub>	orth.	Pnam	733.8(5)	622.9(4)	906.3(6)		<a href="#">74N</a>
UNiSe <sub>2.8</sub>	orth.	Pnam	754.0(4)	622.3(3)	897.6(5)		<a href="#">74N</a>
UPdSe <sub>3</sub>	orth.	Pnam	813.0(3)	627.1(2)	871.7(2)		<a href="#">89DN</a>
<b>An<sub>2</sub>TY<sub>5</sub></b>							
Th <sub>2</sub> FeS <sub>5</sub>	mon.	C2/c					<a href="#">80BFNW</a>
U <sub>2</sub> TiS <sub>5</sub>	orth.	Pcmm	740	790	1169		<a href="#">84NCKS2</a>
U <sub>2</sub> FeS <sub>5</sub>	mon.	C2/c	1469.7(5)	632.6(3)	702.4(5)	96°30(5)'	<a href="#">76NPP</a>
U <sub>2</sub> CoS <sub>5</sub>	mon.	C2/c	1468.5(5)	625.9(4)	702.0(4)	96°25(5)'	<a href="#">73N</a>
U <sub>2</sub> CoS <sub>4</sub> Se	mon.		1472	632	708	95.20°	<a href="#">93CSKM</a>

Compound	Sym- metry	Point group (structure type)	Lattice parameters				Ref.
			<i>a</i> [pm]	<i>b</i> [pm]	<i>c</i> [pm]	$\beta$	
U <sub>2</sub> CoS <sub>3</sub> Se <sub>2</sub>	mon.		1477	635	713	95.05°	<a href="#">93CSKM</a>
U <sub>2</sub> CoS <sub>2</sub> Se <sub>3</sub>	mon.		1485	637	722	94.93°	<a href="#">93CSKM</a>
U <sub>2</sub> CoSSe <sub>4</sub>	mon.		1508	638	728	94.75°	<a href="#">93CSKM</a>
U <sub>2</sub> ZrS <sub>5</sub>	orth.	Pcmn	731	786	1168		<a href="#">84NCKS2</a>
U <sub>2</sub> HfS <sub>5</sub>	cub.		545				<a href="#">84NCKS2</a>
U <sub>2</sub> FeSe <sub>5</sub>	mon.	C2/c	1536.8(9)	659.5(4)	738.6(7)	96°40(5)'	<a href="#">74N</a>
<b>An<sub>3</sub>TY<sub>6</sub></b>							
U <sub>3</sub> ScS <sub>6</sub>	orth.	Pnnm	1635.5(8)	1347.2(7)	382.3(2)		<a href="#">76RT</a>
U <sub>3</sub> TiS <sub>6</sub>	orth.	Pbnm (Sb <sub>2</sub> S <sub>3</sub> )	1027	1056	382		<a href="#">84NCKS2</a>
U <sub>3</sub> ZrS <sub>6</sub>	orth.	Pbnm (Sb <sub>2</sub> S <sub>3</sub> )	1025	1049	385		<a href="#">84NCKS2</a>
U <sub>3</sub> HfS <sub>6</sub>	cub.		545				<a href="#">84NCKS2</a>
<b>An<sub>6</sub>T<sub>2</sub>Y<sub>15.5</sub></b>							
U <sub>6</sub> Rh <sub>2</sub> S <sub>15.5</sub>	cub.	Im3m	1326.4(5)				<a href="#">96DN</a>
U <sub>6</sub> Ir <sub>2</sub> S <sub>15.5</sub>	cub.	Im3m	1324.2(1)				<a href="#">96DN</a>
U <sub>6</sub> Rh <sub>2</sub> Se <sub>15.5</sub>	cub.	Im3m	1373.7(2)				<a href="#">96DN</a>
U <sub>6</sub> Ir <sub>2</sub> Se <sub>15.5</sub>	cub.	Im3m	1375.9(1)				<a href="#">96DN</a>
<b>An<sub>8</sub>TY<sub>17</sub></b>							
U <sub>8</sub> TiS <sub>17</sub>	mon.	C2	1332.6(10)	845.5(4)	1044.5(6)	101°15(5)'	<a href="#">73N</a>
U <sub>8</sub> VS <sub>17</sub>	mon.	C2	1336.5(10)	841.2(4)	1044.2(6)	101°16(5)'	<a href="#">73N</a>
U <sub>8</sub> CrS <sub>17</sub>	mon.	C2/m	1329.0(5)	842.3(2)	1042.7(4)	101°35(3)'	<a href="#">73N,75NPP1</a>
U <sub>8</sub> MnS <sub>17</sub>	mon.	C2	1340.3(10)	840.1(4)	1053.1(6)	101°38(5)'	<a href="#">73N</a>
U <sub>8</sub> FeS <sub>17</sub>	mon.	C2	1338.5(15)	834(1)	1040.3(12)	101°43(5)'	<a href="#">71NPP</a>
			1337.3(8)	840.5(3)	1048.0(5)	101°31(4)'	<a href="#">73N</a>
		C2/m	1334.0(3)	839.9(2)	1044.7(2)	101.49(3)°	<a href="#">97KSB</a>
U <sub>8</sub> CoS <sub>17</sub>	mon.	C2	1336.8(8)	838.9(3)	1044.3(5)	101°36(3)'	<a href="#">73N</a>
U <sub>8</sub> NiS <sub>17</sub>	mon.	C2	1335.2(11)	838.6(5)	1043.1(7)	101°34(6)'	<a href="#">73N</a>
U <sub>8</sub> TiSe <sub>17</sub>	mon.	C2/m	1395.6(9)	878.9(4)	1090.1(8)	101°46(5)'	<a href="#">74N</a>
U <sub>8</sub> VSe <sub>17</sub>	mon.	C2/m	1396.1(9)	877.6(4)	1091.6(8)	101°46(5)'	<a href="#">74N</a>
U <sub>8</sub> CrSe <sub>17</sub>	mon.	C2/m	1391.4(9)	878.6(4)	1091.2(7)	101°48(5)'	<a href="#">74N</a>
U <sub>8</sub> MnSe <sub>17</sub>	mon.	C2/m	1402.6(9)	877.9(6)	1100.7(9)	102°03(6)'	<a href="#">74N</a>
U <sub>8</sub> FeSe <sub>17</sub>	mon.	C2/m	1398.2(9)	876.2(4)	1094.3(7)	101°58(5)'	<a href="#">74N</a>
U <sub>8</sub> CoSe <sub>17</sub>	mon.	C2/m	1396.4(9)	875.2(4)	1093.3(7)	102°02(5)'	<a href="#">74N</a>
U <sub>8</sub> NiSe <sub>17</sub>	mon.	C2/m	1393.5(9)	874.9(4)	1090.4(7)	102°00(5)'	<a href="#">74N</a>
<b>Chevrel phases</b>							
Th <sub>1.2</sub> PbMo <sub>6</sub> S <sub>8</sub>	hex.	R $\bar{3}$	905		1137		<a href="#">78SCRF</a>
Th <sub>0.81</sub> Mo <sub>6</sub> S <sub>8</sub>	hex.	R $\bar{3}$	904.5(2)		1141.4(2)		<a href="#">96DPN</a>
U <sub>1.2</sub> PbMo <sub>6</sub> S <sub>8</sub>	hex.	R $\bar{3}$	905		1132		<a href="#">78SCRF</a>
UMo <sub>6</sub> S <sub>8</sub>	hex.	R $\bar{3}$	900.2(1)		1135.9(2)		<a href="#">96DPN</a>
U <sub>0.82</sub> Mo <sub>6</sub> Se <sub>8</sub>	hex.	R $\bar{3}$	934.3(1)		1180.7(4)		<a href="#">96DPN</a>
NpMo <sub>6</sub> Se <sub>8</sub>	hex.	R $\bar{3}$	945(1)		1191(1)		<a href="#">81DDH</a>
Np <sub>1.2</sub> Mo <sub>6</sub> Se <sub>8</sub>	hex.	R $\bar{3}$	946.2(5)		1191.5(6)		<a href="#">81DDH</a>

Compound	Symmetry	Point group (structure type)	Lattice parameters				Ref.
			<i>a</i> [pm]	<i>b</i> [pm]	<i>c</i> [pm]	$\beta$	
PuMo <sub>6</sub> Se <sub>8</sub>	hex.	R $\bar{3}$	948(1)		1191(1)		<a href="#">81DDH</a>
Pu <sub>1.2</sub> Mo <sub>6</sub> Se <sub>8</sub>	hex.	R $\bar{3}$	947.4(5)		1190.2(6)		<a href="#">81DDH</a>
			946.9(8)		1189(1)		<a href="#">81DDH</a>
AmMo <sub>6</sub> Se <sub>8</sub>	hex.	R $\bar{3}$	944.9(8)		1191(1)		<a href="#">81DDH</a>
Am <sub>1.2</sub> Mo <sub>6</sub> Se <sub>8</sub>	hex.	R $\bar{3}$	946.0(8)		1189(1)		<a href="#">81DDH</a>
			945.5(8)		1190(1)		<a href="#">81DDH</a>
<b>other chalcogenides</b>							
Th <sub>2</sub> CuTe <sub>6</sub>	mon.	P2 <sub>1</sub> /m	617.0(2)	433.2(1)	1042.4(3)	98.85(1)°	<a href="#">98NI</a>
U <sub>2</sub> Cu <sub>0.50</sub> Te <sub>6</sub>	mon.	P2 <sub>1</sub> /m	608.38(12)	421.40(8)	1036.1(2)	98.83(3)°	<a href="#">01PBBK</a>
U <sub>2</sub> Cu <sub>0.66</sub> Te <sub>6</sub>	mon.	P2 <sub>1</sub> /m	609.01(12)	420.83(8)	1033.5(2)	98.95(3)°	<a href="#">01PBBK</a>
U <sub>2</sub> Cu <sub>0.78</sub> Te <sub>6</sub>	mon.	P2 <sub>1</sub> /m	610.0(1)	421.50(7)	1036.5(2)	98.978(3)°	<a href="#">01HI</a>
U <sub>x</sub> Pd <sub>3</sub> S <sub>4</sub>	cub.	Pm3n	663.9(2)				<a href="#">86DN1</a>
x = 0.92		(M <sub>x</sub> Pt <sub>3</sub> O <sub>4</sub> )					
UPd <sub>2</sub> S <sub>4</sub>	tetr.	I4 <sub>1</sub> /a	673.4(1)		1184.1(4)		<a href="#">85DN</a>
U <sub>2</sub> PdS <sub>4</sub>	orth.	Fdd2	1072.5(3)	1314.8(4)	838.1(4)		<a href="#">86DN2</a>
U <sub>3</sub> Cu <sub>2</sub> S <sub>7</sub>	hex.	P6 <sub>3</sub>	973.08(8)		570.45(6)		<a href="#">96DLLN</a>
U <sub>3</sub> Cu <sub>2</sub> Se <sub>7</sub>	hex.	P6 <sub>3</sub>	1013.8(1)		595.25(7)		<a href="#">96DLLN</a>
U <sub>6</sub> Cu <sub>2</sub> S <sub>13</sub>	mon.	C2/c	1038.1(5)	1241.9(5)	1437.0(6)	103°47(5)'	<a href="#">80N,85NP</a>
U <sub>6</sub> Cu <sub>2</sub> Se <sub>13</sub>	mon.	C2/c	1083.9(4)	1291.2(5)	1491.2(7)	103°29(4)'	<a href="#">80N</a>
ThCuKSe <sub>3</sub>	orth.	Cmcm	418.32(8)	1433.5(3)	1085.9(2)		<a href="#">00NI</a>
ThCuCsSe <sub>3</sub>	orth.	Cmcm	421.05(7)	1571.5(3)	1089.7(2)		<a href="#">00NI</a>
UCuKSe <sub>3</sub>	orth.	Cmcm	411.2(2)	1443.7(3)	1067.5(2)		<a href="#">96SAHK</a>
UCuCsSe <sub>3</sub>	orth.	Cmcm	414.43(7)	1578.6(3)	1071.88(18)		<a href="#">01HMI</a>
UCuCsTe <sub>3</sub>	orth.	Cmcm	432.70(10)	1666.1(4)	1133.7(3)		<a href="#">95CI</a>
UTiCsTe <sub>5</sub>	orth.	Pmma	613.0(2)	824.0(2)	1036.3(2)		<a href="#">95CI</a>
UHF <sub>5</sub> Cs <sub>8</sub> Te <sub>30.6</sub>	mon.	P2 <sub>1</sub> /c	1204.3(2)	1872.4(4)	3049.6(6)	97.64(3)°	<a href="#">95CI</a>
U <sub>2</sub> Cu <sub>12</sub> K <sub>6</sub> S <sub>15</sub>	cub.	Ia $\bar{3}$ d	1864.2(7)				<a href="#">00SPSK</a>

**Table B.** Magnetic susceptibility data for actinide pnictides and chalcogenides containing d-electron transition metals.

Compound	$T_N(T_C)$ [K]	Type of fit	Curie-Weiss parameters				Ref.
			$\Theta$ [K]	$p_{\text{eff}}$ [ $\mu_B$ ]	$\chi_0$ [emu/mol]	Temperature range [K]	
URhSb	40	CW	−111	3.25		100...800	<a href="#">85BDPN</a> , <a href="#">87PNVV</a>
UPdSb	(65)	CW	70	2.92		100...800	<a href="#">85BDPN</a> , <a href="#">87PNVV</a>
UCuP <sub>2</sub> sc: $B \parallel c$ $B \perp c$	(75)	MCW	70	2.42	$28 \cdot 10^{-6}$	90...900	<a href="#">91KTN</a>
		CW	80	2.47		120...300	
		MCW	68	2.21	$570 \cdot 10^{-6}$	120...300	
		CW	41	2.62		120...300	
		MCW	30	2.30	$650 \cdot 10^{-6}$	120...300	
UCoAs <sub>2</sub>	(150)	MCW	160	2.15	$248 \cdot 10^{-6}$	160...300	<a href="#">00KNP</a>
UCuAs <sub>2</sub> sc: $B \parallel c$ $B \perp c$	(133)	MCW	127	2.46	$60 \cdot 10^{-6}$	140...900	<a href="#">91KTN</a>
		CW	131	2.77		160...300	
		MCW	133	2.68	$300 \cdot 10^{-6}$	160...300	
		CW	−10	3.08		160...300	
		MCW	22	2.61	$940 \cdot 10^{-6}$	160...300	
UPdAs <sub>2</sub>	240	CW	51	2.88		260...300	<a href="#">90MFK</a>
UNiSb <sub>2</sub>	174	CW	42	2.68		160...300	<a href="#">92K</a>
	175	MCW	57	2.46	$360 \cdot 10^{-6}$	190...300	<a href="#">98KKSM</a>
UCuSb <sub>2</sub>	(106)	MCW	111	2.10	$1060 \cdot 10^{-6}$	120...300	<a href="#">92K</a>
	(114)	MCW	105	2.31	$790 \cdot 10^{-6}$	120...300	<a href="#">98KKSM</a>
URuSb <sub>2</sub>	127	MCW	−40	1.91	$920 \cdot 10^{-6}$	150...300	<a href="#">98KKSM</a>
UPdSb <sub>2</sub>	196	MCW	20	2.43	$630 \cdot 10^{-6}$	210...300	<a href="#">98KKSM</a>
UAuSb <sub>2</sub>	(36)	MCW	42	2.25	$3850 \cdot 10^{-6}$	50...300	<a href="#">98KKSM</a>
UCuBi <sub>2</sub>	15, 51	MCW	31	2.94	$250 \cdot 10^{-6}$	60...300	<a href="#">92K</a>
UCo <sub>2</sub> P <sub>2</sub>	23,115, 199,(225)	CW	239(2)	2.28(3)		250...380	<a href="#">91RVJ</a>
UNi <sub>1.6</sub> As <sub>2</sub> sc: $B \parallel c$ $B \perp c$	175, (220)	CW	−300	3.6		500...1000	<a href="#">93TKKS</a> <a href="#">94TBNK</a>
	95,145,210						
		CW	90	3.10		210...300	
		CW	−200	3.10		200...300	
UFe <sub>4</sub> P <sub>12</sub>	(3.15)	CW	?	2.25		10...60	<a href="#">85MTYM</a>
U <sub>2</sub> Ni <sub>12</sub> P <sub>7</sub>	(29)	MCW	3(2)	1.6(1)	$183 \cdot 10^{-6}$	60...300	<a href="#">98EAJ</a>
U <sub>3</sub> Co <sub>3</sub> Sb <sub>4</sub>	(35)	CW	25	2.5		100...300	<a href="#">85BDPN</a>
	(10)	MCW	11.7	2.1	$667 \cdot 10^{-6}$	30...300	<a href="#">90ENMB</a>
U <sub>3</sub> Ni <sub>3</sub> Sb <sub>4</sub>		CW	−90	3.08		100...300	<a href="#">85BDPN</a>
		CW	−60.8	3.0		200...300	<a href="#">90ENMB</a>
		CW	−99	3.65		100...300	<a href="#">90TMFA2</a>
U <sub>3</sub> Cu <sub>3</sub> Sb <sub>4</sub>	(88)	CW	97.9	3.0		110...300	<a href="#">90ENMB</a>
	(91)	CW	110	3.39		100...300	<a href="#">90TMFA2</a>
U <sub>3</sub> Pd <sub>3</sub> Sb <sub>4</sub>		CW	−98	3.58		100...300	<a href="#">90TMFA2</a>
U <sub>3</sub> Pt <sub>3</sub> Sb <sub>4</sub>		CW	−184	3.68		100...300	<a href="#">90TMFA2</a>
U <sub>6</sub> Ni <sub>20</sub> P <sub>13</sub>	41	MCW	−37(4)	2.1(1)	$342 \cdot 10^{-6}$	60...300	<a href="#">98EAJ</a>
U <sub>6</sub> Rh <sub>20</sub> P <sub>13</sub>	12.7	CW	?	3		?	<a href="#">87GCMS</a>

Compound	$T_N (T_C)$ [K]	Type of fit	Curie-Weiss parameters				Ref.
			$\Theta$ [K]	$p_{\text{eff}}$ [ $\mu_B$ ]	$\chi_0$ [emu/mol]	Temperature range [K]	
UNi <sub>3</sub> P <sub>2</sub>	39	MCW	−28(3)	2.1(1)	$72 \cdot 10^{-6}$	60...300	<a href="#">98EAJ</a>
UMn <sub>4</sub> P <sub>2</sub>	125	CW	?	4.2		200...300	<a href="#">90JTRP</a>
UNi <sub>4</sub> P <sub>2</sub>	(21)	MCW	31(3)	1.9(1)	$48 \cdot 10^{-6}$	60...300	<a href="#">98EAJ</a>
U <sub>2</sub> Cu <sub>4</sub> As <sub>5</sub>	189	MCW	168	1.95	$926 \cdot 10^{-6}$	195...300	<a href="#">91KNT</a>
U <sub>3</sub> Cu <sub>2</sub> Sb <sub>3</sub>	(110)	CW	110	3.36		100...700	<a href="#">86DB</a>
U <sub>3</sub> Ni <sub>3.34</sub> P <sub>6</sub>	(139) Ferri	CW	107(3)	2.1(1)		150...300	<a href="#">95EJ</a>
U <sub>4</sub> Cu <sub>4</sub> P <sub>7</sub>	146	CW	68	2.66		190...300	<a href="#">90KTN</a>
sc: $B \parallel c$		CW	85	2.87		190...300	
$B \perp c$		MCW	−54	2.07	$826 \cdot 10^{-6}$	160...300	
UCuPO	220(2)	CW	0	2.68		230...300	<a href="#">94KANJ</a>
ThMnTe <sub>3</sub>	(~70)	CW	195	5.9 per Mn		210...300	<a href="#">00NI</a>
UCrS <sub>3</sub>	(110)	CW	−165	5.6*		150...1200	<a href="#">76WFBN</a>
	(137)	CW	−32	?		180...500	<a href="#">85NCKS</a>
UNbS <sub>3</sub>	(107)	CW	116	?		110...500	<a href="#">85NCKS</a>
URuS <sub>3</sub>	(26)	MCW	10	2.31	$923 \cdot 10^{-6}$	80...300	<a href="#">87DN</a>
URhS <sub>3</sub>	30	MCW	−51	2.53	$826 \cdot 10^{-6}$	90...300	<a href="#">87DN</a>
UTaS <sub>3</sub>	(113)	CW	100	?		190...500	<a href="#">85NCKS</a>
UPdSe <sub>3</sub>	11	MCW	−46	2.86	$610 \cdot 10^{-6}$	100...300	<a href="#">89DN</a>
U <sub>2</sub> CoS <sub>5</sub>	270	CW	?	6.17*		> 300	<a href="#">79WBFN</a>
U <sub>2</sub> CoS <sub>4</sub> Se	?	CW	−180	6.9*		100...300	<a href="#">93CSKM</a>
U <sub>2</sub> CoS <sub>3</sub> Se <sub>2</sub>	?	CW	−50	5.0*		100...300	<a href="#">93CSKM</a>
U <sub>2</sub> CoS <sub>2</sub> Se <sub>3</sub>	?	CW	−35	4.90*		100...300	<a href="#">93CSKM</a>
U <sub>2</sub> CoSSe <sub>4</sub>	?	CW	−30	4.85*		100...300	<a href="#">93CSKM</a>
U <sub>3</sub> Cu <sub>2</sub> S <sub>7</sub>		MCW	−33	2.50	$238 \cdot 10^{-6}$	50...300	<a href="#">96DLLN</a>
U <sub>3</sub> Cu <sub>2</sub> Se <sub>7</sub>	13	MCW	−28	2.64	$276 \cdot 10^{-6}$	50...300	<a href="#">96DLLN</a>
U <sub>6</sub> Rh <sub>2</sub> Se <sub>15.5</sub>	70	MCW	−192	3.41	?	120...300	<a href="#">96DN</a>
U <sub>6</sub> Ir <sub>2</sub> S <sub>15.5</sub>	57	MCW	−273	3.26	?	120...300	<a href="#">96DN</a>
U <sub>6</sub> Ir <sub>2</sub> Se <sub>15.5</sub>	75	MCW	−196	3.43	?	120...300	<a href="#">96DN</a>
UMo <sub>6</sub> S <sub>8</sub>		CW	−13.6	2.39		?	<a href="#">96DPN</a>
U <sub>0.82</sub> Mo <sub>6</sub> Se <sub>8</sub>	(25)	CW	−8.4	2.70		60...300	<a href="#">96DPN</a>
NpMo <sub>6</sub> Se <sub>8</sub>		CW	5(1)	1.25(5)		15...30	<a href="#">81DDG</a>
Np <sub>1.2</sub> Mo <sub>6</sub> Se <sub>8</sub>		CW	5(1)	1.25(5)		15...30	<a href="#">81DDG</a>
PuMo <sub>6</sub> Se <sub>8</sub>		CW	0	0.85(5)		2.5...30	<a href="#">81DDH</a>
		MCW	0	0.85	$504 \cdot 10^{-6}$	2.5...100	<a href="#">81DDH</a>
Pu <sub>1.2</sub> Mo <sub>6</sub> Se <sub>8</sub>		CW	0	0.85(5)		2.5...30	<a href="#">81DDH</a>
		MCW	0	0.85	$538 \cdot 10^{-6}$	2.5...100	<a href="#">81DDH</a>
U <sub>0.90</sub> Pd <sub>3</sub> S <sub>4</sub>		CW	−23	2.60		50...200	<a href="#">98FSYM</a>
			−26.3	2.71		30...270	<a href="#">98FSYM</a>
U <sub>2</sub> NiS <sub>4</sub>		CW	160	3.98		?	<a href="#">70DPLT</a>
U <sub>6</sub> Cu <sub>2</sub> S <sub>13</sub>		CW	−80	3.26		70...300	<a href="#">80N</a>
U <sub>6</sub> Cu <sub>2</sub> Se <sub>13</sub>		CW	−60	3.27		40...300	<a href="#">80N</a>
UTiCsTe <sub>5</sub>		MCW	−1.5	0.84	$2110 \cdot 10^{-6}$	?	<a href="#">95CI</a>

\* $\mu_B$  per mole

**Table C.** Hyperfine parameters of the  $^{121}\text{Sb}$  Mössbauer spectra of the  $\text{UTSb}_2$  compounds and the related  $\text{USb}_2$  compound [98KKSM]. The isomer shifts (IS) given are relative to the  $\text{CaSnO}_3$  source at 4.2 K or 77 K (measurements performed in the paramagnetic state).  $W$  – the linewidth of the Lorentzian shape;  $H_{\text{hf}}$  – the hyperfine field;  $eV_{zz}Q$  – the effective quadrupole coupling constant. The labels (1) and (2) refer to the Sb1 and Sb2 atoms, respectively (see Fig. 47). The parameters fixed in the fitting procedure are marked by the symbol \*. For the analysis of the data see the original paper.

Compound	$T$ [K]	$H_{\text{hf}}^{(1)}$ [kOe]	$H_{\text{hf}}^{(2)}$ [kOe]	$eV_{zz}Q^{(1)}$ [mm/s]	$eV_{zz}Q^{(2)}$ [mm/s]	IS <sup>(1)</sup> [mm/s]	IS <sup>(2)</sup> [mm/s]	$W$ [mm/s]
UCuSb <sub>2</sub>	125			13.1(3)	−4.7(5)	−9.84(5)	−7.77(4)	2.79(9)
	4.2	115(1)	137(2)	13.1*	−4.7*	−9.65(3)	−7.80(3)	2.82(5)
UNiSb <sub>2</sub>	186			12.8(6)	−6.5(6)	−9.9(1)	−7.93(8)	2.4(2)
	4.2	97(1)	106(1)	11.1(4)	−5.5(4)	−10.14(4)	−7.72(4)	2.40(6)
UPdSb <sub>2</sub>	210			10.7(6)	−7.4(6)	−9.77(5)	−7.76(4)	2.5*
	4.2	120(1)	128(1)	9.9(3)	−7.8(3)	−10.30(3)	−7.48(3)	2.50(6)
URuSb <sub>2</sub>	138			12.0(4)	−5.4(5)	−9.72(6)	−7.44(4)	2.5(2)
	4.2		44(1)	12.1(2)	−5.4*	−10.30(1)	−7.16(2)	2.7(3)
USb <sub>2</sub>	4.2	122(1)	104(1)	9.9(4)	−6.0(3)	−9.68(4)	−8.99(4)	2.92(3)

**Table D.** Contributions of the f-f ( $V_{\text{ff}}$ ), f-d ( $V_{\text{fd}}$ ) and f-p ( $V_{\text{fp}}$ ) hybridisation to the total covalent energy ( $V_{\text{total}}$ ) in  $\text{UTX}_2$  and  $\text{UX}_2$  compounds (T = 3d, 4d, 5d-electron transition metal, X = P, As, Sb) [98KKSM]. The calculations were performed by the Straub & Harrison's method. For the details and the analysis of the results see the original paper.

Compound	$V_{\text{ff}}$ [meV]	$V_{\text{fd}}$ [meV]	$V_{\text{fp}}$ [meV]	$V_{\text{total}}$ [meV]
UP <sub>2</sub>	90		1698	1700
UCuP <sub>2</sub>	91	195	1173	1193
UAs <sub>2</sub>	69		1137	1139
UCuAs <sub>2</sub>	70	190	1006	1026
UNiAs <sub>2</sub>	70	245	1021	1052
UCoAs <sub>2</sub>	68	271	999	1037
UPdAs <sub>2</sub>	65	335	1028	1088
USb <sub>2</sub>	41		882	883
URuSb <sub>2</sub>	36	493	793	934
UPdSb <sub>2</sub>	37	347	810	882

**Table E.** Crystal field parameters Bkq (in  $\text{cm}^{-1}$ ) obtained for  $\text{UCu}_2\text{P}_2$  and  $\text{UCuPO}$  from various ab initio crystal field models [95G]. PCM: point charge model; ECM: extended charge model; GEM: generalized electrostatic model; OVP: overlap model; REN: renormalization model; GPM: generalized perturbation model. For definitions and discussion of the results refer to the original paper. For definition of Bkq see also remark at Table H of section 1.3.3.3.

Compound	CF parameter	PCM	ECM	GEM	OVP	REN	GPM
$\text{UCu}_2\text{P}_2$	B20	711	354	28	115	209	237
	B43	−6228	2855	4638	−5729	−6193	−1555
	B60	980	−1132	765	94	115	−749
$\text{UCuPO}$	B20	−6729	−5064	−132	−66	−551	−638
	B40	−4535	−440	3215	−9053	−11855	−8640
	B60	1029	−760	−1850	3060	3272	1422

**Table F.** Curie-Weiss fit parameters for the magnetic susceptibility of  $\text{U}_8\text{TY}_{17}$  (Y = S, Se) [79NT].

Compound	$T_N$ [K]	$\Theta$ [K]	$p_{\text{eff}}$ [ $\mu_B/\text{f.u.}$ ]	$p_{\text{eff}}$ [ $\mu_B/\text{U atom}$ ]	$p_{\text{eff}}$ [ $\mu_B/\text{T atom}$ ]	Temperature range [K]
$\text{U}_8\text{TiS}_{17}$	-	−65	3.20	3.0	2.83	60...300
$\text{U}_8\text{VS}_{17}$	19	−110	3.54	3.2	3.87	150...300
$\text{U}_8\text{CrS}_{17}$	27	−30	3.41	3.0	4.90	80...300
$\text{U}_8\text{MnS}_{17}$	61	−100	3.86	3.2	5.92	160...300
$\text{U}_8\text{FeS}_{17}$	47	−80	3.70	3.3	4.90	100...300
$\text{U}_8\text{CoS}_{17}$	41	−120	3.93	3.6	4.5	90...300
$\text{U}_8\text{NiS}_{17}$	(40)	−105	3.53	3.4	2.83	130...300
$\text{U}_8\text{TiSe}_{17}$	5.5	−40	3.16	3.0	2.83	60...300
$\text{U}_8\text{VSe}_{17}$	31	−70	3.31	3.0	3.87	160...300
$\text{U}_8\text{CrSe}_{17}$	(60)	−60	3.62	3.2	4.90	100...300
$\text{U}_8\text{MnSe}_{17}$	74	−100	3.88	3.3	5.92	110...300
$\text{U}_8\text{FeSe}_{17}$	67	−60	3.70	3.3	4.90	120...300
$\text{U}_8\text{CoSe}_{17}$	30	−95	3.69	3.3	4.5	80...300
$\text{U}_8\text{NiSe}_{17}$	68	−125	3.56	3.4	2.83	170...300